QUANTIFYING EMISSIONS AND AIR QUALITY IMPACTS FROM UNCONVENTIONAL OIL AND GAS ACTIVITY IN THE EAGLE FORD SHALE

A Dissertation

by

GEOFFREY SCOTT ROEST

Submitted to the Office of Graduate and Professional Studies of
Texas A&M University
in partial fulfillment of the requirements for the degree of

DOCTOR OF PHILOSOPHY

Chair of Committee,	Gunnar Schade
Committee Members,	Sarah Brooks
	Don Collins
	Qi Ying
Head of Department,	Ramalingam Saravanan

December 2018

Major Subject: Atmospheric Sciences

ABSTRACT

Emissions from unconventional oil and gas are poorly constrained in existing inventories and contribute to uncertainties in our understanding of air quality near oil and gas producing regions. Emissions from the Eagle Ford Shale in southern Texas, which is a top oil and gas producing region in the US, are particularly uncertain due to a lack of ambient air quality data and the extensive use of flaring.

First, alkane emissions in the central Eagle Ford Shale were quantified using data collected by the state of Texas in a mass balance approach. The median emission rate from raw natural gas sources in the shale, calculated as a percentage of the total produced natural gas in the upwind region, was 0.7% with an interquartile range (IQR) of 0.5–1.3%, below the US Environmental Protection Agency's (EPA) current estimates. However, storage tanks contributed 17% of methane emissions, 55% of ethane, 82% percent of propane, 90% of n-butane, and 83% of isobutane emissions. The inclusion of liquid storage tank emissions results in a median emission rate of 1.0% (IQR of 0.7–1.6%) relative to produced natural gas, overlapping the current EPA estimate of roughly 1.6%. However, a recently published study using aircraft data suggests that this estimate may be biased low due to the position of the downwind monitor. Nonetheless, we conclude that emissions from liquid storage tanks are likely a major source for the observed non-methane hydrocarbon enhancements in the Northern Hemisphere.

Second, air quality measurements were performed at a field site in the western Eagle Ford Shale. Oil and gas sources dominated ambient VOC concentrations and

plumes from nearby sources were identified. Trace gas ratios suggest that many plumes originated from low-temperature combustion sources, which are likely to be nearby flares based on knowledge of regional emissions sources. Modeling exercises with parameterized flaring emissions show that plumes are capable of reaching Shape Ranch, and the observed emission ratios are within a factor of two of the modeled emission ratios based on EPA emission factors. Flaring emissions should be studied further to understand the scope of air quality impacts associated with widespread flaring.

ACKNOWLEDGEMENTS

I would like to thank my committee members and to my fellow students here at Texas A&M University who have helped me and guided me through my time as a student; to my friends with whom I have spent countless hours working, complaining, and having fun; and most importantly, to my family, who have supported me and my educational pursuits for years. I would not be here without my family.

CONTRIBUTORS AND FUNDING SOURCES

This work was supported by a dissertation committee including Associate Professor Gunnar Schade (advisor), Professor Sarah Brooks, and Professor Don Collins of the Department of Atmospheric Sciences, and Associate Professor Qi Ying of the Department of Civil Engineering.

The work presented in Section 2 was funded internally. Some data analyses in Section 2 were provided by Dr. Gunnar Schade. This work was previously published in the open-source journal *Atmospheric Chemistry and Physics* and is distributed under the Creative Commons Attribution 3.0 License.

The Shape Ranch Field Site was funded via a foundation from Hugh Fitzsimmons. Some data analyses in Section 3 were provided by Dr. Gunnar Schade. The Shape Ranch Field Site was set up, maintained, and visited by myself, Dr. Gunnar Schade, Dr. Sarah Brooks, Jake Zenker, Kristen Collier, Peter Bella, and Freddy Longoria. Dr. Qi Ying has provided guidance for modeling exercises.

NOMENCLATURE

AACOG	Alamo Area Council of Governments
bcf	Billion cubic feet of natural gas
BTEX	Benzene, toluene, ethylbenzene, and xylenes
EIA	Energy Information Administration
EPA	Environmental Protection Agency
GC-FID	Gas chromatograph with flame ionization detection
HYSPLIT	Hybrid Single Particle Lagrangian Integrated Trajectory model
MEK	Methyl ethyl ketone
mmbbl	Million barrels of oil
NAAQS	National Ambient Air Quality Standards
NARR	North American Regional Reanalysis
NMF	Non-negative matrix factorization
NMVOC	Non-methane volatile organic compound
OPE	Ozone production efficiency
RNG	Raw Natural Gas – emissions from natural gas infrastructure, either before or after separation of liquids
TCEQ	Texas Commission on Environmental Quality
TG	Tank Gas – emissions from liquid storage tanks
UOG	Unconventional oil and gas
VOC	Volatile organic compound

TABLE OF CONTENTS

LIST OF FIGURES

LIST OF TABLES

1. INTRODUCTION

Gaseous emissions from the exploration, development, and utilization of fossil fuels play a critical role in many facets of the Earth's climate and ecosystems. Greenhouse gas emissions, such as carbon dioxide (CO_2) and methane (CH_4), contribute strongly to the anthropogenic component of radiative forcing that is driving a gradual warming of the Earth's climate. Emissions of other gases, including hazardous air pollutants such as carbon monoxide (CO), nitrogen oxides ($NO + NO_2 = NO_x$), and reactive volatile organic compounds (VOCs) impact air quality, which has been identified as a chronic public health issue on the global scale (Landrigan et al., 2017).

A renaissance in onshore oil and gas development in the United States – largely due to the advent of new drilling methods – has generated renewed interest in the environmental and public health impacts from petroleum operations. A recurring theme in recent literature is the uncertainty and variability in atmospheric emissions from oil and gas activities. The uncertainty in emissions propagates through impact assessments and continues to be a point of scientific, political, and societal contention. Hence, this dissertation presents a quantification of emissions and an assessment of the associated air quality impacts from the Eagle Ford Shale – a prolific oil and gas producing region in southern Texas.

This introduction presents a literature review of atmospheric emissions from upstream oil and gas processes, the impacts of those emissions on both air quality and climate, an overview of the Eagle Ford Shale, and an outline of the research herein.

1.1. REVIEW OF UNCONVENTIONAL OIL AND GAS EMISSIONS

The development of unconventional oil and gas (UOG) reservoirs has reshaped the infrastructure of oil and gas in the U.S. Shale formations and oil sands have become accessible and economically viable due to developments in drilling methods and technology, notably hydraulic fracturing and horizontal drilling. Hydraulic fracturing is a hydrocarbon recovery process that uses a pressurized fluid to fracture shale formations. The fractures in the shale, which are held open by a proppant (e.g. sand), provide pathways for hydrocarbons to migrate into the wellbore from where they flow to the surface. Hydraulic fracturing is often used in combination with horizontal drilling, in which the wellbore axis is turned to run parallel to the shale formation, thereby maximizing the length of the well that is exposed to hydrocarbons (Yew & Weng, 2015).

From 2007 to 2016, oil production from shale plays increased from 157 to 1,551 million barrels (mmbbl) per year (U.S. Energy Information Administration, 2017a) while natural gas production from shale plays increased from 1,990 to 16,582 billion cubic feet (bcf) per year (U.S. Energy Information Administration, 2017b). Several shale areas in Texas have contributed to the increase in UOG production. The Permian Basin shales in Texas and New Mexico have become the most prolific oil producing shale plays in the United States, followed by the Eagle Ford Shale in Texas and the Bakken Shale in North Dakota. While natural gas production is dominated by the Marcellus Shale in northern Appalachia, the Eagle Ford Shale, the Haynesville Shale, and the Barnett Shale in Texas make notable contributions to natural gas production.

Oil and gas exploration, production, and transportation in these shale areas has introduced vast networks of infrastructure that serve as sources for atmospheric emissions of trace gases. Generally, emissions sources can be grouped into two categories: 1) combustion sources emit pollutants that are produced from burning fuel, while 2) evaporative and fugitive sources emit gases species directly into the atmosphere. Combustion of hydrocarbons produces CO_2, CO, VOCs produced via pyrolysis (Pikelnaya et al., 2013), and NO_x, which is produced in high-heat environments (Flagan & Seinfeld, 1988; Zeldovich, 1992). The combustion of hydrogen sulfide (H_2S), which is a component of sour natural gas, results in the emission of sulfur dioxide (SO_2) (Pikelnaya et al., 2013). Combustion emissions sources include flares, which are controlled, open-air flames used to destroy excess natural gas, and combustion engines, which provide power to drilling rigs, well-pad equipment such as compressor engines and electrical generators, and trucks used to transport petroleum and equipment.

Evaporative emissions from oil and gas exploration and production refer to the evaporation of liquid hydrocarbons. Evaporatives may be released from openings in liquid storage containers, including fuel containers for engines and large storage containers that are used to store produced petroleum prior to transportation to downstream processing facilities. Evaporative emissions may also come from frac water (water used for hydraulic fracturing, then returned to the surface), produced water (water in the hydrocarbon-containing geological formation that is produced along with oil and gas), and layers of Earth that are brought to the surface during the drilling process. Lastly, fugitive sources are unintentional leaks of gases from piping connections, such as

valves and flanges, and from routinely operating equipment, including pneumatic pumps, pneumatic controllers, and compressors. The composition of evaporative and fugitive emissions will vary regionally, with methane dominating emissions in natural gas producing areas while heavier VOCs will be emitted from oil producing areas. Evaporative and fugitive emissions may also contain species that are used in equipment during exploration and production, such as methanol (CH_3OH) , which is used to prevent methane hydrates from forming (Lyman et al., 2018).

The exploration process requires heavy duty machinery to clear and install a well pad, diesel trucks to transport materials and personnel, and eventually a drilling rig to drill the well, which is then tested for hydrocarbons. During the drilling process, drilling mud may be filtered in mud tanks to be reused. Some evaporative emissions may result from the degassing of drilling muds. Once the well has reached the targeted depth, the hydraulic fracturing process will commence. Before the well begins to produce hydrocarbons, some of the water used to fracture the shale returns to the surface and is often stored in open pits, which serve as another source for evaporative emissions (Lyman et al., 2018; Tran et al., 2018). Produced hydrocarbons are often partially processed on the well pad before transportation. On-site processing may include separation of crude oil, gases, and produced water. Glycol dehydrators may also be used to remove excess water. Sulfur may be removed by a variety of desulfurization processes (Abdel-Aal et al., 2003). Natural gas is compressed before it is sent into pipelines. While liquid hydrocarbons may also be transported via pipeline, storage tanks are often used to store liquids in shale areas until they are unloaded into trucks for transportation. Since

production rates from oil and gas wells will decrease overtime as the reservoir loses pressure, either drilling rigs are used to drill sidetracks from existing well bores, or exhausted wells are re-fractured to reestablish or enhance production.

1.2. ATMOSPHERIC EMISSIONS FROM UNCONVENTIONAL OIL AND GAS

1.2.1. IMPACTS OF SHALE ON CLIMATE

Greenhouse gas emissions from UOG have received attention in the atmospheric science community due to the potential impacts on Earth's climate (Intergovernmental Panel on Climate Change, 2015). While CO_2 is emitted from all carbon-based fuels, including coal, conventional oil, and biofuels, petroleum production in shale plays may have a comparatively large impact on radiative forcing due to high methane emission rates. The ratio of radiative forcing of a gas compared during its atmospheric lifetime versus that of CO_2 is expressed as the CO_2 equivalent forcing, or CO_2e. Methane has a CO_2e of 34 on a 100-year time scale and 108 on a 10-year time scale (Intergovernmental Panel on Climate Change, 2015), so curbing methane emissions is critically important to reducing the climate impact of fossil fuel as an energy source. The climate impacts of various energy sources can be compared by estimating the radiative forcing of emissions normalized to energy production (e.g. W m^{-2} MJ^{-1}). Howarth (2014) presented a meta-analysis of radiative forcing associated with various fossil fuel sources, including coal, conventional oil, and natural gas from shale plays. Alvarez et al. (2012) found that radiative forcing per unit energy due to electricity generation from natural gas power

plants would match that of coal fired power plants if methane emissions did not exceed 3.2% by volume during the entire natural gas lifecycle.

Methane emissions from UOG development in the US are poorly quantified due to widely varying and largely uncertain emission estimates. According to the US Environmental Protection Agency's (EPA) 2016 greenhouse gas inventory (U.S. Environmental Protection Agency, 2016a), approximately 6,570 Gg of methane was emitted from all oil and gas field production in the US and in offshore federal waters in 2011 when voluntary emission reductions are included. This corresponds to 12×10^9 m^3 of natural gas at 1 atm and 15 °C, assuming an average methane content of 80% by volume in raw US natural gas (Pétron et al., 2012). During the same year, nationwide gross natural gas production from oil and gas wells totaled 756×10^9 m^3 (U.S. Energy Information Administration, 2017b). Therefore, the EPA's emission rate of natural gas from oil and gas field production in the US in 2011 was 1.6% relative to the volume of produced natural gas. The EPA's 2016 greenhouse gas inventory estimated methane emissions of 6,985 Gg in 2013, which, when compared to the 2013 US natural gas production of 853×10^9 m^3, yields a relative emission rate of 1.5 %, a slight reduction from 2011. However, the EPA's methane emission estimates from US oil and gas field production in the 2016 greenhouse gas inventory increased from the 2015 EPA greenhouse gas inventory (U.S. Environmental Protection Agency, 2015a). In the 2015 greenhouse gas inventory, the estimated methane emissions from US oil and gas field production for 2013 totaled 2,722 Gg or 0.6% of produced natural gas by volume. The

increase between the 2015 and 2016 greenhouse gas inventories is due, in part, to updated emission factors for methane emissions.

Several so-called top-down studies, in which observed methane emissions are attributed to source types, found that methane emission rates from shale gas exceeded 3.2%. Notably, (Pétron et al., 2014) measured an emission rate of 4.1% (1 σ uncertainty of ± 1.5%) from Weld County in the Denver-Julesburg Basin in the Colorado Front Range. Karion et al. (2013) found emissions of 6.2-11.7% (1 σ) from the Uintah Basin in Utah. Peischl et al. (2018) used aircraft measurements over several shale plays to estimate basin-wide emissions during the SONGNEX campaign in 2015. Their emissions estimates included the eastern and western portions of the Eagle Ford Shale, for which they estimated 3.2% ± 1.1% and 2.0% ± 0.6%, respectively, of the produced natural gas was emitted into the atmosphere. Additional emissions estimates relative to produced natural gas were 5.4% ± 2.0% for the Bakken Shale, 1.5% ± 1.0% for the Barnett Shale, 2.1% ± 0.9% for the Denver-Julesburg basin, and 1.0% ± 0.5% from the Haynesville Shale. Meanwhile, Allen et al. (2013) performed a bottom-up study, in which emissions from individual components were measured and extrapolated to the shale play scale using equipment inventories and emission factors, finding a U.S. average methane emission rate of 0.42% by volume from shale plays. While this study has been lauded by industry as evidence of low emission rates, it has been criticized, among other issues, for an apparent equipment malfunction that caused methane emissions to be underestimated (Howard et al., 2015, Howard, 2015). Nonetheless, similar bottom-up emissions estimates have shown comparatively low emissions rates,

suggesting that shale gas has a lower radiative forcing compared to coal when normalized to energy production.

The discrepancy between top-down and bottom-up emission estimates has become a focal point of research projects. Coordinated surface- and aircraft-based campaigns have attempted to reconcile this difference. A 2013 campaign sponsored by the Environmental Defense Fund produced a series of studies in the Barnett Shale in the Fort Worth, Texas, metropolitan and adjacent areas, in which top-down and bottom-up emissions were reasonable comparable. Karion et al. (2015) used aircraft measurements to estimate a top-down methane gas emission rate of 1.3 – 1.9%. Smith et al. (2015) used fast-response ethane (C_2H_6) measurements to constrain methane emissions from natural gas, as ethane is the second most abundant compound in natural gas (Xiao et al., 2008) and is not known to be produced by microbial processes (Simpson et al., 2012). Lyon et al. (2015) used surface-based methane measurements in the Barnett Shale to produce a bottom-up estimate of 1.0 – 1.4%. The uncertainty bounds of these coordinated studies overlapped and suggest methane production from the Barnett Shale may be favorable to coal when considering radiative forcing. More recently, Alvarez et al. (2018) estimated emissions over nine oil and gas producing basins, accounting for roughly 30% of nationwide production, using ground-based and facility scale measurements and validated using aircraft measurements. They find a net methane emission rate from the surveyed regions that is equal to 2.3% (2.0 - 2.7%) of the produced natural gas. While this emission rate exceeds the US EPA greenhouse gas inventory, it is still less than the 3.2% threshold identified by Alvarez et al. (2012).

While ground-based and aircraft-based trace gas measurements provide comprehensive data that can be used to elucidate information about regional emissions, these methods are limited in their spatial and temporal representation of the atmosphere over an oil and gas producing region. However, satellite-based measurements of methane provide continuous, regional observations of atmospheric methane concentrations. A study of the U.S. Four Corners region (Kort et al., 2014) demonstrated an underestimation of methane emissions in bottom-up inventories from oil, gas, and coalbed methane. Schneising et al. (2014) used satellite-based measurements to quantify methane concentration trends over the Eagle Ford Shale and the Bakken Shale in North Dakota between 2006-2008 and 2009-2011. The increased methane concentrations were compared to increased petroleum production in a mass-balance approach, and the resulting emissions estimate for the Eagle Ford Shale was 9.1% ± 6.2% of produced energy, indicating that the methane emissions in this region have a larger impact on radiative forcing than coal. Similarly, an emission rate of 10.1% ± 7.3% was found for the Bakken Shale.

Despite the wealth of information from recent studies of methane emissions from UOG development in the US, some uncertainty remains in the climate impacts from shale oil and gas production. While difference between top-down and bottom-up estimates have been constrained in certain regions, there are many shale areas where limited data has prevented comprehensive emissions estimates. Emissions from these shale areas, which are often rural and recently-developed, remain poorly quantified. This

is especially true of shale areas with unique infrastructure and processes, such has liquids-rich shale areas.

1.2.2. IMPACTS OF SHALE ON AIR QUALITY

In addition to the relatively inert greenhouse gas emissions, more reactive gases are also emitted from oil and gas operations. These gases, and/or their reaction products, pose threats to human health and ecosystems. The U.S. Environmental Protection Agency (EPA) monitors six "criteria pollutants" (U.S. Environmental Protection Agency, 2014) – O_3, particulate matter (PM), NO_2, SO_2, lead (Pb), and CO - in addition to so-called "hazardous air pollutants" (U.S. Environmental Protection Agency, 2015e), all of which pose air quality risks. Many of these pollutants are associated with emissions from oil and gas operations. Note that PM, SO_2, and Pb are not covered in this study.

1.2.2.1. CARBON MONOXIDE

Carbon monoxide (CO) is emitted from the incomplete combustion of carbon-based fuels. Exposure to high CO concentrations is associated with an increased risk of heart disease, in addition to acute symptoms such as headaches and dizziness. Epidemiological studies of long-term exposure to ambient atmospheric CO concentrations have demonstrated an increased mortality associated with CO, though these studies are largely uncertain as CO often coexists in high ambient concentrations with other pollutants (Wilbur et al., 2012). To the author's knowledge, there exists no

literature specifically quantifying the impact of UOG development on ambient CO concentrations. However, as CO is emitted from combustion sources, any development that utilizes combustion engines or natural gas flares will be associated with CO emissions, though these emissions may be offset by reduced emissions in other sources and/or locations.

1.2.2.2. NITROGEN OXIDES

Gaseous nitrogen emissions from high-temperature processes through thermal N_2 fixation (Flagan & Seinfeld, 1988; Zeldovich, 1992) have many impacts on air quality. Nitrogen oxide ($NO + NO_2 = NO_x$) emissions are regulated by the EPA due to their acute impacts on human health. Exposure to high NO_2 concentrations has been linked to increased susceptibility to infections (Chauhan et al., 1998), emphysema-like lesions (Wegmann et al., 2005), and airway inflammation (Poynter et al., 2006). However, acute health impacts of NO_x exposure, such as asthma, may be mostly due reaction products of NO_x – namely ozone and particulate matter, which are discussed in latter sections.

Satellite-based measurements of tropospheric NO_2 have shown decreasing trends across much of the United States since 2005, especially over populated areas (Duncan et al., 2016). This trend is due to decreased NO_x emissions from vehicles (Lamsal et al., 2015, Simon et al., 2015) and other anthropogenic sources. The development of unconventional natural gas has been associated with reduced NO_x emissions at power plants as natural gas has replaced coal (de Gouw et al., 2014). Meanwhile, local and regional emissions of NO_x will be impacted in UOG producing regions due to the

utilization of combustion processes, including on-site power generation (Field et al., 2014), flaring (Torres et al., 2012, Pikelnaya et al., 2013), and industry-related traffic (Goodman et al., 2016).

Duncan et al. (2016) highlighted increasing NO_2 column abundances over three shale areas: the Eagle Ford, the Permian Basin, and the Bakken Shale. While these three shale areas all feature extensive flaring (Elvidge et al., 2015), the individual sources contributing to the observed NO_2 increase have yet to be determined (Parrish et al., 2017). The potential contributions from flaring are particularly poorly quantified, as flaring emissions depend on the flaring efficiency (Strosher, 2000) and flaring may be underreported in existing emissions inventories (Willyard, 2017).

1.2.2.3. VOLATILE ORGANIC COMPOUNDS

Volatile organic compounds (VOCs) consists of many organic compounds present in the gas phase. VOCs are emitted from both natural and anthropogenic sources, including oil and gas production. While the primary interest in air quality impacts from VOC emissions is the formation of ozone, many VOCs are classified as hazardous air pollutants (HAPs) for their harmful impacts on human health. Alkanes are found in abundance in petroleum, from methane in natural gas through long-chain alkanes with tens of carbon atoms in crude oil. Very high concentrations of alkanes such as n-pentane, n-hexane, and n-nonane can cause neurological health issues (McKenzie et al., 2012; U.S. Environmental Protection Agency, 2009). A group of aromatic compounds known as BTEX – benzene, toluene, ethylbenzene, and xylenes – are found in crude oil and in

combustion emissions. Benzene has been shown to be a cause of leukemia (Vigliani & Forni, 1976) and is listed as a carcinogen (U.S. Centers for Disease Control, 2014), while chronic exposure to benzene has been linked with impacts to the endocrine system (Bahadar et al., 2014). Toluene and xylenes have been associated with neurological and renal effects, and ethylbenzene impacts the respiratory system (Hinwood et al., 2007).

VOC emissions from UOG development, and their subsequent role in ambient air quality, vary between shale plays. High VOC concentrations have been observed over liquids-rich shale plays, such as the Eagle Ford Shale, the Bakken Shale, and the Permian Basin (Schade & Roest, 2016; Kort et al., 2016; Koss et al., 2017), where evaporative emissions from liquid storage tanks have been identified as a major VOC emission source (Hendler et al., 2009; Lyon et al., 2016). Emission rates of VOCs and their impacts on ambient air quality and human health remain somewhat uncertain due to the number of compounds emitted (Koss et al., 2017), the role of other VOC emissions sources (Watson et al., 2001; Ying & Krishnan, 2010), and the effects of other trace gases and meteorology (Seinfeld & Pandis, 1998).

1.2.2.4. OZONE

Ozone (O_3) is a pollutant that can cause respiratory irritation and exacerbate chronic health conditions including asthma, bronchitis, and emphysema (U.S. Environmental Protection Agency, 2015b). Worldwide, O_3 was estimated to have caused 300,000 premature deaths in 2015 (Landrigan et al., 2017). In the U.S., 116 million

people live in counties that are designated as nonattainment areas by the US EPA for O_3 (U.S. Environmental Protection Agency, 2016b).

Emissions of VOCs and NO_x contribute to the formation of O_3 in the presence of sunlight via the production of peroxy-radicals and their reactions with NO (Crutzen et al., 1999; Seinfeld & Pandis, 1998):

$$RH + OH \rightarrow R + H_2O \qquad (R = \text{organic “Rest”, e.g. } C_4H_9) \tag{1.1}$$

$$R + O_2 + M \rightarrow RO_2 + M \tag{1.2}$$

$$RO_2 + NO \rightarrow RO + NO_2 \tag{1.3}$$

$$RCH_2O + O_2 \rightarrow RCHO + HO_2 \tag{1.4}$$

$$HO_2 + NO \rightarrow OH + NO_2 \tag{1.5}$$

$$NO_2 + h\nu\ (\lambda < 400\ \text{nm}) \rightarrow NO + O(^3P) \tag{1.6}$$

$$O + O_2 + M \rightarrow O_3 + M \tag{1.7}$$

During daytime, O_3 is photolyzed to produce OH radicals starting the oxidation chain:

$$O_3 + h\nu\ (\lambda < 340\ \text{nm}) \rightarrow O_2 + O(^1D) \tag{1.8}$$

$$O(^1D) + H_2O \rightarrow 2\ OH \tag{1.9}$$

Furthermore, its reaction with NO

$$NO + O_3 \rightarrow NO_2 + O_2 \tag{1.10}$$

followed by reactions 1.6 and 1.7 creates a null-cycle, which drives diurnal changes in ozone based on incident UV-radiation. Additional (excess) ozone is formed via reactions 1.3 and 1.5 followed by reactions (2 ×) 1.6 and 1.7 without loss of ozone in reaction 1.10. Thus, net daytime ozone formation results from the creation of two peroxy-

radicals, oxidizing two NO to NO_2, which photolyzes to produce O_3 via reactions 1.6 and 1.7. At very low NO_x abundances, peroxy-radicals may react with ozone itself

$$HO_2 + O_3 \rightarrow OH + 2O_2 \quad (1.11)$$

while at very high NO_x abundances, OH radicals oxidize NO_2 faster than it photolyzes

$$OH + NO_2 + M \rightarrow HNO_3 + M \quad (1.12)$$

In either case, daytime ozone production efficiency is lowered. The threshold for net ozone formation corresponds to approximately 0.02 ppb NO, which is exceeded essentially everywhere in the continental boundary layer.

The potential for O_3 formation from a source depends on the emissions from the source, the background concentrations and other regional sources of pollutants, and meteorology. However, daytime O_3 enhancements have been attributed to oil and gas emission sources in several shale plays (Ahmadi & John, 2015; Ahmadov et al., 2015; Cheadle et al., 2017; Swarthout et al., 2015; Ying & Krishnan, 2010). Small-scale modeling has shown localized O_3 enhancements of up to 10 ppb downwind from a natural gas flare (Olaguer, 2012). Pacsi et al. (2015) found O_3 enhancements of up to 2.5 ppb in San Antonio and 1.9 ppb in Austin due to emissions from the Eagle Ford Shale, though a previous modeling study by the Alamo Area Council of Governments (AACOG, 2013) showed an O_3 enhancement of less than 1 ppb at O_3 monitoring sites between low- and high-production scenarios for the Eagle Ford Shale. However, these regional modeling exercises rely on emissions inventories that are highly uncertain, especially for certain emissions sources such as flaring. Meanwhile, in the presence of NO emission sources, O_3 is titrated at night via reaction 1.10. Thus, in oil and gas fields

with large combustion emissions, nighttime O_3 titration often occurs, with rapid O_3 formation as NO_2 is photolyzed on the following day.

1.3. THE EAGLE FORD SHALE

The state of Texas has been one of the top oil and gas producing regions in the U.S. for decades (U.S. Energy Information Administration, 2018c). However, Texas has reestablished dominance in onshore energy production within the past decade due to the development of numerous shale areas (Fig. 1). These regions include the Haynesville Shale in northeast Texas and Louisiana, the Barnett Shale in north-central Texas, the Permian Basin shales in western Texas and New Mexico, and the Eagle Ford Shale in south-central Texas. The Eagle Ford Shale extends eastward from the U.S.-Mexico border, between Laredo and Del Rio, through numerous counties south and east of San Antonio, and northeastward into the Brazos River Valley (Fig. 2). Oil and gas production began developing rapidly in the center of the shale in 2008, when 0.002 billion cubic feet (bcf) of natural gas per day (U.S. Energy Information Administration, 2018a) and 0.6 thousand barrels of oil (kbbl) per day (U.S. Energy Information Administration, 2018b) were produced. In 2017, shale gas and oil production had increased to 4.0 bcf per day and 12,926 kbbl per day, respectively, making the Eagle Ford Shale the second largest oil producing shale and the fifth largest natural gas producing shale in the United States in 2017. Figure 3 shows gross oil and gas production and the drilling rig count from 2007 through 2017 (U.S. Energy Information Administration, 2018d). Note that production values in this figure are higher than the

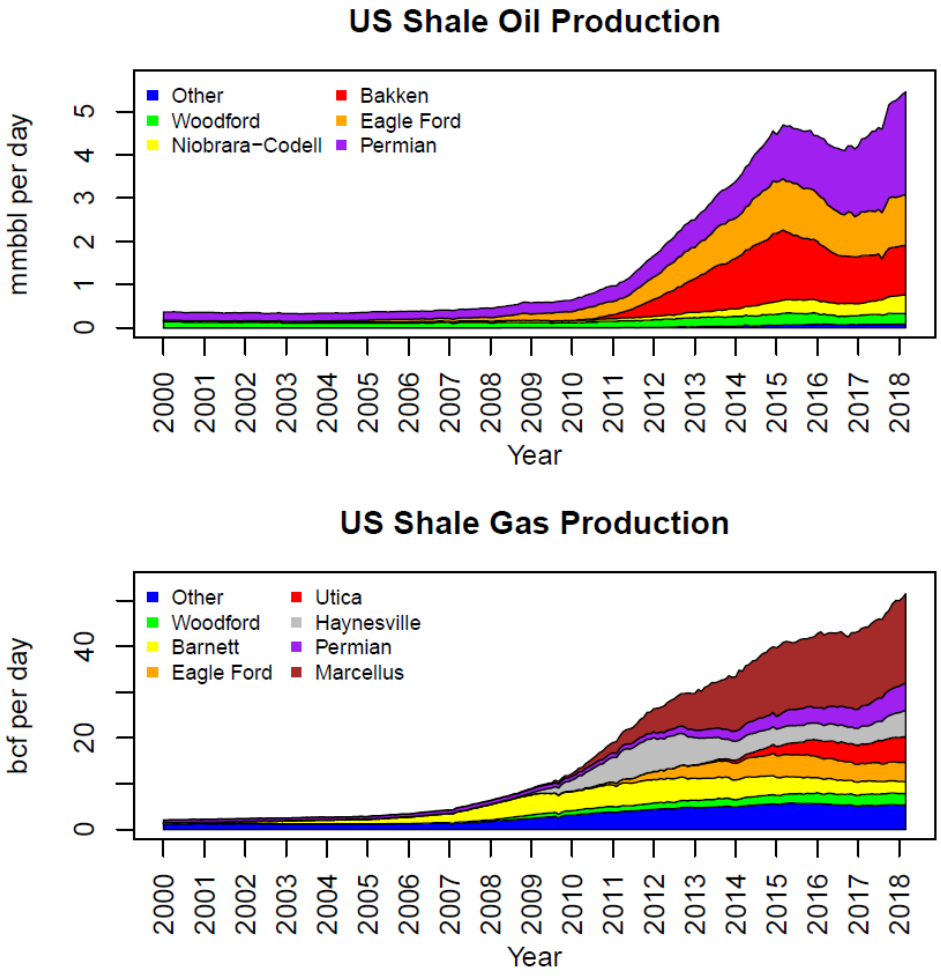

Figure 1: Timeline of oil (top) and gas (bottom) production in US shale plays from January 2011 to March 2018 (U.S. Energy Information Administration, 2018a, 2018b).

shale oil and gas production noted above, as gross production, including legacy natural gas, is included in Fig. 3. The rig count peaked at 279 in May 2012 and stayed above 200 from July 2011 through January 2015. This period represents the shale “boom”, when favorable oil and gas prices led to intensive drilling and new production. While drilling has slowed since oil prices dropped at the end of 2014 (U.S. Energy Information Administration, 2018e), the Eagle Ford continues to be a highly-productive shale play.

As the Eagle Ford Shale rapidly developed in rural Texas, a limited pipeline network led to widespread flaring to destroy gas that would otherwise be emitted into the atmosphere. Flaring is often used at oil wells to destroy co-produced natural gas, known as "associated gas" or "casinghead gas". Because oil is more profitable than natural gas, operators may choose to destroy associated gas because of the high initial cost of so-called "vapor recovery", in which the associated gas is captured and either sold to market or used to fuel equipment on the well pad. Instead, resources are focused on the

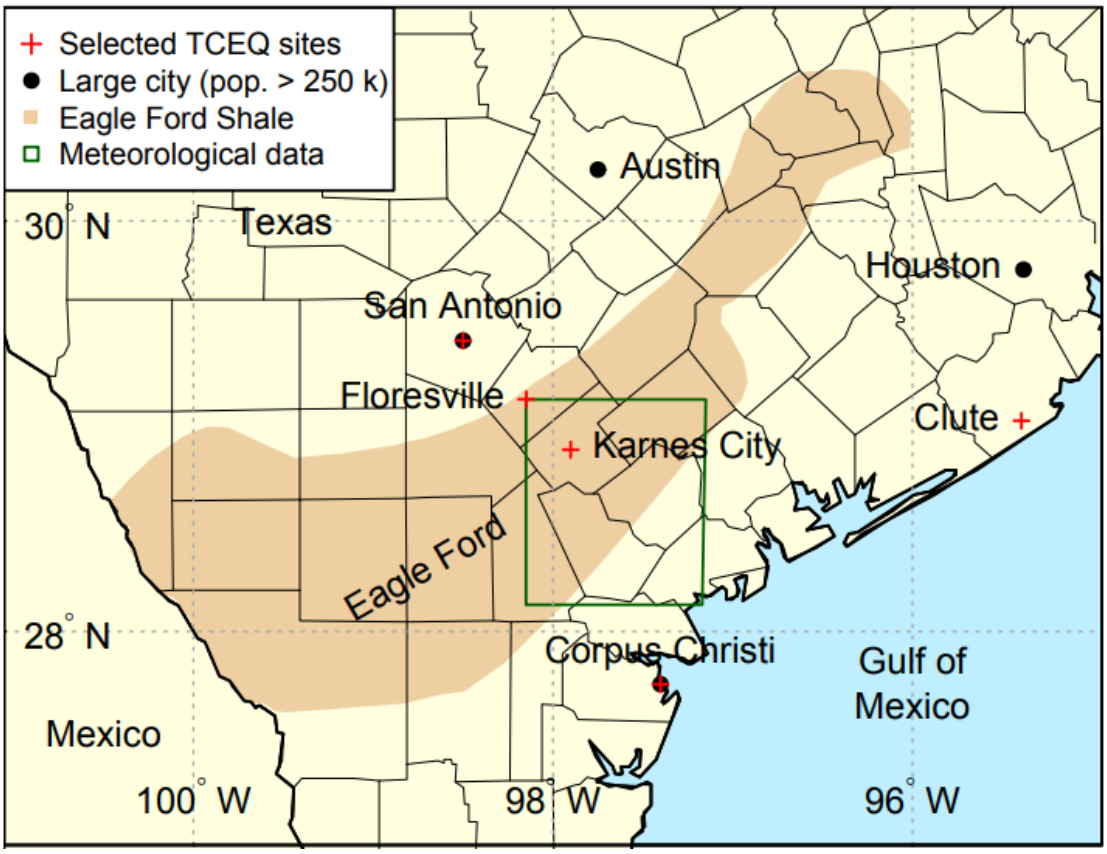

Figure 2. Selected TCEQ NMVOC monitoring sites and large cities near the Eagle Ford, as discussed in Sect. 2. The green box shows the 1° latitude by 1° longitude box in which the meteorology was assessed (Sect. 2).

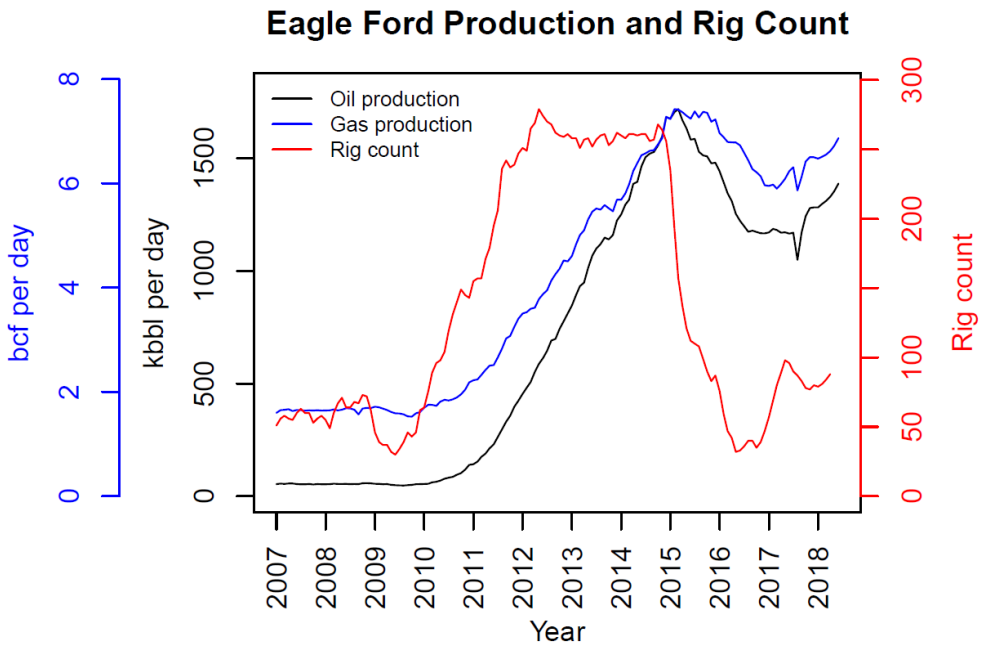

Figure 3: A timeline of gross oil production, natural gas production, and the drilling rig count in the Eagle Ford Shale, including legacy oil and gas production (U.S. Energy Information Administration, 2018d).

more valuable oil. Flaring has been widely used in the Eagle Ford Shale to destroy excess natural gas produced at oil wells and headspace vapors at midstream processing and storage facilities. The Eagle Ford Shale, along with the Bakken Shale and the Permian Basin, has been identified in satellite imagery as a region with a high density of observed flares (Elvidge et al., 2015), as shown in Fig. 4. However, the air quality impacts associated with flaring in the Eagle Ford Shale cannot be properly assessed using existing inventories and regional modeling since it appears that flaring volumes are underreported (Willyard, 2017), and flaring emission factors are highly uncertain (Strosher, 2000; Torres et al., 2012; U.S. Environmental Protection Agency, 2016c).

Emissions from flaring may have significant air quality impacts on a local- to regional-scale (Olaguer, 2012) and need to be better quantified.

The proximity of the Eagle Ford Shale to the city of San Antonio has raised air quality concerns, as the city's ozone design values have consistently been above the EPA's 8-hour ozone National Ambient Air Quality Standard (NAAQS) for several years. However, due to the large uncertainties in emissions from oil and gas, the age of the shale, the use of flaring, and the sparsity of ambient air quality measurements, the local and regional air quality impacts of the Eagle Ford Shale remain poorly quantified. Thus, emissions from various sources within the oil and gas fields need to be properly quantified before the air quality impacts can be accurately assessed.

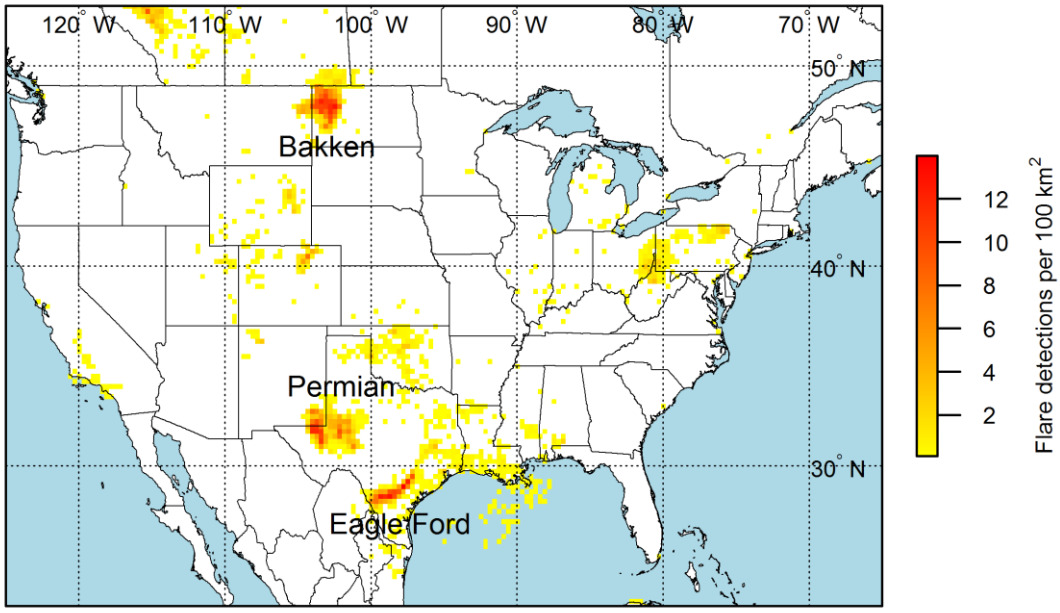

Figure 4: Flaring densities from 2012 to 2016 using data from the VIIRS instrument (Elvidge et al., 2015)

1.4. STUDY OBJECTIVES

To develop sensible policy actions to address air quality issues related to unconventional oil and gas development, the emissions and subsequent air quality impacts need to be quantified. Two studies are presented to address these issues as follows:

1. In Section 2, alkane emissions in the central Eagle Ford Shale are quantified using state-run air quality monitoring data in a mass-balance approach – a meteorology-based model that does not depend on *a priori* emissions information. Therefore, it serves as an independent check on VOC emissions estimates in existing inventories, such as that of the AACOG inventory for the Eagle Ford Shale. Methane emissions are also quantified and are used to assess the representativeness of emissions rates from existing inventories – many of which suggest that natural gas is preferable to coal in terms of radiative forcing. Lastly, this study uses a Monte Carlo simulation to identify factors that contribute largely to the uncertainty in the resultant emissions estimates.
2. Section 3 presents a thorough assessment of ambient air quality measurements on Shape Ranch – a working bison ranch in southwestern Dimmit County in the western Eagle Ford Shale. This site, which is far removed from urban emissions, provides important data for ambient air quality in the more rural regions of the Eagle Ford Shale. This assessment provides crucial information about the exposure to pollution of rural communities in the Eagle Ford Shale, and the air-mass composition that may be advected into major urban areas, such as San

Antonio. This measurement site was also downwind of several flares, and an analysis of plume compositions and potential source attribution is presented. Lastly, a scalable, Eulerian photochemical transport model is used to assess the potential air quality impacts of nearby flares. Flaring emissions factors used in bottom-up emissions inventories are at times poorly constrained. Comparing modeled flare emissions to the ambient air quality data on Shape Ranch serves as a validation of existing flaring emission factors. The local and regional impacts of flaring emissions are also assessed with modeling exercises, furthering our knowledge of air quality impacts in flaring-dense regions.

2. QUANTIFYING REGIONAL ALKANE EMISSIONS*

This study uses the atmospheric enhancement of short-chain alkanes – ethane (C_2), propane (C_3), isobutane (iC_4), n-butane (nC_4), isopentane (iC_5), and n-pentane (nC_5) – between upwind and downwind measurement locations to estimate alkane emissions from a region in southeastern Texas including the core of the Eagle Ford Shale. Alkanes dominate atmospheric OH radical reactivity at a TCEQ monitoring site north of the Eagle Ford Shale (Schade & Roest, 2016) and the emission estimates for these short-chain alkanes are needed to assess the potential air quality impacts from the Eagle Ford Shale. We focus on ethane as a tracer for oil and gas emissions as it is the second-most abundant compound in natural gas (Xiao et al., 2008) and, unlike methane, it is not emitted by microbial sources in significant quantities (Simpson et al., 2012). Recent increases in ethane abundance in the Northern Hemisphere have been linked to UOG production in the US (Franco et al., 2016; Helmig et al., 2016; E. A. Kort et al., 2016). Ethane has thus been used in previous oil and gas emission estimates (Schwietzke et al., 2014; Smith et al., 2015), and statistically significant increases in ethane mixing ratios have been observed downwind of the Eagle Ford Shale during its development (Schade & Roest, 2015). The C_3 and C_4 alkane-to-ethane enhancement ratios are used to estimate the relative contributions of raw natural gas emissions and vented gases from liquid storage tanks, two major sources of gaseous emissions from upstream UOG that have varying compositions (Brantley et al., 2014; Field et al., 2014; Kort et al., 2016;

Lyon et al., 2015). A mass balance approach and a Monte Carlo simulation are then used to estimate the emissions of C_2–C_4 alkanes from raw natural gas emissions and liquid storage tank venting, as well as the associated uncertainties. Methane emissions are also estimated using methane-to-ethane ratios in raw natural gas and vented storage tank gas. Lastly, the methane emission rate is expressed as a fraction of the produced natural gas to compare our emission estimate with other top-down studies.

2.1. METHODS

2.1.1. TCEQ DATA

The TCEQ operates a network of air quality monitoring sites across the state of Texas, some of which measure non-methane VOCs (NMVOCs) including alkanes, alkenes, cycloalkanes, and aromatics. The TCEQ collects NMVOC data to the east and southeast of the Eagle Ford Shale in Clute and at several sites in Corpus Christi, including Hillcrest and Oak Park (Fig. 2), which were selected for use in this study due to data availability and their location. Other sites in Corpus Christi are immediately downwind of major local point sources when winds are blowing from the Gulf of Mexico. To the northwest of the Eagle Ford Shale, NMVOC data have been collected since summer 2013 in Floresville, a small city immediately north of the shale area, and in northwest San Antonio (Old Highway 90). Descriptions of the five sites that are used in this study are presented in Table 1. Data from these sites have been previously used to demonstrate trends in ethane mixing ratios near the Eagle Ford Shale (Schade & Roest, 2015). The emission estimates in this study were performed using hourly ethane data

Table 1. Description of TCEQ sites used in this study.

Site name	AQS Code	Lat (°N)	Long (°W)	Sample durations	Samples Collected	Use in study
Clute	480391003	29.01	95.40	24 h	Once every 6 days	Long-term trends
Corpus Christi – Hillcrest	483550029	27.81	97.42	24 h	Once every 6 days	Long-term trends
Corpus Christi – Oak Park	483550035	27.80	97.43	40 min	Hourly, automated	Emission estimate
Floresville Hospital Boulevard	484931038	29.13	98.15	40 min	Hourly, automated	Emission estimate
San Antonio – Old Highway 90	480290677	29.42	98.58	24 h	Once every 6 days	Long-term trends

from the automated ozone precursor monitoring sites in Floresville and Corpus Christi – Oak Park (hereafter referred to as Oak Park). While the Oak Park site was installed before the oil and gas boom in the Eagle Ford Shale, data for Floresville are only available since 19 July 2013. Therefore, direct data comparisons were performed only for a 30-month period from July 2013 through December 2015.

Alkane mixing ratios at Floresville and Oak Park were compared under south to southeasterly flow regimes, when Corpus Christi is upwind of the Eagle Ford Shale and Floresville is downwind. South to southeasterly flow regimes were identified using 48 h back trajectories originating at Floresville from the Hybrid Single-Particle Lagrangian Integrated Trajectory (HYSPLIT) model (Stein et al., 2015). The trajectories were run four times per day at an interval of 6 h beginning at 06:00 UTC (00:00 LST). The EDAS 40 km dataset (National Centers for Environmental Prediction (NCEP), 2016) was used

for meteorology in the HYSPLIT model. This dataset, which adequately captures synoptic scale flow, was chosen for computational efficiency.

In order to identify days with mostly southeasterly flow, 48 hour back trajectories were obtained, with start times of 06:00, 12:00, and 18:00 UTC each calendar day, and 00:00 UTC the following calendar day. The origins of the trajectories were binned by their passage through a series of polygons, as shown in Fig. 5. The vertices of the polygons are provided in Table 2. Back trajectories ending at the San Antonio – Old Highway 90 site were used to identify southeasterly flow when assessing long term alkane trends at San Antonio – Old Highway 90, Clute, and Corpus Christi – Hillcrest.

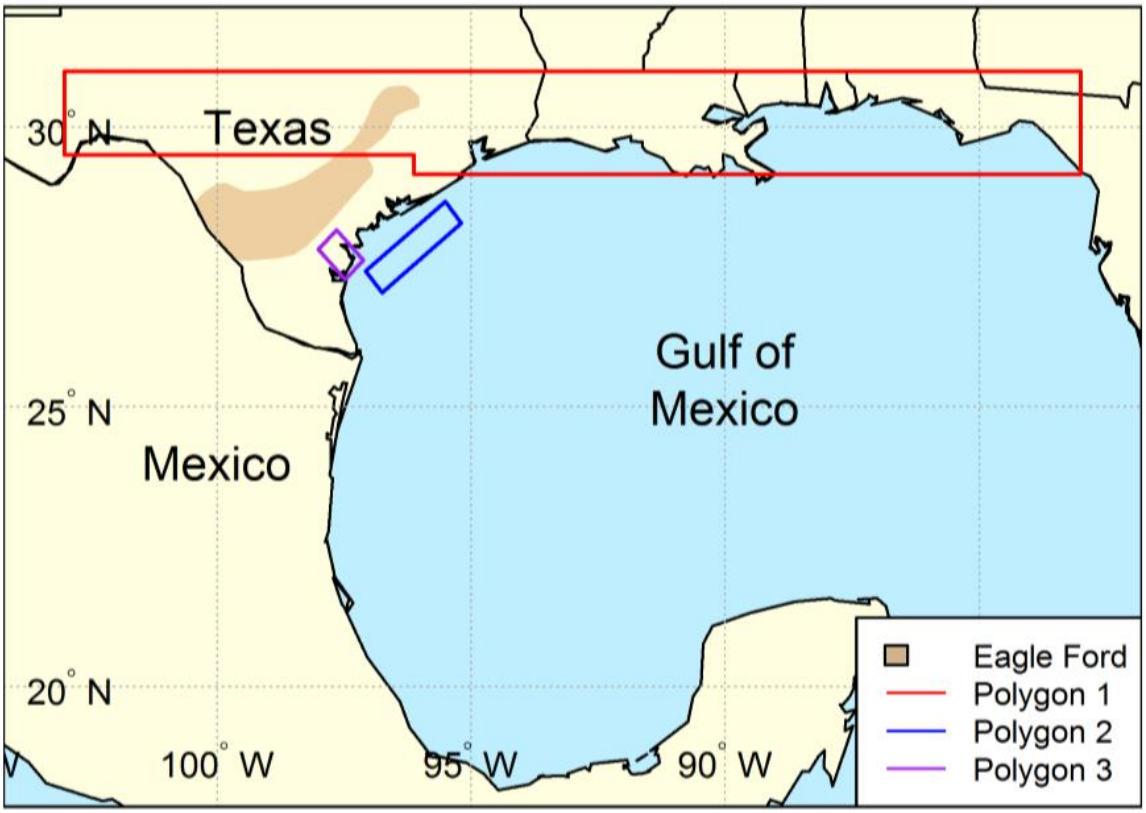

Figure 5. Polygons used to identify trajectories as southeasterly with maritime origins. See Table 2 for corners of the vertices.

Table 2. Vertices of polygons used to bin HYSPLIT trajectories, as shown in Fig. 5.

Polygon	Vertex 1	Vertex 2	Vertex 3	Vertex 4	Vertex 5	Vertex 6
1	29.16° N, 96.12° W	29.16° N, 83.00° W	31.00° N, 83.00° W	31.00° N, 103.00° W	29.50° N, 103.00° W	29.50° N, 96.12° W
2	27.04° N, 96.75° W	27.43° N, 97.07° W	28.67° N, 95.50° W	28.28° N, 95.19° W	-	-
3	27.27° N, 97.48° W	27.81° N, 98.00° W	28.16° N, 97.64° W	27.62° N, 97.12° W	-	-

All trajectories that passed through Polygon 1 were assumed to have continental origins and were removed. Polygon 2 was selected to represent the central Texas Coast region, roughly extending from the coastal waters southeast of Corpus Christi to the waters south of Clute. Trajectories that did not pass through this polygon were also removed, leaving generally southeasterly trajectories of maritime origin remaining. Days with 3 out of 4 southeasterly trajectories were used to compare long term alkane trends at these sites. For the alkane emission calculation using data from Oak Park and Floresville, back trajectories ending at Floresville were removed if they passed through Polygon 1. Again, this was to remove air masses which were influenced by continental emissions prior to moving ashore. Trajectories were also removed if they did not pass through Polygon 3, which encompasses Corpus Christi and the surrounding region of the Texas Coast. Days with 3 out of 4 trajectories were used to quantify the afternoon alkane enhancement between Oak Park and Floresville. Additionally, only days with at least 75% completeness (i.e., at least 18 hours of NMVOC data) at both Floresville and Oak Park were used.

The TCEQ sites in Floresville and Oak Park measure hydrocarbons using nearly identical automated GC-FID systems which record continuous hourly data from 40 min,

600 mL air samples. Standard operating procedures for these instruments are available from the Field Operations Division of the TCEQ (Texas Commission on Environmental Quality, 2005). The method detection limit is 0.4 ppbC, and instrument precision is measured using weekly injections of propane and benzene standard gases. Data are quality assured by the TCEQ if the relative difference between standard gas measurements remains less than 20%. We have assumed that this value is representative of the 2-standard-deviation uncertainty of an individual measurement. The mean afternoon alkane mixing ratios for each day were calculated at both sites by averaging hourly mixing ratios during the afternoon hours (15:00 to 18:00 LST), when daytime convection allows for mixing throughout the planetary boundary layer (Stull, 2009). The alkane enhancement for each day was determined by subtracting the mean of three afternoon alkane mixing ratios at the upwind site of Oak Park from the mean afternoon mixing ratio at the downwind site in Floresville. The relative standard error of the three hourly measurements at each site is 5.8%, and the uncertainty in the enhancement is equal to the sum of the absolute errors of the afternoon mixing ratios at each site.

2.1.2. ALKANE SOURCES

In this study, we assumed that regional alkane emissions are dominated by UOG operations in the Eagle Ford Shale. Other sources of ethane emissions were assumed to be negligible as no regional biomass burning was reported during the study period (Randerson et al., 2015). However, the mixing ratios of longer-chain alkanes (notably C_5 and higher) may be influenced by evaporative and tailpipe emissions from nearby

automotive traffic (Tsai et al., 2006; Ho et al., 2009; Simpson et al., 2012). Emissions from UOG come from multiple sources and can include emissions of raw natural gas from compressors, flowback events, and unintentional leaks. The compositions of these gases are dominated by the most volatile hydrocarbons, i.e., methane and ethane. In comparison, emissions from storage tanks, used to store liquids from wells prior to transportation and further processing, have been shown to contribute largely to hydrocarbon emissions in UOG shale plays (Lyon et al., 2015, 2016). Since gas produced at the well is separated from liquids prior to storage, the headspace in storage tanks is primarily composed of hydrocarbons heavier than ethane, notably short-chain alkanes such as propane, butanes, and pentanes, although methane and ethane may still be present. We assume that regional short-chain alkane emissions are dominated by gases produced at the wellhead (referred to as "raw natural gas") and emissions from liquid storage tanks (referred to as "tank gas"). Table 3 shows the available compositions

Table 3. Ethane content in raw natural gas and tank gas samples by mol percent and associated ethane/alkane ratios.

Ratio	C_2 (mol %)	C_2/C_1	C_2/C_3	C_2/iC_4	$C_2/nC4$	$C_2/(iC_5 + nC_5)$
Raw natural gas	4.51[a]	0.05	2.20	9.40	8.84	11.00
	9.15[b]	0.11	2.97	8.55	9.24	9.63
	13.20[b]	0.17	2.63	12.34	10.08	18.86
	15.88[b]	0.22	2.55	36.93	12.70	31.76
Mean	10.69	0.14	2.59	16.80	10.22	17.79
Tank gas	13.07[c]	0.84	0.75	2.52	1.08	0.47
	16.83[c]	0.72	1.13	3.21	1.59	0.78
	14.04[c]	0.61	0.89	3.32	1.45	0.65
	13.58[c]	0.47	0.96	4.02	1.54	0.64
Mean	13.48	0.66	0.93	3.27	1.42	0.64

[a] (Pring, 2012). [b] (Todd, 2011). [c] (ENVIRON International Corporation, 2010)

of raw natural gas samples from the Eagle Ford Shale and tank gas samples from the Barnett Shale. To our knowledge, no tank gas composition data are publicly available for the Eagle Ford Shale. The sampled emissions from liquid storage tanks in the Barnett Shale are variable in composition and this is incorporated into our error analysis. The composition of emissions from oil and condensate storage tanks in conventional production areas in Texas (Hendler et al., 2009) is also largely variable. We assume that the average composition of liquid storage tank emissions in the Eagle Ford falls within the variability of the Barnett Shale samples, although this assumption introduces an unquantified source of uncertainty into our analysis.

Observed alkane enhancement ratios can be partitioned into emissions from multiple sources, including raw natural gas and tank gas emissions. Equation (2.1), which is derived in Appendix A, shows the partitioning of observed propane-to-ethane ratios into raw natural gas, tank gas, and all other sources.

$$\left(\frac{C_3}{C_2}\right)_{observed} = f_{RNG}\left(\frac{C_3}{C_2}\right)_{RNG} + f_{TG}\left(\frac{C_3}{C_2}\right)_{TG} + f_{other}\left(\frac{C_3}{C_2}\right)_{other} \quad (2.1)$$

where $(C_3/C_2)_{RNG}$, $(C_3/C_2)_{TG}$, and $(C_3/C_2)_{other}$ represent the C_3/C_2 ratios in emissions from raw natural gas, tank gas, and other sources, respectively, and the relative contributions to the observed ratio from each source (f_{RNG}, f_{TG}, and f_{other}) add up to 1. If raw natural gas and tank gas sources dominate regional alkane emissions and other sources can be considered negligible, then $f_{RNG} + f_{TG} \approx 1$ and

$$\left(\frac{C_3}{C_2}\right)_{observed} = f_{RNG}\left(\frac{C_3}{C_2}\right)_{RNG} + (1 - f_{RNG})\left(\frac{C_3}{C_2}\right)_{TG} \quad (2.2)$$

$$f_{RNG} = \frac{\left(\frac{C_3}{C_2}\right)_{observed} - \left(\frac{C_3}{C_2}\right)_{TG}}{\left(\frac{C_3}{C_2}\right)_{RNG} - \left(\frac{C_3}{C_2}\right)_{TG}} \quad (2.3)$$

Here, f_{RNG} is found using C_3/C_2 ratios, and verified using iC_4/C_2 or nC_4/C_2 ratios. This number represents the fraction of ethane attributed to emissions from raw natural gas sources, such that $C_{2,RNG} = f_{RNG} \bullet C_{2,observed}$ and $C_{2,TG} = (1 - f_{RNG}) \bullet C_{2,observed}$. The expected methane enhancement can then be estimated using Eq. (2.4).

$$C_1 = C_{2,observed}\left(f_{RNG}\left(\frac{C_1}{C_2}\right)_{RNG} + (1 - f_{RNG})\left(\frac{C_1}{C_2}\right)_{TG}\right) \quad (2.4)$$

Similarly, the methane enhancement estimate, along with other alkanes, can be attributed to raw natural gas and tank gas sources as follows.

$$C_{1,RNG} = C_{2,RNG}\left(\frac{C_1}{C_2}\right)_{RNG} \quad (2.5)$$

$$C_{1,TG} = C_{2,TG}\left(\frac{C_1}{C_2}\right)_{TG} \quad (2.6)$$

2.1.3. MASS BALANCE APPROACH

Short-chain alkane emissions from a region encompassing the central section of the Eagle Ford Shale were quantified using a mass balance approach that has been adapted to an area source (Eq. 2.7), in which emissions are considered to be spatially and temporally homogenous.

$$F = (\overline{U} \cdot \cos\alpha) \cdot \overline{n} \cdot \int_{Z_0}^{Z_{PBL}} \rho(z)\, dz \cdot \Delta x \quad (2.7)$$

A different form of this mass balance method has been used in previous emission estimates for emission plumes from oil and gas systems (Caulton et al., 2014; Karion et al., 2013, 2015; Pétron et al., 2014; Smith et al., 2015). This estimate can be biased low

as it does not account for the entrainment of air from the free troposphere into the planetary boundary layer (PBL) (Karion et al., 2015), but it can also be biased high if nearby emissions produced unmixed plumes. We consider the Floresville site to be sufficiently downwind of ethane sources such that it is not impacted by discrete plumes if the PBL is well mixed. In our approach, we assume that the component of the wind that is parallel to the transect between upwind and downwind measurement sites ($\overline{U} \cdot \cos\alpha$, where α represents the angular deviation in wind from the direction of the transect) is representative of the general trajectories of air masses in the PBL being advected from the Gulf of Mexico. While actual trajectories that do not follow straight paths may stay over emission sources for long periods of time, large spatial deviations in wind direction will result in a reduction of the magnitude of $\overline{U} \cdot \cos\alpha$. Therefore, the time an air mass spends over an emission source will be reflected in the magnitude of the resultant wind. In a well-mixed PBL, the alkane mixing ratios are assumed to be near constant with height, and the mixing ratio enhancement ($\bar{n}$) multiplied by the integrated molar density ($\int_{Z_0}^{Z_{PBL}} \rho(z)\, dz$) from the surface ($Z_0$ = 122 m at Floresville) to the top of the PBL (Z_{PBL}) provides an estimate of the molar flux between the upwind and downwind locations. It is assumed that $\rho(z) = \rho_0 \cdot \exp(-z/H)$, where scale height $H = R_{air} \cdot T/g$, R_{air} = 287 J kg^{-1} K^{-1} , g = 9.81 m s^{-2} , and the molar density of air at sea level ρ_0 = 42.29 mol m^{-3} (United States Committee on Extension to the Standard Atmosphere, 1976). Lastly, a horizontal dimension (Δx) is necessary to produce an alkane flux for the region that is affecting the downwind receptor location. This was estimated as outlined in Sect. 2.1.4.

Meteorological data used in the mass balance approach were obtained from NOAA's North American Regional Reanalysis (NARR) (Mesinger et al., 2006), a combined model and assimilated dataset with a horizontal resolution of approximately 32 km. Temperature and PBL height data for each date were obtained for the 3 h period from 15:00 to 18:00 LST, representing general afternoon hours when the PBL is well mixed. Wind data were obtained for the previous 3 h period of 12:00 to 15:00 LST when parcels were being advected over the Eagle Ford Shale. Temperature and wind components at 950 mb were assumed to be representative of boundary layer conditions. Days with complicated meteorological conditions (e.g., precipitation, fronts, dry lines, or strong wind shear in the PBL) were discarded. The boundary layer heights from the NARR have been shown to have no strong bias compared to objectively determined PBL heights from sounding data at a site in Oklahoma (Schmid & Niyogi, 2012), although the correlation is moderate (as high as $R = 0.58$ in the winter and as low as $R = 0.39$ in the spring). While the use of the NARR introduces some uncertainty in the meteorological variables, we consider this to be the best available information for this data-sparse region where only surface observations are available. The uncertainty assigned to the meteorological variables is discussed in Sect. 2.1.5.

2.1.4. HORIZONTAL DIMENSION AND PRODUCTION REFERENCE AREAS

The horizontal dimension in previous mass balance applications using aircraft data has typically come from an observation of background mixing ratios at the "edge" of the emission plume (e.g., Karion et al., 2015), where upwind and downwind mixing

ratios become indistinguishable. Since the Eagle Ford Shale can be considered a line source, but only one downwind measurement site is available, we defined the "edge" of the emission plume using HYSPLIT's backward dispersion modeling tool in STILT mode (Hu et al., 2015). Model resolution was set to a 0.05° latitude × 0.05° longitude output grid (approximately 5 km resolution at these latitudes) using 12 km North American Mesoscale Model (NAM) meteorology input data. The model was set up to release 5000 particles equally distributed in the PBL above the Floresville monitor site at 16:00 LST on each selected day using the estimated boundary layer depth from the NARR data. Particles were followed backwards for 20 h and an integrated emission impact map was created from particles entering the lowest layer (50 m agl). In almost all cases, the map was no longer changing after 8–14 h of backward integration because all boundary layer particles had moved offshore. Particle plots were used to further exclude days with significant wind shear in the boundary layer, as they do not fulfill the requirements for the mass balance technique. The emission impact map was assessed in two ways:

1. The near-field plume width was measured at the southern edge of the Eagle Ford Shale as the representative horizontal measure necessary for the mass balance equation (Eq. 2.7) by assessing grid cell distances between the eastern and western edges of the plume. This choice was based on the assumption that alkane emissions are dominated by emissions in the Eagle Ford Shale, that this width corresponds to the spread of back trajectory ensembles from the receptor location in Floresville, and that this dimension corresponds to the width of a plume under

the uniform advection conditions necessary for mass balance had a continuous downwind measurement taken place for a source centered on the Eagle Ford Shale.

2. The gridded map was overlaid with a map of natural gas and associated gas production for the 30-month period from July 2013 to December 2015, developed from county production data (Railroad Commission of Texas, 2016) equally distributed into the grid based on our assumption of a homogenously distributed source. All gas production in nonzero grid cells was accumulated to provide a reference number of upwind production potentially contributing to the measured downwind mixing ratios at the Floresville receptor. These numbers thus varied on a daily basis with wind direction and turbulence affecting the integrated impact map. Note that this estimate is based on the single receptor location, assuming it to be equivalent to an actual boundary layer "curtain" measurement undertaken via flying aircraft. Simulating the aircraft's "curtain" measurement via a particle release from numerous upwind locations would not substantially alter the result because of counteracting consequences: a multi-point release throughout the downwind boundary layer would increase the width of the plume (impact map cross section at southern Eagle Ford Shale edge), increasing the total emission estimate according to Eq. (2.7), but at the same time would also increase the production reference area where potential emissions occur. Thus, our results would only change significantly if either upwind emissions or production were strongly non-homogenously distributed.

2.1.5. MONTE CARLO SIMULATION

The errors arising from the variability and uncertainties of the alkane enhancement and the parameters derived from regional meteorology inputs were assessed using a Monte Carlo simulation, in which the emissions for each day were calculated 1 million times by randomly sampling the input parameters from either empirical or assumed probability distributions. A Monte Carlo simulation was performed for each day, allowing for the temporal variability and the dependence of the emissions on input variables to be assessed. The simulation was performed using the "mc2d" package in *R* (Pouillot & Delignette-Muller, 2010). The absolute uncertainty in the afternoon alkane mixing ratios at each site associated with the precision of the instrument was represented by normal distributions about the afternoon alkane mixing ratios with relative standard deviations of 5.8%, as discussed in Sect. 2.1.1. The compositions of four raw natural gas and four tank gas samples shown in Table 2 were used to produce normal distributions of the alkane ratios in raw natural gas and tank gas. The u and v components of the wind and the temperature were assigned normal distributions using the mean and standard deviation of the spatial variability in the NARR data over a 1° latitude by 1° longitude box situated in the central Texas coastal plain, with Floresville located at the northwest corner (Fig. 2). It is assumed that the meteorology in this region represents the general conditions to which air masses were subjected as they traveled inland from the Texas coast towards Floresville.

There are several objective methods used to determine the PBL depth, and the uncertainty in the PBL depth has been shown to contribute to the uncertainty in previous

mass balance measurements (e.g., Karion et al., 2015). To the authors' knowledge, the uncertainty in the NARR PBL depth, which is estimated using the profile of turbulent kinetic energy (TKE), has not been quantified by the NARR maintenance team (Mesinger et al., 2006). However, the NARR has been compared to PBL depths estimated from radiosonde data. Lee & De Wekker (2016) found that objectively analyzed PBL depths using radiosonde data in Virginia differed from PBL depths estimated using a bulk Richardson method with the NARR data. The standard deviation of the difference between the two methods was 453 m when averaged over 1 year and the NARR PBL depths exhibited a high bias of 157 m when compared to the radiosonde PBL depths. A similar study at a site in Oklahoma (Schmid & Niyogi, 2012) examined the difference between objectively analyzed PBL depths using radiosonde data and the standard NARR PBL depths using the TKE method. The correlation between the NARR and the radiosonde PBL depths were slightly lower in this study when compared to Lee & De Wekker (2016). To be consistent with these authors' findings, we have assumed that the uncertainty in the NARR PBL depth may be represented by a standard deviation of 500 m, which is an average of ~ 28% of the NARR PBL depth over the days used in the study (Sect. 2.2.2). Therefore, the PBL depths are represented in the Monte Carlo error estimate as a normal distribution centered on the average of the NARR PBL depths over the 1° latitude by 1° longitude box and a standard deviation of 500 m.

2.2. RESULTS AND DISCUSION

2.2.1. ETHANE TRENDS

Schade & Roest (2015) briefly discussed long-term trends in ethane mixing ratios at TCEQ sites around the Eagle Ford Shale, and an update is provided in Fig. 6. Here, we present the results from the Kruskal–Wallis rank sum and Dunn tests (Dunn, 1964; Kruskal & Wallis, 1952) performed on ethane mixing ratios vs. year. At the Corpus Christi – Hillcrest site, no set of years exhibited statistically significant ($p < 0.05$) differences in ethane mixing ratios under southeasterly wind regimes. At Clute, ethane was statistically significantly higher ($p < 0.05$) in 2015 than it was in 2007– 2011, though no other years showed significant differences. We attribute recent increases in ethane mixing ratios in Clute to changes in emissions from local point sources, as the neighboring city of Freeport is a hub of petroleum processing and transportation (Bonney, 2014; Ryan, 2014). The data suggest that background ethane levels over the Gulf of Mexico did not significantly change during the development of the Eagle Ford Shale. However, ethane mixing ratios at the San Antonio site are statistically significantly higher ($p < 0.05$) in later years than in earlier years. Ethane was higher in 2011 than 2007–2009, higher in 2012 than 2007–2011, and higher in 2013–2015 than in 2007–2010. The Floresville site was not installed until 2013 so the long-term trend in ethane mixing ratios at that location is unknown. However, Floresville observed the highest ethane mixing ratios in the region from 2013 to 2015. While there is no evidence that ethane mixing ratios along the coast increased over time during southeasterly flow, ethane did increase downwind of the Eagle Ford Shale during its development.

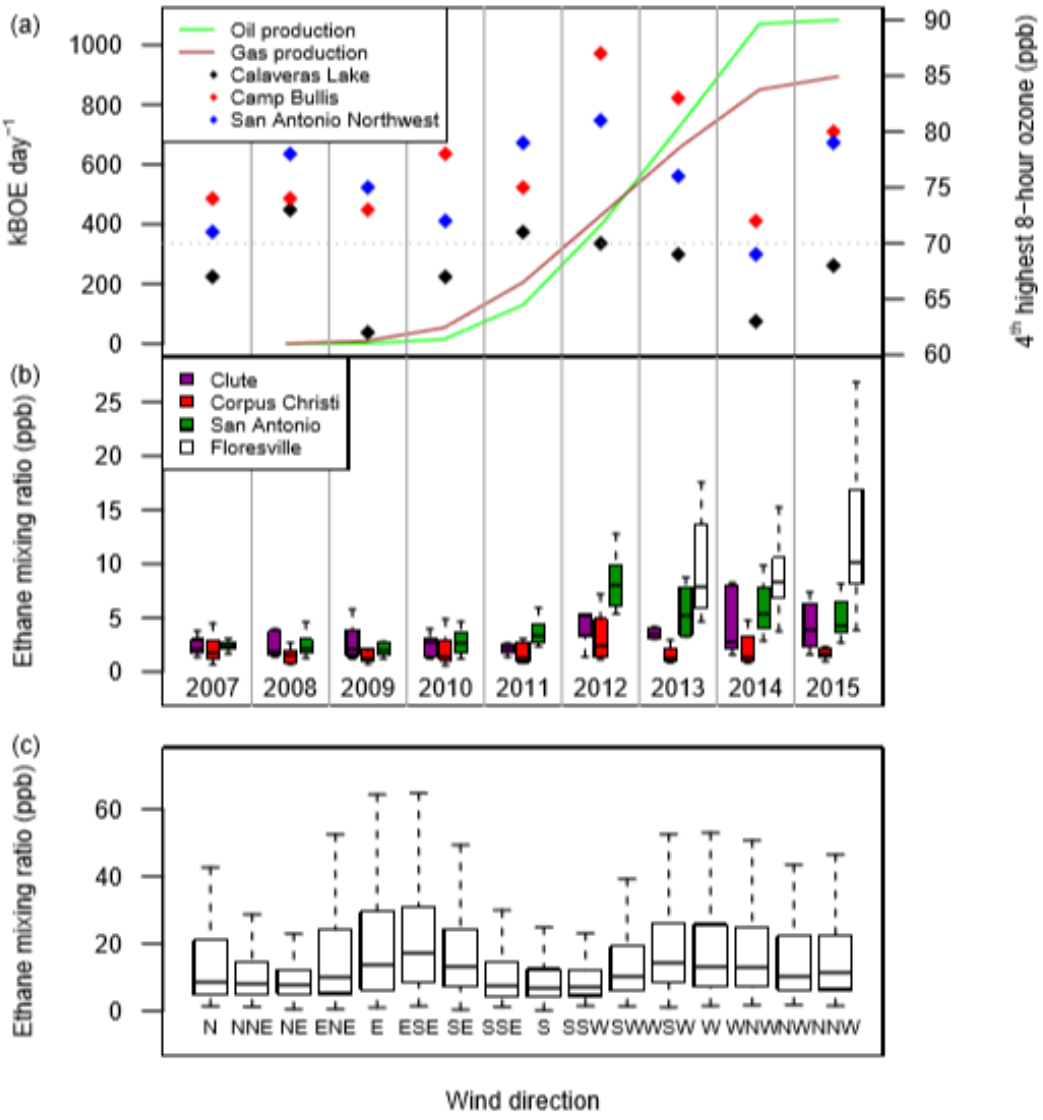

Figure 6. Adapted version of Fig. 2 in (Schade & Roest, 2015), updated to include data through 2015. (a) Oil and gas production rates in the Eagle Ford and fourth-highest maximum 8 h ozone values at three sites in San Antonio. (b) Timeline of 24 h ethane mixing ratios at four sites near the Eagle Ford Shale. Days were used only if three out of four back trajectories originating from San Antonio – Old Highway 90 were binned as southeasterly. Data at Floresville begin in July 2013. (c) Ethane mixing ratios vs. wind direction at Floresville, with elevated mixing ratios under E to SE or SW to W winds, when trajectories would generally allow for the accumulation of emissions because winds have a component that is parallel to the shale axis. Ethane is also elevated under NW winds, likely due to higher ethane in continental air masses and local emissions from the San Antonio metropolitan area.

2.2.2. ALKANE ENHANCEMENT

During the 30-month period from July 2013 through December 2015, a total of 69 days were found to have 3 out of 4 trajectories identified as southeasterly, appropriate meteorological conditions, and 75% completeness at both Floresville and Oak Park. One of these days (18 March 2015) had alkane enhancement values that were outliers. Since we cannot exclude that the downwind measurement site of Floresville was influenced by a plume on this date, it was not considered for analysis. The majority of the remaining 68 dates, which occurred between August 2013 through August 2015, fell into the summer and fall months, when southerly and southeasterly flow are commonplace in south-central and coastal Texas (Texas Commission on Environmental Quality, 2015). The median alkane enhancements for the set of 68 days were as follows: 2.4 ppb for ethane with an interquartile range (IQR) of 2.0–3.1 ppb; 1.9 ppb for propane (IQR of 1.4–2.5); 0.8 ppb for *n*-butane (0.6–1.1); and 0.4 ppb for isobutane (0.3–0.5). All observed alkane enhancements were positive.

Figure 7 shows a timeline of the afternoon ethane mixing ratios at both Oak Park and Floresville for the set of 68 days with southeasterly flow. Ethane mixing ratios during the warm season (summer and fall) were generally low at both Oak Park and Floresville and higher at the two sites during the cool season (winter and spring). This seasonal variability conforms to current understanding of seasonal hydrocarbon variability (Helmig et al., 2016). The enhanced photochemical oxidation of ethane during the summer months explains the low background ethane observed in the onshore flow at Oak Park (Haman et al., 2012).

2.2.3. PARTITIONING OF ALKANE SOURCES

The enhancements of propane, butanes, and pentanes were highly correlated with ethane enhancements between Oak Park and Floresville, suggesting a co-emission from sources of natural gas. The strongest correlation was observed between ethane and propane (Fig. 8). Pentanes (and to a lesser extent, butanes) may be impacted by emissions from automotive traffic (Ho et al., 2009; Simpson et al., 2012; Tsai et al., 2006) and chemistry, as pentanes have atmospheric lifetimes of ~ 1.5 days (298 K, [OH] = 2.0×10^6) (Atkinson & Arey, 2003). Therefore, pentanes were not used to partition emissions from raw natural gas and tank gas sources and an emission rate was not calculated. Nonetheless, the isopentane to n-pentane enhancement ratio between Oak Park and Floresville (Fig. 9), which will remain close to constant despite chemistry, was 1.17 ($p < 0.001$), indicating that alkane emissions are largely influenced by oil and gas (Gilman et al., 2013). By comparison, the same ratio at the Old Highway 90 site in San Antonio was 2.25, which falls within the bounds of the traffic emission driven urban pentane ratio. For these reasons, the enhancements of short-chain alkanes during advection over the Eagle Ford Shale are most likely dominated by emissions from oil and gas production. The alkane enhancement distributions are skewed, with the upper bounds possibly representing the influence of individual plumes from UOG exploration activities.

Propane-to-ethane ratios were used to partition emissions from raw natural gas and tank gas sources. Within each Monte Carlo simulation, the fraction of the ethane

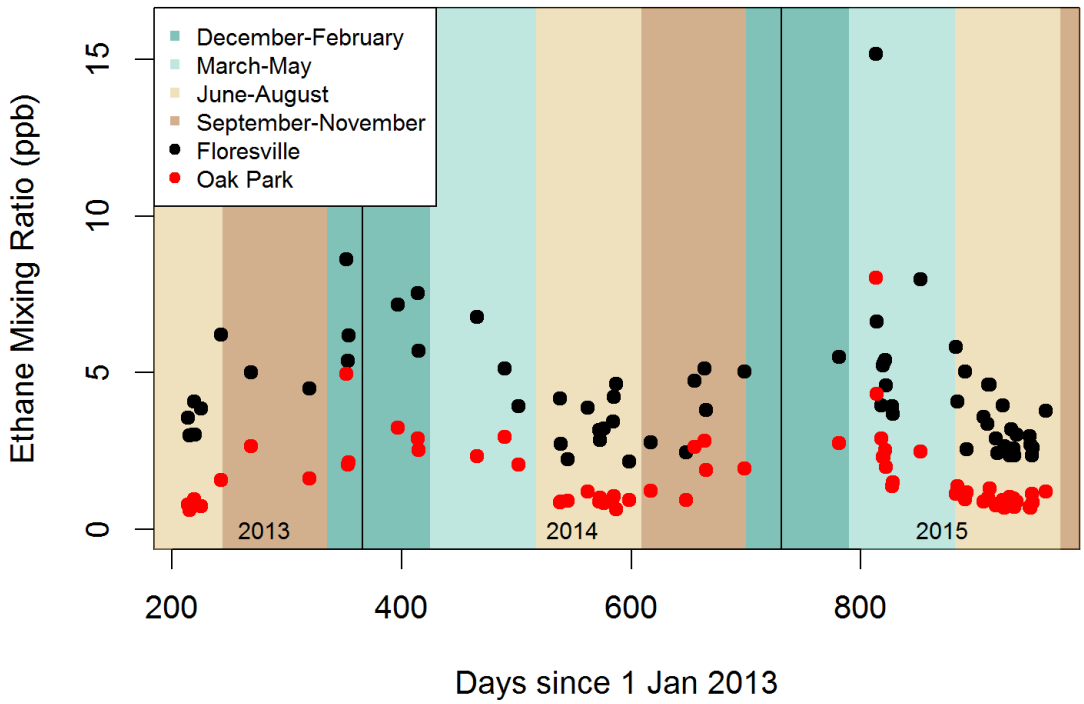

Figure 7. Scatterplot of afternoon ethane mixing ratios at the upwind site (Oak Park), the downwind site (Floresville) over 68 days with southeasterly flow. Note that each mixing ratio has a relative uncertainty of ±5.8% and the uncertainty of the enhancement is equal to the sum of the uncertainties of the upwind and downwind sites. The background colors show the warm and cool seasons. Ethane mixing ratios are generally lower at both the upwind and downwind sites during the summer and fall and higher in the winter and spring.

enhancement from raw natural gas sources varied largely, with the 95% confidence interval often bounded by physically unreasonable numbers. This was due to the large uncertainty of the propane-to-ethane ratios in raw natural gas and tank gas samples. However, the median fraction for each day showed less variability, with a median of 45% (IQR of 34–52%) of ethane attributed to raw natural gas sources. The raw natural gas source estimate was significantly more constrained due to the availability of raw gas composition data, while no tank gas composition data were available for the Eagle Ford Shale. The median methane enhancement estimate for all 68 days was 8.9 (IQR of 6.8–

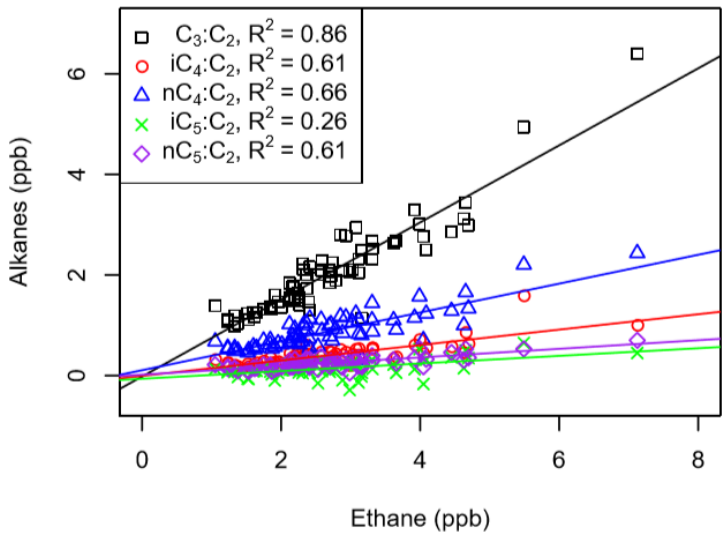

Figure 8. Correlations of propane, butane, and pentane enhancements with ethane enhancement. All correlations were highly statistically significant ($p < 0.001$). While ethane and propane showed the strongest correlation, all alkanes showed a positive correlation with ethane.

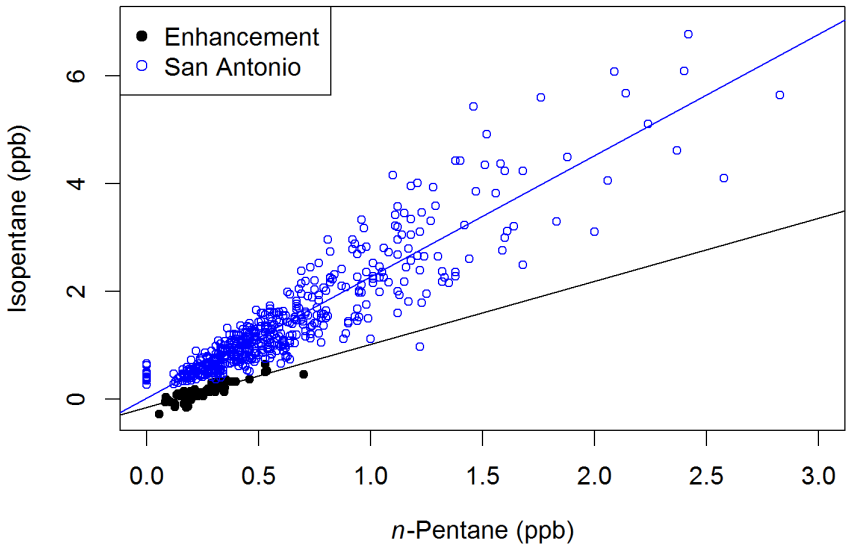

Figure 9. Scatterplot of afternoon isopentane and *n*-pentane enhancements observed between Oak Park and Floresville over 68 days with southeasterly flow. Also shown are isopentane and *n*-pentane mixing ratios in San Antonio for 24 hour canister samples from 2007 to 2015. The slopes of both linear regressions are highly statistically significant ($p < 0.001$). The isopentane-to-n-pentane ratio in San Antonio is 2.25, which is indicative of urban emissions. Meanwhile, the slope of the ratio for the enhancements is 1.17, indicating emissions from petroleum production.

12.4) ppb, of which 83% (IQR of 76–86%) was attributed to raw natural gas sources. Higher alkanes were also partitioned, and their relative contributions from raw natural gas sources over the 68 days were 18% for propane (IQR of 11–22%); 10% for *n*-butane (7–13%); and 17% for isobutane (11–22%). While the majority of methane emissions were due to emissions of raw natural gas, liquid storage tanks dominated the emissions of these higher alkanes.

The raw natural gas source fractions based on *n*-butane-to-ethane and isobutane-to-ethane ratios often did not match that of propane-to-ethane for individual days, although their probability distribution functions over all days overlapped (Fig. 10), suggesting that the partitioning is consistent and reasonable when integrated over multiple sources in a larger region. It should be noted, however, that Floresville is located closer to the oil-producing window of the Eagle Ford Shale than the gas producing window and the influence of raw natural gas production may be somewhat diminished due to this distance. Nonetheless, the contribution of tank gas sources to observed alkane enhancement ratios suggests that liquid storage tanks are a very important source of alkane emissions between Oak Park and Floresville, a result that agrees with hydrocarbon emission studies in many other liquid-rich US shale plays.

2.2.4 MASS BALANCE RESULTS

2.2.4.1 DISPERSION PLUMES AND UPWIND PRODUCTION AREAS

Figure 11 shows a representative backward dispersion plume output overlaid on a gridded production map to illustrate the relative emission estimate. Emission plumes for

other days varied in width but generally overlapped the same counties. Since the Eagle Ford Shale is assumed to be a line source, all overlapping grid cells with nonzero production numbers were weighed equally. This area includes portions of several

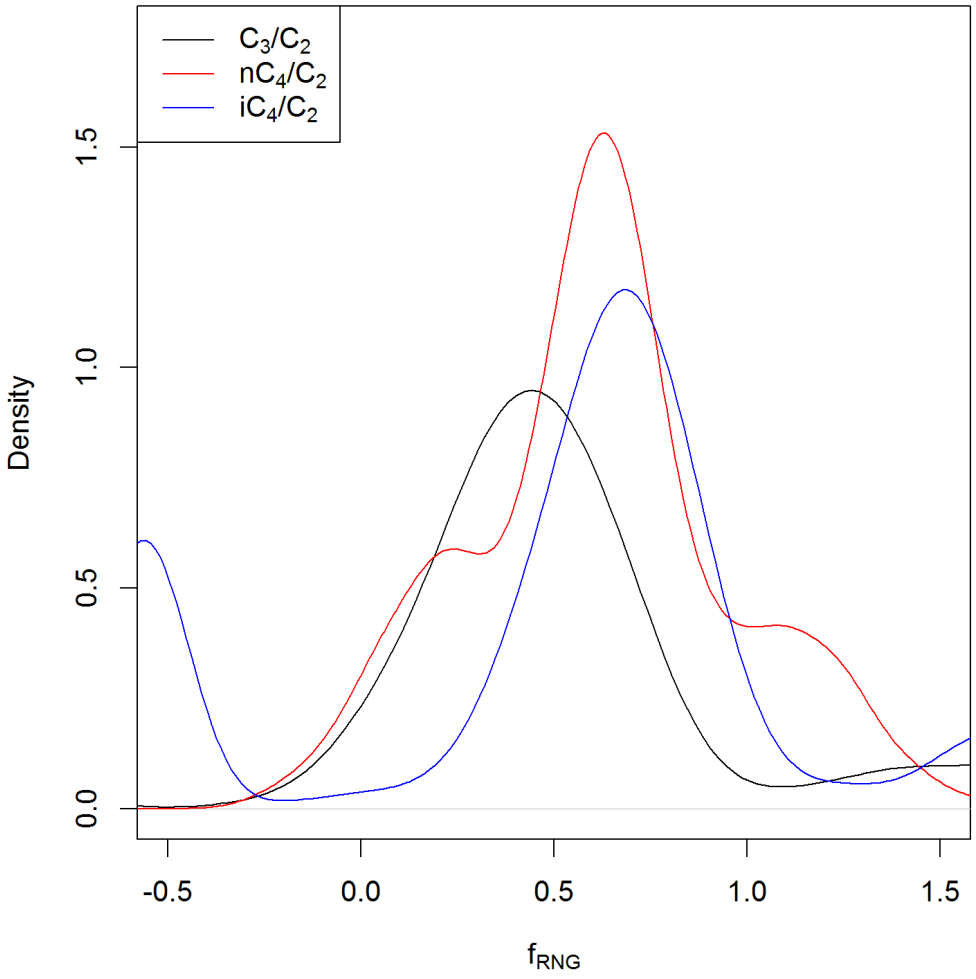

Figure 10. Probability distribution functions for the fraction of observed alkane ratios that can be explained by emissions of raw natural gas (f_{RNG}). Note that the x-axis extends to numbers that are physically unreasonable. This is due to the assumption that alkane ratios can be explained by emissions from raw natural gas and vented tank gas alone (the compositions of which are highly uncertain), and other sources and sinks are neglected. Nonetheless, there is general agreement between the fractions derived from the C_3/C_2 ratio, the nC_4/C_2 ratio, and the iC_4/C_2 ratio, suggesting that the above assumption creates results that are reproducible using these three alkane ratios.

counties in the Eagle Ford Shale – notably Atascosa, Bee, Karnes, Live Oak, and Wilson counties – which are members of AACOG (Alamo Area Council of Governments (AACOG), 2015). Pacsi et al. (2015) found that, among all counties in the Eagle Ford Shale, NO_x emissions from these counties had the greatest impact on ozone enhancement in Bexar County, home to the city of San Antonio. Therefore, quantifying emissions from these counties in the core of the Eagle Ford Shale is a particularly important step in assessing the air quality impacts of oil and gas operations in the San Antonio area. While production was considered over all grid cells overlapped by the backward dispersion plume, counties in the Eagle Ford Shale dominate regional production and are likely responsible for the observed alkane enhancements.

2.2.4.2 EMISSION ESTIMATES

The alkane emission estimates from the upwind production regions were estimated using a Monte Carlo simulation for each day, and the distributions of the median emission rates were found as follows: 189×10^3 kg day^{-1} for methane (IQR of 136–376 $\times 10^3$); 97×10^3 kg day^{-1} for ethane (68–168 $\times 10^3$); 109×10^3 kg day^{-1} for propane (75– 185 $\times 10^3$); 64×10^3 kg day^{-1} for *n*-butane (46–104 $\times 10^3$); and 27×10^3 kg day^{-1} for isobutane (18–52 $\times 10^3$). In comparison, VOC emissions estimated by AACOG (not including ethane) for the set of central Eagle Ford Shale counties from southeast to southwest of Floresville were only 88×10^3 kg day^{-1} for calendar year 2012 (AACOG, 2013b), while total Eagle Ford Shale VOC emissions were estimated at 203 ×

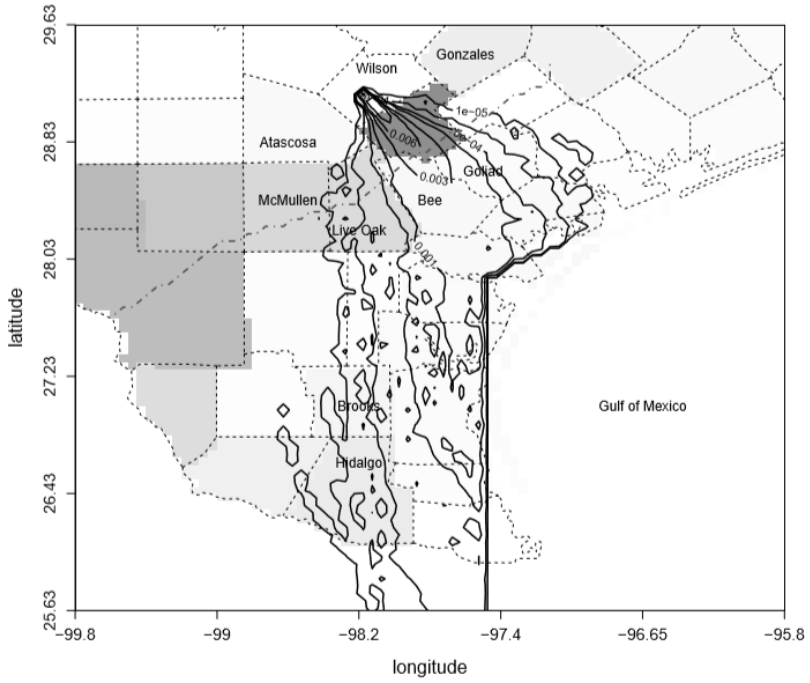

Figure 11. An example of an integral backward dispersion plume map created from 5000 particles released above the Floresville receptor site and followed backwards in time (20 h) into the model lowest vertical level (< 50 m agl) to assess surface emitter impacts. The raw map was normalized to its total after removing all surface impacts over the Gulf of Mexico. The grey shading underlying the plume map identifies counties with the sum of natural gas and associated gas production, with darker shading indicating higher production rates. The darkest shading indicates Karnes County, not labeled for clarity. Many counties, including Wilson County where Floresville is located, are lightly shaded due to the relatively low production of natural gas. The dark grey jagged line extending from the west-southwest near the Mexican border to the east-northeast south of Gonzales County marks the southern "edge" of the Eagle Ford Shale.

10^3 kg day^{-1}. This suggest that Eagle Ford Shale VOC emissions used in ozone modeling may be underestimated by at least a factor of 2, likely more.

To estimate relative methane losses, the raw natural gas-only and the total mass emission of methane were converted into a volume of natural gas using the ideal gas law at standard temperature and pressure for natural gas volume reporting (Texas Statutes,

1977) and a natural gas methane content based on available raw natural gas data (Table 2). The volume of the emitted natural gas was then compared to the produced natural gas at gas wells and associated gas at oil wells in the production reference area outlined in Sects. 3.2.4 and 3.3.4.1. Emission rates for individual days were highly uncertain, with the bounds of the 95% confidence interval often spanning an order of magnitude (Fig. 12). However, median emission rates over all days were less variable, with a median total emission rate of 1.0% (IQR of 0.7–1.6%) and a raw natural gas-only emission rate of 0.7% (0.5–1.3%). While the EPA's estimated emission rate of 1.6% falls within the bounds of our total emission estimate, our median emission rate is lower than that of the EPA. Our emission rate is also lower than the emission rate of 3.2% ± 1.1% for the eastern Eagle Ford Shale given by Peischl et al. (2018), which was based on two flights on 2 and 7 April 2015 during the SONGNEX campaign. Figure 13 shows the measured methane mixing ratios during those two flights near the Eagle Ford Shale. With wind directions from the east-southeast, our downwind receptor site at Floresville was receiving a smaller enhancement across the shale than areas to the northeast or southwest along the shale axis. This is especially noticeable on the 7 April flight, when areas to the southwest observed a methane concentration more than 20 ppb higher than the area near Floresville (marked with a dotted line). This suggests that our emission rate may be biased low as Floresville appears to be downwind of a region of the shale with relatively low emission rates.

The emission rate displayed no significant trend over the 2013–2015 time period, and its correlations with independent meteorological variables and ethane enhancement

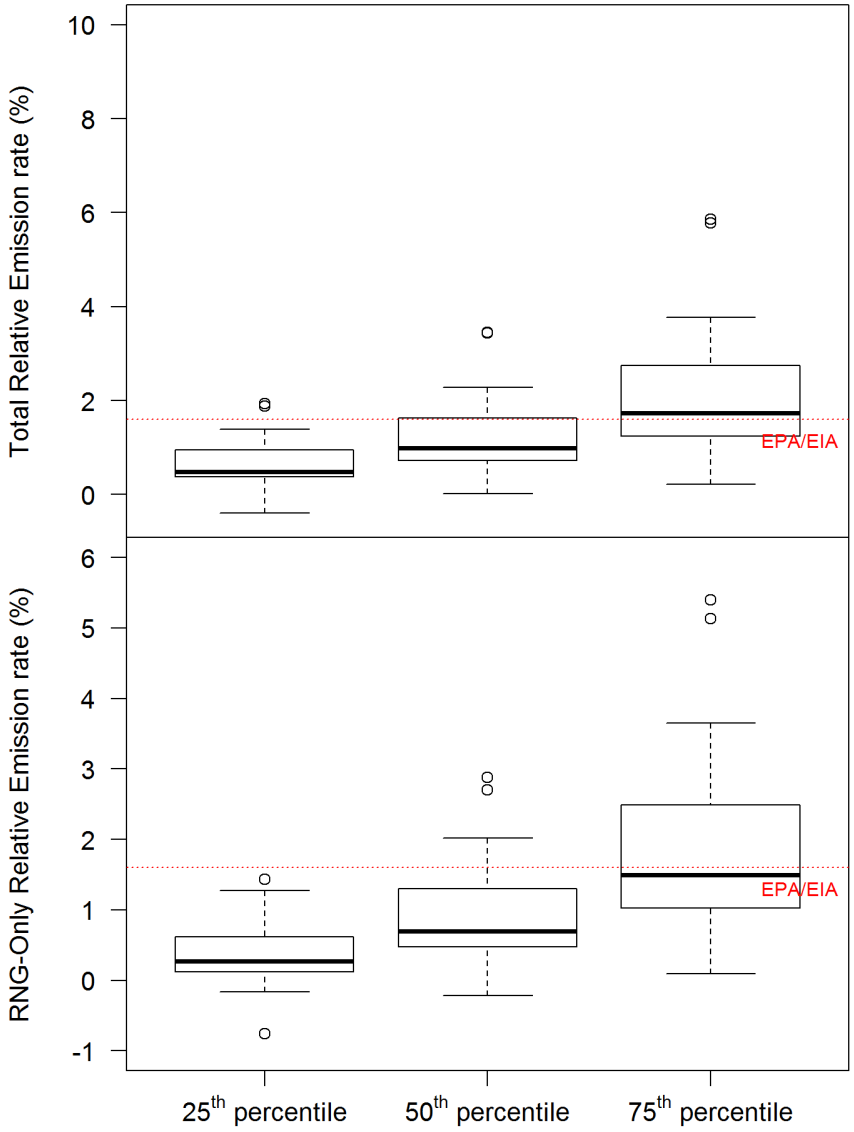

Figure 12. Distributions of the 25th, 50th, and 75th percentile of relative emissions over all 68 days. Methane emissions were converted to a volume of natural gas using methane to natural gas ratios (Table 2) and compared to natural gas production. The top panel shows total relative emission rate while the bottom panel shows only emissions from raw natural gas (RNG) sources and excludes emissions from liquid storage tanks. Some outliers of the lower bound were less than zero due to large uncertainties in the methane enhancement which occasionally produced a negative methane flux within the Monte Carlo simulations. The upper bound of the total emission rate is often close to that of the EPA/EIA emission estimate for nationwide natural gas and associated gas production in 2011. The emission rate for raw natural gas emissions alone was generally lower than the EPA/EIA estimate. Note that the emission rate estimate has a slightly skewed distribution, with the upper bound possibly influenced by plumes from large emitters.

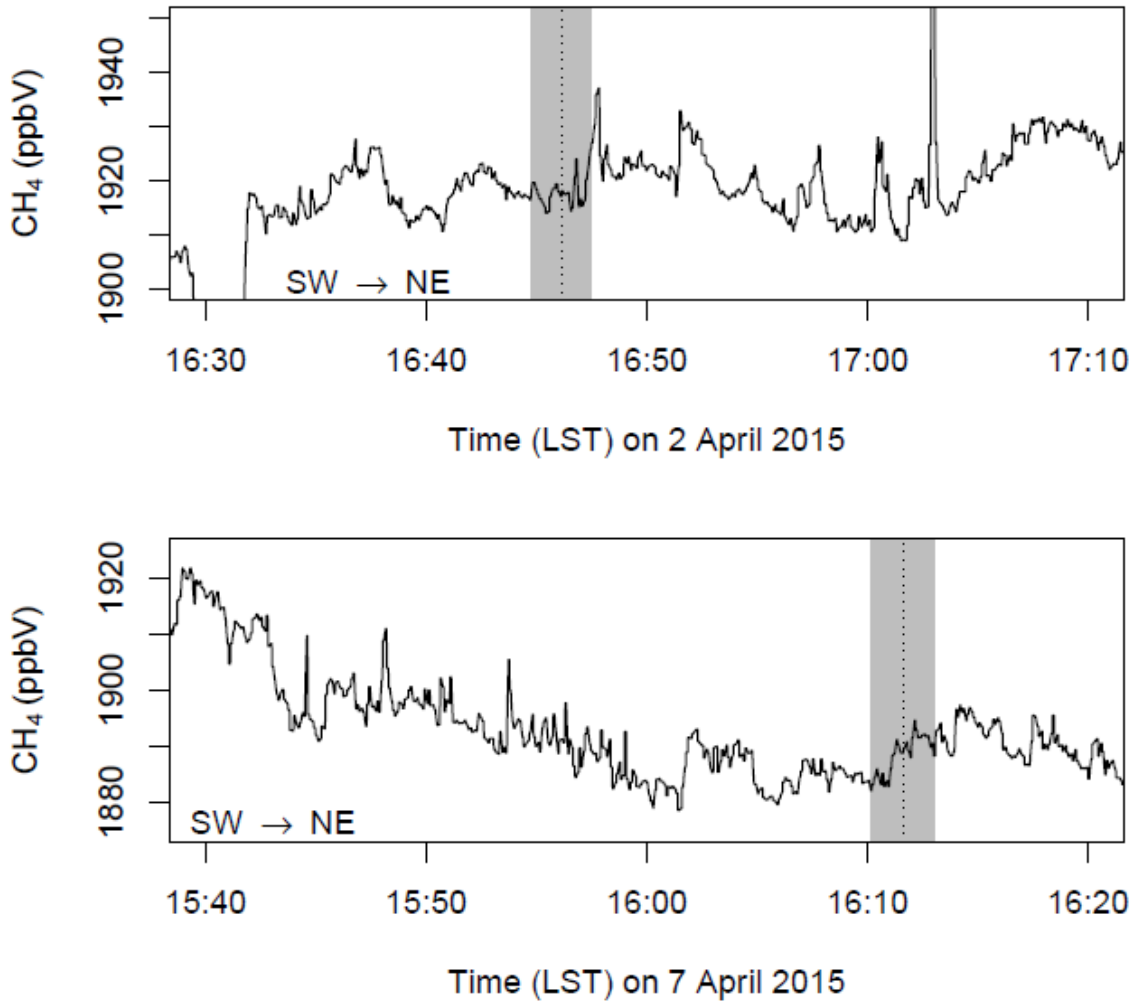

Figure 13: Methane measured downwind of the Eagle Ford Shale on 2 and 7 April 2015 during the SONGNEX campaign (Peischl et al., 2018). Both panels show measurements over time during a transect from the southwest towards the northeast. The closest pass to Floresville along each transport is shown with a vertical dotted line, and measurements within 10 km of Floresville are indicated with by the grey swath.

over time were weak (Figs. 14 and 15), which is to be expected for a continuous anthropogenic emission source. However, the uncertainty in the emission rate within each Monte Carlo simulation showed a strong dependence on the uncertainty of the ethane content in raw natural gas samples – a variable with large relative uncertainty that

was used to estimate methane emissions – and, to a lesser extent, meteorology (Fig. 16). We find that the lack of data regarding the composition of both raw natural gas and vented gases from liquid storage tanks impedes a higher precision top-down emission rate estimate. Nonetheless, repeated emission estimates over a large set of days show consistent and reasonable emission rates that can be attributed to UOG operations.

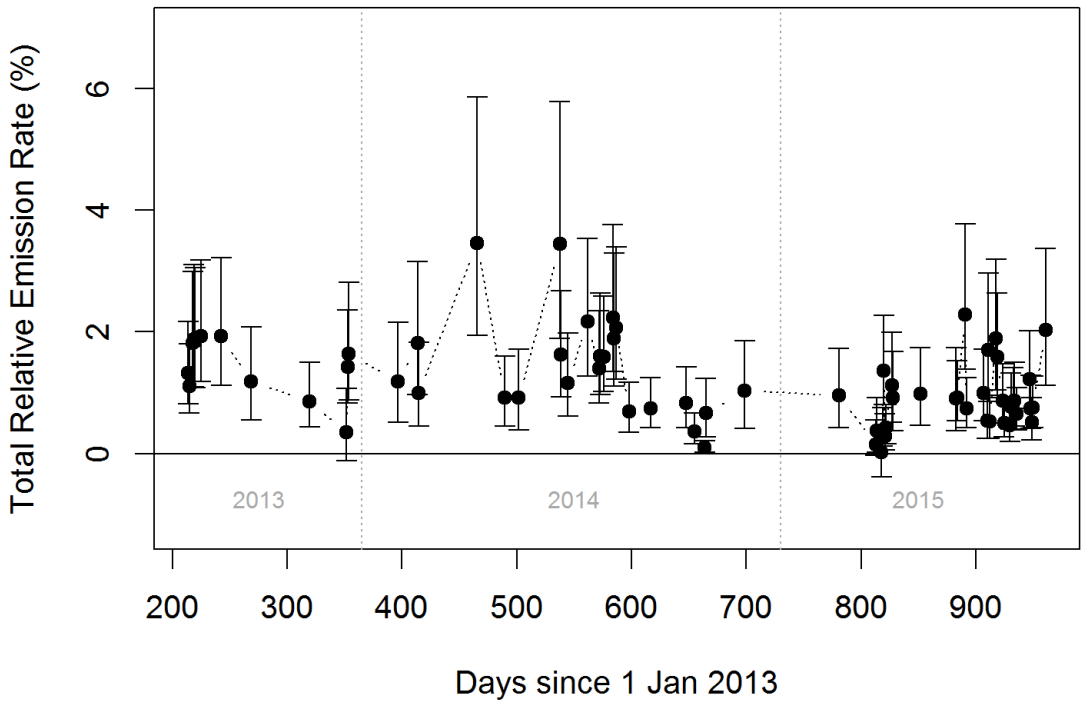

Figure 14. Timeline of the median emission rate for each day with the interquartile range represented by whiskers. The emission rate showed neither apparent seasonality nor trend over time, which is to be expected of a continuous emission source that does not depend on meteorological variables.

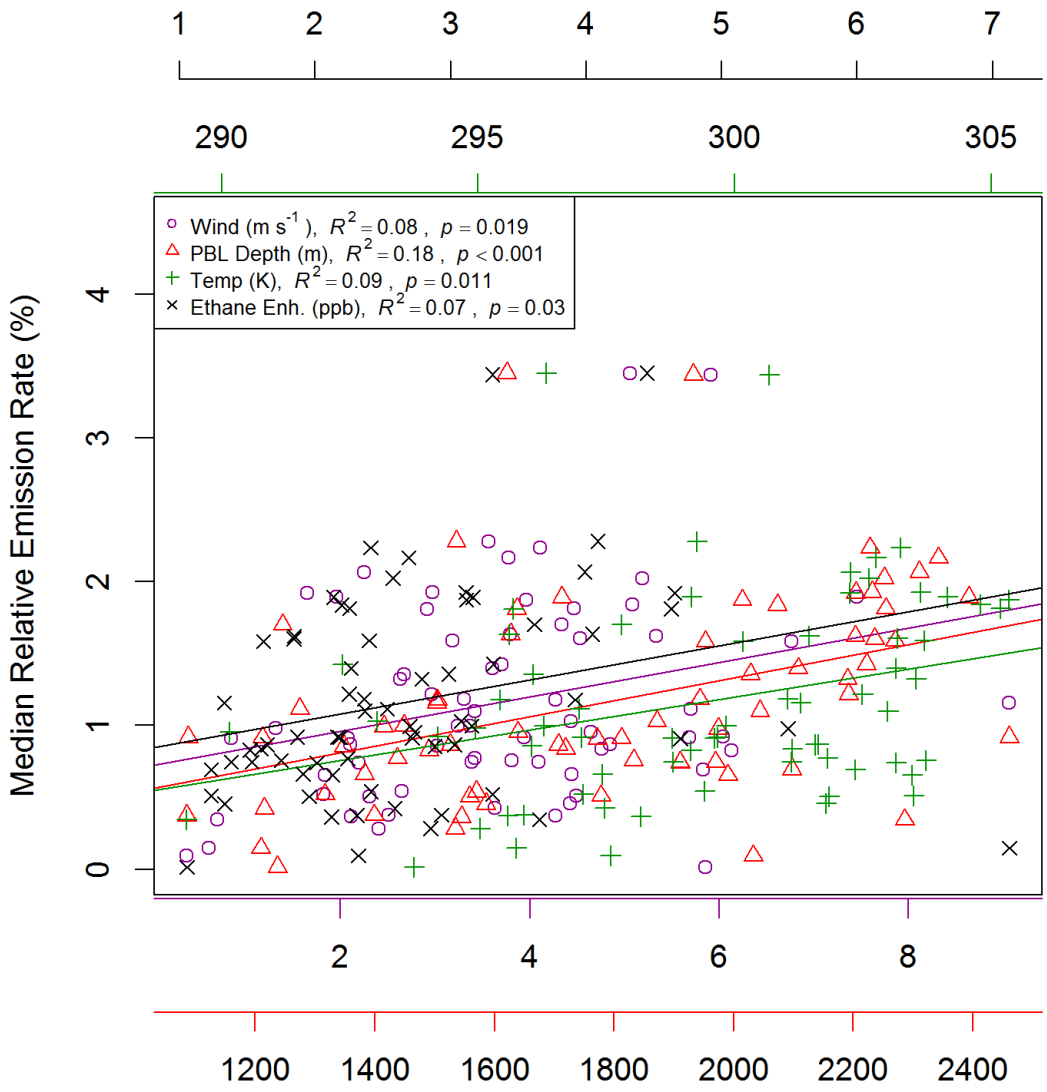

Figure 15. The median emission rate for each of the 68 days plotted against wind speed (component parallel to the transect between Corpus Christi and Floresville), PBL depth, temperature, and ethane enhancement. While there were statistically significant correlations with wind speed, temperature, and ethane enhancement, these correlations were weak. While the PBL depth showed the strongest correlation with the emission rate ($R^2 = 0.18$, $p < 0.001$), the emission rate was not strongly driven by meteorological variability.

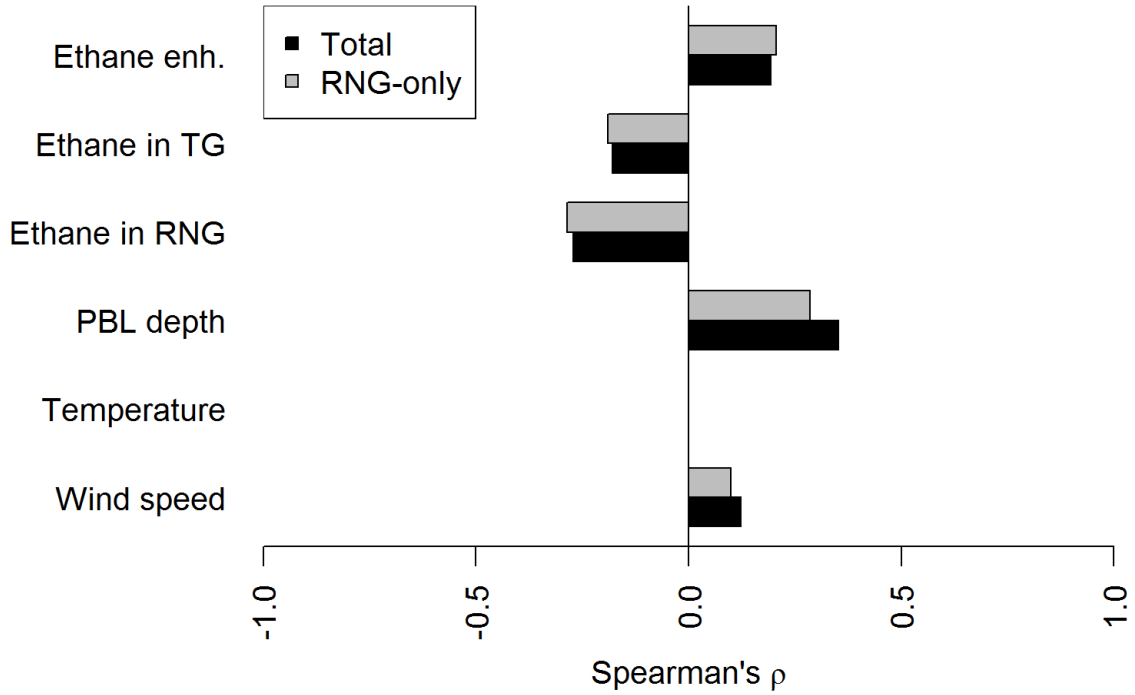

Figure 16. Example of a tornado plot from a Monte Carlo simulation for 2 August 2013. The total emission rate depended largely on the composition of raw natural gas (RNG), with lower ethane content in natural gas (which was used, in part, to estimate methane emissions) resulting in a higher emission rate. The RNG-only emission rate shows a negative correlation with the ethane content in both RNG and vented gas from liquid storage tanks (TG), as these numbers were used to partition emissions between RNG and TG sources. Both the total and RNG-only emission rates showed positive correlations with wind speed and planetary boundary layer (PBL) depth, but not temperature. The rates were also positively correlated with the ethane enhancement.

2.3. CONCLUSIONS

Our study used ethane as a tracer for alkane emissions from UOG emissions for a region in southern Texas, where oil and gas production is dominated by the core of the Eagle Ford Shale. Data from the TCEQ show that alkane mixing ratios downwind from the shale have increased in tandem with oil and gas production rates in the Eagle Ford Shale. This trend, along with the strong correlation of ethane enhancements with both

propane and butane enhancements, show that emissions from UOG production in the Eagle Ford Shale are responsible for the observed alkane enhancements across the shale. Using a mass balance approach and a Monte Carlo error estimation, we calculate ethane emissions of 97 (IQR of 68–168) × 10^3 kg day^{-1} from areas between the Texas coast and the downwind receptor site in Floresville for a set of 68 days from August 2013 through August 2015. Using typical ethane-to-methane ratios (an average of 0.14), we estimate methane emissions of 189 (136–376) × 10^3 kg day^{-1}. These emissions represent 1.0% (0.7–1.6%) of the produced natural gas – including associated gas at oil wells – in the region upwind of Floresville. We show through the partitioning of raw natural gas and tank gas emissions that raw natural gas sources account for three quarters of all methane emissions, with a raw natural gas-only relative emission rate of 0.7% (0.5–1.3%). Note that these emission rates are expressed as a fraction of produced natural gas as opposed to produced energy. In liquid-rich shale plays such as the Eagle Ford Shale, expressing emission rates as a fraction of produced energy may be a more appropriate measure of emissions, especially when comparing energy losses to other sources (e.g., coal). However, our findings suggest that energy losses in the form of VOC emissions may also be an important consideration when estimating energy losses from liquid-rich shale plays, and that the measurement location may have biases.

We find that tank gas sources account for more than half of higher alkane emissions – notably 90% of *n*-butane emissions. Since the petroleum production in this region is dominated by counties within the Eagle Ford Shale, we conclude that UOG activities in the shale area are largely responsible for these emissions. Our natural gas

emission rate estimate falls within the bounds of other top-down studies (Peischl et al., 2015) and overlaps the EPA's most recent methane emission estimates from its 2016 greenhouse gas inventory (U.S. Environmental Protection Agency, 2016a). However, our median total emission rate including tank gas sources is lower than the EPA's emission rate. While this may suggest that methane emissions in the Eagle Ford Shale are lower than current average nationwide emission rates in bottom-up inventories, data collected during the SONGNEX campaign indicate that Floresville may be downwind of a part of the Eagle Ford Shale with slightly lower emissions when compared to other sections of the shale (Peischl et al., 2018). In addition, VOCs co-emitted with methane are likely underreported and underestimated in inventories used for air quality modeling studies in southern Texas. The partitioning of emissions from raw natural gas sources and liquid storage tanks confirms that tank gas is an important source of short-chain alkane emissions in the Eagle Ford Shale, with the enhancement of propane during air mass transport over the Eagle Ford Shale nearly as large as that of ethane. Furthermore, a recent assessment of hemispheric short-chain hydrocarbon emission trends highlighted an unknown source with a methane-to-ethane ratio that is lower than that of RNG (Helmig et al., 2016). Existing data for raw natural gas and tank gas compositions show that the typical methane-to-ethane ratio in tank gas emissions are relatively low compared to that of raw natural gas emissions. Our results show that emissions of alkanes from liquid storage tanks account for 17% of methane, 55% of ethane, 82% of propane, 90% of *n*-butane, and 83% of isobutane emissions from the Eagle Ford Shale.

These emissions are likely to contribute to the unknown NMHC source identified by Helmig et al. (2016).

While alkanes have been shown to dominate the OH reactivity at Floresville, the scarcity of trace gas measurements within the Eagle Ford Shale prevents more thorough VOC emission estimates. Our calculations indicate that propane and butanes emissions alone exceed current inventory numbers for the Eagle Ford Shale by approximately a factor of 2, which can have significant impacts on ozone modeling, particularly if NO_x emissions are underestimated as well. Hence, we stress the need for increased spatial coverage of VOC, NO_x, and greenhouse gas monitoring in and around the shale area to improve upon existing emission inventories. Such improvements are needed before the air quality impacts of the Eagle Ford Shale can be accurately quantified. As the unconventional oil and gas industry in the Eagle Ford Shale continues to grow, the climate and air quality impacts associated with emissions from the shale need to be addressed. This is especially true as the San Antonio metropolitan area may be designated as a nonattainment area by the EPA. However, existing emission estimates are uncertain and variable, and they need to be improved before the impacts on air quality can be quantified.

3. AIR QUALITY AT SHAPE RANCH

While the TCEQ air quality monitors provide valuable insight for regional emissions and transport, the air quality in the midst of the Shale continues to be poorly quantified due a lack of monitoring. The only TCEQ-operated monitor within the oil and gas producing regions in the Eagle Ford Shale is in Karnes City (Fig. 1). The air quality at the monitor is impacted by nearby oil and gas activities, although urban emissions, including traffic, also contribute to observed trace gas observations (Schade & Roest, 2018). Hence, we deployed a research trailer outfitted with meteorology and trace gas instrumentation to a rural location in the western Eagle Ford Shale, far removed from urban centers. This environment served as an opportunity to assess the ambient air quality impacts of surrounding oil and gas activity in an otherwise clean, rural continental air mass. The motivation for the study was to assess the potential health impacts on individuals working and living on the ranch where the trailer was deployed. The data collected also provided valuable information about the episodic nature of emissions from local point sources, including flares. The modeled emissions from nearby flares were compared to observations to assess the impact of flaring emissions on ambient air quality.

3.1 MEASUREMENTS

3.1.1 SITE LOCATION AND ENVIRONMENT

The trailer was placed on Shape Ranch – a large, working bison ranch near the southwestern corner of Dimmit County in southern Texas. The trailer was parked on a

lot where a new house was being built. This location provided access to a reliable line power and would provide the homeowners with information about their exposure to pollution near their new home. Figure 17 shows the location of the trailer on a regional land use map. The nearest active drill site, located 6.3 km east-southeast of the trailer, is also indicated. The local and regional land is dominated by tropical or subtropical grass- and shrublands. Some croplands are also located within the region, especially to the northeast of the ranch near the cities of Carrizo Springs and Crystal City. These are also the nearest sizable urban centers, while other urban areas exist along the Rio Grande to the west and northwest of the site – especially near Eagle Pass, Texas. The city of Laredo is located further south along the Rio Grande, outside of the map boundaries.

Figure 18 shows aerial imagery of the ranch and surrounding lands. The mixed grass- and shrubland in the region can be seen, with an example of the local vegetation shown in Fig. 19. Mesquite trees were the dominant vegetation type on the ranch, with black brush, live oak, date palms, twisted acacia, brasil bush, guajillo bush, and cacti also present. Among these species, only live oak and date palms are known isoprene emitters (Benjamin et al., 1996). More than seventy small olive trees, which are known to emit monoterpenes (Benjamin et al., 1996) were growing on the lot north of the trailer. Figure 18 also shows the nearest major road – Highway 186, known as Faith Ranch Road – indicated in red. This road serves as a main thoroughfare for local ranchers as well as oil and gas industry vehicles. The active drill site was located along a private dirt road which separates Shape Ranch on the north side from San Pedro Ranch to the south. A network of private dirt roads lies between Highway 186 and the trailer

location. Note that several well pads exist around the trailer within 2 km. Many of these sites are legacy oil and gas wells with some ongoing production but little new activity. The terrain on the ranch is gently rolling, with elevations generally varying by tens of meters on the property (Fig. 20). There are a number of small tributaries near Shape Ranch that drain into the Rio Grande. Much of the ranch, including the trailer and the nearby drilling rig, are between 200-250 m above sea level, while the bottom of the nearby Rio Grande Valley is approximately 150 m above sea level. To the west of the map extent, the foothills of the Sierra Madre exceed 1,000 m.

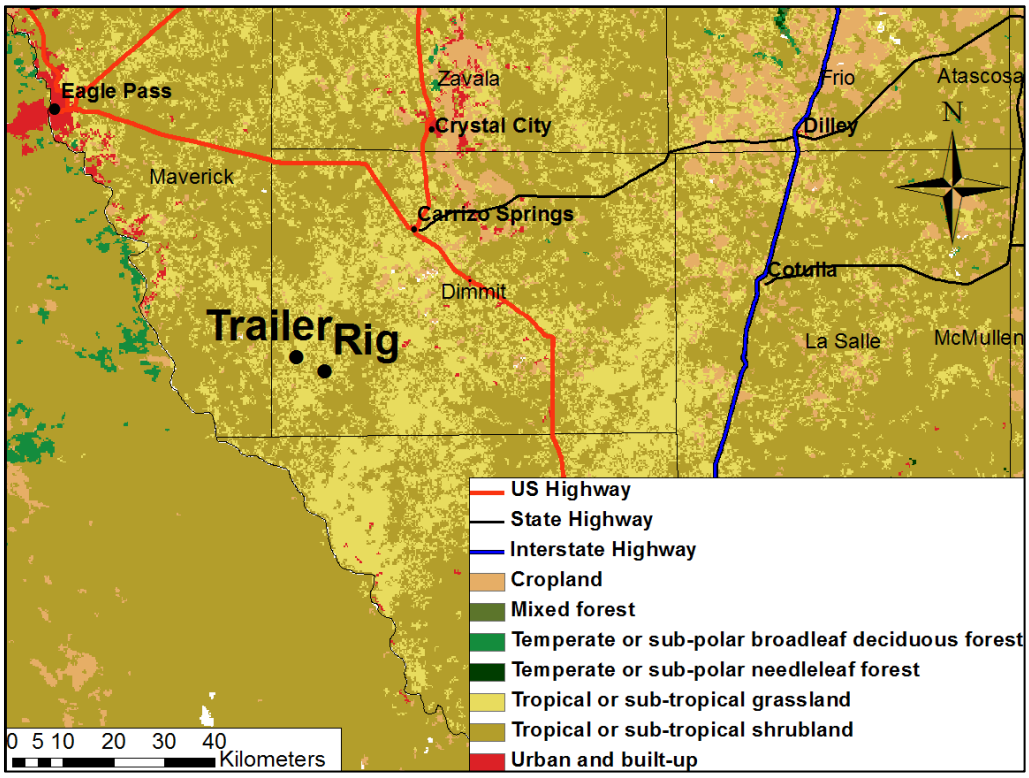

Figure 17: Land use in the region surrounding Dimmit County, which is dominated by tropical or sub-tropical grasslands and shrublands (Homer et al., 2015). Note the location of the trailer (28.321636 °N, 100.068450 °W) and the nearest active drilling site (28.299222 °N, 100.017972 °W).

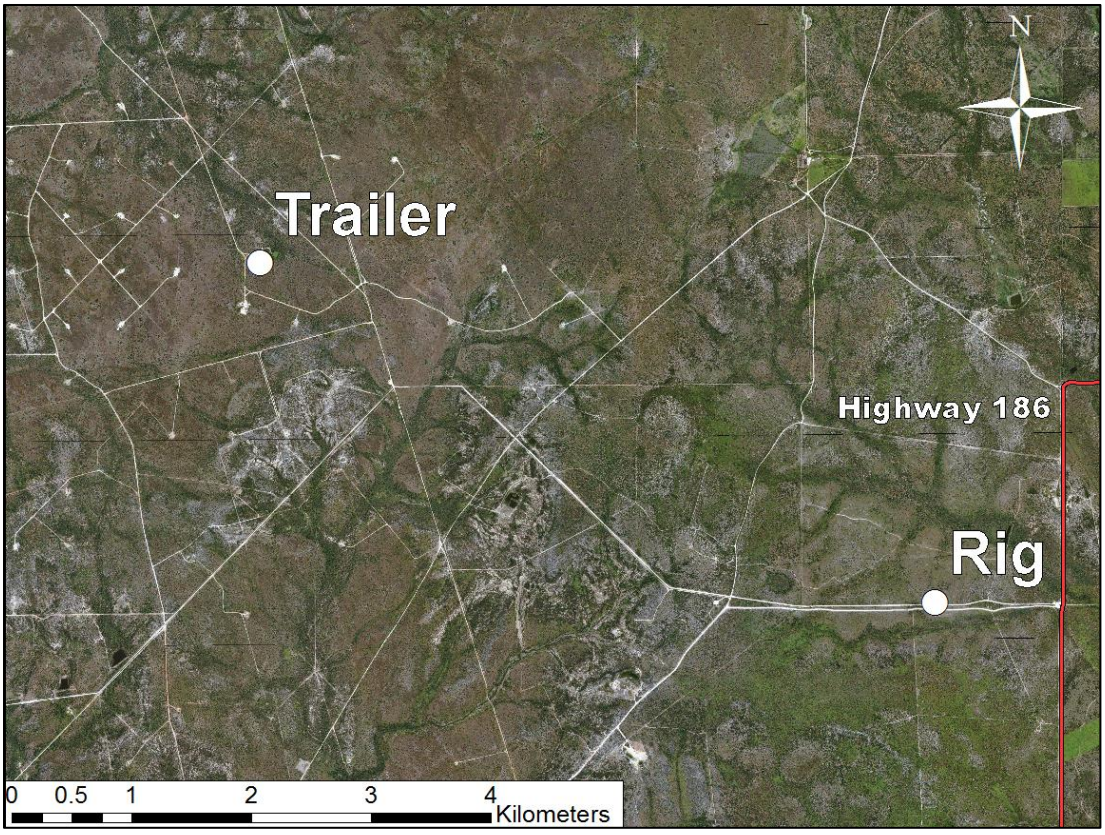

Figure 18: Aerial imagery of Shape Ranch and the surrounding areas (U.S. Department of Agriculture, 2014). Highway 186 is highlighted in red and the locations of the trailer and the nearest active drilling rig are shown. The trailer is surrounded by shrublands and grasslands and there are several well pads within 2 km of the site – mostly legacy oil and gas wells.

3.1.2. INSTRUMENTATION AND DATA

The trailer, shown in Fig. 21, was located 50 m away from the building site of the ranch owners' new home. An air conditioner on the trailer's roof cooled the inside, which housed all trace gas instrumentation, a Campbell Scientific CR1000 data logger, and a Dell Precision T3400 PC. Trace gas instrumentation included a NO/NO_x analyzer, a Gas-Filter-Correlation (GFC) CO analyzer, an NDIR CO_2/H_2O analyzer, a UV-absorption O_3 analyzer, and a dual-channel gas chromatograph (GC) with FIDs.

Figure 19: Vegetation on the lot where the trailer was located.

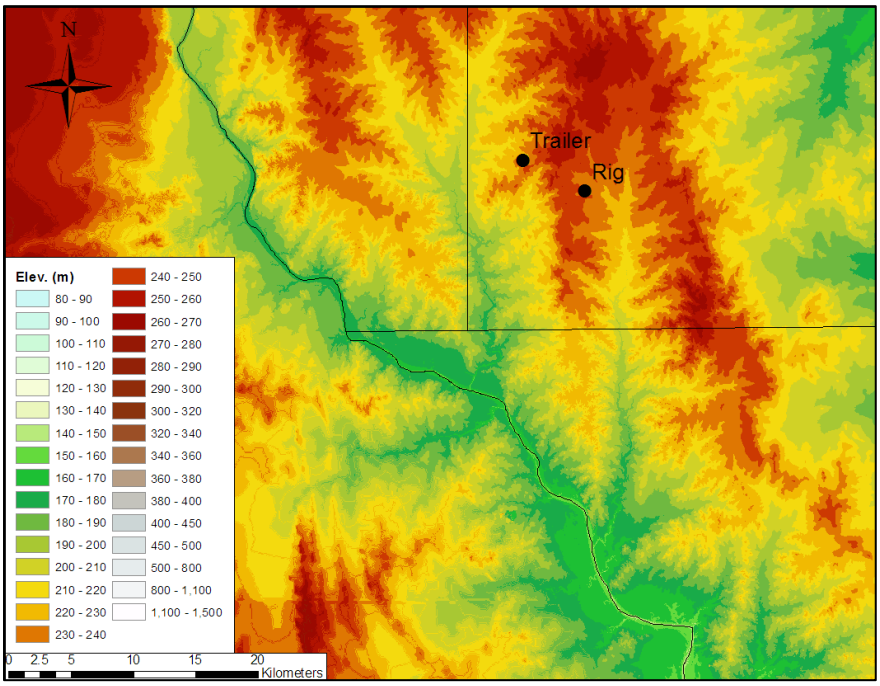

Figure 20: Elevation map of southwestern Dimmit County, where Shape Ranch is located, and nearby sections of the Rio Grande Valley (U.S. Geological Survey, 2013).

Specifications for these instruments are shown in Tables 4 and 5. Meteorological instrumentation from Campbell Scientific included a temperature and relative humidity sensor, a tri-cup anemometer, a barometer, a pyranometer, and a tipping-bucket rain gauge. Meteorology and trace gas concentrations, except for the hydrocarbon measurements, were recorded by the CR1000 data logger as 10 s averages.

The NO_x analyzer was set up to output concentrations expressed as a 20 s moving average. Zero and span calibrations were performed during each site visit – approximately once every ten days. Interference from nitric acid (HNO_3) was avoided as a nylon membrane was used in the inlet filter. For data analyses using the 10 s averages, the NO_x data were shifted forward by 50 s to account for the instrument's response time relative to the ozone and CO_2 measurements. The CO analyzer was also set up to record 20 s moving averages and it was also zeroed and calibrated during each site visit. However, the measurements from this instrument are more temperature sensitive, so automated zeroing was performed once every 6 h to counteract electronic drift. The ozone analyzer was run with a factory calibration and was regularly zero checked using an ozone scrubber. Carbon dioxide was measured using a single channel NDIR instrument (LI-840, Licor Inc.) calibrated using a CO_2 standard, while water vapor measurements relied on a factory calibration.

The gas chromatograph was set up to perform half hourly hydrocarbon measurements to maximize temporal resolution, at the expense of measuring more compounds. Samples were collected on two-stage activated carbon adsorption micro-traps, one containing Carbopack B with Carbotrap X backup for C_5 and higher

hydrocarbons, and one containing Carbotrap X and Carboxen 1000 to trap short-chain hydrocarbons. The former sample, injected into a 60-m, wide-bore MTX-624 column, was collected directly from ambient air before injection. The latter sample, injected into a 30-m, wide-bore PLOT-Alumina column, was first dried through a Nafion dryer, except for a period from 7-28 August when a Drierite desiccant tower was used instead. The flow then passed through an Ascarite II CO_2 scrubber with additional potassium perchlorate to remove any leftover moisture. Both samples were thermally desorbed directly into two wide-bore 5-m retention gaps ahead of the chromatographic columns, similar to Park et al. (2010) (Table 5). Sampling time was twenty minutes for both samples, from 8 to 28 min into each 30 min period. Thermal desorption at 200 °C occurred for 2 min at the beginning of each run, after which the traps were allowed to cool down to approximately room temperature before sampling began. A ppm-level internal standard was diluted into the main sampling line to quantify observed hydrocarbon peaks in the chromatograms. Other standard gases, including mixes of normal alkanes, branched alkanes, alkenes, methyl ethyl ketone (MEK), and BTEX were injected into the main sampling line inlet using a syringe during selected site visits. An automated zero-air run was performed once every 15 hours to monitor for contamination. A mixture of hydrogen gas and zero air produced using onsite hydrogen and zero air generators was used for the FIDs, as well as carrier gas (H_2).

The non-hydrocarbon trace gas and meteorological data were reduced to 30 min resolution to align with the hydrocarbon measurements. This was performed by finding the median measurement for each variable in 15 min periods and then averaging the

Figure 21: The trailer parked on Shape Ranch. Meteorological instrumentation and the inlet for trace gas instruments were mounted on a pole on the southeast corner of the trailer at a height of approximately 3 m.

Table 4: Technical information for trace gas measurements.

Gas	Instrument	LoD	Precision	Accuracy	Zero/Calibration
NO/NO_x	Thermo Electron Corp. Model 42C	0.4 ppb	± 0.4 ppb	-	zero: CO in zero air standard* span: NO standard* at 103.5 ppb ±5%
CO	Thermo Electron Corp. Model 48C	40 ppb	± 20 ppb	-	zero: internal catalytic zero every 6 h span: CO in zero air standard* at 547 ppb ±2%
CO_2	Licor Model 840A	0 ppm	RMS noise < 1 ppm	± 1% of reading	zero: CO in zero air standard* CO_2 in zero air standard* at 454 ppm ±1%
H_2O		0 ‰	RMS noise < 0.01 ‰	± 1.5% of reading	CO in zero air standard* Factory calibration
O_3	2BTech Model 202	3 ppb	± 1.5 ppb or ± 2% of reading, whichever is greater		external zero using ozone scrubber Factory calibration
Hydro-carbons	SRI model 8610c GC w/ dual-channel FID	~0.07 ppbC	± 1.8% for internal standard	± 7.3% **	Zero air generator 2-2-Dimethylbutane in N_2 standard at 20.52 ppm ±2%

* Standard gases form Scott Marrin Inc.
** 5% accuracy for each of two flow meters and 2% accuracy for standard gas concentration, added in quadrature.

Table 5: Columns used in dual-channel GC-FID.

Column	Target Compounds	Polarity	Length	Inner Diameter
MTX-624	BTEX	Low to mid	60 m	0.53 mm
PLOT-Al	Short chain alkanes up to C_6	Non-polar	30 m	

medians for the two 15 min periods to create each 30 min data point. The exceptions were rainfall, which was totaled for each 30 min period, and wind speed and direction, for which a resultant mean (vector averaging) was used. Medians were chosen to remove artificial instantaneous spikes in the measurements.

Electronic spikes occurred as UPCs turned on or off during significant drops in the voltage of the trailer's power source. While this issue was rectified in July, voltage drops were a recurring problem during the first portion of the field campaign, especially when the air conditioner went through a power cycle on hot afternoons. Once 30 min data were obtained, regular invalid measurements (e.g. automated zeroes) were flagged for removal and other invalid measurements (e.g. contamination, bad readings related to power issues, irregular zeroes and calibrations) were flagged and removed manually. For certain analyses, the original 10 s resolution data were used. In these instances, quality control was performed for the relevant subset of data.

The hydrocarbon data were recorded and analyzed offline using SRI PeakSimple Software (SRI Instruments, Version 3.88, 2010). Data were removed as power issues in the trailer resulted in the failure of the hydrogen generator, which extinguished the flames in the FIDs, or sampling periods or thermal desorption were interrupted. Other data were flagged for removal, including a number of runs after the instrument was started to allow for the traps to be cleaned, and zero runs and injections of standard gases performed.

Hydrocarbons were identified in the laboratory and in the field via retention times using injections of standard gases from Scotty transportable cylinders, and/or

knowledge of expected hydrocarbons in a rural, continental oil and gas field environment. Gases that were not included in standard injections were tentatively identified based on their relative retention times. This introduces some uncertainty as compounds cannot be identified with FIDs, and some compounds may coelute, such as, e.g. n-octane and toluene. Furthermore, temperature fluctuations in the trailer impacted the retention times of more volatile compounds as the column oven was not always able to cool to the set start temperature (40 °C). Breakthrough of short-chain hydrocarbons, such as propane and propene, were assessed by examining the propane peaks for tailing and by testing the ratios of injected alkanes and alkenes at near-ambient to above-ambient concentrations. No issues with breakthrough were identified. Shifting retention times were addressed by integrating chromatographic peaks in small batches and adjusting expected retention times as needed.

An internal standard gas containing 2,2-dimethylbutane ("neohexane", Scott Marrin Inc., 20.52 ppm ± 2% in N_2) was used to quantify hydrocarbon concentrations. This compound was chosen as its atmospheric concentration was expected to be negligible, its retention time known, and its elution nearly unaffected by other hydrocarbons. The period from 17-25 September 2015 was selected to calculate chromatographic performance using the internal standard peak because there was continuous, uninterrupted data collection. During this period, the internal standard was introduced at 2 mL min^{-1} at the head of the main sampling line, where the net flow was approximately 1430 mL min^{-1}, resulting in the internal standard being diluted to 28.1 ppb (168.6 ppbC). The variability of the chromatographic peaks for the internal standard

provided an estimated precision of ±1.8% (2σ). The uncertainty in the internal standard concentration of ±2% and the precision of the two flow meters (±5% each) assessing standard and main line flows, resulted in an estimated hydrocarbon measurement uncertainty of ±8% (±13.5 ppbC for the internal standard) when added in quadrature.

For FIDs, it is assumed that the instrument response is a function of the number of carbons and the relative mass of carbon within the molecule (Lamanna & Goldstein, 1999). Thus, the relative response factor of a compound is:

$$RRF_i = \frac{n_{C,i} \cdot F_i}{n_{C,IS} \cdot F_{IS}} \tag{3.1}$$

where $n_{C,i}$ and $n_{C,IS}$ are the number of carbon atoms in an arbitrary species *i* and the internal standard, respectively, and F_i and F_{IS} are the fractions of carbon by mass. The mixing ratio of each species was then calculated as

$$x_i = \frac{A_i x_{IS}}{RRF_i \overline{A_{IS}}} \tag{3.2}$$

where A_i is the area of each chromatogram peak for species *i*, $\overline{A_{IS}}$ is the mean area of the internal standard peaks from 17-25 September 2015, and x_{IS} = 28.1 ppb is the corresponding mixing ratio of the internal standard. The limit of detection corresponded to a chromatographic peak with an area of 1, which is approximately 0.07 ppbC.

3.2. ANALYSIS METHODS

3.2.1. SOURCE IDENTIFICATION USING NONNEGATIVE MATRIX FACTORIZATION

A number of source types were expected to contribute to observed trace gas variability on Shape Ranch. In addition to emissions from local and regional oil and gas activities, there will be emissions from vegetation, soils, livestock and agriculture, distant urban sources, and local and regional vehicle emissions. However, it should be noted that much of the vehicle emissions will be from traffic associated with the oil and gas industry, as traffic counts on the nearby FM 186 increased by more than a factor of 10 between 2010 to 2015 (Texas Department of Transportation, 2018). There will also be a strong influence on trace gas concentrations due to meteorology. Some emissions sources, including (e.g.) biogenic emissions and evaporative hydrocarbon emissions, are strongly dependent on temperature (Guenther et al., 2012; Rubin et al., 2006), with biogenic and soil emissions also depending on moisture availability (Guenther et al., 2012; Vinken et al., 2014).

Varying wind directions allow for different air masses to be transported towards Shape Ranch. Air over the Gulf of Mexico to the southeast is relatively clean (Gilman et al., 2009), while continental air masses, with emissions from distant urban centers such as San Antonio, are located to the east and to the north. Westerly winds were very rare during the field campaign, as discussed in section 3.3.

Several methods are available to identify source types contributing to observed trace gas variability. Traditional matrix factorization techniques have been employed,

such as singular value decomposition (SVD) and positive matrix factorization (PMF). The latter, which was originally developed by Paatero and Tapper (1994), is a preferred source apportionment method often used by the US EPA (Reff et al., 2007). Several new PMF variations have been developed and are referred to as non-negative matrix factorization (NMF), a name that was popularized by Lee and Seung (1999). NMF models have been developed for a variety of applications, including image decomposition (Lee and Seung, 1999), metagenomic analysis (Brunet et al., 2004), and atmospheric pollutant source attribution (e.g. Thiem et al., 2012). The NMF models work as follows:

1. A number of factors is prescribed by the user. This choice must be made carefully to allow for a sufficiently informative number of factors, though too many factors will cause results that cannot be physically explained or explain a negligible fraction of the total variability in the dataset.
2. Two matrices are initialized – the first is the contribution of individual variables (trace gases in the case of Shape Ranch) within each factor (***W***), and the second is the expression of each factor during every time step in the database (***H***), such that the matrix multiplication of ***W*** and ***H*** are an approximation of the observed dataset ***V***:

$$\boldsymbol{V} \approx \boldsymbol{WH} + \boldsymbol{\varepsilon} \quad (3.3)$$

where $\boldsymbol{\varepsilon}$ is the residual error. The initialization of ***W*** and ***H*** may be based on other matrix factorization methods, such as non-negative SVD; it may be randomly generated based on the observed distributions of variables; or it may be

prescribed by the user. For random initializations, the NMF model should be run a number of times to identify the best solution based on the large number of possible starting points.

3. The initial guess is improved upon to reduce the error between the observed dataset and the modeled dataset – i.e., the matrix multiplication of the variables within each factor by the expression of each factor over time. There are a number of algorithms to reduce this error.

The least-squares NMF (LS-NMF) algorithm (Wang et al., 2006) was chosen because this method allows for the resulting factors to be weighted by uncertainties in the observed dataset, such that highly-uncertain variables have less of an influence on the solution than highly certain variables.

The *NMF* package (Gaujoux & Seoighe, 2010) in the *R* programming language (R Core Team, 2018) was used to perform a source apportionment of the Shape Ranch dataset. This package includes several initialization methods and error-reducing algorithms. Both the SVD and random-seed initializations were tested with the LS-NMF algorithm. The SVD has the advantage of performing a high-quality initial guess, resulting in relatively small errors between the observed and modeled datasets and a low computational cost. Meanwhile, the random-seed initialization, while relatively slow due to the large number of runs needed, may result in a lower residual error if one of the random initializations converges towards a true solution.

Data were prepared in a manner following Guha et al. (2015). Observations that were missing hydrocarbon measurements – e.g., during zero runs – were removed.

Ethylbenzenes and xylenes were summed for the NMF due to periodic misidentifications associated with the near-coelution of ethylbenzene and m/p-xylene. The limit of detection (LOD) for each trace gas species was assumed to be the minimum non-missing measurement in the timeline. Missing CO and CO_2 values were linearly interpolated. Missing NO_x and VOC concentrations were replaced with random values between zero and 0.5 × LOD. The top 1% of concentrations for each species were considered to be extreme. These values were scaled downward to equal the 99^{th} percentile of the distribution of concentrations in an NMF run to limit the influence of episodic plumes on the overall source attribution. The background concentration for each species, assumed to be the minimum concentration in the timeline, was subtracted to remove the background but a value of e^{-5} was added back in to avoid concentrations of zero in the NMF model. Uncertainties were quantified based on instrument precision and concentration, as shown in Table 6, with absolute uncertainties converted to relative uncertainties using the concentration time series for the associated species. Lastly, the concentrations for each species were normalized such that the maximum concentration was equal to one for each species.

Table 6: Assumed uncertainties for the LS-NMF dataset.

Species	Uncertainty	Source
CO	20 ppb	Instrument precision
CO_2	1%	Instrument accuracy
O_3	3 ppb	Instrument precision and accuracy
NO_x	0.2 ppb	Instrument precision
VOCs	2 × LOD for concentrations < LOD	Guha et al. (2015)
	$[(8\% \times [VOC]_i)^2 + LOD^2]^{0.5}$	Equation from Guha et al. (2015), Value of 8% is instrument measurement uncertainty

The US EPA has developed a VOC emission factor database for anthropogenic sources known as SPECIATE (U.S. Environmental Protection Agency, 2015c). The source factors from the NMF model were compared to the SPECIATE sources to identify source categories that may be associated with the NMF factors. The comparison is performed by calculating the dot product of normalized emission factors, following eq. 5 from Kota et al. (2014):

$$\theta = \frac{\sum_{i=1}^{n} f_i s_i}{\sqrt{\sum_{i=1}^{n} f_i^2 \sum_{i=1}^{n} s_i^2}} \tag{3.4}$$

where f_i and s_i are the NMF and SPECIATE scores for VOC i for an arbitrary paring of emission factors from the NMF model output and SPECIATE database. A value of $\theta = 1$ implies a perfect match between the NMF and SPECIATE factors where as $\theta = 0$ would result from orthogonal vectors.

3.2.2. FLARING EMISSIONS ESTIMATE USING PHOTOCHEMICAL GRID MODEL

The proximity of the Shape Ranch field site to potentially highly-emitting point sources raises the issue of distinct, local plumes impacting ambient air quality on the ranch. A small point source, such as a flare, could potentially have significant impacts at a small (i.e. sub-kilometer) spatial scale (Olaguer, 2012). However, this means that the near-scale impacts from such a point source will not be resolved by traditional photochemical grid models, such as WRF-Chem and CMAQ (Brasseur & Jacob, 2017), which operate at kilometer scales. While Gaussian dispersion models like AEROMOD

and CALPUFF are often applied at the meter-to-kilometer scale, their photochemical mechanisms are relatively simple.

Another option is to run a scalable, community-scale photochemical grid model as an appropriate solution to model the local impacts from flares while utilizing a robust chemical mechanism. Olaguer (2012) has previously demonstrated the success of localized photochemical grid models in quantifying localized ozone impacts from flares. However, his modeling exercise assessed the impacts of one large flare at a refinery. Within the Eagle Ford Shale, flares are often used on oil well pads to destroy excess natural gas and at midstream facilities during processing, creating dense clusters of relatively small flares. These flaring emissions are not reported to the state if they operate as part of a facility that does not exceed emission thresholds for VOCs and criteria pollutants (Texas Administrative Code). Therefore, the air quality impacts of a dense network of small flares remains unknown.

Recent developments in remote sensing data retrieval techniques have allowed for the detection of flares as radiant heat sources that are distinct from biomass burning. Elvidge et al. (2015) created a global database of flares using radiant heat detections from the VIIRS instrument on the Suomi NPP satellite (Elvidge et al., 2013; T. E. Lee et al., 2006). This database includes an estimate of annual flared natural gas volumes for each flare based on its detection frequency and its average radiant heat output. Meanwhile, the individual daily VIIRS data files list the flares detected during each pass and, for flares of sufficient radiance, the natural gas flaring rate and blackbody temperature. The combination of daily VIIRS flare detections and the flaring database

from Elvidge et al. (2015) allows for an estimation of local flaring emissions for a given day that can be used in local-scale air quality modeling.

3.2.2.1. PARAMETERIZING FLARING EMISSIONS USING VIIRS NIGHTFIRE DATA

The Elvidge et al. (2015) database includes the location, average temperature, annual flaring volume in billions of cubic meters (R_{BCM}), annual clear-sky observations (n_{clear}), and annual clear-sky detection frequency (f_{clear}), i.e. the percentage of clear-sky observations during which the flare was observed. Therefore, assuming each flaring observation represents 24 hours of flaring, the flaring rate in cubic feet per hour (R_{CF}/hr) can be estimated as:

$$R_{CF}/hr = \frac{R_{BCM} \cdot 35.3147\times10^{9}\ CF\ BCM^{-1}}{n_{clear} \cdot \frac{f_{clear}}{100} \cdot 24\ hr\ d^{-1}} \quad (3.5)$$

Emission factors for flares are based on the energy released by the flare. The EPA's AP-42 (U.S. Environmental Protection Agency, 2016c) estimates flaring emissions of 0.068 pounds per million British Thermal Units (lb/10^6 BTU) for NO_x, 0.37 lb/10^6 BTU for CO, and 0.14 lb/10^6 BTU for hydrocarbons from an elevated flare combusting a mix of 80% propylene and 20% propane. Meanwhile, the EIA estimates 120.6 lb/10^6 BTU for CO_2 from a "natural gas" flare (U.S. Energy Information Administration, 2016). The heating value for flares can vary greatly with the composition of the fuel, with diluted gases reduced to less than 300 BTU ft^{-3} and pure propylene exceeding 2,000 BTU ft^{-3} (Torres et al., 2012; U.S. Environmental Protection Agency, 2016c).

Assuming an average heating value of 1,000 BTU ft^{-3} and using the EPA and EIA flaring emission factors, the flaring emissions in moles per second can be approximated as follows:

$$R_{mol,i}/s = \frac{R_{CF}}{hr} \cdot H \cdot \frac{F_i}{M_i} \cdot \frac{1\ hr}{3{,}600\ s} \tag{3.6}$$

where H is the heating content of natural gas in BTU ft^{-3}, F_i is the emission factor for species *i* in grams per BTU, and M_i is the molar mass of species *i*.

Many flares are only occasionally detected and there is some variance in the location of individual detections. In order to quantify flaring emissions for a specific date, the VIIRS Nightfire flaring detections were cross referenced with the Elvidge et al. (2015) database. It was assumed that an individual daily VIIRS Nightfire flare detection corresponded to the nearest flare in the database, and the emission rates as calculated in Eq. 3.6 were assigned to that flare. The flaring emissions were then distributed into a spatial grid for use in the TAMNROM-3D photochemical transport model.

3.2.2.2. MODELING FLARING EMISSIONS USING TAMNROM-3D

The TAMNROM-3D model is a three-dimensional Eulerian air quality model that was developed for near-road applications (Kota et al., 2010). The modeling domain is a scalable 100 × 100 cell (horizontal) by 10 layer (vertical) gridded plane with inputs for gridded meteorology, gridded emissions sources, and gridded vehicle density and speed. Photochemical modeling is performed using a revised SAPRC-99 mechanism with added air toxics from mobile sources, which “lumps” many species within organic groups based on the OH reaction rate constant. Presently, meteorology is assumed to be

spatially homogenous within each vertical layer but is allowed to vary with time on an hourly basis.

An *R* script was used to identify the indices of grid cells containing the Shape Ranch trailer and nearby flaring emissions. A separate script pulled meteorology from the 3 h NARR reanalysis. The meteorology from the NARR grid cell containing the Shape Ranch trailer location was applied to the modeling domain. The NARR contains skin temperatures; 2 m temperature and relative humidity; 10 m winds; and temperature, relative humidity, and winds at pressure levels from 1000 to 100 mb in increments of 100 mb, with additional levels at 975, 950, and 925 mb, and several levels above 100 mb. The meteorology for the TAMNROM-3D model layer midpoints were interpolated from soundings created from the NARR data, starting from the surface with the skin temperature and near-surface meteorology and moving upwards using pressure-level meteorology. It was assumed that the surface winds (0 m agl) were 0 m s^{-1}. Hourly profiles were developed between the NARR's 3 h resolution by linearly interpolating variables in time between the previous and following profiles.

Table 7 summarizes the sources for trace gases and lumped species in the SAPRC-99 mechanism. Initial and boundary conditions for trace gas concentrations were estimated using the Shape Ranch trailer data for O_3, CO, and NO_x, CO_2 (modeled as SF_6), and most VOCs. For missing values of O_3, CO, and CO_2, the median concentration from all non-missing observations during the corresponding hour was assumed. For NO_x and VOCs, 0.5 x LOD (assumed to be the minimum non-missing observation) was assumed for all missing values. Other trace gas concentrations were

assumed based on the SONGNEX flights on 2 and 7 April 2015 (Peischl et al., 2018). The median concentration for observations within the boundaries of the Eagle Ford Shale were found for the species for each flight and the average between the two flights was used as a constant boundary condition. Nitrous acid (HONO) and hydrogen peroxide (H_2O_2) were assumed from literature data.

Table 7: Species and lumped groups in the SAPRC-99 mechanism.

Modified SAPRC-99 mechanism ID	**Species**	**Include in model**	**Source (or reason for omission if not included in model)**
O_3	Ozone	Yes	Shape ranch
NO	Nitric oxide		
NO_2	Nitrogen Dioxide		
HO.	Hydroxyl radical	Yes	10^6 cm^{-3}
HONO	Nitrous acid	Yes	Lammel and Cape, 1996
CO	Carbon monoxide	Yes	Shape ranch
SO_2	Sulfur dioxide	Yes	SONGNEX
HCHO	Formaldehyde		
CCHO	Acetaldehyde		
RCHO	Lumped C_3+ Aldehydes	No	No data
ACET	Acetone	Yes	SONGNEX
MEK	Ketones and other non-aldehyde oxygenated products which react with OH radicals slower than 5×10^{-12} cm^3 $molec^{-2}$ s^{-1}		
MEOH	Methanol		
COOH	Methyl hydroperoxide	No	No data
ROOH	Lumped higher organic hydroperoxides		
GLY	Glyoxal	Yes	SONGNEX
MGLY	Methyl glyoxal	No	No data
BACL	Biacetyl		
PHEN	Phenol		
CRES	Cresols		
NPHE	Nitrophenols		
BALD	Aromatic aldehydes	Yes	SONGNEX
MVK	Methyl vinyl ketone	No	No data

Table 7: Continued.

Modified SAPRC-99 mechanism ID	Species	Include in model	Source (or reason for omission if not included in model)
PROD2	Ketones and other non-aldehyde oxygenated products which react with OH radicals faster than 5×10^{-12} cm^3 $molec^{-2}$ s^{-1}.	No	No data
RNO3	Lumped organic nitrates		
DCB1	Reactive Aromatic Fragmentation Products that do not undergo significant photodecomposition to radicals		
DCB2	Reactive Aromatic Fragmentation Products which photolyze with alpha-dicarbonyl-like action spectrum		
DCB3	Reactive Aromatic Fragmentation Products which photolyze with acrolein action spectrum		
ALK1	Alkanes and other non-aromatic compounds that react only with OH, and have $k_{OH} < 5 \times 10^2$ ppm^{-1} min^{-1} (primarily ethane)	No	Low reactivity
ALK2	Alkanes and other non-aromatic compounds that react only with OH, and have k_{OH} between 5×10^2 and 2.5×10^3 ppm^{-1} min^{-1} (primarily propane and acetylene)	Yes	Shape Ranch
ALK3	Alkanes and other non-aromatic compounds that react only with OH, and have k_{OH} between 2.5×10^3 and 5×103 ppm^{-1} min^{-1}		
ALK4	Alkanes and other non-aromatic compounds that react only with OH, and have k_{OH} between 5×10^3 and 1×10^4 ppm^{-1} min^{-1}		
ALK5	Alkanes and other non-aromatic compounds that react only with OH, and have k_{OH} greater than 1×10^4 ppm^{-1} min^{-1}		

Table 7: Continued.

Modified SAPRC-99 mechanism ID	Species	Include in model	Source (or reason for omission if not included in model)
ARO1	Aromatics with $k_{OH} < 2 \times 10^4$ ppm^{-1} min^{-1}	Yes	Shape Ranch
ARO2	Aromatics with $k_{OH} > 2 \times 10^4$ ppm^{-1} min^{-1}		
OLE1	Alkenes (other than ethene) with $k_{OH} < 7 \times 10^4$ ppm^{-1} min^{-1}		
OLE2	Alkenes with $k_{OH} > 7 \times 10^4$ ppm^{-1} min^{-1}	No	No data
SULF	Sulfates		
SF6	Sulfur hexafluoride (tracer)	Yes	Shape Ranch (CO_2)
NO3	Nitrate radical	No	No data
N2O5	Nitrogen pentoxide		
HNO3	Nitric acid	Yes	SONGNEX
HO2.	Hydroperoxide radicals	No	No data
HNO4	Peroxynitric acid		
HO2H	Hydrogen peroxide	Yes	Sakugawa et al., 1990
C-O2.	Methyl peroxy radicals	No	No data
RO2-R.	Peroxy Radical Operator representing NO to NO_2 conversion with HO_2 formation		
R2O2.	Peroxy Radical Operator representing NO to NO_2 conversion without HO_2 formation		
RO2-N.	Peroxy Radical Operator representing NO consumption with organic nitrate formation		
CCO-O2.	Acetyl Peroxy Radicals		
PAN	Peroxy Acetyl Nitrate	Yes	SONGNEX
RCO-O2.	Peroxy-Propionyl and higher peroxy-acyl Radicals	No	No data
PAN2	PPN and other higher alkyl PAN analogues	Yes	SONGNEX
BZCO-O2.	Peroxy-acyl radical formed from Aromatic Aldehydes	No	No data
PBZN	PAN analogues formed from Aromatic Aldehydes		

Table 7: Continued.

Modified SAPRC-99 mechanism ID	Species	Include in model	Source (or reason for omission if not included in model)
MA-RCO3.	Peroxyacyl radicals formed from methacrolein and other acroleins	No	No data
MA-PAN	PAN analogue formed from Methacrolein		
MACR	Methacrolein		
IPROD	Other Unsaturated Aldehydes		
ETHENE	Ethene		
ISOPRENE	Isoprene	Yes	Shape Ranch
TERP	Monoterpenes		
NH3	Ammonia	Yes	SONGNEX
HCL	Hydrochloric acid	No	No data
BENZ	Benzene	Yes	Shape Ranch benzene
ACROLEIN	Acrolein	No	No data

3.3. RESULTS

3.3.1. AMBIENT AIR QUALITY AT SHAPE RANCH

The following section presents a discussion of general air quality at Shape Ranch during the field campaign. The meteorology and trace gas dataset being used for this analysis is the half-hourly data discussed in Sect. 3.1.2. Trace gas data availability is shown in Fig. 22. Data for O_3, CO_2, and H_2O are available for the entire time period from 9 April to 24 November 2015, except for bad data points and calibrations. The CO analyzer failed on 8 November due to a dying infrared light source, while the NO_x analyzer failed on 15 September due to an electrical issue. Hydrocarbon concentrations have sparse data availability before 29 July when an electrical issue in the trailer was corrected. After 6 October, when one of the hydrocarbon trap heaters failed, the two

hydrocarbon channels were alternated to collect periods of data for all hydrocarbons in the dataset.

3.3.1.1. METEOROLOGY

The observed meteorology at Shape Ranch in 2015 is compared to climatological means (1981-2010) at Carrizo Springs (Arguez et al., 2010) in Table 8. Meteorology on Shape Ranch was not observed during the earliest days of April and the final days of November – the climatologically coolest parts of those two months – so the temperatures for these months would be biased high, and the precipitation would be biased low. Temperatures and precipitation were near average from April through June. July and August, however, were hot and dry, with average daily maximum temperatures over 100 °F and only 0.01 inches of rain in July with no rain in August. Below-average rain remained for September with near-normal rain in October and November. These months continued to be warmer than average, with daily mean temperatures and daily minimum temperatures exceeding the average respective temperatures by more than 6 °F in both October and November.

Figure 23 shows the seasonal progression of wind speed and direction in 2015 using monthly wind roses. Springtime cold fronts, bringing cold, continental air masses into Texas from the north and northwest ceased in April, after which predominantly southeasterly flow continued through September. Cold fronts returned in October and November, when northwesterly winds are observed again. The northwesterly winds from cold fronts also tended to be the strongest, often exceeding 5 m s^{-1}. Note that the

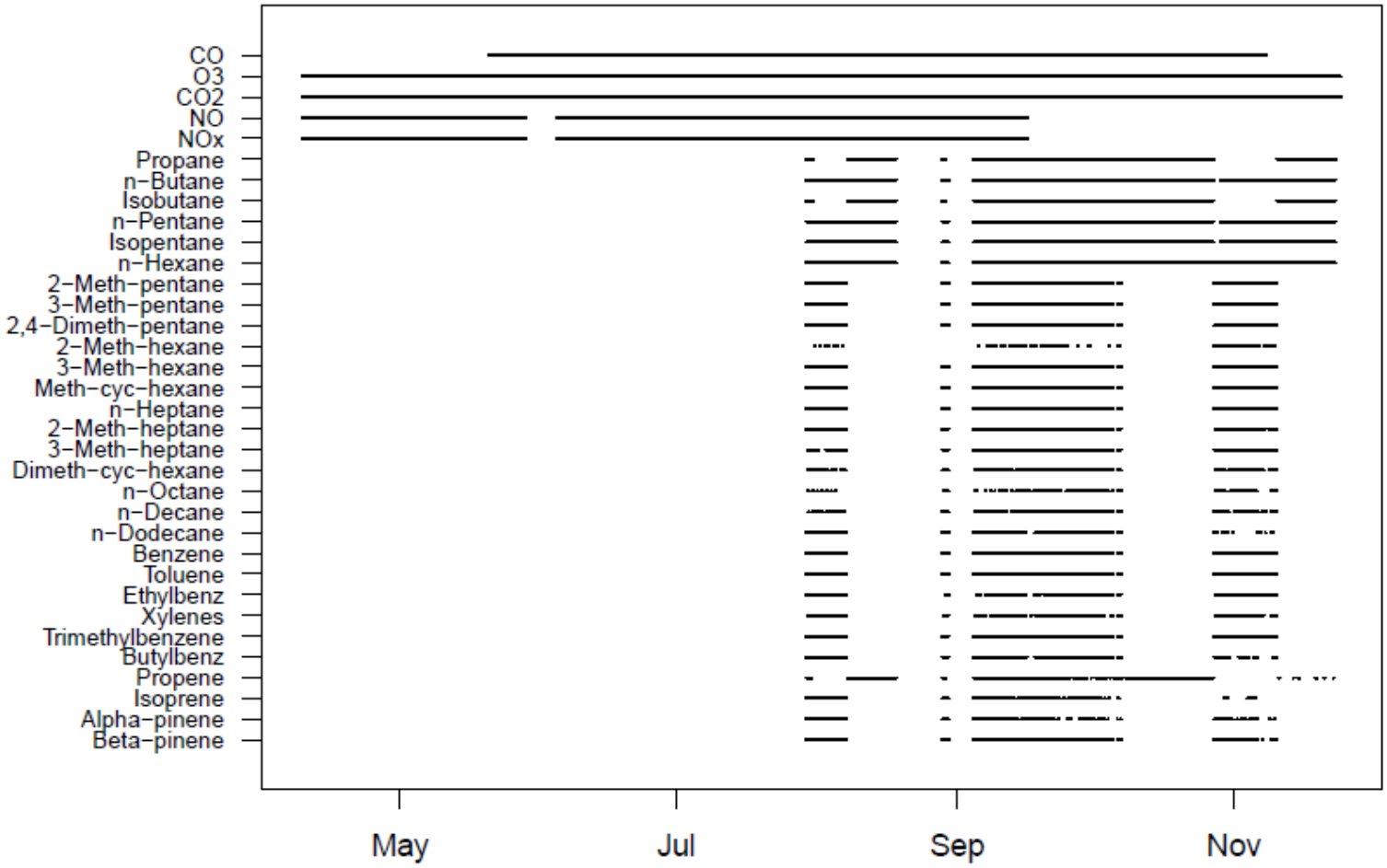

Figure 22: Trace gas measurement availability at Shape Ranch.

Table 8: Summary of meteorology at Shape Ranch (red) in 2015, compared to 1981-2010 climatology for Carrizo Springs (blue) (Arguez et al., 2010).
* April and November temperatures and precipitation at Shape Ranch are based on an incomplete month of measurements.

Month	April*	May	June	July	August	September	October	November*
Average daily max temp (°F)	83.1	88.1	94.2	101.0	103.6	99.5	91.8	79.6
	85.3	91.1	96.3	97.8	98.9	92.7	84.7	74.9
Average daily mean temp (°F)	72.9	78.3	82.8	88.1	89.9	85.9	78.9	68.6
	72.4	79.2	84.7	86.2	86.8	81.0	72.5	62.1
Average daily min temp (°F)	63.9	70.0	73.1	75.3	75.9	73.6	67.6	58.7
	59.5	67.3	73.2	74.6	74.8	69.4	60.3	49.4
Monthly precip (in.)	0.79	2.67	2.69	0.01	0.00	0.54	2.25	1.51
	1.59	2.82	2.06	1.96	1.53	2.42	2.12	1.12

percentage of calm observations increased greatly from July through November. This is thought to be associated with increased resistance from aging bearings in the tri-cup anemometer, thereby increasing the detection limit of low wind speeds. The diurnal variation in wind speed and direction is shown in Fig. 24. Wind speeds reached a daily minimum between 03:00 to 06:00 LST, prior to sunrise. Wind speeds increased during the day, before peaking in the late evening and early overnight hours. The timing of this peak may be associated with downward mixing of a nocturnal low-level jet over the Rio Grande Valley (Walters et al., 2008). However, the late evening and overnight hours also had a relatively high frequency of calm observations, suggesting that the late-evening peak in wind speeds is not always present. While southeasterly winds remained prevalent throughout the diurnal cycle, easterly winds were frequently observed during the afternoon and evening hours.

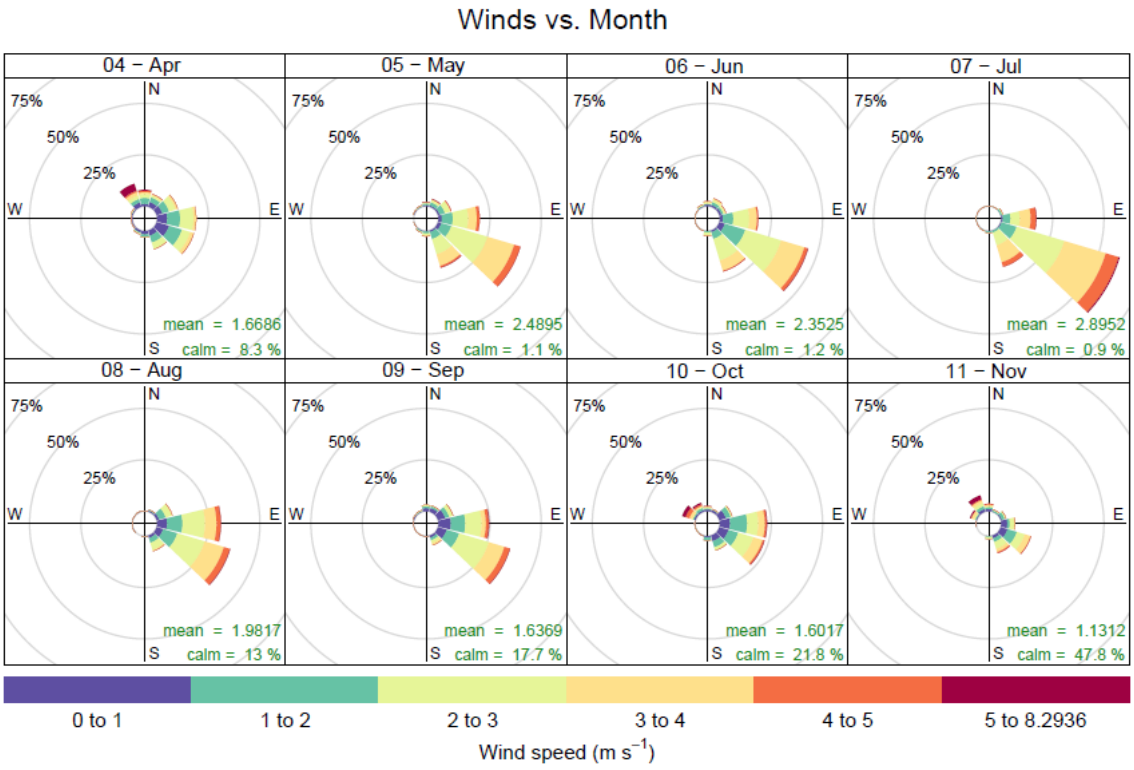

Figure 23: Wind roses for monthly observations at Shape Ranch. Note that April and November do not have a full month of observations. The increasing frequency of calm observations during the second half of the field campaign was likely due to debris in the bearings of the anemometer.

3.3.1.2. CARBON DIOXIDE

Figure 25 shows the diurnal cycle of CO_2 mixing ratios at Shape Ranch, with low CO_2 during the daytime and elevated CO_2 during the night. From 10:00 to 18:00 LST, CO_2 never exceeded 450 ppm. However, numerous outliers exist overnight, between 20:00 to 08:00 LST. Several measurements during the early morning hours exceeded 500 ppm, with peak CO_2 mixing ratios reaching 567 ppm. The high overnight CO_2 values were likely associated with combustion sources and respiration from biogenic sources (Olsen & Randerson, 2004). The effect of precipitation increasing ecosystem

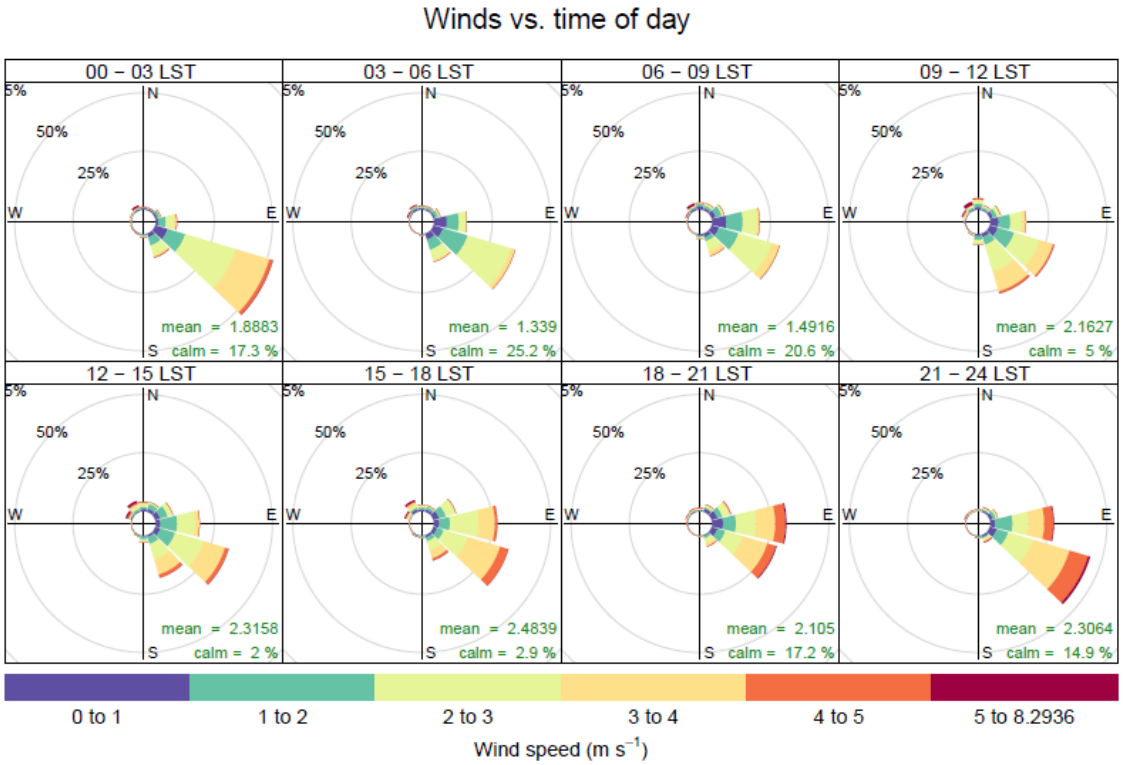

Figure 24: Wind roses for three-hourly time periods showing the diurnal cycle of winds at Shape Ranch.

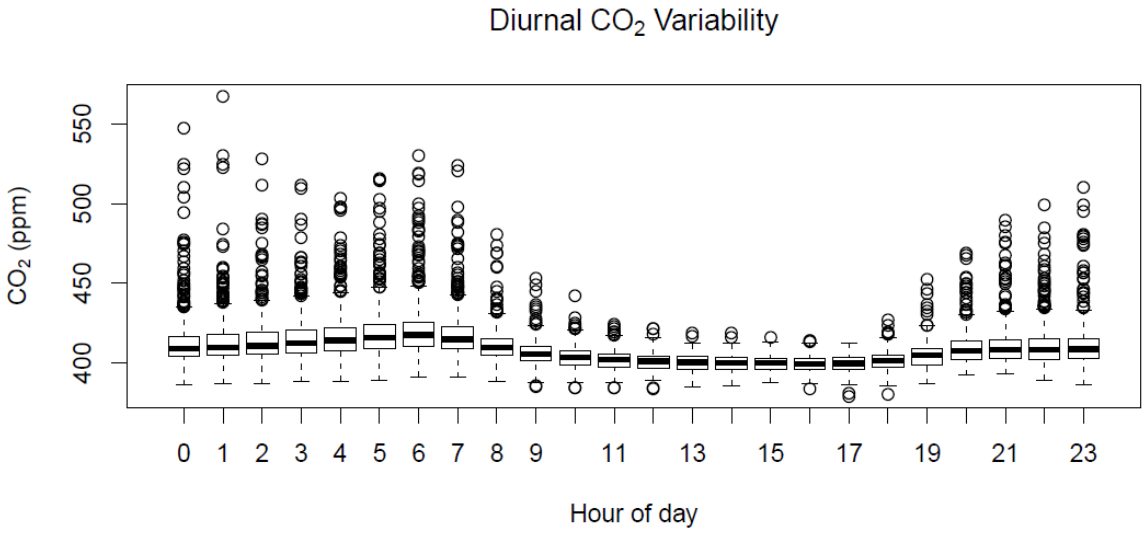

Figure 25: The diurnal cycle of CO_2 at Shape Ranch.

respiration is presented in Fig. 26. Nighttime CO_2 mixing ratios between 00:00 to 06:00 LST are plotted against the amount of time since the previous pulse of rainfall that exceeded 5 mm (0.12 in., Hao et al., 2010). All CO_2 exceeding 500 ppm occurred within two weeks after a rainfall event, with the peak CO_2 level of 567 ppm occurring less than four days after the event. One notable peak in overnight CO_2 occurred approximately four weeks after a rainfall event, with mixing ratios approaching 500 ppm. However, no other peaks exceeded 450 ppm more than four weeks after rainfall. This suggests that the most elevated CO_2 mixing ratios measured at Shape Ranch were associated with nighttime emissions due to enhanced ecosystem respiration as a result of increased soil moisture from recent rainfall.

3.3.1.3. CARBON MONOXIDE

Carbon monoxide at Shape Ranch was low, with a median mixing ratio of 97 ppb. This concentration is lower than past urban observations (Baker et al., 2008) and at remote continental locations (Chin et al., 1994) (Fig. 27). Low CO mixing ratios compared to other remote areas is sensible considering the observed decreasing trend in CO in recent decades (Worden et al., 2013), since the measurements in Chin et al. (1994) were made in the late 1980's and early 1990's. The diurnal cycle of CO showed higher medians during the daytime as compared to overnight. However, the highest observations (above 200 ppb) often occurred during the late evening and overnight hours. These observations were possibly associated with combustion plumes in a stable nighttime boundary layer.

3.3.1.4. NITROGEN OXIDES

Like CO, NO_x concentrations were low at Shape Ranch, with median mixing ratios of 0.1 ppb for NO and 1.7 ppb for NO_x. Distant urban emissions are unlikely to increase concentrations at Shape Ranch as NO_x is relatively short-lived. However, the role of local emissions in NO_x abundance is evident in the data. Figure 29 shows the diurnal cycle of NO, total NO_x, and the ratio of NO/NO_x. During the nighttime, NO remained low as any emissions will react with O_3 to produce NO_2 (Sect. 1.2.2.4). Increased NO mixing ratios during the early morning hours may represent emissions from local traffic. While background NO remained low through the evening, several

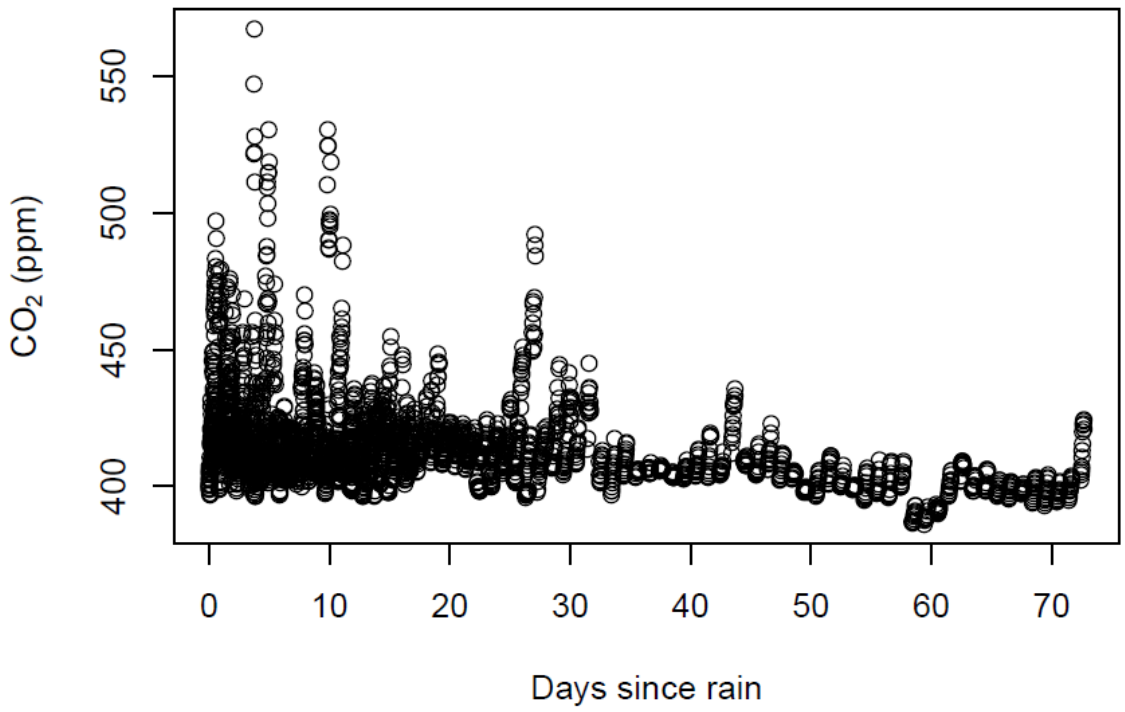

Figure 26: Nighttime (00:00 to 06:00 LST) CO_2 concentrations were plotted based on the elapsed time since a precipitation pulse of at least 3 mm (0.12 in, Hao et al., 2010). Several extended periods without precipitation occurred.

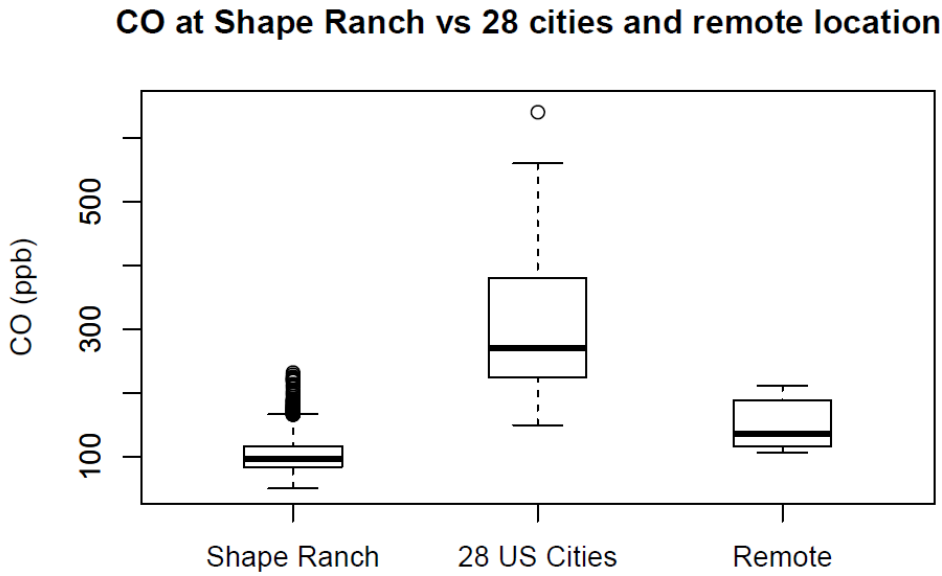

Figure 27: Shape Ranch CO concentrations compared to 28 US cities (Baker et al., 2008) and remote locations (Chin et al., 1994).

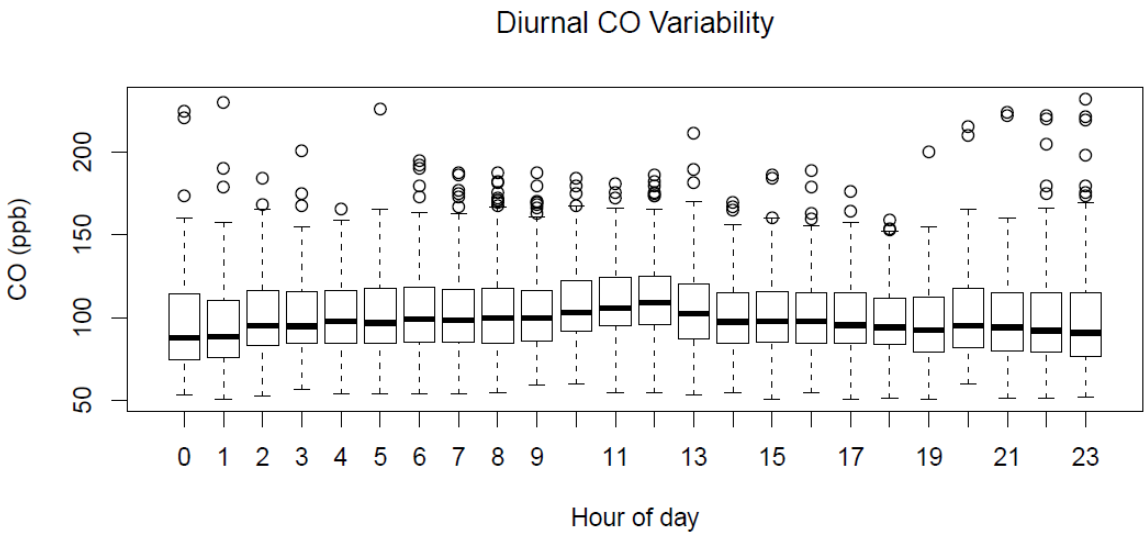

Figure 28: Diurnal variability of CO at Shape Ranch.

outliers above 4 ppb suggest NO plumes may be detected from nearby combustion sources. Total NO_x was elevated during the nighttime, likely due to local emissions into a shallow nocturnal boundary layer. Again, elevated NO_x abundance in the morning may indicate local traffic emissions. During the afternoon, NO_x remained relatively low, likely due to mixing in a deep, convective boundary layer. Later, NO_x mixing ratios tended to increase into the evening and overnight hours. The ratio of NO/NO_x demonstrates the role of photolysis, with elevated NO relative to total NO_x during the daytime. This is especially true during the morning hours, when lower O_3 may delay the conversion of NO from local sources to NO_2. Many outliers occurred during the afternoon and evening hours with NO/NO_x exceeding 0.8, meaning that NO mixing ratios were at least four times larger than NO_2. These data points may represent fresh plumes from nearby sources.

In addition to nearby combustion sources, NO is emitted from microbial activity in soils (Williams et al., 1992). These emissions are dependent on soil moisture content, with adequate moisture needed to support microbial activity without suppressing aeration. Given that there were long dry periods in the study, topsoil moisture likely varied greatly. Figure 30 shows nighttime (00:00 to 06:00 LST) NO and NO_x mixing ratios as a function of the elapsed time since the previous rainfall observation (3 mm, 0.12 in.). While elevated NO_x can occur after extended dry periods, several high-NO_x observations were made shortly after rainfall events. Furthermore, while the highest NO observations were made shortly after rainfall, a number of NO observations above 1 ppb were made weeks after rainfall. This suggests that some high-NO_x events were

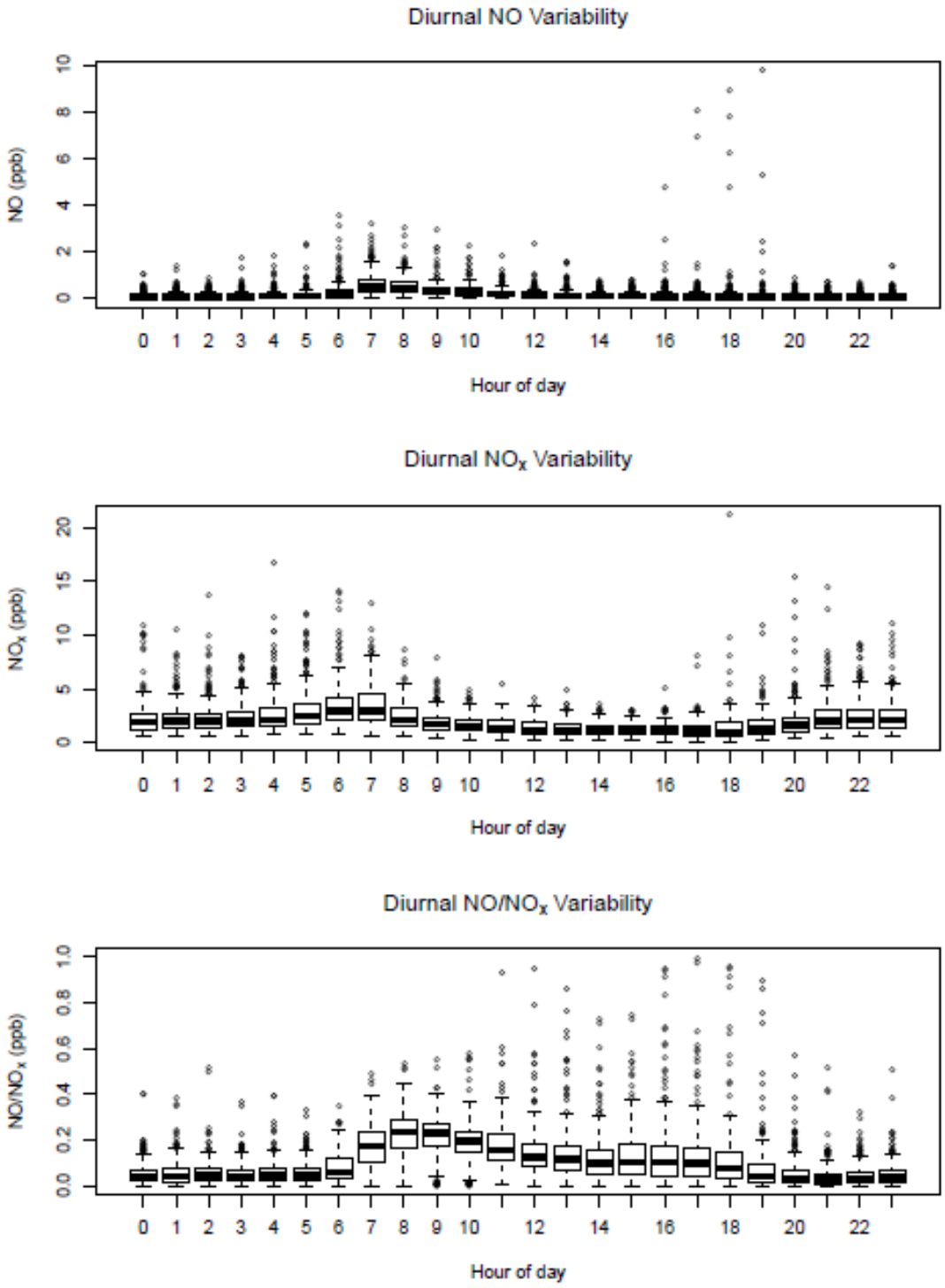

Figure 29: Diurnal variability of NO, total NO_x, and NO/NO_x. The third panel shows evidence of NO_2 photolysis with elevated NO/NO_x ratios during the daytime, while NO emissions quickly react with O_3 at night to form NO_2.

associated with higher NO emissions from soil after rainfall events, though there are other sources of NO that are not associated with rainfall.

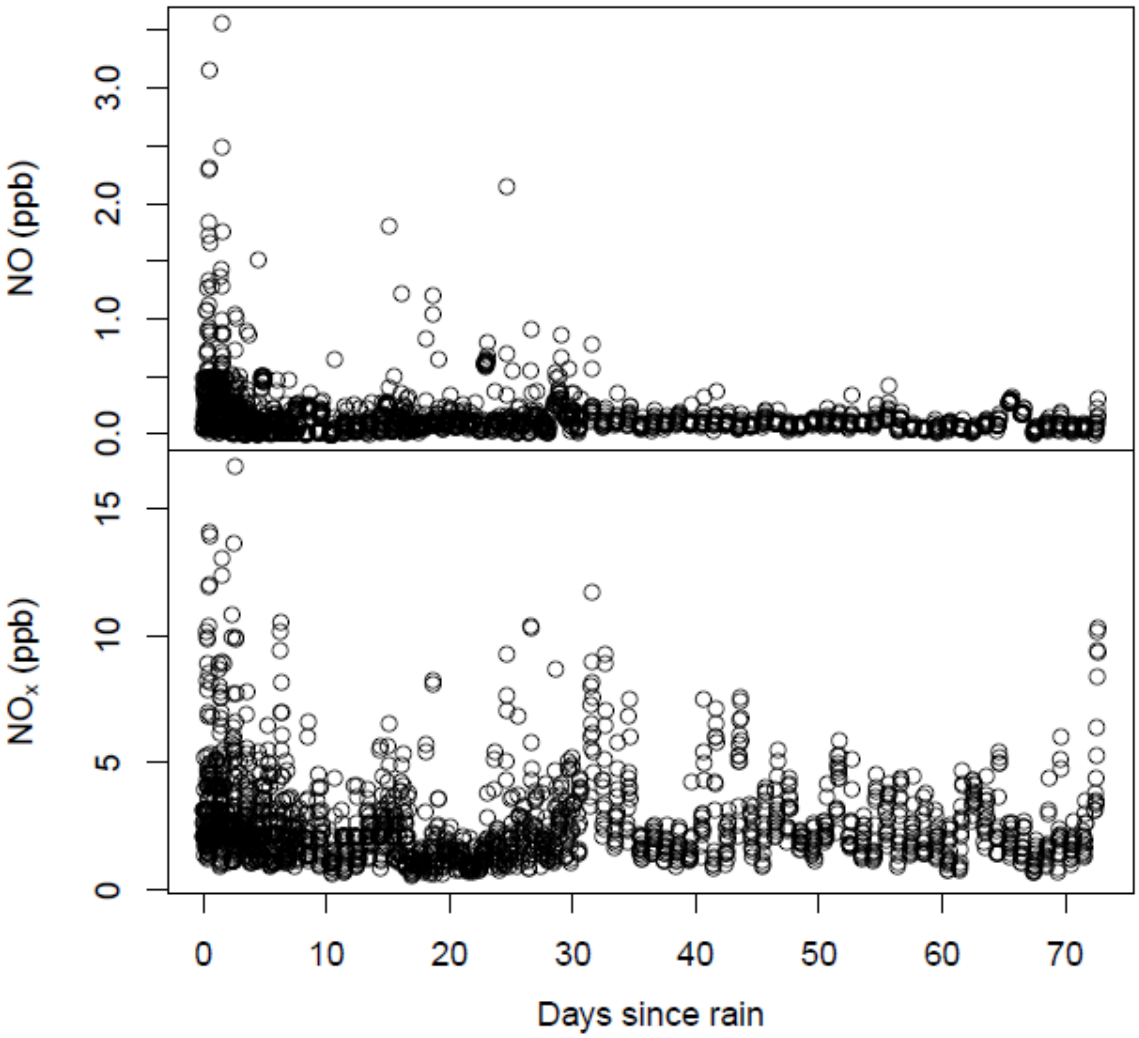

Figure 30: Nighttime (00:00 to 06:00 LST) NO and total NO_x mixing ratios vs. the elapsed time since measured rain (at least 3 mm or 0.12 in).

3.3.1.5. VOLATILE ORGANIC COMPOUNDS

Several sources impact VOC concentrations at Shape Ranch – notably evaporative emissions of hydrocarbons and emissions from combustion sources. Figure 31 shows the log-normal distributions of several hydrocarbons compared to the median observations in 28 US cities (Baker et al., 2008). The median mixing ratios for propane, butanes, pentanes, n-hexane, n-heptane, and n-octane were all higher than the median of the 28 US cities. The ratio of isopentane to n-pentane is shown in Fig. 32. The observed slope of 1.11 was close to that observed for the pentane enhancement over the central Eagle Ford Shale (Fig. 9) and is much lower than in most urban areas. The high alkane levels and the isopentane to pentane ratio suggest that evaporative emissions from oil and gas activity dominate the observed alkane concentrations. Concentrations of alkenes and BTEX species at Shape Ranch were generally lower than in the 28 cities (Fig. 31), which suggests that internal combustion sources contribute to higher concentrations of these species in urban areas. Note that the benzene to toluene ratio in the 28 cities is 0.16 (Fig. 33, $R^2 = 0.52$, $p < 0.001$) which is indicative of fresh automotive emissions combined with evaporative emissions of toluene (Baker et al., 2008). The ratio of 1.09 ($R^2 = 0.87$, $p < 0.001$) at Shape Ranch serves as evidence of a higher benzene to toluene ratio from local emissions sources. This is confirmed by the retention of this ratio during high VOC episodes, which result from an accumulation of local emissions in the boundary layer (Fig. 34). However, there are observations of benzene, toluene, and o-xylene at Shape Ranch that are higher than all of the median observations in the 28 cities.

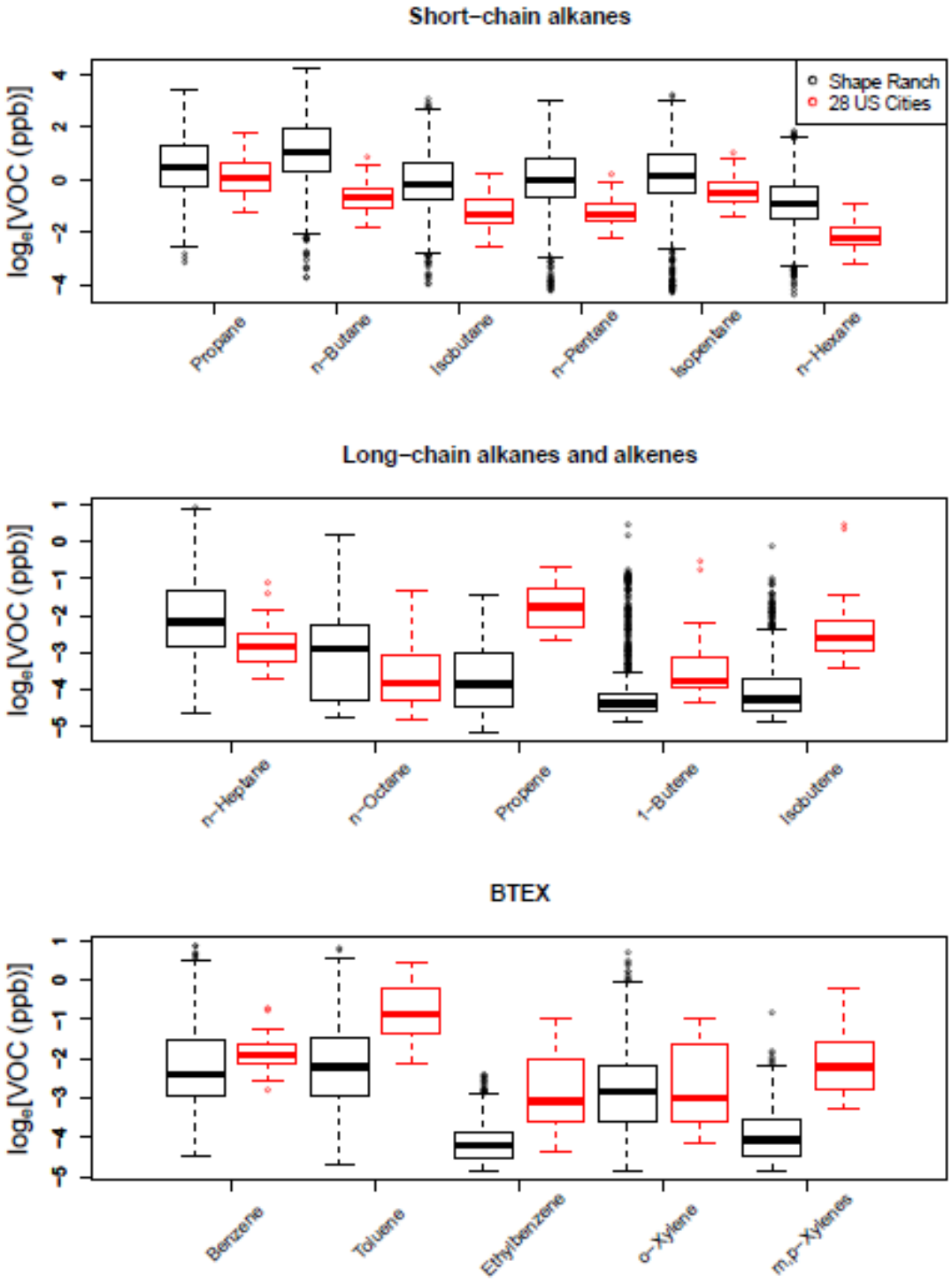

Figure 31: A comparison of VOC concentrations at Shape Ranch vs 28 US cities (Baker et al., 2008). Note that the axis is each panel is log-normal. Alkanes are higher at Shape Ranch than in the 28 cities while alkenes and BTEX are lower.

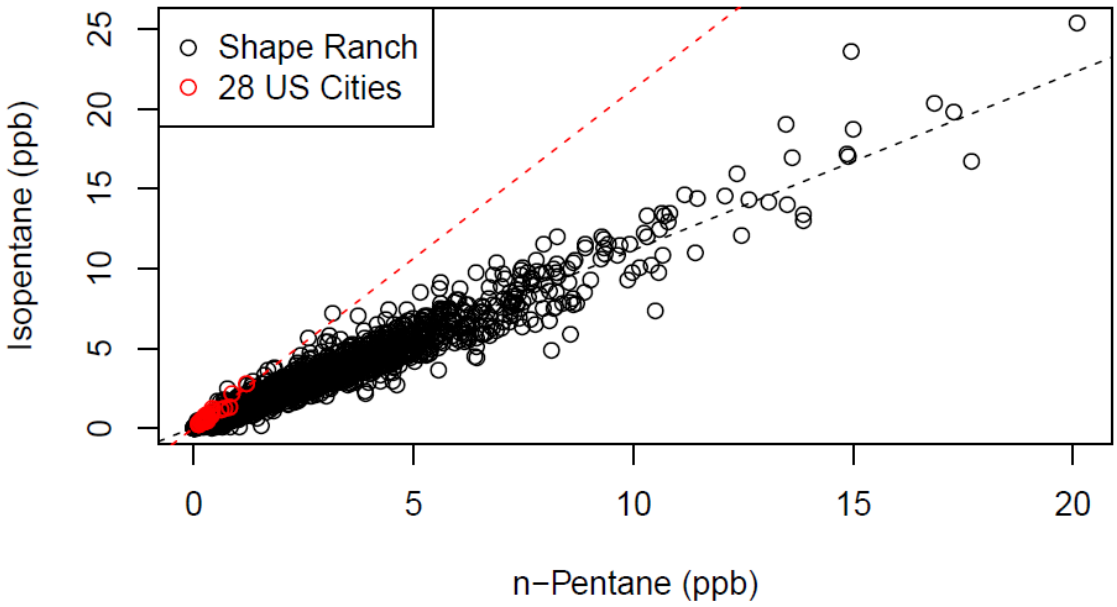

Figure 32: Isopentane vs pentane at Shape Ranch and 28 US cities (Baker et al., 2008). The ratio at Shape Ranch was 1.11 (R^2 = 0.95, p < 0.001) while the ratio in the 28 cities was 2.12 (R^2 = 0.92, p < 0.001).

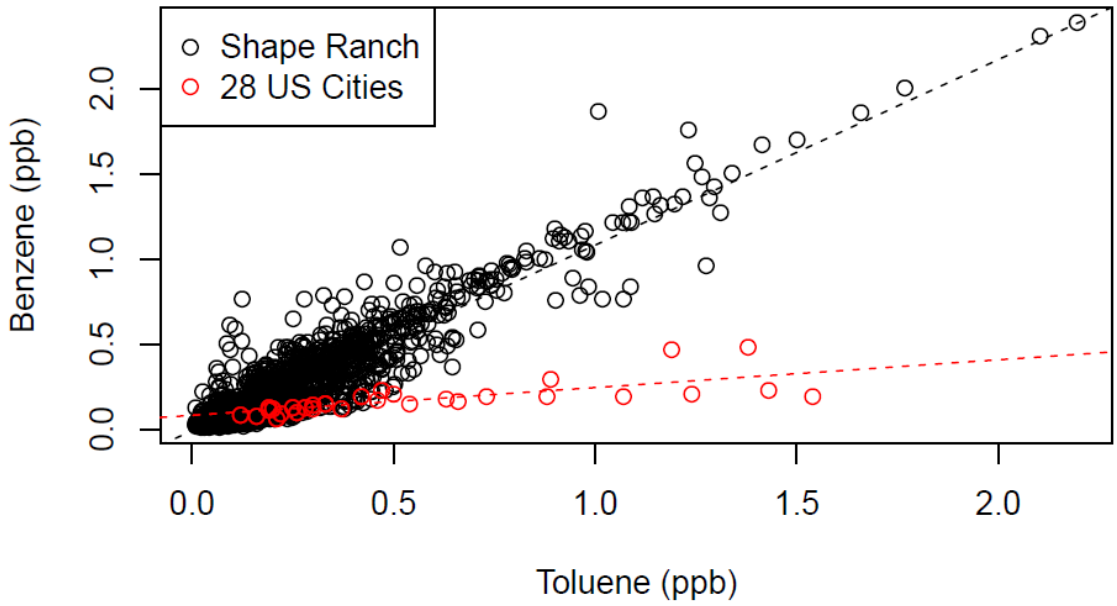

Figure 33: Benzene vs toluene at Shape Ranch and 28 US cities (Baker et al., 2008). The ratio at Shape Ranch was 1.09 (R^2 = 0.87, p < 0.001) while the ratio in the 28 cities was 0.16 (R^2 = 0.52, p < 0.001).

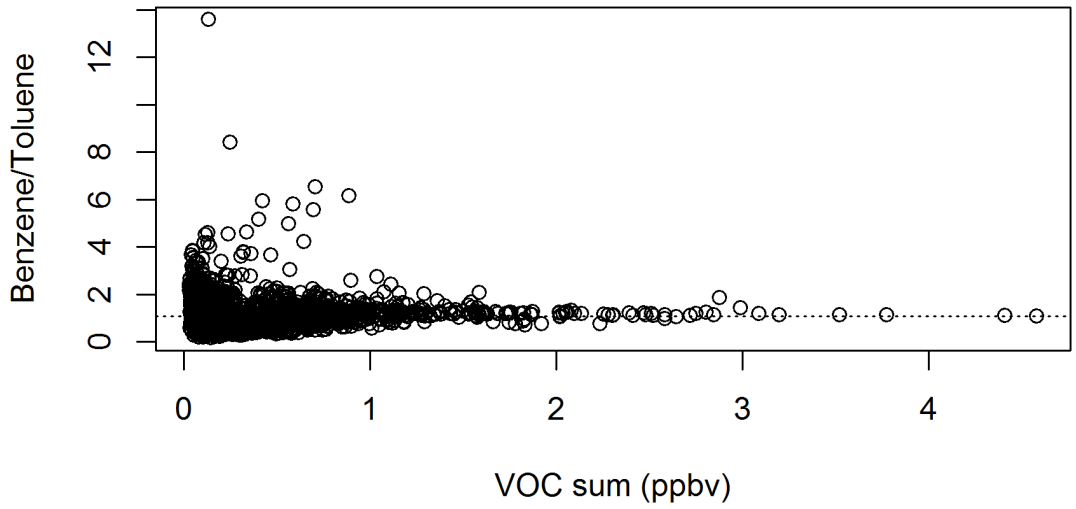

Figure 34: The benzene/toluene ratio at Shape Ranch as a function of the summed benzene and toluene mixing ratios (ppbV). The slope of the benzene vs. toluene relationship is shown as a dotted line.

Figure 35 shows that the alkanes and BTEX species were elevated at night, so high mixing ratios were likely associated with accumulation of local and regional emissions in a shallower nocturnal boundary layer. Propene and isoprene were both elevated during the day, however. While isoprene is known to be emitted during the day, the relatively high propene during the day may be indicative of local emissions during the day time (Goldstein et al., 1996).

Figure 36 shows correlations of selected VOCs with other trace gases. Propane, n-pentane, and benzene were all positively correlated with CO, CO_2, and NO_x. These positive correlations were likely associated with the boundary layer dynamics that contribute to elevated concentrations during the nighttime. The exception is CO, which did not share the diurnal cycle with alkanes, BTEX, CO_2, and NO_x. Propene had no meaningful correlation with CO or O_3. Propene and isoprene were elevated during the

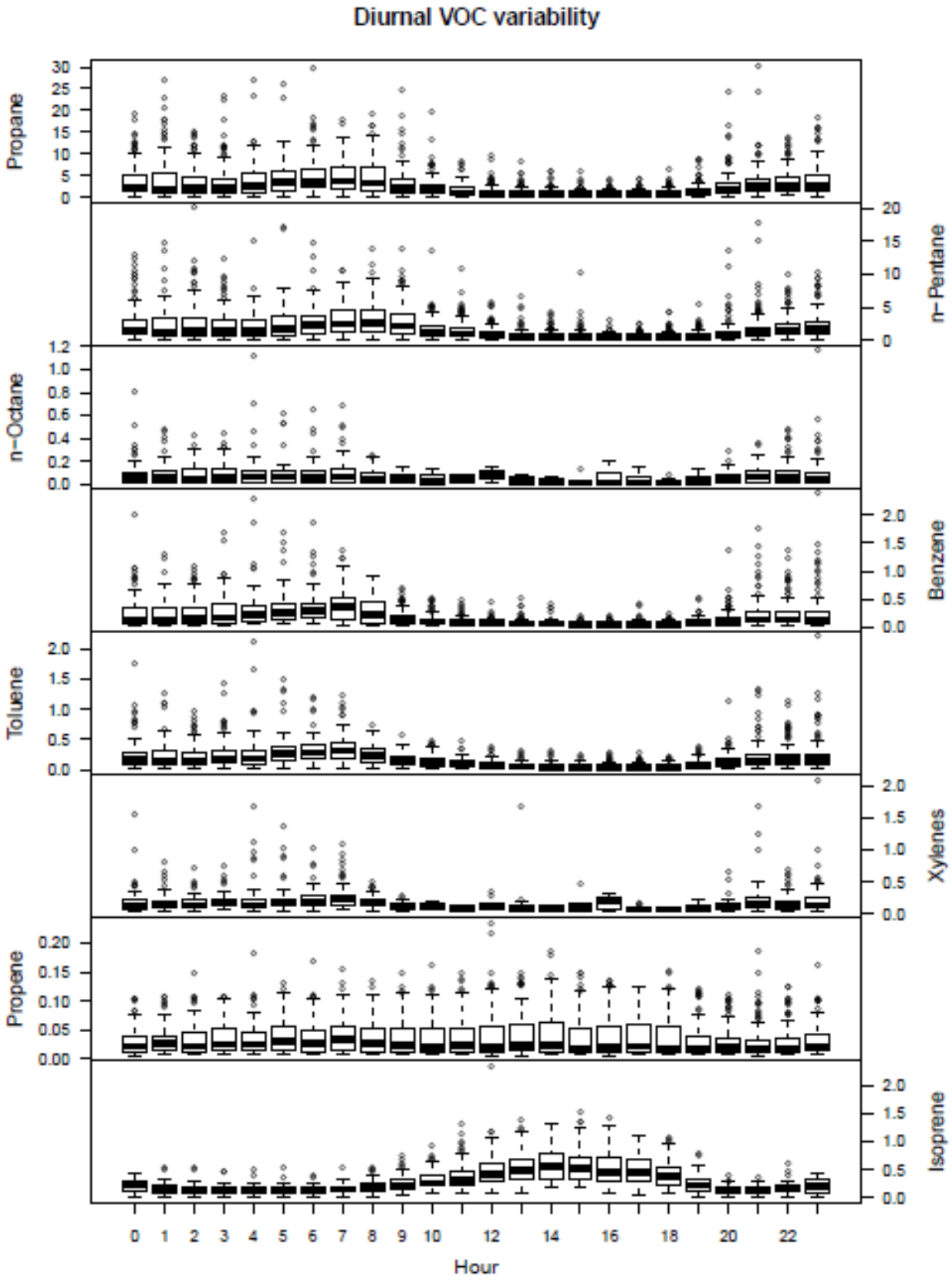

Figure 35: Diurnal variability of selected VOCs. All units are in ppb.

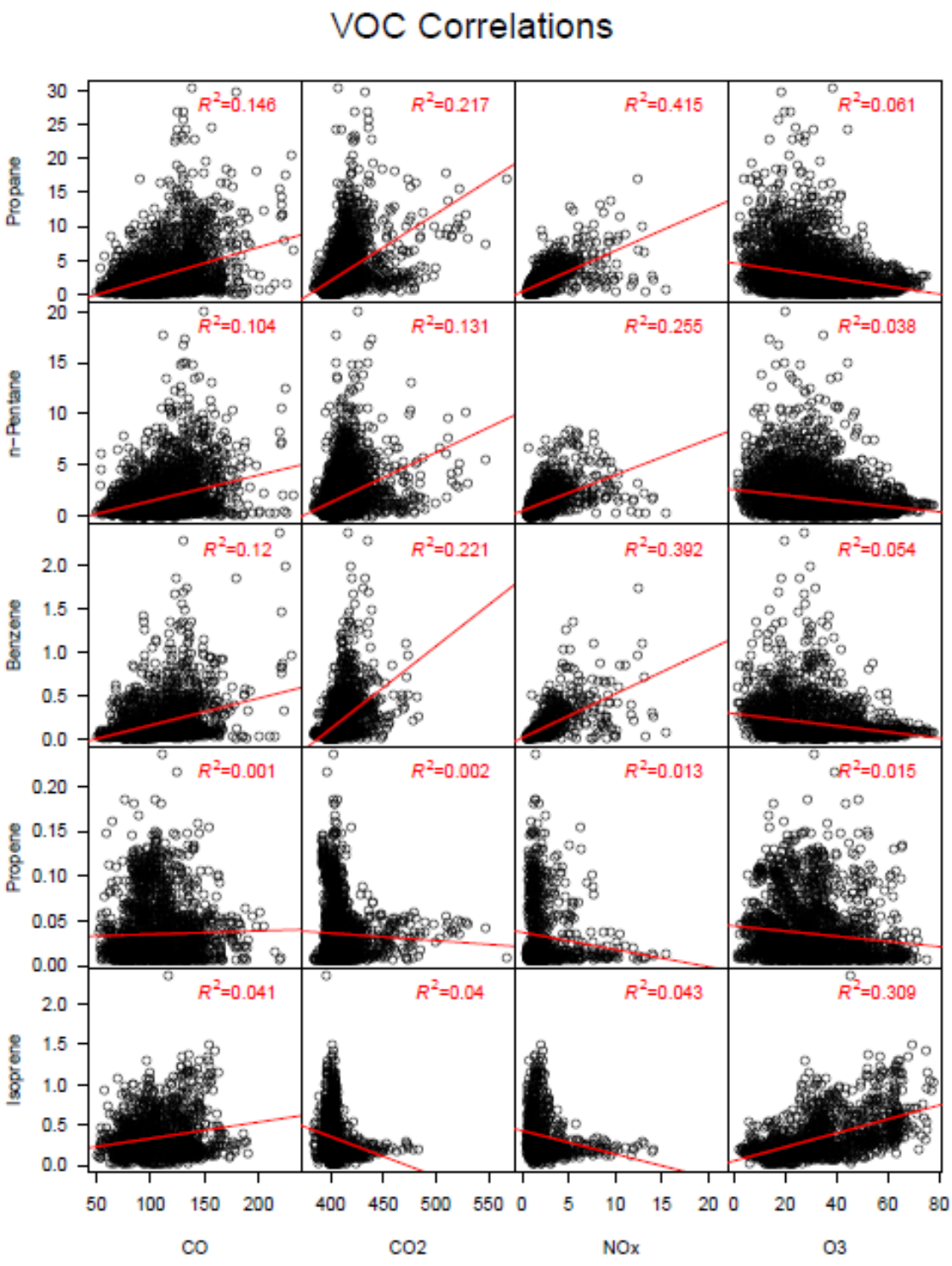

Figure 36: Correlations of selected VOCs with other trace gases. All correlations are statistically significant with $p < 0.001$, except for propene and CO_2 ($p = 0.04$) and propene and CO ($p = 0.17$). All units are in ppb.

day when CO_2 and NO_x were low, and low during the night when CO_2 and NO_x were high. This appears in Fig. 36 as two clusters in the correlation plots for these compounds. Isoprene shared a positive correlation with O_3 as isoprene emissions and photochemical O_3 production occur during the daytime.

The labeling of chromatogram peaks as pinenes was based on knowledge of expected compounds and retention times (Lamanna & Goldstein, 1999). However, several aromatic compounds and long-chain, saturated alkanes have similar retention times, and the flame-ionization detectors are unable to distinguish between compounds with similar retention times – especially if the peaks are shifting due to temperature changes. Figure 37 shows correlations between aromatic compounds and the pinenes. Alpha-pinene was most strongly correlated with xylenes ($R^2 = 0.13$, $p < 0.001$) and trimethylbenzene ($R^2 = 0.15$, $p < 0.001$). However, two distinct clusters are visible in the xylenes vs. alpha-pinene plot – the first with high alpha-pinene and low xylenes, and the second with high alpha-pinene and high xylenes. Such grouping suggests that some "alpha-pinene" observations may be misidentified peaks of a compound associated with aromatic compounds. Beta-pinene was even more strongly correlated with the aromatic compounds as evident in Fig. 37, except for trimethylbenzene. The strongest correlations were observed with xylenes ($R^2 = 0.49$, $p < 0.001$) and butylbenzene ($R^2 = 0.55$, $p < 0.001$). These relationships suggest that "beta-pinene" observations were also misidentified and instead consist wholly or partially of aromatic compounds.

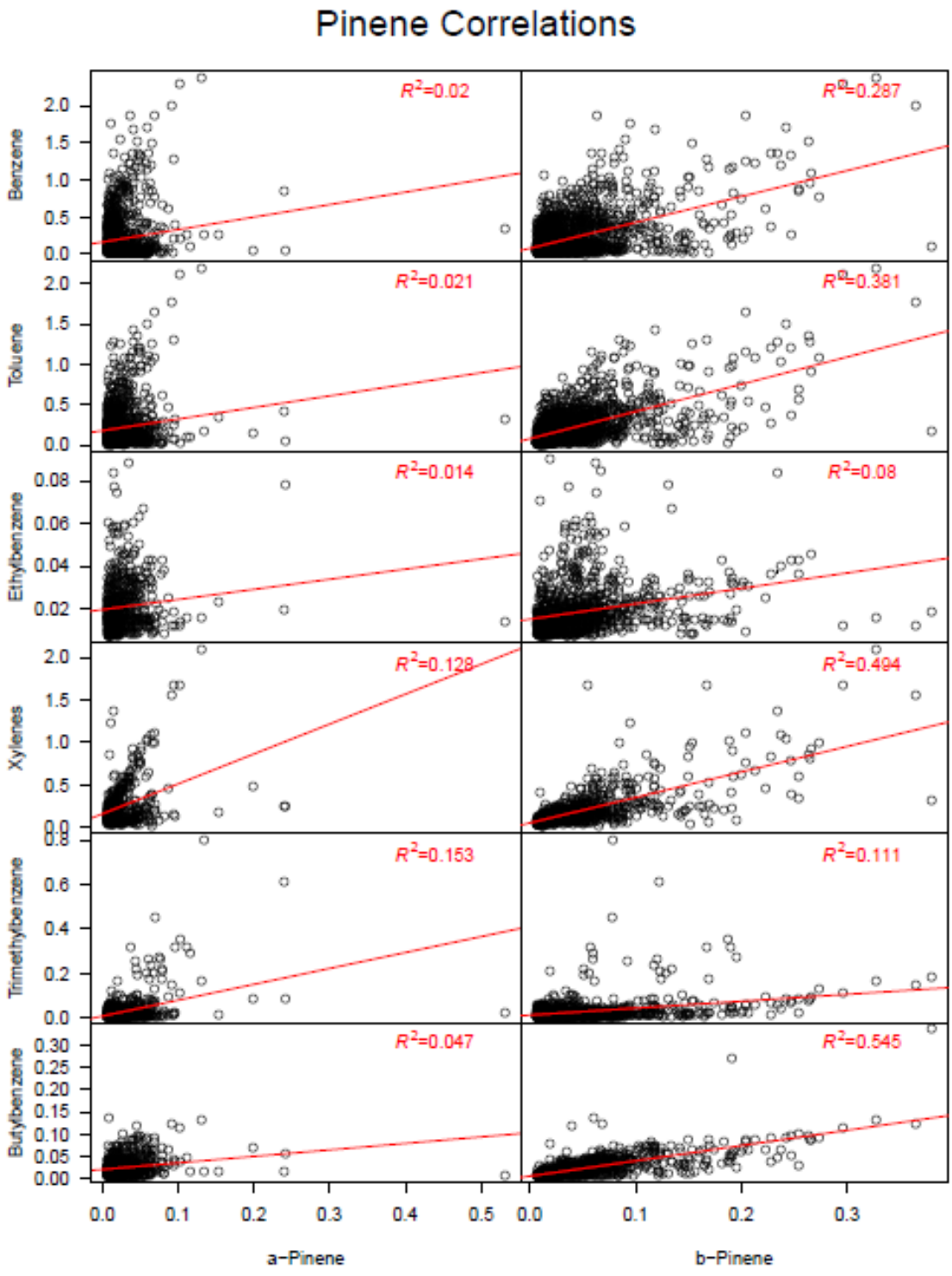

Figure 37: Correlations of BTEX species, trimethylbenzene, and butylbenzene with alpha- and beta-pinene. All correlations are statistically significant with $p < 0.001$, except for ethylbenzene and alpha-pinene ($p = 0.004$). All units are in ppb.

3.3.1.6. OZONE

During the entire field campaign, the maximum daily 8-hour average O_3 concentration exceeded the current EPA standard (U.S. Environmental Protection Agency, 2015d) on only one day (1 August 2015, Fig. 38). The fourth-highest maximum daily 8 h O_3 concentration – the three-year average of which is used to compare against the EPA's standard – was 65 ppb, 5 ppb below the standard. It is unclear if other days outside of the measurement period would have exceeded this value. The diurnal cycle of O_3 concentrations and $\partial O_3/\partial t$ in ppb (30 min)$^{-1}$ is shown in Fig. 39. The concentrations followed a typical pattern with high concentrations during the daytime, followed by decreasing concentrations through the nighttime and reaching a minimum in the early morning hours. The rate of change of ozone mixing ratios, estimated as 30 min ozone mixing ratio changes, reflected this diurnal cycle, though there was a large spread in the rates. During the morning hours, the rapid increase in O_3 was associated with mixing of the shallow nocturnal boundary layer with higher O_3 mixing ratios in the elevated residual boundary layer after sunrise (Rappenglück et al., 2008), with photochemical ozone production contributing to a slower increase in O_3 during the daytime. Outliers for every hour of the day include both positive (O_3 production or transport of high-O_3 air) and negative rates (O_3 destruction or transport of low-O_3 air). The ozone concentration change rate ranged from -21 to +29 ppb (30 min)$^{-1}$.

Ozone production efficiency (OPE) is a measure of the number of O_3 molecules produced from NO_2 photolysis (reaction 1.6) per NO_x molecule consumed (reaction 1.12) (Liu et al., 1987). Without NO_y measurements, the OPE cannot be properly

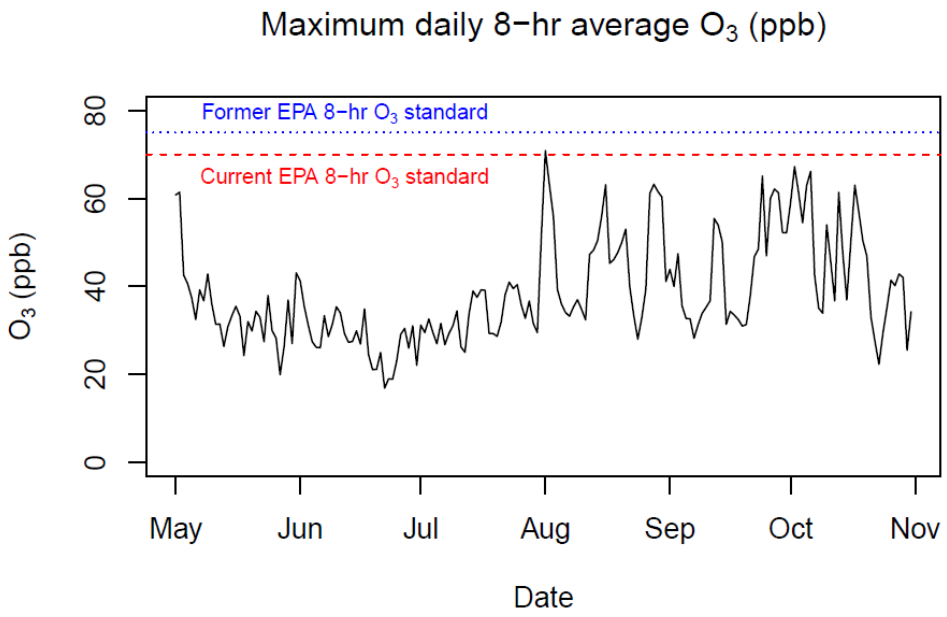

Figure 38: Maximum daily 8 h average O_3 concentrations at Shape Ranch compared to the EPA standard. One day (1 August 2015) exceeded the current EPA standard of 70 ppb with a maximum 8 h average O_3 mixing ratio of 71 ppb. There were no exceedances of the previous standard of 75 ppb.

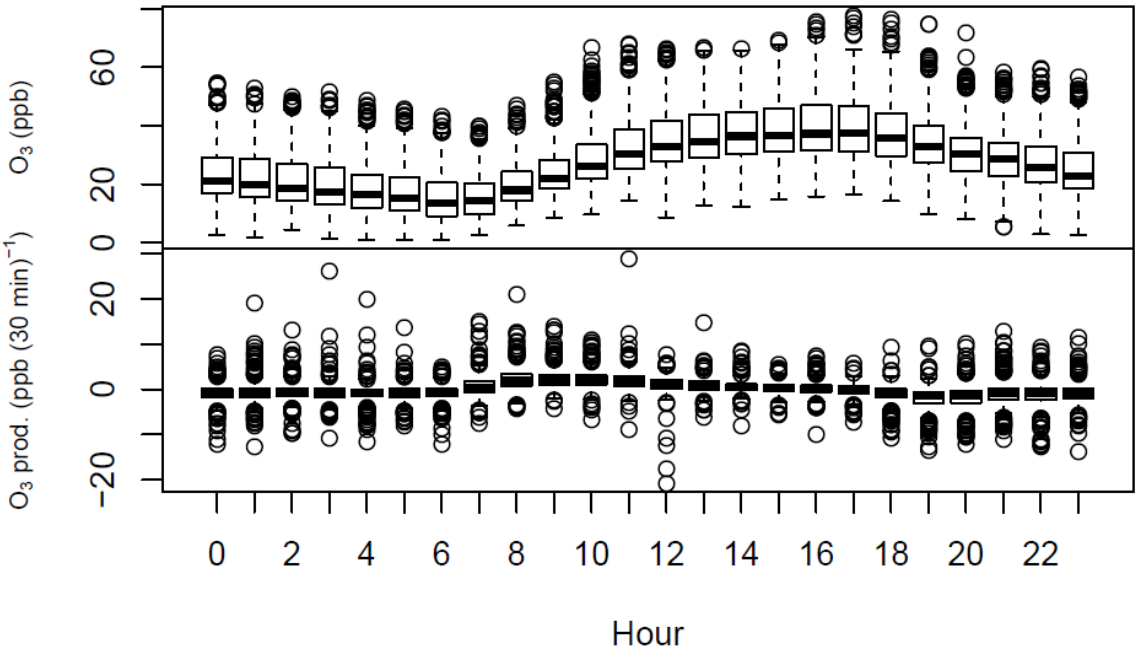

Figure 39: Diurnal variability of O_3 concentrations and $\partial O_3/\partial t$ at Shape Ranch.

assessed at Shape Ranch. However, if ambient NO_x measurements are assumed to be indicative of regional NO_x emissions (and subsequently oxidized NO_x, aka NO_y), the OPE can be investigated using NO_x mixing ratios. Because photochemical ozone production depends on the concentrations of NO_x and VOCs, as well as sunlight, the production rate was compared to mean NO_x mixing ratios between 12:00 to 15:00 LST, when the daytime boundary layer is well developed and there is sufficient sunshine for photochemistry. Figure 40 shows the dependence of the ozone production rate on NO_x mixing ratios, measured as the change in O_3 from 12:00 to 15:00 LST to the mean NO_x mixing ratio during the same time period. This three-hour period was chosen because the boundary layer is usually well-developed by 12:00 LST and ozone formation continued into the afternoon hours. Only days with sufficient sunlight (> 600 W m^{-2} average from 12:00 to 15:00 LST) and increasing O_3 mixing ratios were used. The change in O_3 concentrations had a weak, positively correlation with NO_x ($R^2 = 0.04$, $p < 0.05$). Despite the weak correlation, the generally low NO_x concentrations during the afternoon hours suggest that photochemical O_3 production may be strongly NO_x-limited at Shape Ranch.

3.3.1.7. AMBIENT AIR QUALITY SUMMARY

The air quality at Shape Ranch was often clean relative to urban air masses, especially during the day. However, alkanes are elevated in this area, and the isopentane to pentane ratio indicates natural gas emissions as the dominant source. Other species, including aromatic compounds and alkenes, showed typical log-normal distributions,

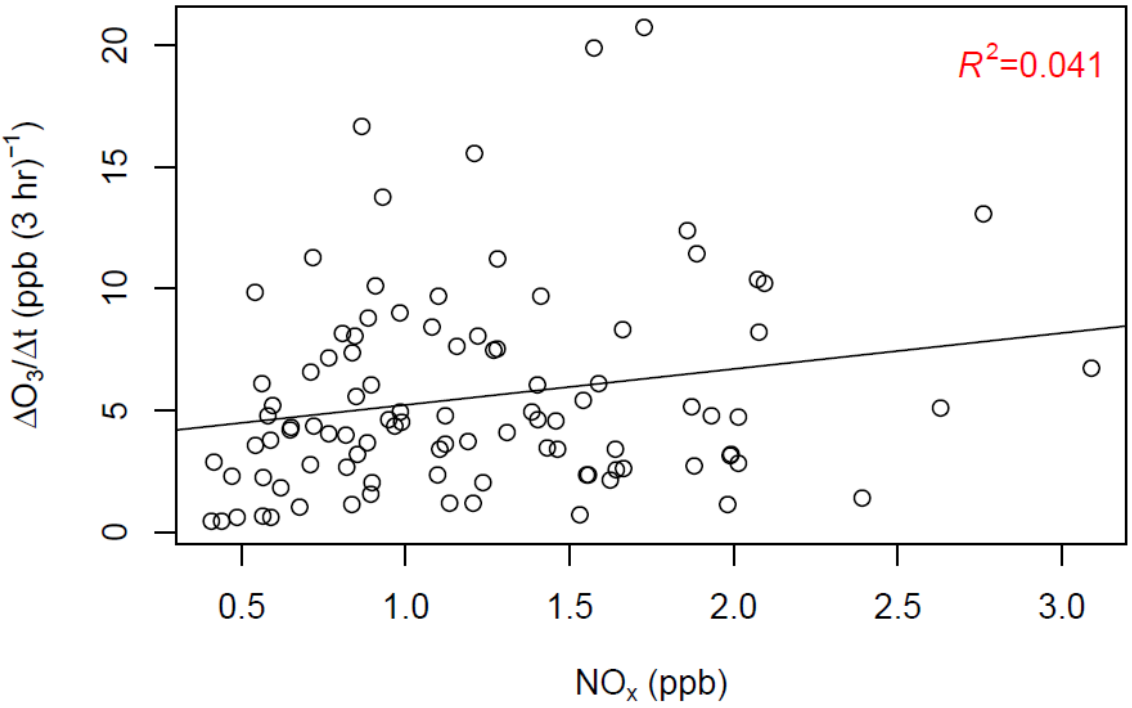

Figure 40: The correlation of $\partial O_3/\partial t$ (ppb (3 h)$^{-1}$) with average 3-h NO_x levels ($R^2 \approx 0.04$, $p < 0.05$).

with low background levels and episodes of very high mixing ratios. These are likely associated with local and regional emission sources, especially during the nighttime when emissions accumulate in a shallow boundary layer. With low background concentrations of reactive VOCs during the day and generally low NO_x, the ozone production rate showed a weak dependence on NO_x. We conclude that without NO_y data, the ozone production efficiency in this region cannot be properly assessed.

3.3.2. EMISSION SOURCES IMPACTING SHAPE RANCH

A source attribution was performed for the Shape Ranch dataset for a period from 13:00 LST 4 September to 9:30 LST 5 October 2015, when most trace gas

instruments functioned without interruption except for calibrations. However, due to an instrument failure, NO_x data are missing after 15 September and have therefore not been included in the NMF source attribution. During this time, temperatures were characteristically warm with only one day of observed precipitation (Fig. 41). Resultant winds averaged over 3-day periods demonstrate air mass transport generally from the SE to ESE. The typical meteorological diurnal cycle is shown in Fig. 42.

Several LS-NMF runs were performed with varying numbers of factors and seeding methods. Fig. 43 shows the performance of two through seven factor runs compared to runs with randomized data for which there should be no distinct factors. Runs with three, four, and five factors performed relatively well compared to two, six, or seven factor runs. The three-factor run was selected over the four- and five-factor runs due to the physical interpretation of the factors and the stability of the three-factor run, as measured by a bootstrap with replacement analysis (Norris et al., 2008). Each factor of the three-factor run was replicated with at least 96% accuracy after resampling the data 1,000 times, while the four- and five-factor runs had factors that were replicated with as little as 11% and 8% accuracy, respectively. However, the five-factor run is presented below to illustrate the appearance of potentially meaningful factors beyond the three-factor run.

The random seed and non-negative SVD seed produced similar factors with a slightly smaller residual error for the random seed (Fig. 44). Therefore, the SVD seed was chosen due to its lower computational cost. Reducing the highest concentrations for each trace gas to the 99^{th} percentile produced results with lower residual errors. These

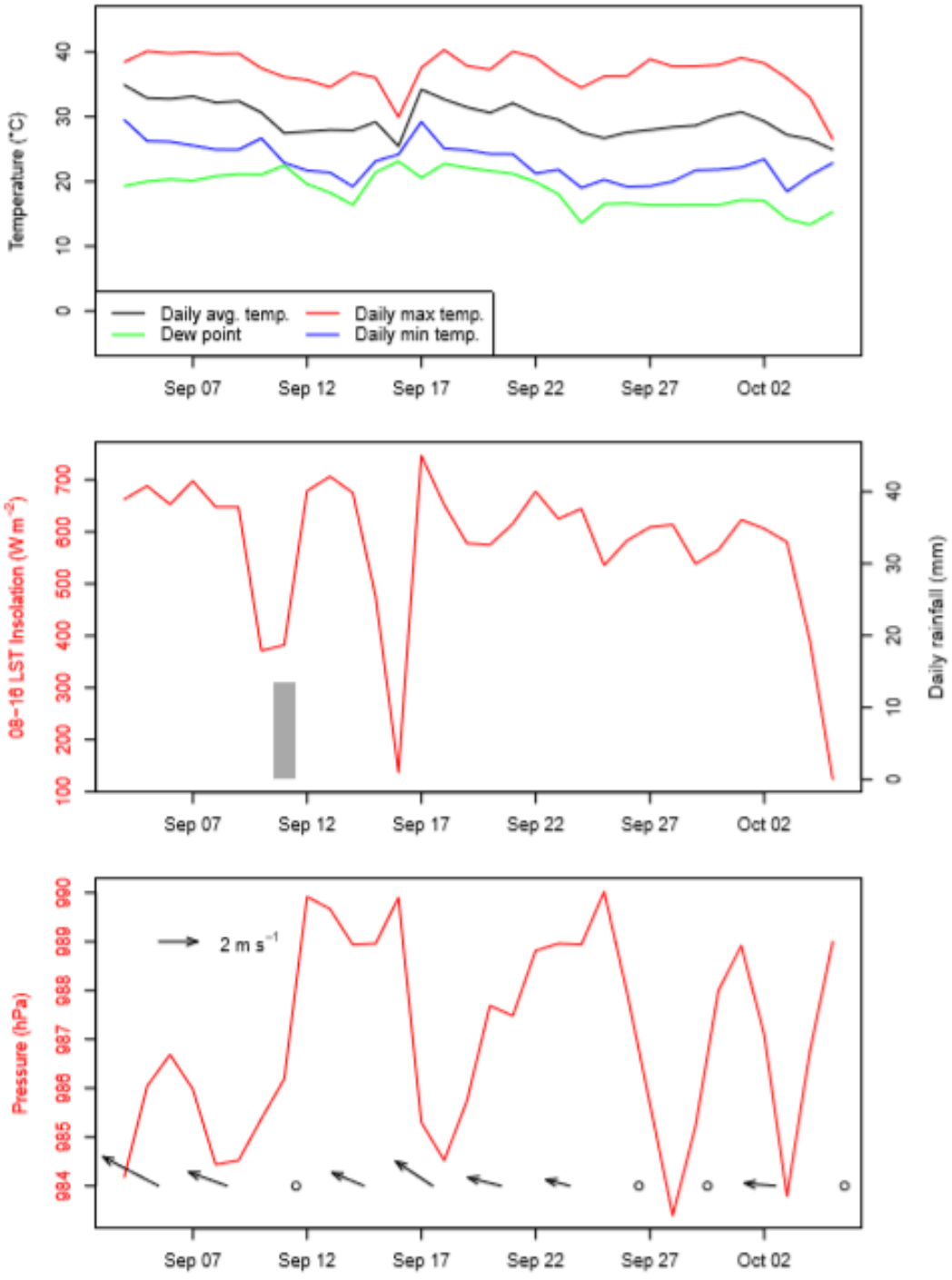

Figure 41: Meteorology for the period encompassing the NMF model. Note that the 3 day averaged resultant winds in the bottom panel represent the general air mass transport. Empty circles with no wind vector are for periods with resultant averaged winds of less than 1 m s^{-1}.

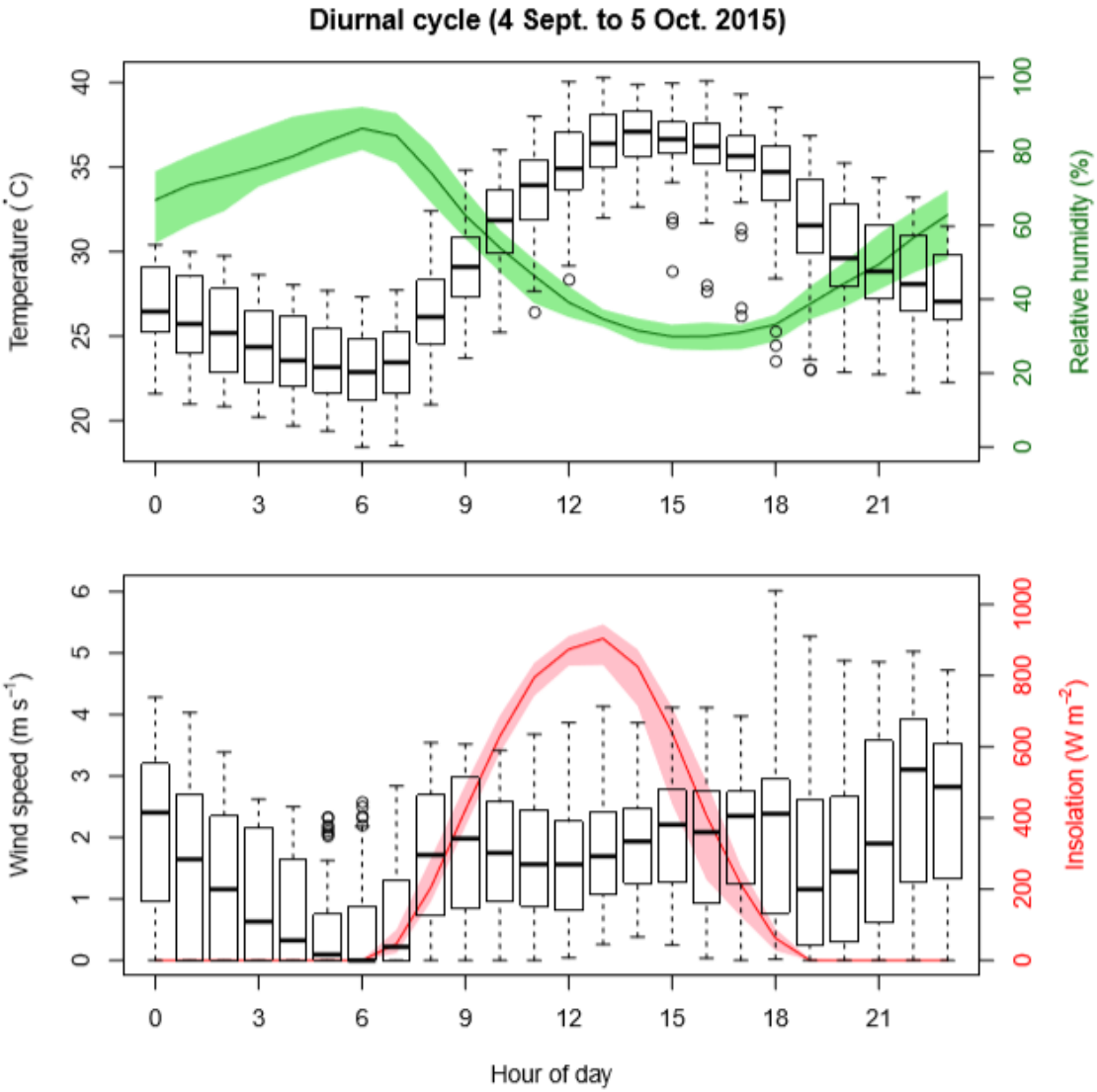

Figure 42: The average diurnal meteorological cycle over the NMF model period. The shaded envelopes represent the interquartile range. Note the relatively large variability in the afternoon insolation due to occasional cloud cover. A bimodal pattern can be seen in the wind speeds with moderate winds during the day time followed by a secondary peak prior to midnight, probably associated with a nocturnal low-level jet (Walters et al., 2008). Wind speeds generally reach a minimum prior to sunrise.

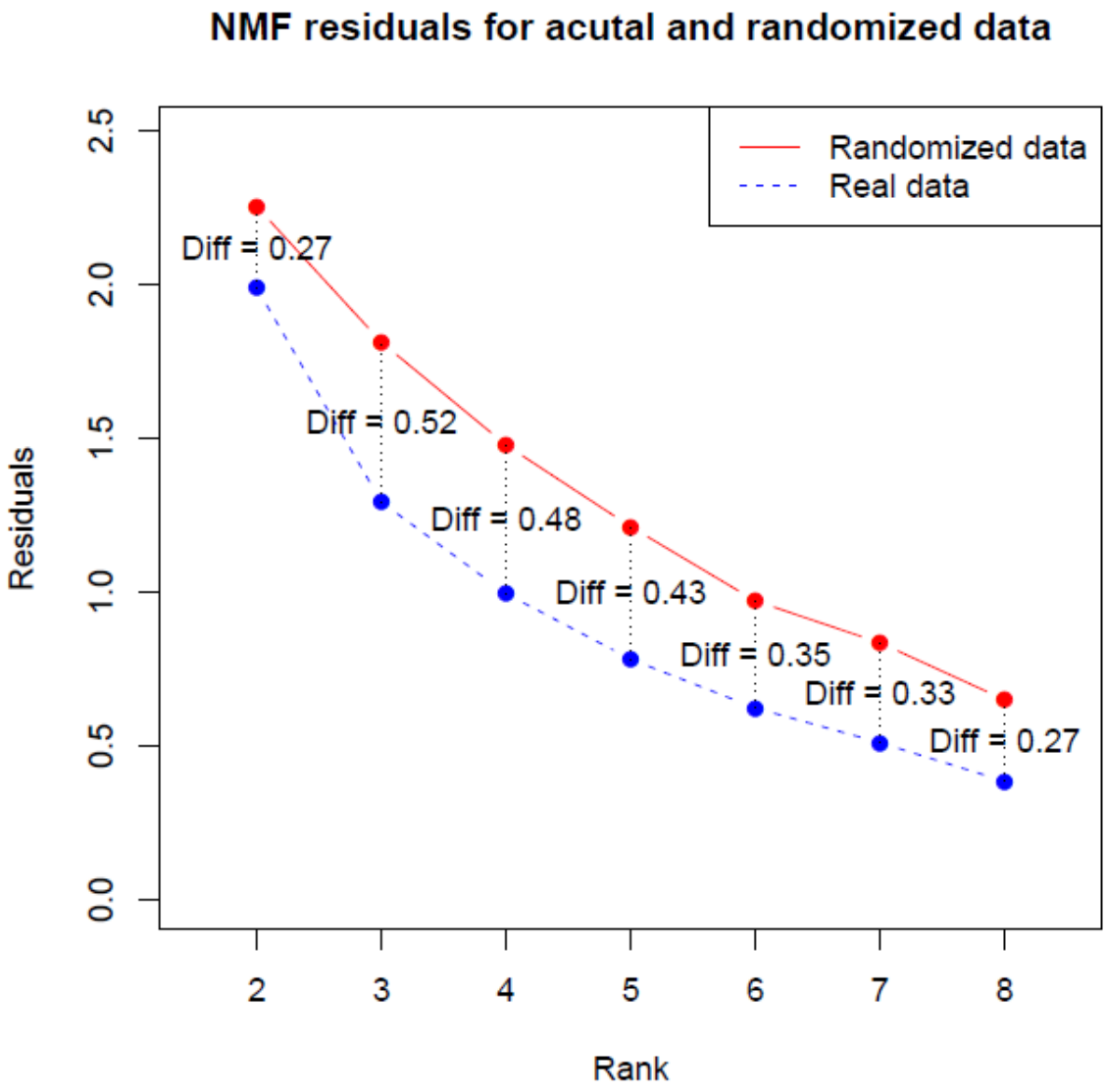

Figure 43: Comparison of residuals from LS-NMF results for two through seven factors for the original dataset (blue dots) and a randomized dataset (red dots). The *randomize* function in the *NMF* package in *R* was used to produce the randomized data. Even with randomized data, the NMF will be able to produce factors that partially explain the dataset, and additional factors will reduce the residual error between the dataset and the factorization. The difference between the residuals for the randomized dataset and the original dataset indicate the performance of the LS-NMF run for each factor relative to the randomized dataset. Three factors produced the largest difference in the residuals, with four- and five-factor solutions also producing large differences in residuals.

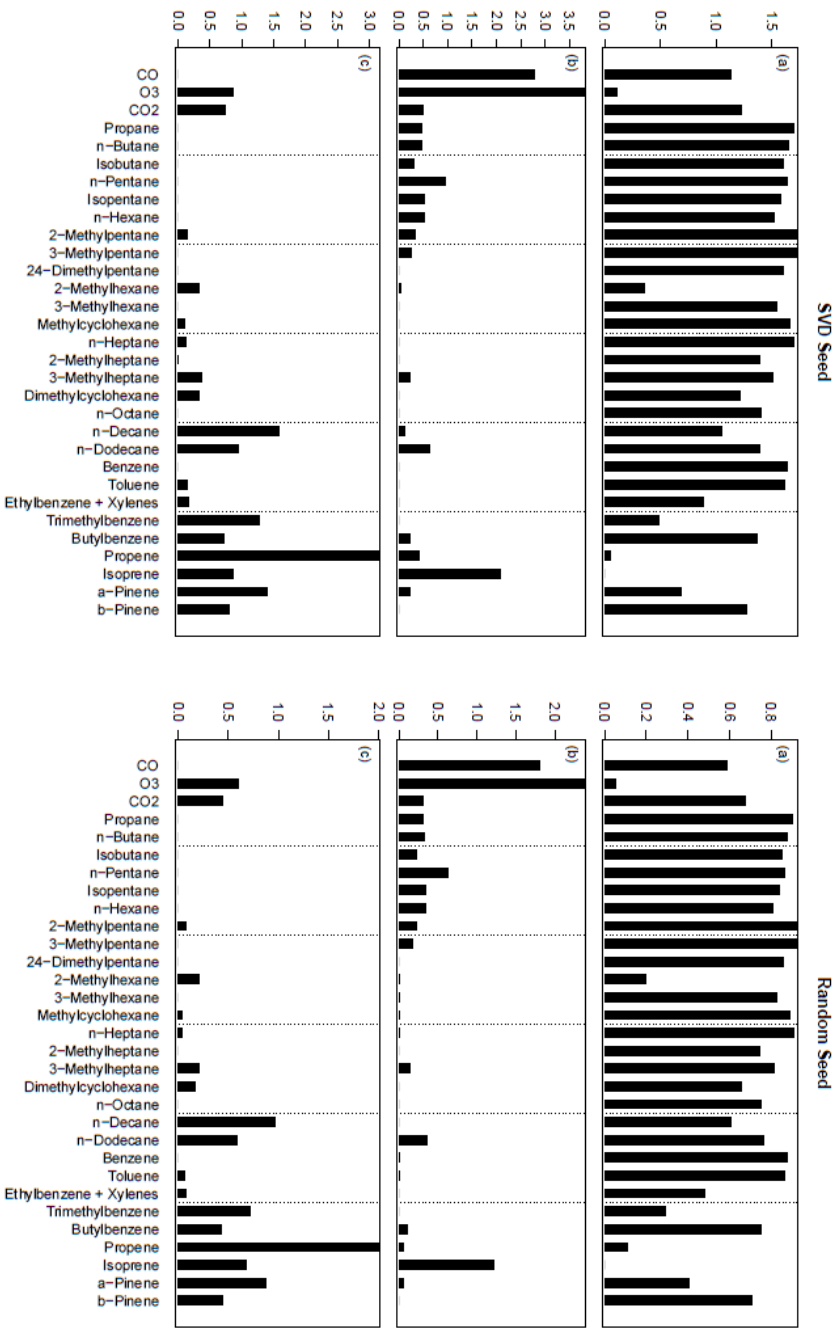

Figure 44: Three-factor LS-NMF runs with non-negative singular value decomposition (SVD) seed and optimized random seed. Nearly identical factors are produced, though there are noteworthy differences. For example, propene is virtually absent from the second factor of the random seed factorization while it is present in the second factor of the SVD seed. The panels labeled (a) are the first factor presented below (oil and gas field), panels labeled (b) are the second factor (transport/diurnal), and panels labeled (c) represents the third factor (compressor exhaust/flaring).

lower residual errors resulted from a reduction in the median normalized abundances by a factor of two compared to when these peaks were retained. I decide to show the results are for a LS-NMF run with the peaks reduced to the 99th percentile, thereby limiting the influence of extreme, short-term changes on the general source attribution. Lastly, a LS-NMF run with only nighttime data is presented to illuminate the influence of photochemistry on the factorization.

Figures 45-47 show the results from the non-negative SVD-seed three-factor LS-NMF. The dominant factor (Fig. 45) features most of the measured trace gases, except for O_3, propene, and isoprene. This factor appears when winds were from the easterly direction, with many outliers indicating episodic periods of high hydrocarbon abundances. This factor followed a diurnal pattern that is largely dictated by boundary layer dynamics, with surface emissions accumulating in a shallow nocturnal boundary layer before being mixed into a deeper layer during the daytime. This factor most closely matched gasoline exhaust, gasoline headspace vapor, and oil field sources, including natural gas wells and condensate tanks, in the EPA SPECIATE database. Hence, this factor was attributed to general oil field emissions. It explained 53% of the variability in the dataset.

The second factor (Fig. 46) was dominated by CO and O_3. The dominant hydrocarbon in this factor was isoprene, though several relatively long-lived alkanes had low scores as well. This factor had the highest scores when winds were from the northeast sector, indicating a continental origin. It features a diurnal cycle that peaked in the afternoon and slowly declined overnight, with a minimum near sunrise. There were

no reasonable matches in the SPECIATE database because the dominant hydrocarbon – isoprene – is generally biogenic while the SPECIATE database consists of anthropogenic sources. Due to the diurnal cycle and continental origin, we attributed this "source" to transport of regional O_3 and isoprene during the daytime, with distant urban sources explaining elevated CO levels due to direct emissions and hydrocarbon oxidation. This factor explained 28% of the data set's variability.

The third factor (Fig. 47) features propene as the dominant factor, with CO_2, O_3, and some long-chain hydrocarbons also present. This factor was highest when winds were from the southeast sector. There was no apparent diurnal cycle in the median scores for this factor, though the upper quartile shows elevated scores during the overnight and morning hours and slightly lower scores during the afternoon hours. This factor matched gasoline exhaust in the EPA SPECIATE database, and we attribute this factor to

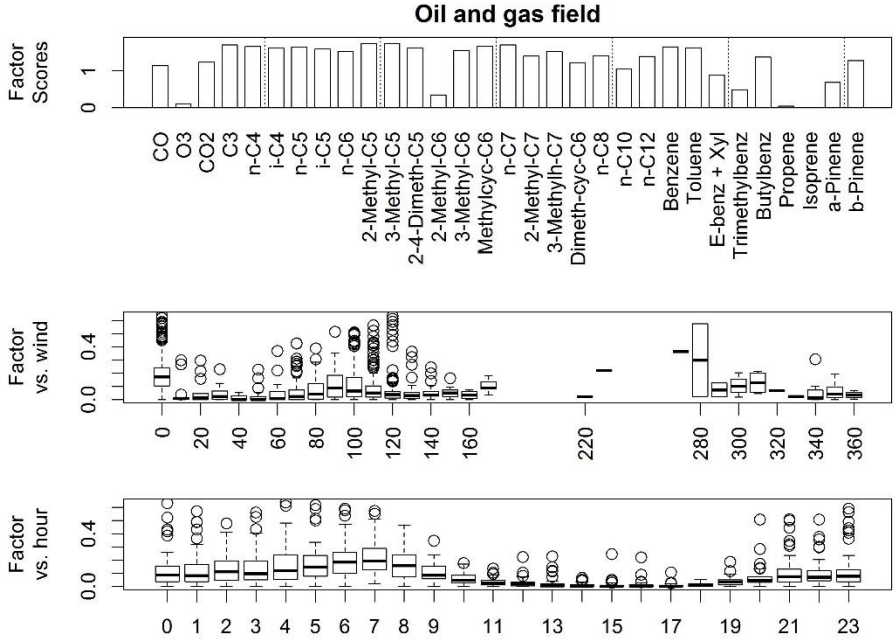

Figure 45: "Oil field" factor from the LS-NMF model.

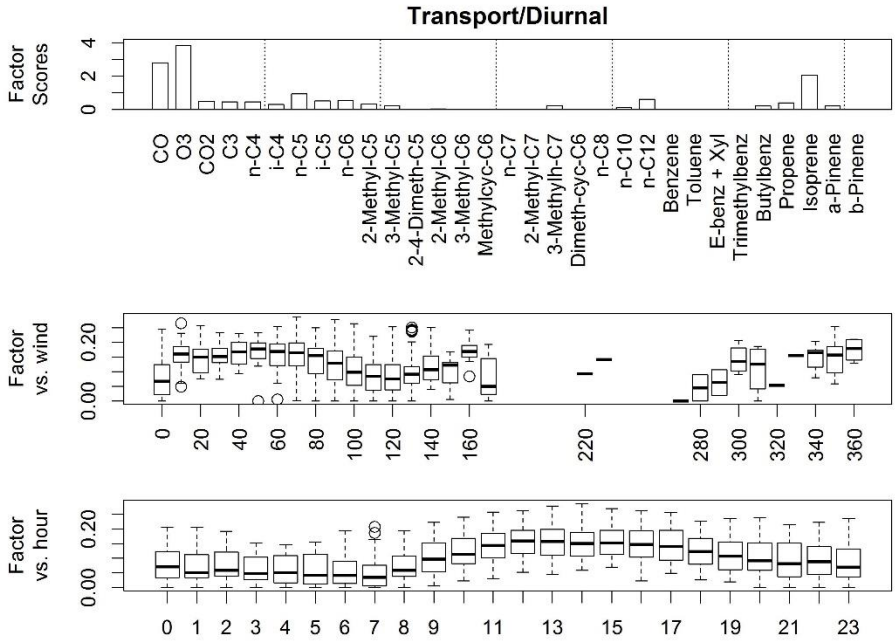

Figure 46: "Transport/diurnal" factor from the LS-NMF model.

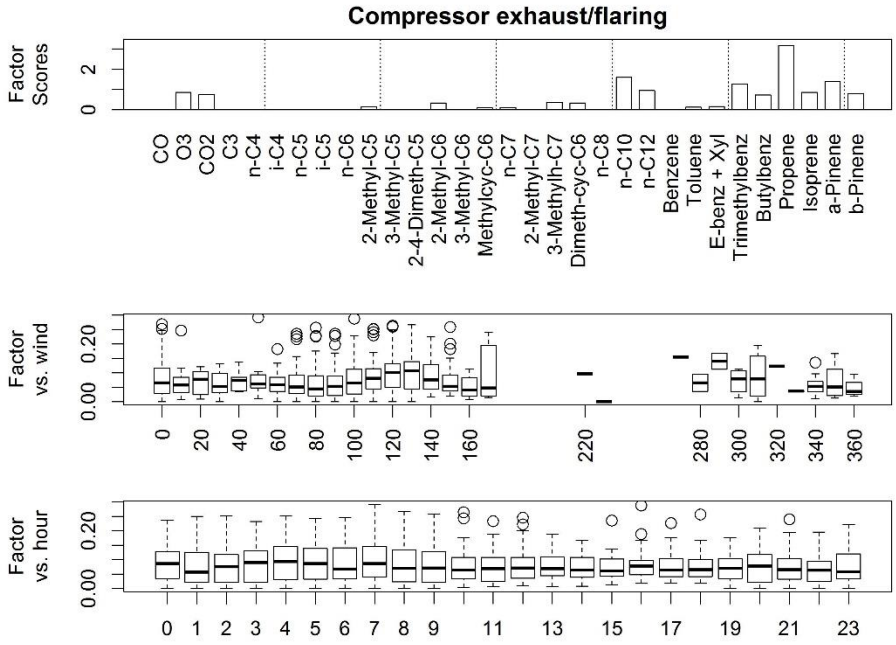

Figure 47: "Combustion" factor from the LS-NMF model.

combustion sources including engine exhaust and flaring. It explained 18% of the data set's variability.

Figures 48-52 show the results from a five-factor LS-NMF run with the SVD seed. The first factor from the three-factor LS-NMF run was apparently split into two new factors – one with mostly lighter alkanes, CO, and CO_2 (Fig. 48), and another with heavier hydrocarbons (Fig. 49). Both factors showed similar temporal and wind direction dependences to the "oil and gas field factor" from the three-factor LS-NMF run described above. While the light and heavy hydrocarbons may be indicative of natural gas liquids and crude oil emission sources, respectively, it is not clear if they represent two distinct emissions sources given the similar timing and wind directions under which these factors appear. Figure 50 shows a factor that is similar to the daytime transport factor from the three-factor run, but this factor lacks light alkanes. Otherwise, the factor still contains CO, O_3, and isoprene during the daytime and under NE winds. The final factor from the three-factor run, which was attributed to combustion (possibly including flaring), was also seemingly split into two new factors – the first featuring propene as the major component, with n-decane and some short alkanes also present (Fig. 51), and another factor with C_3+ aromatic species, n-dodecane, and CO_2 (Fig. 52). Again, the alpha- and beta-pinene scores may represent misidentified hydrocarbons (e.g. branched aromatics). Note that the propene factor maximized during the nighttime and early morning hours and under northeast winds, while the aromats factor was elevated during the daytime and with less of a wind direction dependence. The presence of spurious compounds such as n-decane in the propene factor, and the lack of a clear explanation

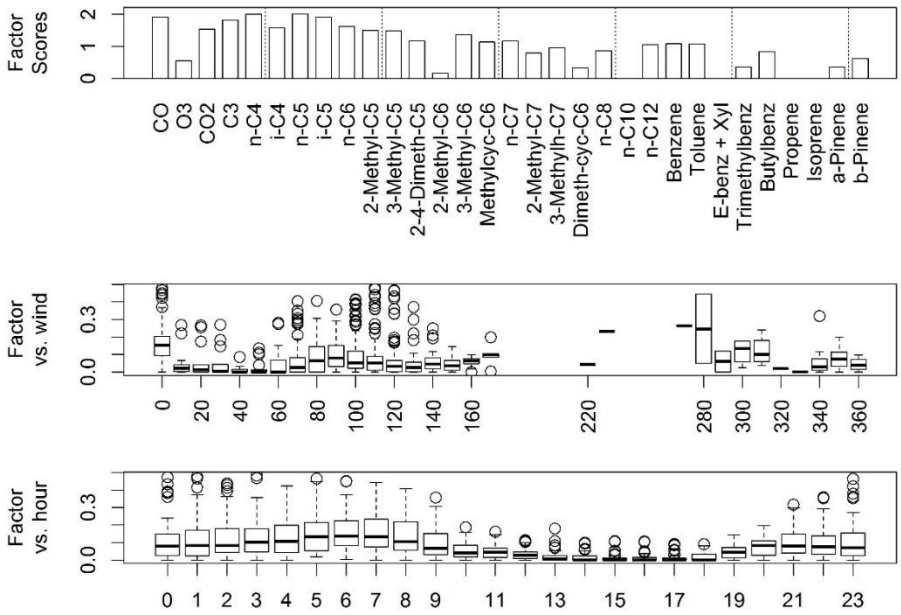

Figure 48: Light-alkane factor from the five-factor LS-NMF run.

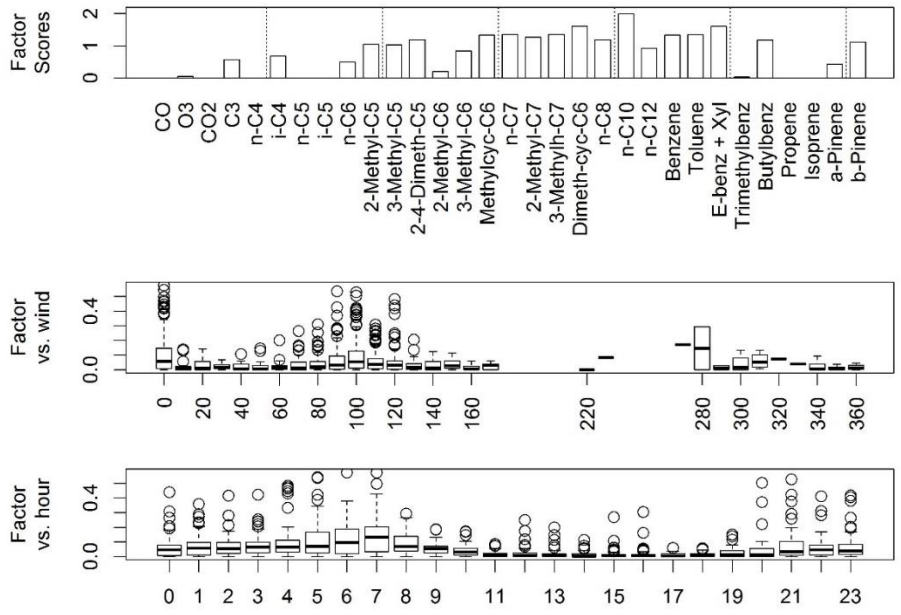

Figure 49: Heavy-alkane factor from the five-factor LS-NMF run.

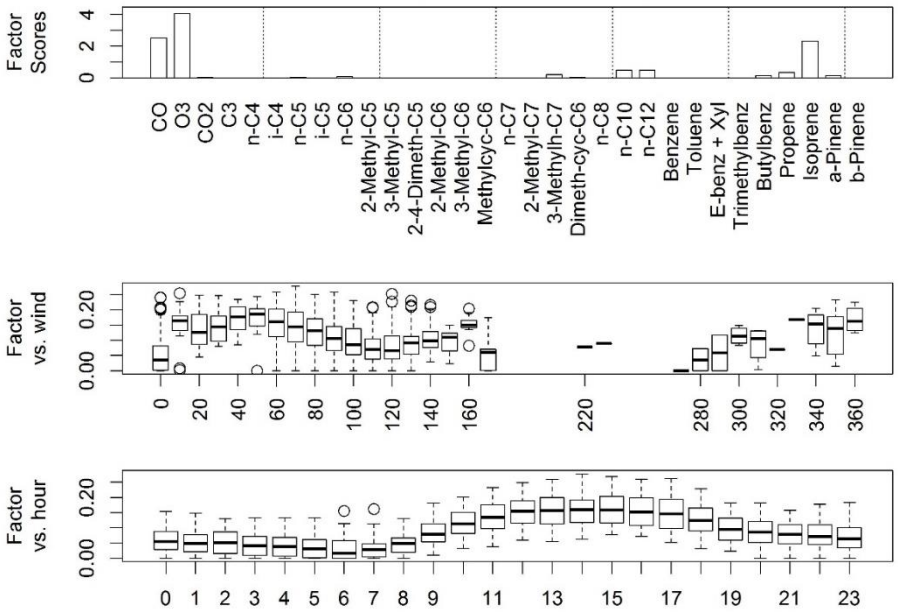

Figure 50: Diurnal/transport factor from the five-factor LS-NMF run.

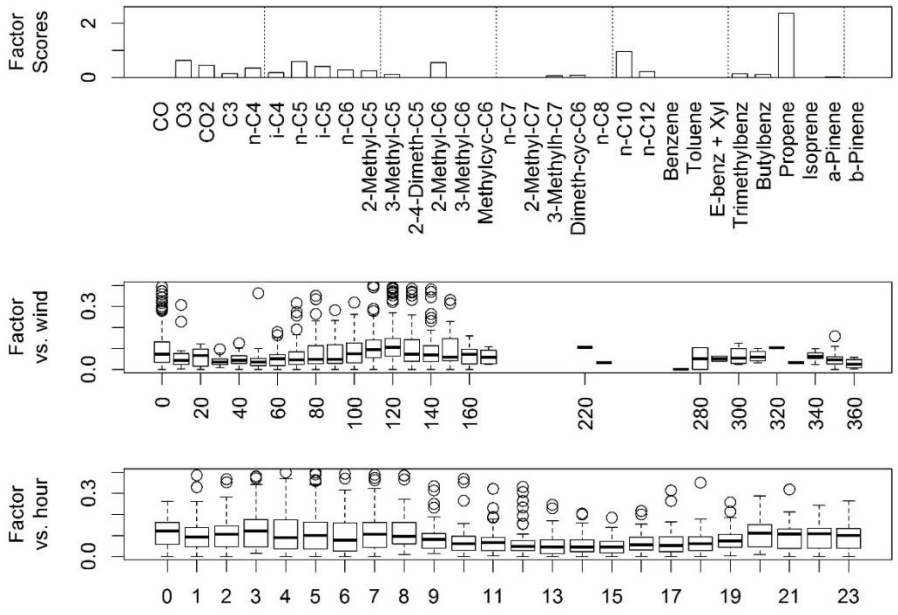

Figure 51: Propene factor from the five-factor LS-NMF run.

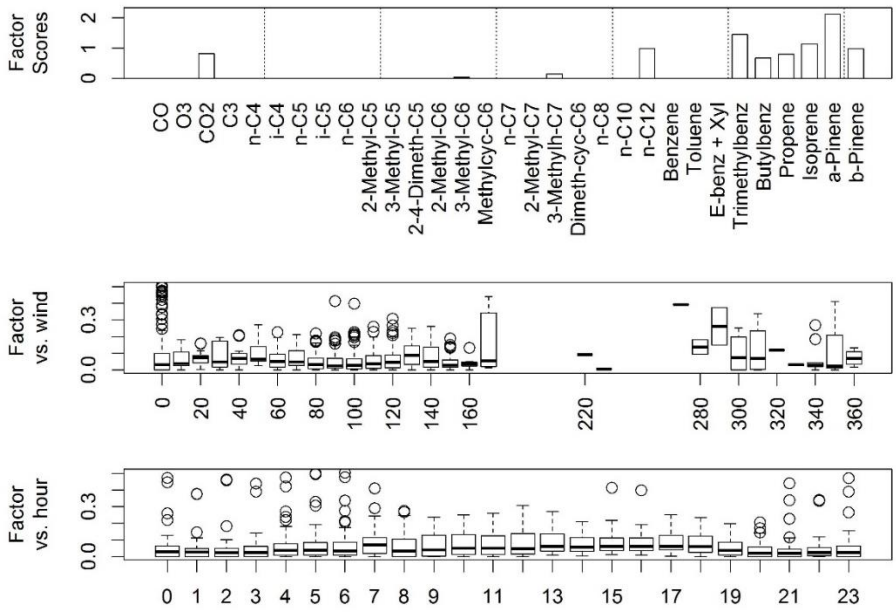

Figure 52: Higher aromats factor from the five-factor LS-NMF run.

for the diurnal and wind direction dependences undermines our confidence in the validity of these two factors. In summary, while this factorization provided insight into potential emission types that impacted shape ranch, some of the factors cannot be physically explained and justified.

A three-factor LS-NMF focusing on nighttime data only (23:00 to 07:00 LST) was performed and is presented in Figs. 53-55. The first two factors (Figs. 53 and 54) were similar to the first two factors for the five-factor LS-NMF run with all data. While the first nighttime factor, featuring light alkanes, CO, CO_2, and O_3, appeared to maximize during ENE winds, the lack of data under NE winds prevents a more thorough analysis of the wind dependence of this factor. The second factor (Fig. 54), featuring heavier hydrocarbons, maximized under ESE winds. The third factor was similar to the

combustion factor from the three-factor LS-NMF run. Adding a fourth factor caused the combustion factor to again split into a propene factor and an aromats factor, similar to the final two factors of the five-factor NMF run presented above. Again, while the LS-NMF runs using only nighttime data provided similar, potentially meaningful results when compared to the 5-factor daytime LS-NMF, they remain somewhat inconclusive.

3.3.3. NATURAL GAS FLARING

A number of flaring sites were located within 10 km of the site. The VIIRS Nightfire product suggests that many of these flares were operating intermittently, but there is evidence of frequent plumes from combustion sources, including flares, at the Shape Ranch site. An assessment of the in-plume chemistry is presented and the broader impacts of flaring on local air quality are modeled using TAMNROM-3D.

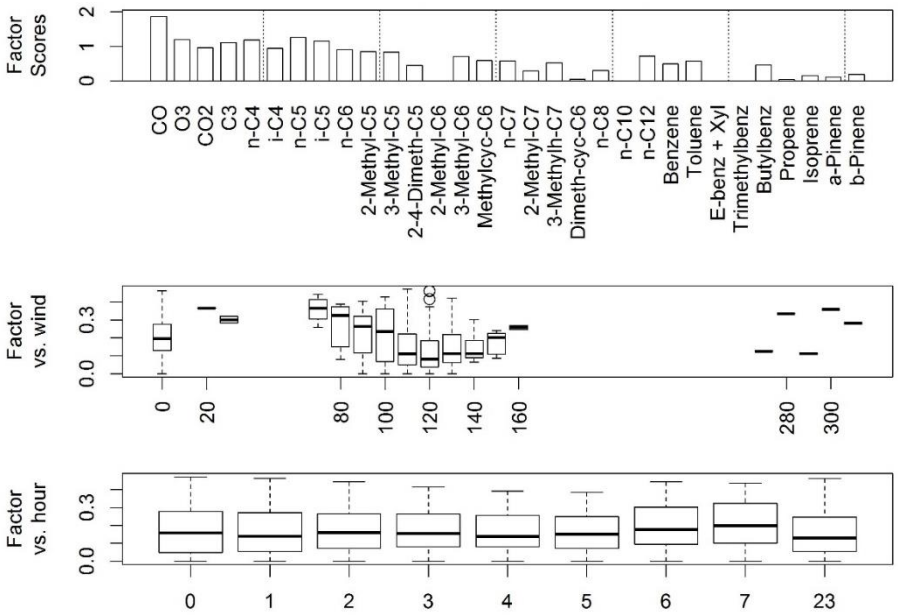

Figure 53: Light-alkane factor from the three-factor nighttime-only LS-NMF run.

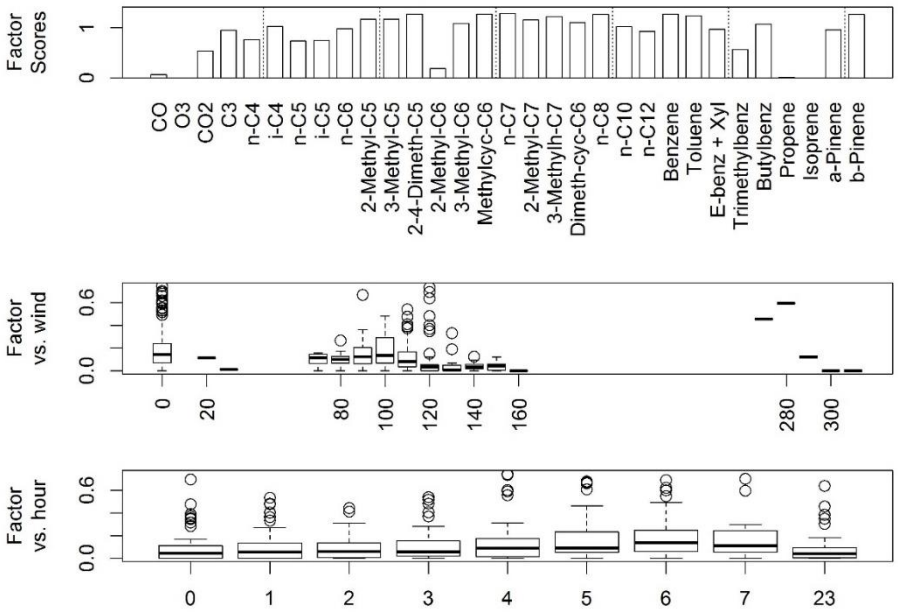

Figure 54: Heavy-alkane factor from the three-factor nighttime-only LS-NMF run.

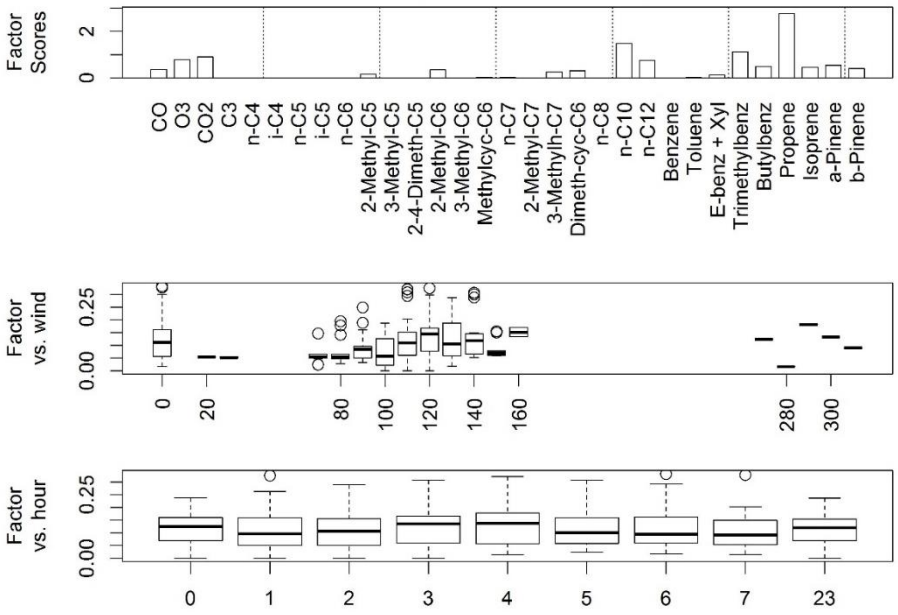

Figure 55: Combustion factor from the three-factor nighttime-only LS-NMF run.

3.3.3.1. GENERAL PLUME IDENTIFICATION USING TRACE GAS ENHANCEMENT RATIOS

Plumes from combustion sources were identified using a combination of NO_x and O_3 concentrations. The ratio of NO_x/O_3 serves as a sensitive indicator of combustion plumes, particularly at night, as O_3 is rapidly titrated by NO emissions from high-temperature combustion sources to form NO_2. During the nighttime, NO_2 is not photolyzed and the NO_x/O_3 ratio remains elevated as the plume is transported downwind. However, during the daytime, NO_2 is photolyzed and O_3 increases again further downwind from the emission source. Therefore, this method does not capture distant combustion sources during the daytime. It may also fail to capture plumes that occur in a high background O_3 environment, as the NO_x/O_3 ratio may remain low even within a plume. Note that other peak identification algorithms, including Bayesian methods such as Kalman filtering, have not been performed with this dataset.

Initially, a NO_x/O_3 threshold of 1/4 was used to identify times of substantial O_3 reductions by NO based on ambient concentrations. There were a total of 749 thirty-min periods when NO_x/O_3 exceeded 1/4. These periods showed a strong diurnal dependence with increasing frequency after sunset, peaking during the early morning near 06:00 LST (Fig. 56). Of the 749 detected peaks, only one occurred between 11:00-17:00 LST. This is likely due to higher ambient O_3 concentrations during daylight hours, and efficient mixing in a turbulent daytime PBL reducing the number of defined plumes that reach the measurement site. Figure 57 shows the correlation between benzene and toluene when $NO_x/O_3 > 0.25$ ($R^2 = 0.74$, $p < 0.001$). Most of these observations exceeded the median

benzene and toluene observations during the field campaign, suggesting that this method does generally capture air masses with elevated concentrations of gases associated with combustion. Figure 58 shows the relationship between CO_2 and NO_x enhancements above background when NO_x/O_3 exceeded 0.25. The background levels for NO_x, CO, and CO_2 were assumed to be moving 10^{th} percentiles over a moving 12 h window. Only a weak, but statistically significant correlation between CO_2 and NO_x was observed ($R^2 = 0.01$, $p < 0.01$). However, there were distinct clusters of data points with high CO_2 and low NO_x, low CO_2 and high NO_x, and high CO_2 and high NO_x. While high NO_x episodes were likely associated with combustion plumes and possibly episodic high soil emissions, high CO_2 events can also be associated with respiration, especially during wet periods (Meyers, 2001, Fig. 26). Figure 59 shows that there is also a weak relationship between NO_x and CO when $NO_x/O_3 > 0.25$, with $R^2 = 0.025$ ($p < 0.001$). The slope of NO_x/CO in that case was 0.03.

A higher NO_x/O_3 threshold of 1 was used to isolate plumes with increased ozone titration. This threshold identified 103 observations, with a similar diurnal pattern as the observations when NO_x/O_3 exceeded 1/4. Benzene and toluene showed a slightly weaker but still highly significant relationship ($R^2 = 0.67$, $p < 0.001$). In contrast, the relationship between CO_2 and NO_x remained very weak and statistically insignificant, with a wide range of NO_x/CO_2 ratios. The CO to NO_x relationship was also weak but with marginal statistical significance ($R^2 = 0.03$, $p = 0.075$). The weak correlations between NO_x and both CO and CO_2 suggest that a general threshold NO_x/O_3 ratio and assumed background concentrations equal to a moving 10^{th} percentile provides limited

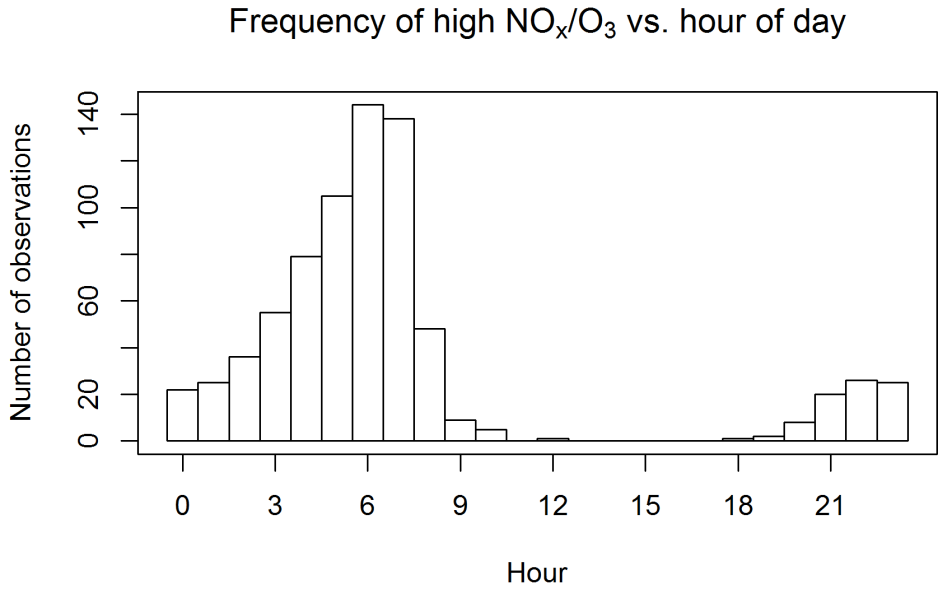

Figure 56: Histogram of the hour of day when NO_x/O_3 exceeds 0.25. These periods tend to begin after sunset and peak in frequency in the early morning hours. Very few peaks occur during the afternoon hours when ambient O_3 is high.

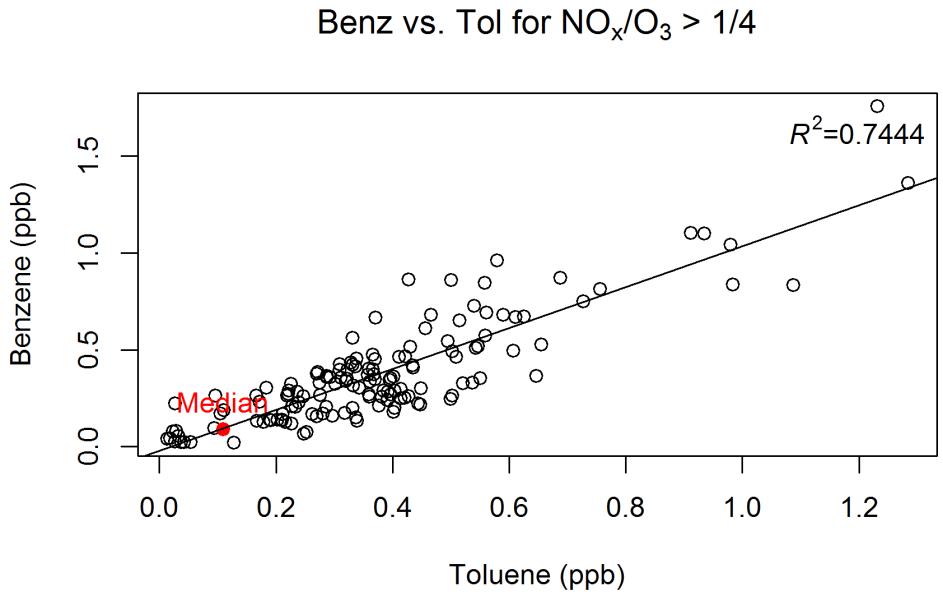

Figure 57: Benzene and toluene concentrations when $NO_x/O_3 > 0.25$. The high concentrations compared to the median at Shape Ranch suggest this subset of observations has elevated concentrations of pollutants associated with combustion.

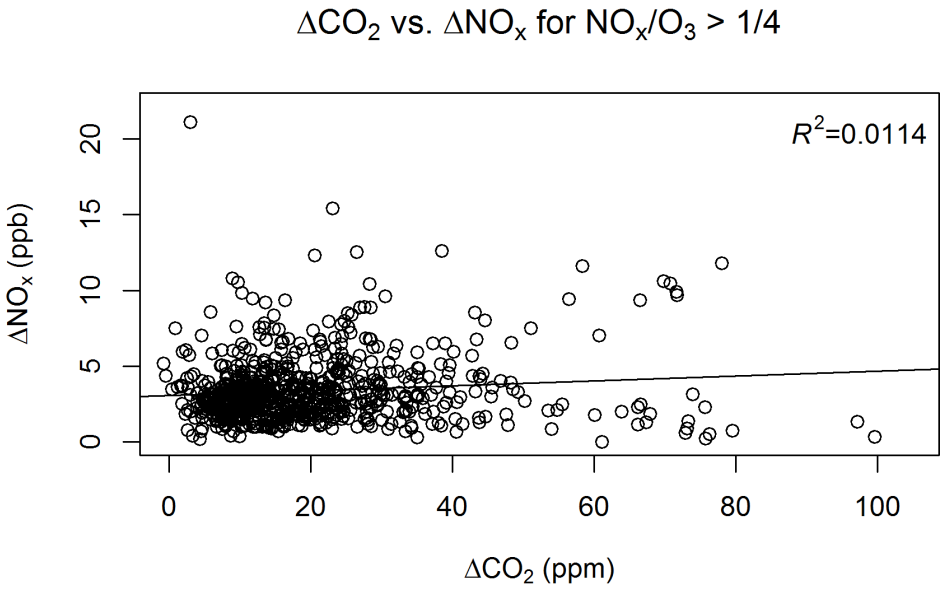

Figure 58: ΔNO_x and ΔCO_2 concentrations when $NO_x/O_3 > 0.25$. The linear relationship is statistically significant ($p < 0.01$) but weak ($R^2 = 0.01$), with a wide range of observed ratios.

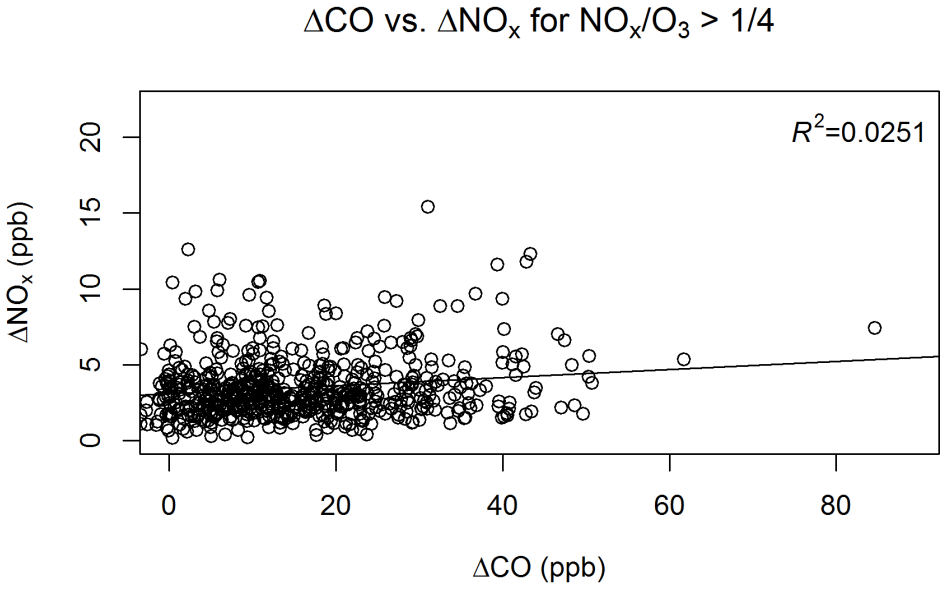

Figure 59: ΔNO_x and ΔCO concentrations when $NO_x/O_3 > 0.25$. The linear relationship is weak, though it is statistically significant ($p < 0.001$).

insight into the nature of specific combustion sources types affecting the air quality at Shape Ranch. Instead, it is likely that a variety of sources, including both high- and low-temperature combustion sources and biogenic emissions of NO_x and CO_2, contribute to the observed enhancements above background.

3.3.3.2. CARBON DIOXIDE AND NITROGEN OXIDE RATIOS WITHIN PLUMES

The high temporal resolution of the original 10 s data set may provide more insight into the plumes identified above. However, due to the poor precision of the 10 s CO data, the NO_x/CO ratio was excessively noisy. Therefore, only the NO_x/CO_2 ratio was analyzed in more detail. A NO_x/O_3 ratio of 1/4 was used to filter 30 min data. Consecutive 30 min periods with NO_x/O_3 greater than 1/4 were assumed to be one continuous (combustion) plume event. For each of these events, 30 min was added before and after the time period to include pre- and post-plume observations. This expanded time period was then used to analyze the corresponding 10 s data. The moving 10^{th} percentile from the 30 min dataset was linearly interpolated to a 10 s resolution to represent the background concentrations, which were then subtracted from the 10 s time series to obtain trace gas enhancements. For each plume event, the 10 s NO_x/CO_2 enhancement ratios were assessed when ambient NO_x/O_3 exceeded 1/4.

Many combustion events had a statistically insignificant relationship between NO_x and CO_2 enhancements ($p \geq 0.05$) or a weak relationship, defined here as $R^2 \leq 0.25$. Other events produced negative relationships ($R < 0$), which indicates that combustion was not captured in the 10 s enhancements of NO_x and CO_2. Furthermore, events with

significant rainfall (> 3 mm, Hao et al., 2010) observed in the previous three days were discarded to minimize the influence of nitrification and ecosystem respiration on high NO_x and CO_2 concentrations, respectively. Lastly, events prior to the end of May were discarded as the precision of the NO_x instrument was poor during the early portion of the field campaign. Out of an identified 176 plume events, 21 met the criteria of a meaningful, positive, and statistically significant relationship ($R^2 > 0.25$, $R > 0$, $p < 0.05$), akin to a combustion plume and without rainfall in the previous three days. Figure 60 shows the slope and the R^2 value for each of these events. A range of slopes was observed, with a cluster of events having slopes (in ppb/ppm) of less than 0.5, and a broader cluster of points with slopes between 0.5 and 2.

An example of a plume event is presented in Fig. 61, which is circled in red in Fig. 60. This event on the evening of 24 July 2015 was indicative of a combustion plume from a low-temperature source, such as a flare. The NO_x/CO_2 enhancement ratio of 1.8 is within a factor of four of the ratio of AP-42 emission factors for flares (NO_x/CO_2 = 0.54), and is an order of magnitude smaller than the emission factors for controlled diesel engines (NO_x/CO_2 = 11.0) and large, uncontrolled diesel engines (NO_x/CO_2 = 25.7) (U.S. Energy Information Administration, 2016; U.S. Environmental Protection Agency, 2016c). The high correlation coefficient of the NO_x/CO_2 relationship suggests that this event was very likely a plume from a low-temperature combustion source, although with an apparently higher temperature than the EPA and EIA emission factors for flares suggest, because higher temperature combustion produces more NO_x (Flagan & Seinfeld, 1988; Zeldovich, 1992), as was observed.

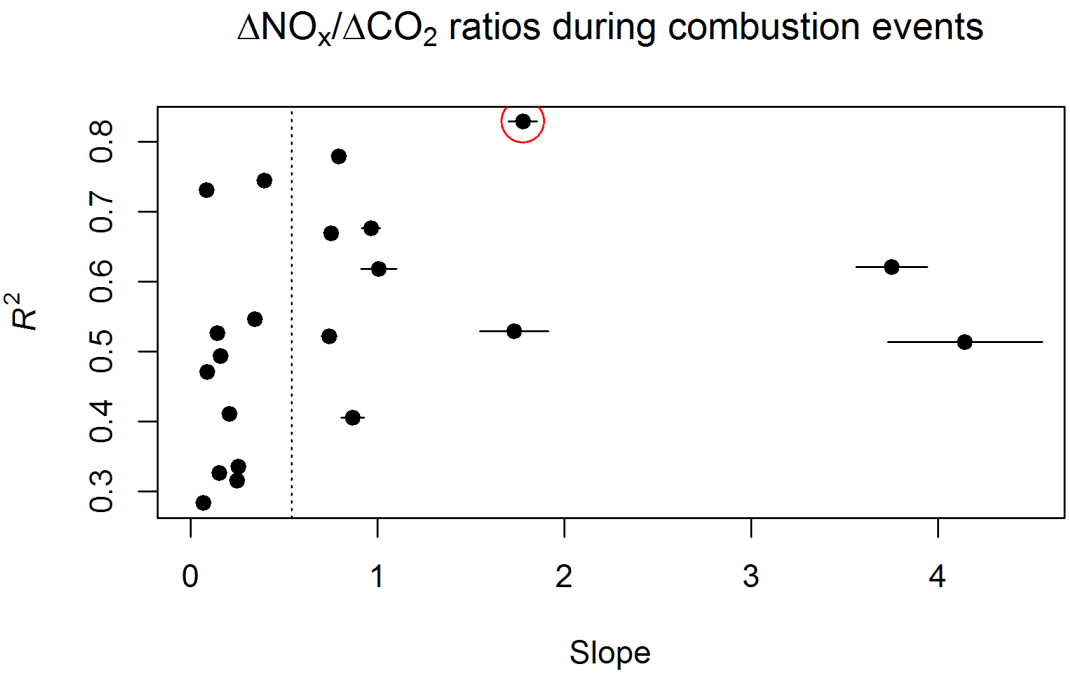

Figure 60: The slope and R^2 values for $\Delta NO_x/\Delta CO_2$ for each of the 21 combustion events with meaningful ($R^2 > 0.25$, $R > 0$), statistically significant ($p < 0.05$) relationships, and without significant rainfall (> 3 mm, Hao et al., 2010) during the previous three days. A cluster of data points have slopes of less than 0.5 with relatively weak relationships ($R^2 < 0.6$). Several data points have slopes between 0.5 and 2, and many of these points have the strongest relationships ($R^2 > 0.6$). Two points have slopes near 4. One data point identified with a red circle was used as a case study in Fig. 58. The NO_x/CO_2 emission factor ratio for flares (0.54) is indicated with a dotted black line (U.S. Energy Information Administration, 2016; U.S. Environmental Protection Agency, 2016c).

An example for a combustion event that did not meet the criteria for a meaningful and statistically significant relationship is shown in Fig. 62. On 17 July 2015, a prolonged episode of NO_x/CO_2 exceeding 1/4 occurred from approximately 05:00 to 07:00 LST. Most of this time period featured $NO_x/O_3 < 1/2$, except for two distinct NO_x plumes when NO_x/O_3 approached 3. During these plumes, NO_x increased by several ppb while CO_2 varied by less than 1 ppm. Though the overall NO_x/CO_2 ratio

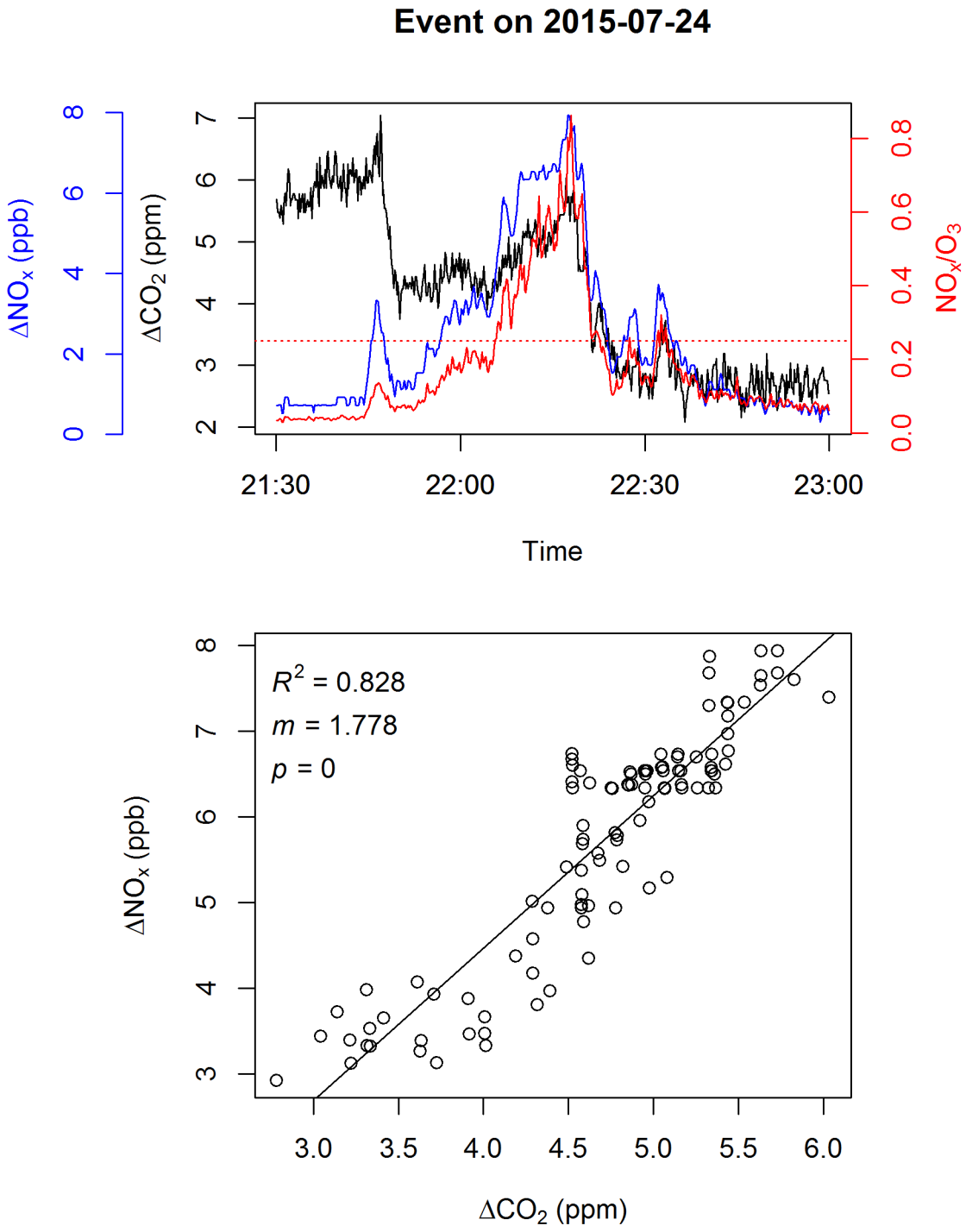

Figure 61: NO_x and CO_2 enhancements for a plume on 24 July 2015. The data points in the bottom panel correspond to the NO_x and CO_2 enhancements above background when NO_x/O_3 exceeded 1/4.

showed a relationship (R^2 = 0.219, slope = 0.437), the two distinct NO_x plumes appeared as a cluster of data points with a much higher NO_x/CO_2 ratio (3-7). These two plumes may have been associated with a high-temperature combustion source due to the elevated NO_x plumes with relatively small changes in CO_2.

A second example of high-temperature combustion appeared on the morning of 10 September 2015, when several short, distinct plumes occurred between 07:00 and 07:30 LST (Fig. 63). A marginally elevated NO_x/O_3 ratio during the preceding hours resulted in a weak correlation, with the distinct plumes appearing as outliers in the bottom panel of Fig. 63. Due to the very brief duration of these plumes, and the high NO_x/CO_2 ratio of the associated data points, it is likely that a nearby high-temperature combustion source, such as truck or generator exhaust, was responsible for the plumes. Overall, the combustion events that met the correlation and statistical significance criteria imply that low-temperature combustion sources with low NO_x/CO_2 emission ratios are often responsible for combustion plumes observed at Shape Ranch. The median NO_x/CO_2 ratio of the 20 combustion events of 0.4 is close to the ratio of 0.54 for emission factors for flaring (U.S. Energy Information Administration, 2016; U.S. Environmental Protection Agency, 2016c). However, the interquartile range of the NO_x/CO_2 ratio for these events ranged from 0.2 to 1.0, suggesting that numerous combustion plumes showed NO_x/CO_2 ratios that are more than a factor of 5 higher than the expected ratio for such events. Overall, these results imply that:

1) low-temperature combustion sources responsible for these events, which are assumed to include many flares, have widely varying emission factors, and/or

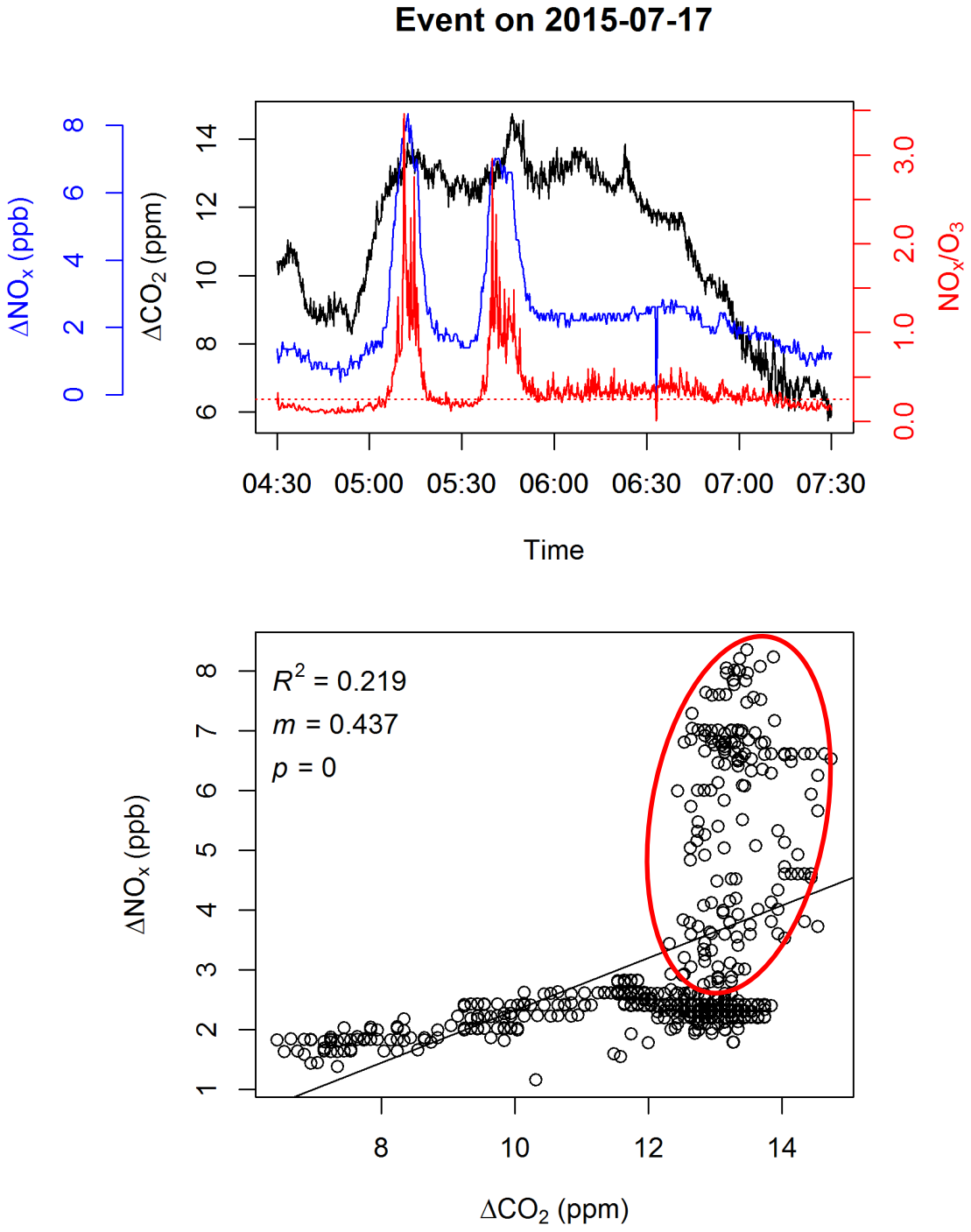

Figure 62: NO_x and CO_2 enhancements for a plume on 17 July 2015. A distinct cluster of data observations with elevated NO_x enhancements and relatively stable CO_2 enhancements is indicative of high-temperature combustion.

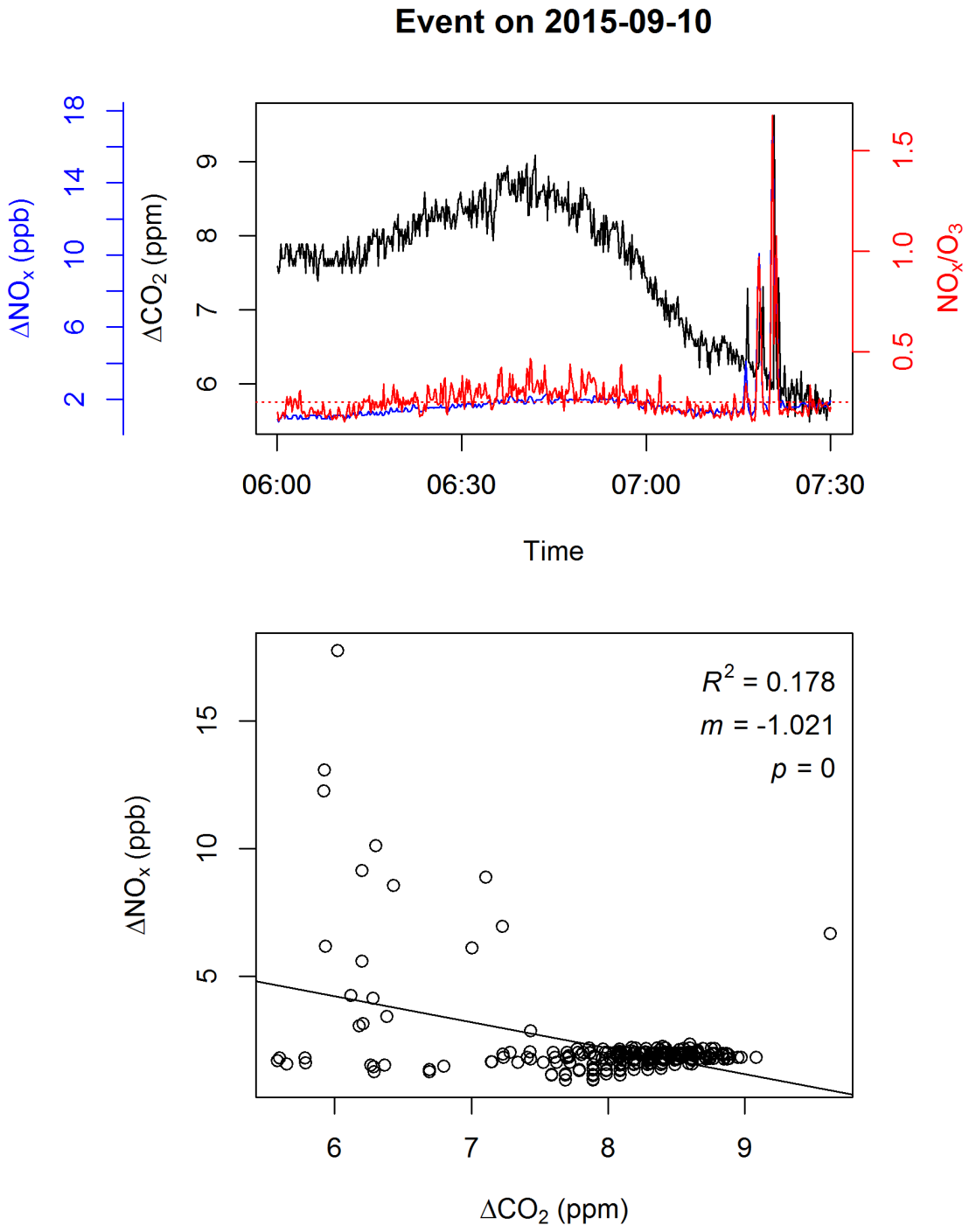

Figure 63: NO_x and CO_2 enhancements for a plume on 10 September 2015. Several brief plumes of very high NO_x enhancements and smaller CO_2 enhancements is indicative of a nearby high-temperature combustion source.

2) A combination of other sources of NO_x and CO_2, including biogenic sources, as well as atmospheric transport and chemistry, may interfere with the detection of distinct plumes from distant combustion sources.

3.3.3.3. PLUME IDENTIFICATION CASE STUDIES

Several distinct episodes of elevated NO_x, CO_2, CO, and decreased O_3 were identified in the time series for Shape Ranch. While trace gas ratios show mixed source types for general plume identifications, individual plumes and clusters of plumes exhibited clearer relationships between trace gases. Two notable case studies are presented in this section.

The first example shown is for the period of 30 July through 1 August 2015 (Fig. 64). Several plumes were identified during this three-day period. It is noteworthy that 1 August was the day with the highest observed O_3 mixing ratios, with a maximum 8-h average of 71 ppb – exceeding the current NAAQS 8-h ozone design value of 70 ppb. Elevated NO_x/O_3 was observed in the early morning hours, prior to sunrise, on each of the three days. A maximum NO_x/O_3 ratio was observed during the early morning hours of August 1, when NO_x mixing ratios exceeded 5 ppb for several hours and peaked above 10 ppb. Meanwhile, O_3 mixing ratios dropped below 10 ppb. After sunrise, ozone mixing ratios increased at a rate exceeding 10 ppb per hour from 07:00 to 09:30 LST, likely due to high ozone levels in the residual layer mixing to the surface. Note that CO, CO_2, toluene, and benzene were also elevated prior to sunrise, strongly suggesting an accumulation of emissions from combustion sources in a stable nocturnal surface layer.

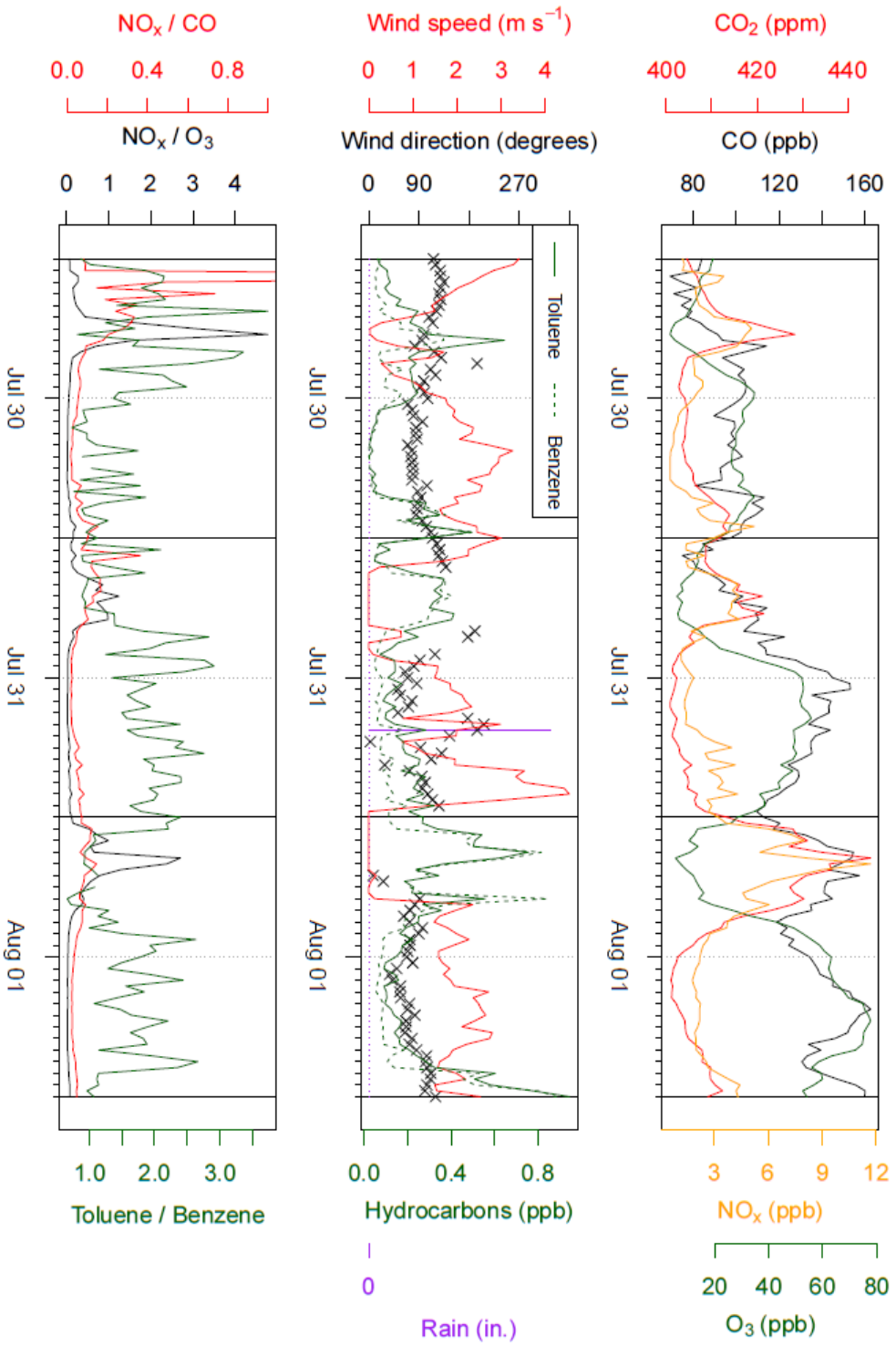

Figure 64: Trace gas concentrations, ratios, and winds for 30 July to 01 August 2015. The left panel shows the ratio of NO_x to above-background CO, assumed to be the minimum observed CO concentration during the three-day period.

To estimate emission ratios, plumes were again assumed to be present when the NO_x/O_3 ratio exceeded 1/4. The background levels of CO and CO_2 were assumed to be the minimum observed values during the time period (1 ppb CO and 1 ppm CO_2 were added back to avoid zeroes in the ratios), while the background NO_x mixing ratio was assumed to be 2 ppb based on near-plume observations. A linear regression (forced through the origin) of 30 min enhancements of NO_x and CO above background is shown in Fig. 65. The ratio of NO_x/CO enhancements was 0.065 ($p < 0.001$, $R^2 = 0.86$). This ratio is approximately a factor or two smaller than the NO_x/CO ratio of 0.112 calculated from the US EPA's flaring emission factors from its AP-42 document (U.S. Environmental Protection Agency, 2016c), and is more than an order of magnitude lower than the ratio associated with uncontrolled diesel emissions (NO_x/CO = 2.8) and large, controlled diesel engines (NO_x/CO = 1.4). This suggests emissions from an inefficient combustion source accumulating in the boundary layer during the overnight hours and contributing to high nighttime NO_x. Figure 66 shows the NO_x vs. CO_2 enhancements for the same episodes when NO_x/O_3 ratio exceeded 1/4. Again, the NO_x/CO_2 ratio is lower than that of flaring emissions (approximately a factor of three), and roughly one order of magnitude lower than that of controlled or uncontrolled diesel engines. This again provides strong evidence that dominantly low-temperature combustion was contributing to the observed plumes from 30 July to 1 August 2015.

Individual plumes can also be assessed by examining the original dataset which was recorded at a 10 s resolution. The CO analyzer had a comparatively low precision (±20 ppb), so the 10 s data were too noisy to identify small enhancements associated

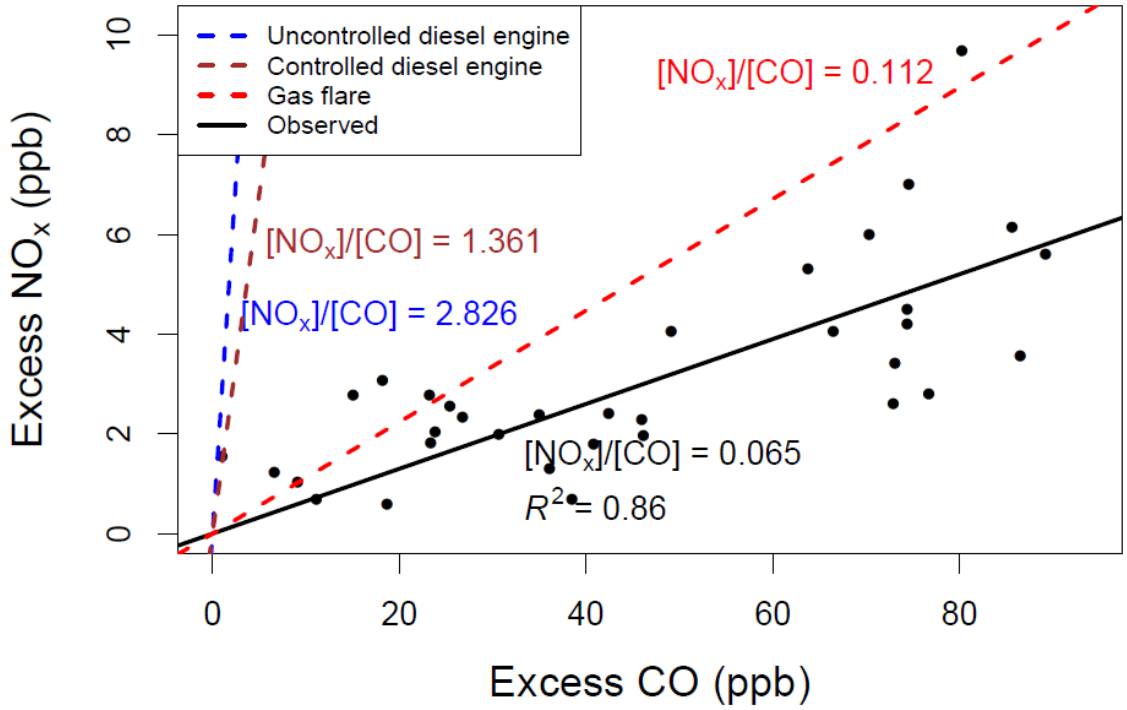

Figure 65: Excess CO and NO_x above background during half-hourly periods when $NO_x/O_3 \geq 0.25$ from 30 July to 01 August 2015. The ratio indicates that the plumes were associated with a relatively low-temperature combustion source – i.e. flaring.

with plumes – even with a 1 min moving average filter, which was applied to the trace gas data in this analysis. However, the relatively high precision of the NO_x and CO_2 data allowed for the identification of combustion plumes. A notable example is an approximately 30 min enhancement of NO_x and CO_2 during the evening of 31 July (Fig. 67), when outflow from a nearby thunderstorm caused a change in wind direction from the east-southeast to the north. During this time, CO_2 and NO_x mixing ratios increased by several ppb above background while there was a notable decrease in O_3. The trace gas ratios show that this plume featured high NO_x/O_3 and high NO_x/NO ratios, indicating O_3 titration. The 5 min periods preceding and following the plume episode (blue shading in the bottom panel) were used to identify the background levels, which

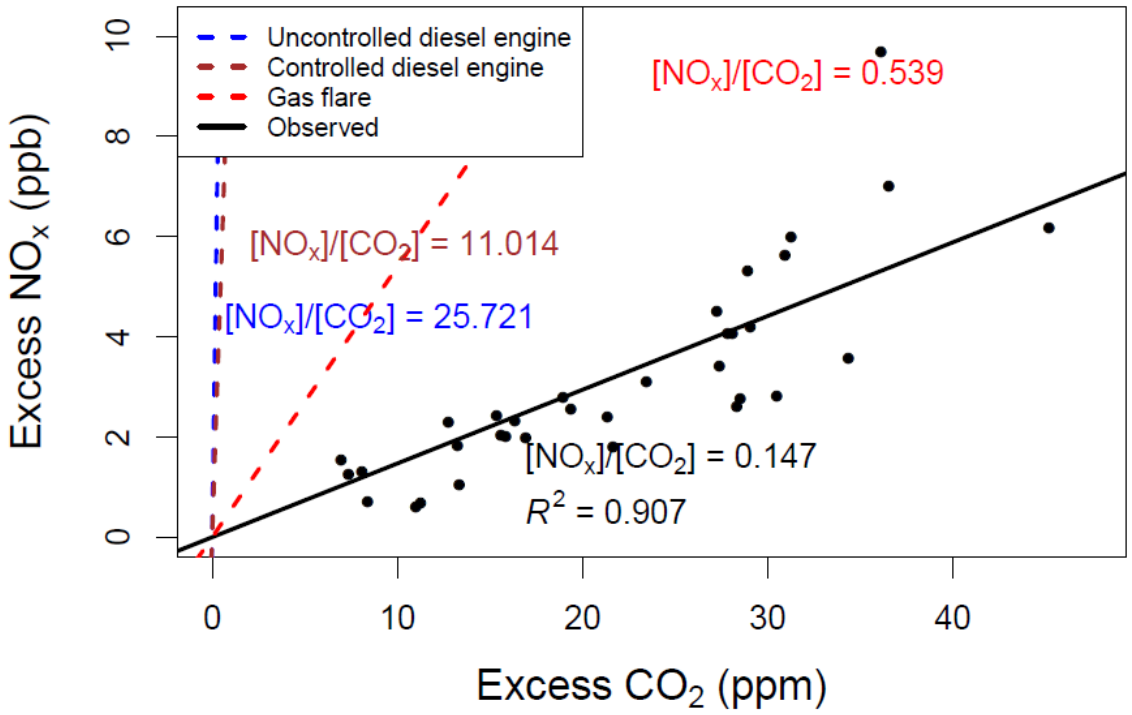

Figure 66: Excess CO_2 and NO_x above background during half-hourly periods when $NO_x/O_3 \geq 0.25$ from 30 July to 01 August 2015. The ratio indicates that the plumes were associated with a relatively low-temperature combustion source – i.e. flaring.

were estimated by drawing a line between the minimum NO_x and CO_2 mixing ratios during the preceding and following 5-min periods. This line was subtracted from the NO_x and CO_2 concentrations to quantify the enhancement above the background during the plume, shown as the gray shaded regions. The NO_x and CO_2 enhancements are shown as a linear regression in Fig. 68. The $\Delta NO_x/\Delta CO_2$ ratio of 0.96 ($R^2 = 0.93$, $p < 0.001$) is within a factor of two of the flaring ratio of 0.54 obtained from the AP-42 NO_x factor and the EIA natural gas flaring factor for CO_2 (Fig. 60), but it is more than an order of magnitude smaller than the NO_x/CO_2 ratio for an uncontrolled diesel engine or a large, controlled diesel engine from the AP-42 document. There is uncertainty in the

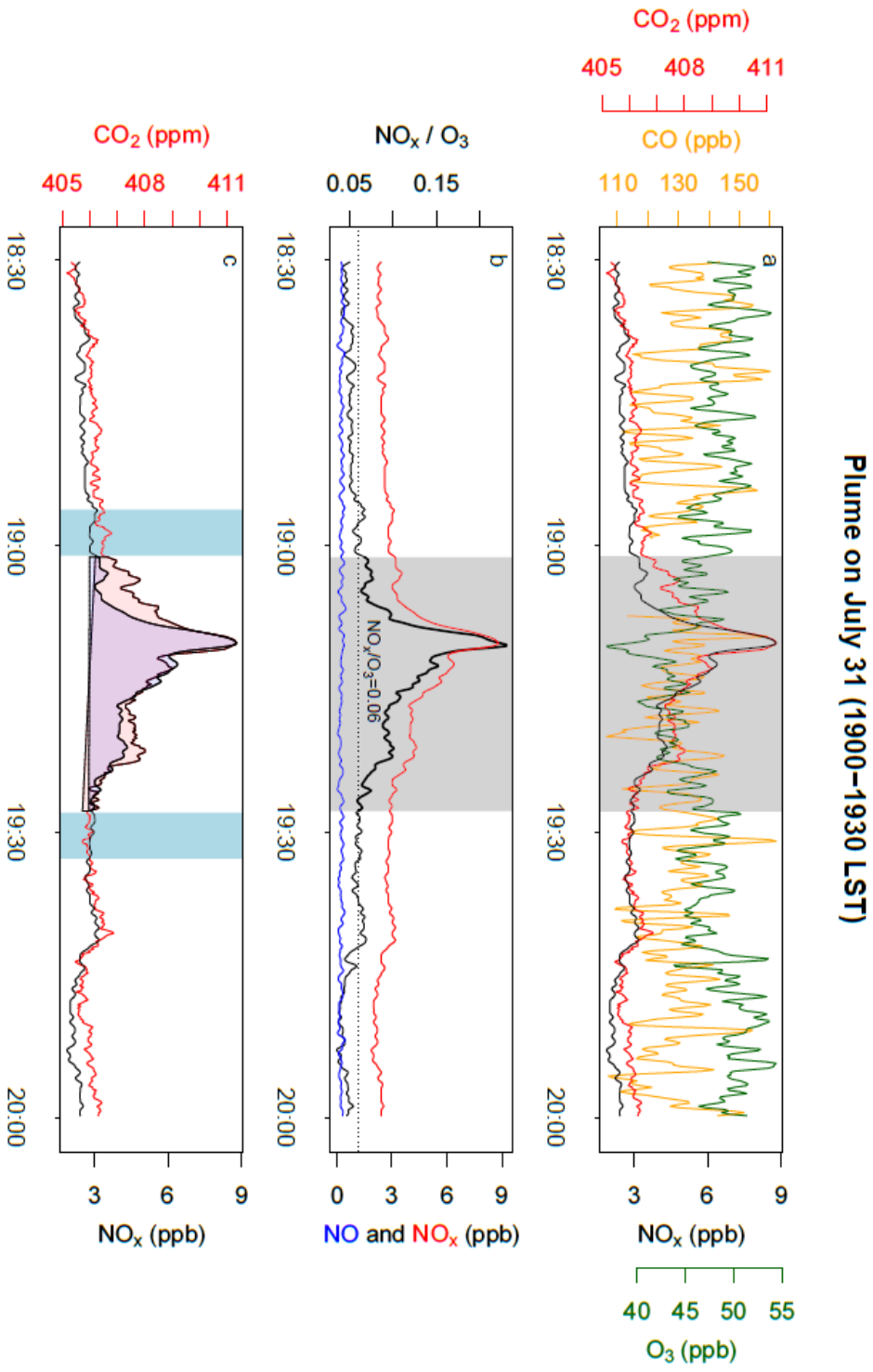

Figure 67: Trace gas measurements from 18:30 to 20:00 LST 31 July 2015. The plume episode was defined to be the roughly 30 min period when $NO_x/O_3 \geq 0.06$.

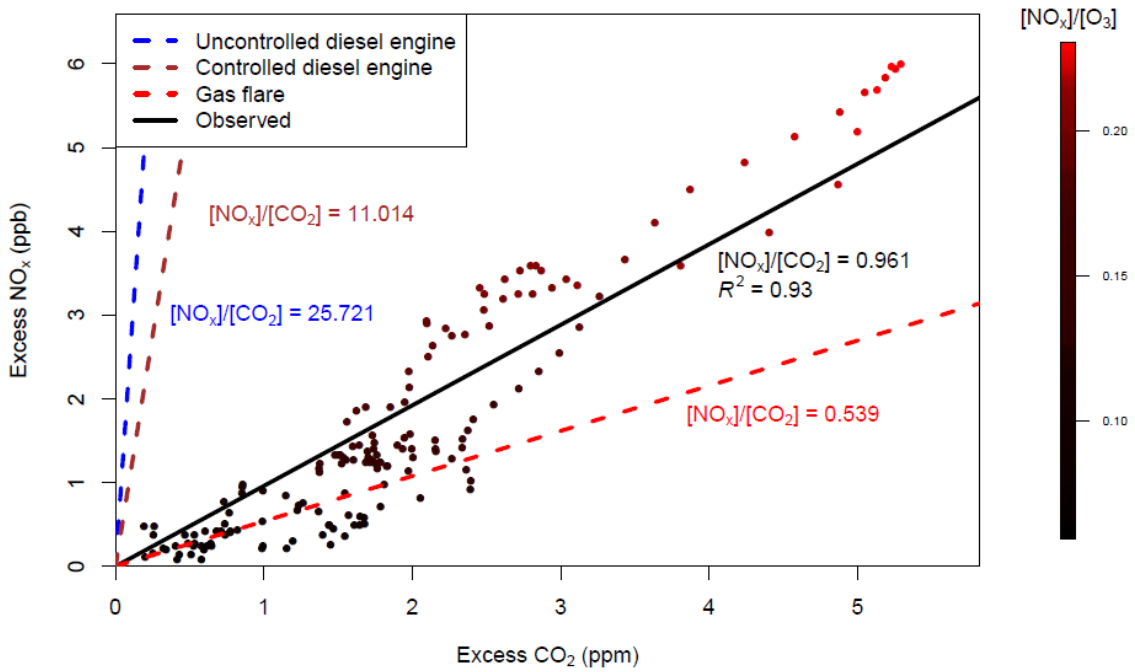

Figure 68: A linear regression of the NO_x and CO_2 enhancements above background in the plume observed on the evening of 31 July 2015 plume. The coloring of the points indicates the NO_x/O_3 ratio during the plume, with high NO_x/O_3 ratios corresponding to large enhancements of NO_x and CO_2.

source of these enhancements, however, due to the influence of the outflow from the thunderstorm.

The second example consists of a multiday episode featuring several plumes during 10-13 September 2015 (Fig. 69). NO_x mixing ratios during that period exceeded 10 ppb on more than one night with concurrent CO and CO_2 peaks and O_3 minima. Rain was observed on the evening of 11 September with a brief frontal passage, followed by northwesterly winds until midday on 12 September when easterly flow returned. Over the four-day time period, background NO_x was assumed to be 2 ppb while background CO and CO_2 were assumed to be the minimum mixing ratios over the time period (with 1 ppb CO and 1 ppm CO_2 added to the time series to avoid zeroes). Figure 70 shows

excess NO_x and excess CO over background. The ratio of excess NO_x/CO was 0.07 ($R^2 = 0.24$, $p < 0.001$), which is within a factor of 2 of the ratio for flares from the AP-42 emission factors. It should be noted that there is a cluster of data points with excess CO less than 20 ppb while ΔNO_x was elevated. The $\Delta NO_x/\Delta CO$ ratio for these data points lies in between the ratios expected for flares and diesel engines, wherefore these data points may represent plumes from a hotter combustion source. Figure 71 shows the excess NO_x and CO_2. The ratio of 0.095 ($R^2 = 0.46$, $p < 0.001$) is more than a factor of five smaller than the ratio expected for flares, and more than one order of magnitude smaller than the ratio for diesel engines. Again, the data points with elevated NO_x/CO are shown in orange. These data points mostly have a $\Delta NO_x/\Delta CO_2$ ratio below the linear regression line, indicating a more efficient combustion process.

Elevated NO_x/O_3 ratios on the evening of 12 September also coincided with elevated CO_2 concentrations (Fig. 72). Again, the 10 s CO data were very noisy, so enhancements are not evident in the figure. Local winds were frequently recorded at 0 m s^{-1} indicating weak near-surface transport. We used nearby Faith Ranch Airport (KFTN) observations to verify persistent light easterly winds during the evening hours on 12 September. Repeated peaks in the NO_x/O_3 ratio and CO_2 occurred between 19:00 to 21:00 LST 12 September 2015. Figure 73 shows this two-hour time period in more detail. A NO_x/O_3 ratio of 0.35 was used as a threshold to identify combustion, and the minimum NO_x and CO_2 concentrations observed while NO_x/O_3 exceeded 0.35 were assumed to represent background. Figure 67 shows the correlation between NO_x and CO_2 enhancements. A line is drawn between data points in the time series to illustrate

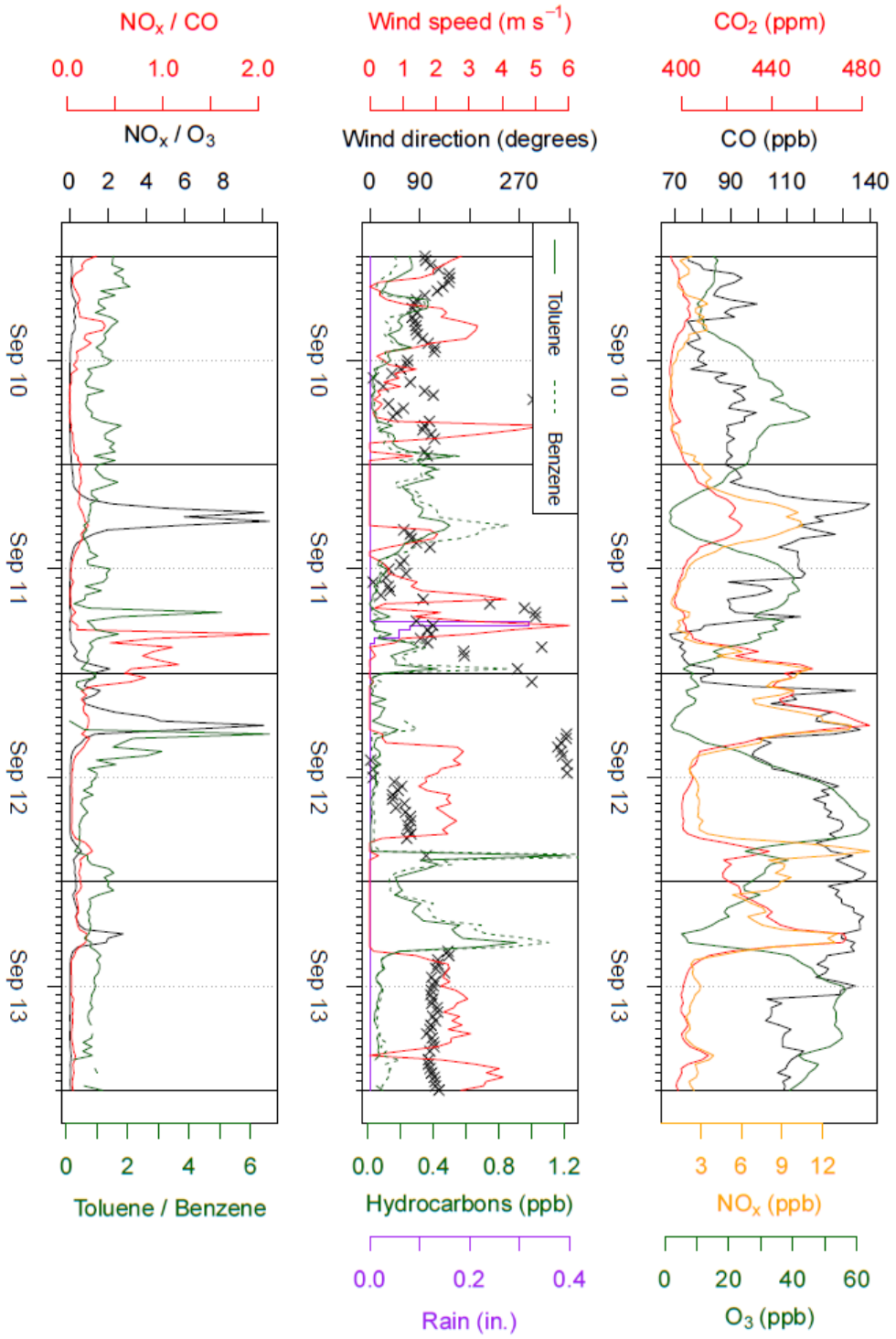

Figure 69: Trace gas concentrations, ratios, and winds for 10 to 13 September 2015. The bottom panel shows the ratio of NO_x to above-background CO, assumed to be the minimum observed CO concentration during the three-day period.

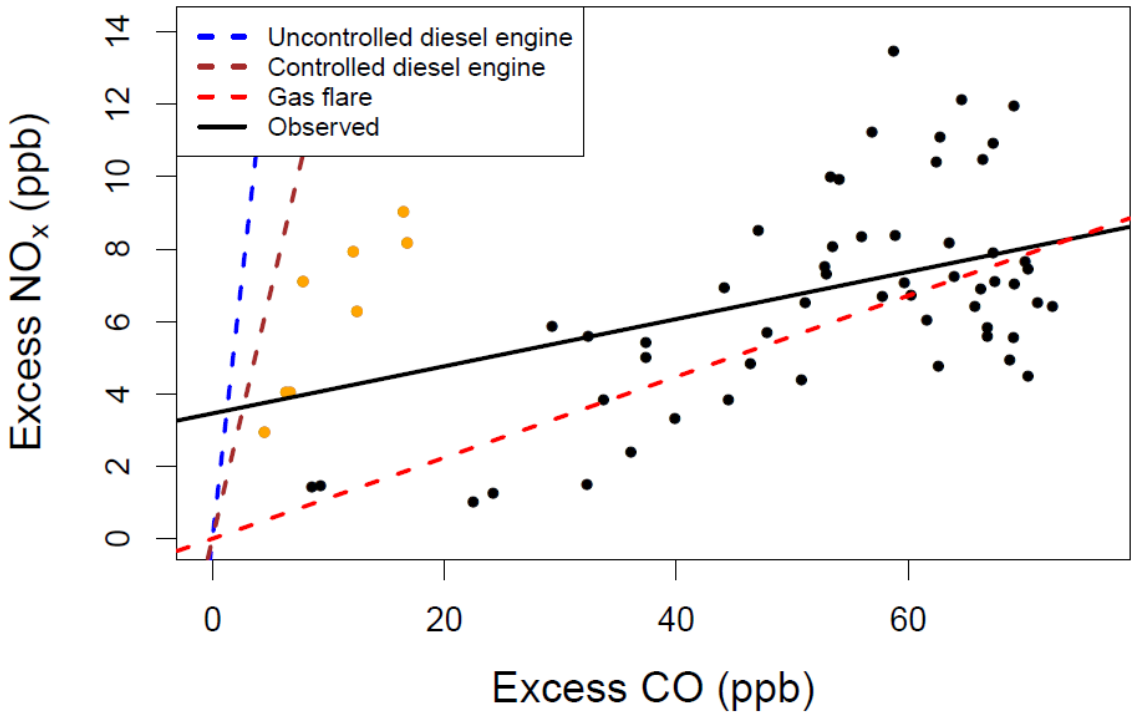

Figure 70: Excess CO and NO_x above background during half-hourly periods when $\Delta NO_x/\Delta CO \geq 0.25$ from 10 to 13 September 2015. Observations with an excess NO_x/CO ratio greater than 0.4 are shown in orange. The expected NO_x/CO emission ratios are shown as dashed lines, with flaring in red (NO_x/CO = 0.112), controlled diesel engines in brown (1.361), and large, uncontrolled diesel engines in blue (2.826).

the changing enhancement ratios over time. Overall, the $\Delta NO_x/\Delta CO_2$ ratio of 0.27 (R^2 = 0.43, $p < 0.001$) is a factor of two smaller than the NO_x/CO_2 ratio for flares and more than an order of magnitude smaller than the ratio for diesel engines. However, at the beginning of the time period with elevated NO_x/O_3 ratios, NO_x was 1 to 2 ppb above background while CO_2 was between 0 to 1 ppm above background. After multiple peaks in NO_x and CO_2, NO_x dropped to less than 1 ppb above background while CO_2 remained close to 10 ppm above background. This likely represents a change in background CO_2 levels. At closer inspection, two distinct clusters of points with similar slopes and

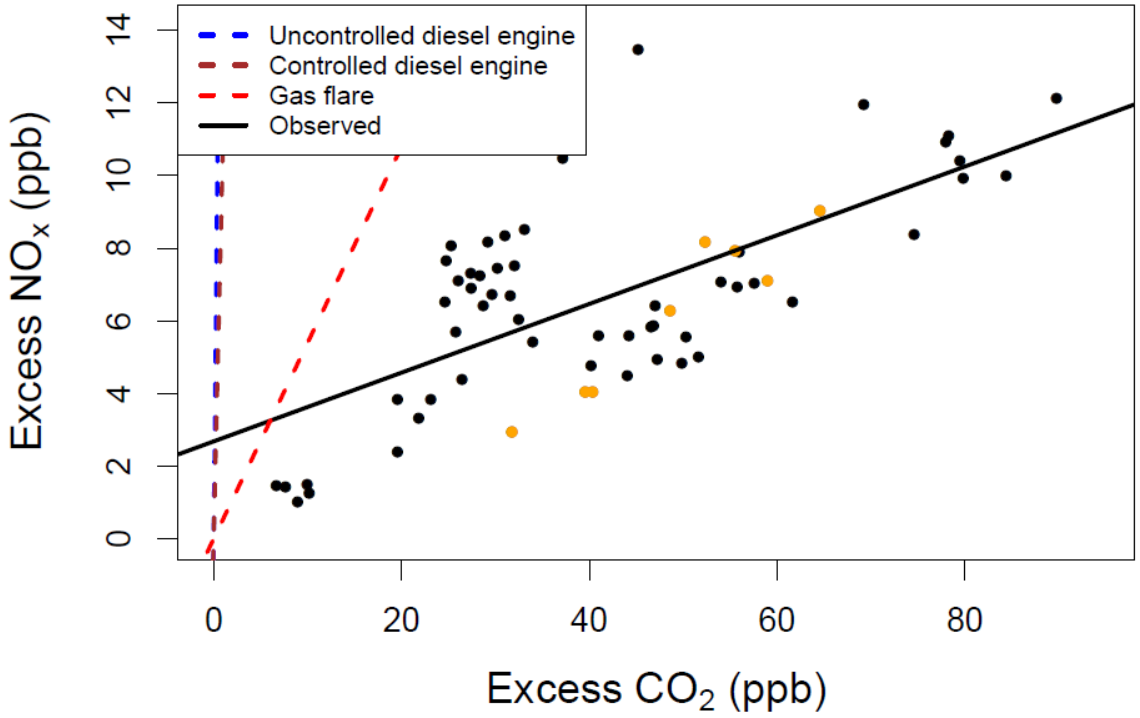

Figure 71: Excess CO_2 and NO_x above background during half-hourly periods when $NO_x/CO \geq 0.25$ from 10 to 13 September 2015. The ratio indicates that the plumes were associated with a relatively low-temperature combustion source – i.e. flaring. Observations with an excess NO_x/CO ratio greater than 0.4 are shown in orange. The expected NO_x/CO_2 emission ratios are shown as dashed lines, with flaring in red (NO_x/CO_2 = 0.539), controlled diesel engines in brown (11.014), and large, uncontrolled diesel engines in blue (25.721).

different x-axis intercepts are visually apparent in Fig. 74. To account for this apparent change in the CO_2 background, the time period with NO_x/O_3 exceeding 0.35 was split into two subsets: the first subset was defined to be the period before (and including) the highest CO_2 observation during the plumes, and the second subset included all of the following observations. The $\Delta NO_x/\Delta CO_2$ ratios for the two data subsets are shown in Fig. 74, with the linear regressions for the first subset of data points in brown and the second subset in green. The $\Delta NO_x/\Delta CO_2$ ratios of each subset were similar: 0.34 for the

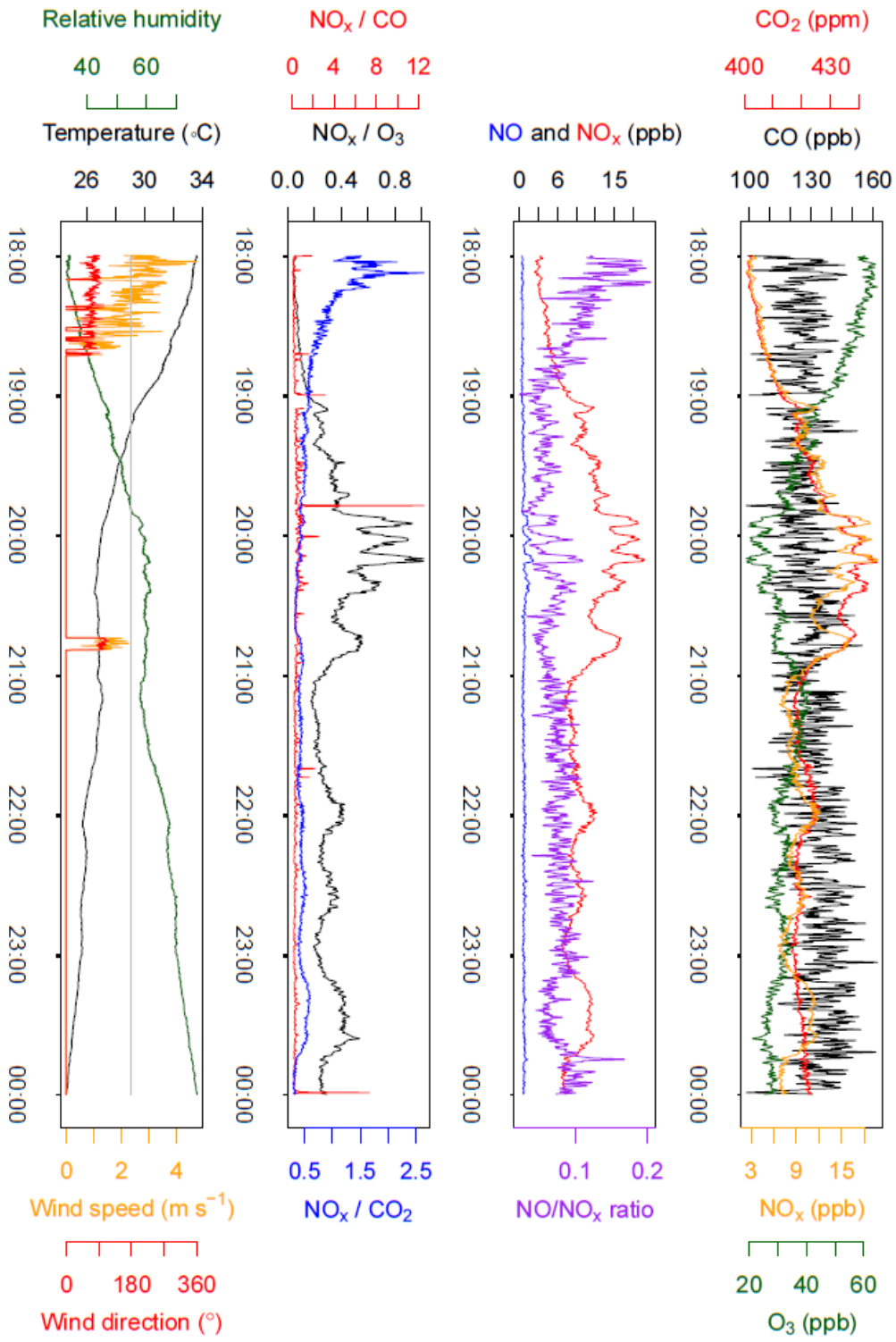

Figure 72: Trace gas measurements from 18:00 LST 12 September to 00:00 LST 13 September 2015.

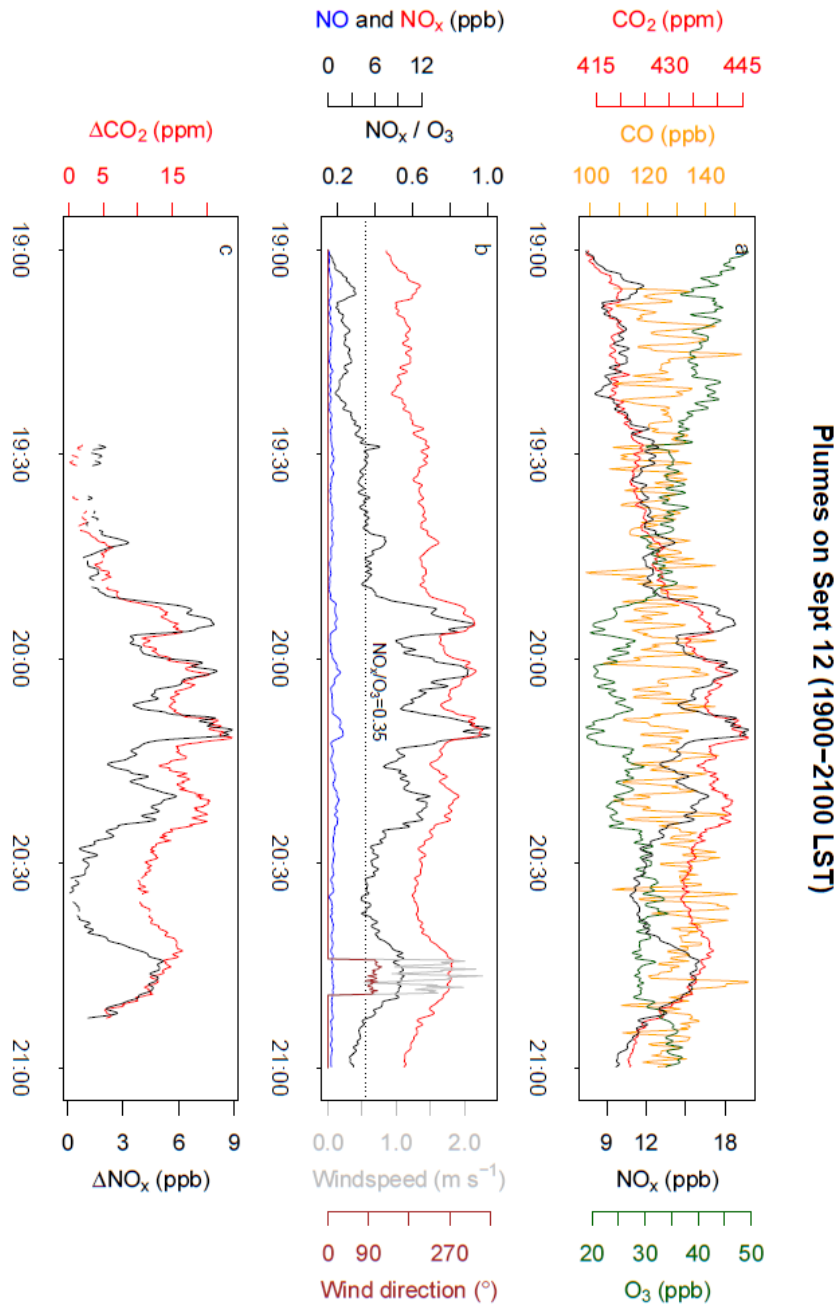

Figure 73: Trace gas concentrations, ratios, and enhancements above background for 19:00 to 21:00 12 September 2015. Only one brief period of easterly winds were observed, though the nearby Faith Ranch Airport (KFTN) recorded persistent easterly winds. A threshold of $NO_x/O_3 = 0.35$ was used to identify combustion plumes, and background concentrations for NO_x and CO_2 were assumed to be the minimum observed concentrations while $NO_x/O_3 > 0.35$. The third panel shows the enhancement above background for NO_x and CO_2.

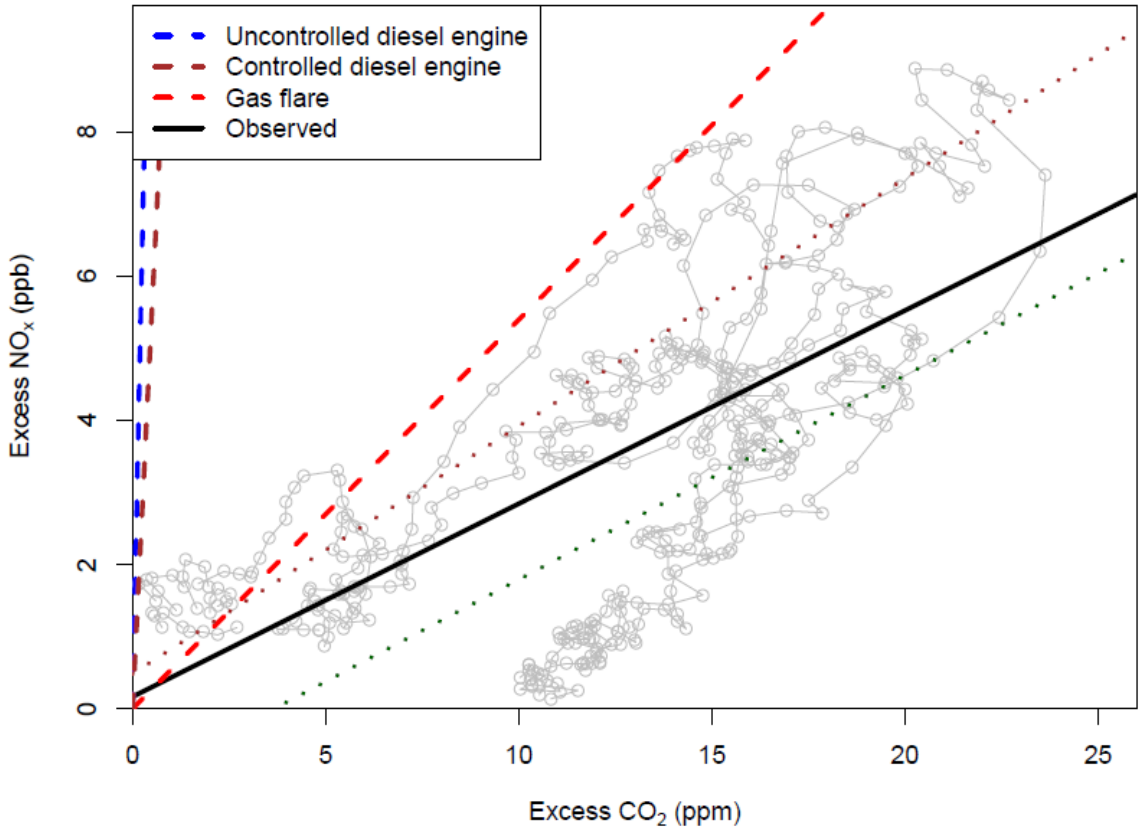

Figure 74: Enhancements of NO_x and CO_2 above background when NO_x/O_3 exceeded 0.35 for 19:00 to 21:00 12 September 2015. The line connecting the data points represents the timeline of the NO_x and CO_2 enhancements during the plume events. Note that the time period with low-CO_2 is not the same as the time period with low NO_x, suggesting a changing background while the plumes were passing. A linear fit for the data points prior to and including the peak CO_2 observation is shown in brown and a linear fit for the following subset of points is shown in green. The expected NO_x/CO_2 emission ratios are shown as dashed lines, with flaring in red (NO_x/CO_2 = 0.539), controlled diesel engines in brown (11.014), and large, uncontrolled diesel engines in blue (25.721).

first subset (R^2 = 0.83, $p < 0.001$) and 0.28 for the second subset (R^2 = 0.35, $p < 0.001$). These ratios are less than a factor of two smaller than the ratio expected for flaring and more than one order of magnitude smaller than the ratios for controlled and uncontrolled diesel engines.

Based on the ratios of NO_x/O_3, $\Delta NO_x/\Delta CO$, and $\Delta NO_x/\Delta CO_2$, this multiday event features several plumes that are associated with a relatively low-temperature combustion source, such as a flare. The two-hour episode detailed above includes several peaks in NO_x and CO_2 that are attributable to a similar source. The $\Delta NO_x/\Delta CO_2$ ratios for combustion plumes during the entire four-day period are a factor of five lower than the ratio of the emission factors from the US EPA AP-42 document (U.S. Environmental Protection Agency, 2016c) and the US EIA CO_2 emission factors for flares (U.S. Energy Information Administration, 2016), and ratios during the two-hour episode on 12 September were within a factor of two. Likewise, the $\Delta NO_x/\Delta CO$ ratio for the 10-13 September period was within a factor of two of the ratio for US EPA flaring emission factors.

The VIIRS Nightfire product indicated a nearby flaring detection in the early morning hours of 12 and 13 September, located less than 3 km to the southeast of the Shape Ranch trailer. Based on these flare detections, the wind direction, and the observed trace gas ratios, it is highly likely that the observed plumes presented in Figs. 73 and 74 above were associated with this particular flare, though this assumption cannot be verified. Nonetheless, this flare was used for a modeling exercise, which is described in the next section.

3.3.3.4. MODELED AIR QUALITY IMPACTS FROM FLARING

The $\Delta NO_x/\Delta CO$ and $\Delta NO_x/\Delta CO_2$ ratios in plumes within the observational dataset suggest that the EPA AP-42 flaring emission factors are accurate within a factor

of two, and that flaring plumes can lead to enhancements of criteria pollutants by several ppb at the Shape Ranch trailer. The air quality impacts associated with nearby flares were assessed using the TAMNROM-3D model. The model setup for the flaring episode is presented for the observed plume on the evening of 31 July 2015. The following night, two VIIRS Nightfire detections were located very close to a flare in the Elvidge et al. (2015) database, which was located 11.5 km NE of the Shape Ranch site. This flare was assumed to have been burning during the previous evening with an estimated flaring rate of 180,683.2 ft^3 hr^{-1} based on the radiant heat of the flare and assigning the AP-42 emission factors to the flare. The preliminary initial and boundary trace gas concentrations are defined following Table 7 and additional model parameters are shown in Table 9. The modeling domain was a 150 m horizontal resolution with the Shape Ranch site centered in the 45^{th} grid cell inward from the left and 10^{th} grid cell inward from the bottom (Fig. 75). The model was run from 18:00 to 19:30 LST using hourly NARR meteorology. The enhancement within the plume above background was assessed by running the model without the emission source and subtracting the modeled concentrations from the model run with the flare included.

Note that the 10 s meteorology observed at the Shape Ranch site shows a brief shift in wind directions – from ESE to N winds – while the plume was observed (Fig. 76). This wind shift was associated with outflow from a thunderstorm to the north, and suggests that the site would have been downwind of the detected flare, which we concluded was the source of the plume. However, this wind shift was not resolved in the NARR meteorology, so the modeled plume did not pass over the trailer. Furthermore,

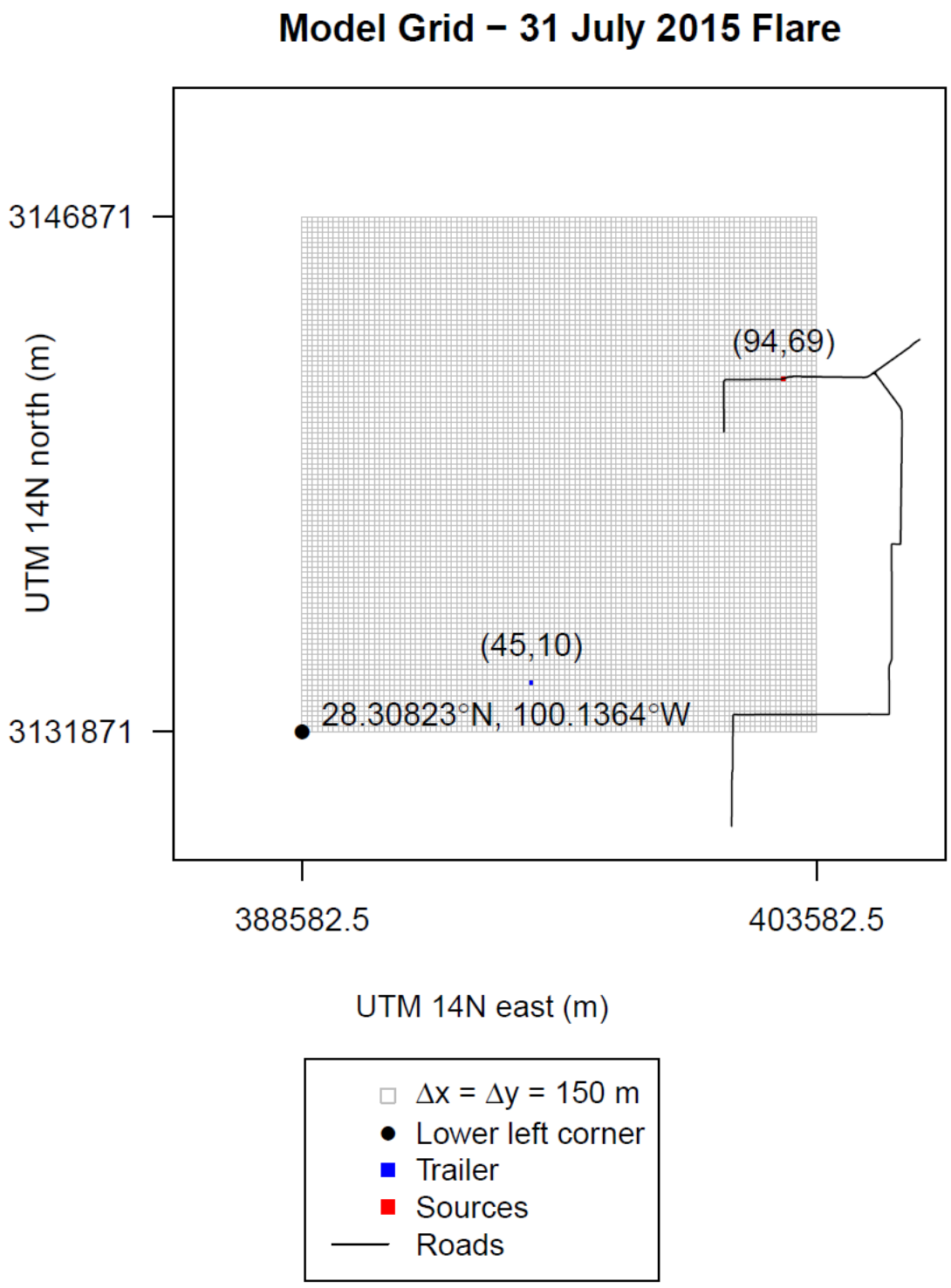

Figure 75: Model grid for the plume on the evening of July 31, 2015.

the thunderstorm outflow introduced a source of uncertainty in the transport of plumes from nearby sources, and their trace gas composition. Nonetheless, the in-plume ratios

Table 9: TAMNROM-3D model parameters for 31 July 2015.

Parameter	Prescribed condition
Mixing height	500 m
Land use type	Shrub and brush rangeland
Grid cell size	150 m × 150 m
Lower left corner of grid	28.30366 °N, 100.0732 °W
Trailer grid cell	Row 10, column 45
Flare grid cell	Row 69, column 94
Flare NO_x emissions	3.37×10^{-2} mol s^{-1}
Flare CO emissions	0.3 mol s^{-1}
Flare CO_2 emissions (modeled as tracer SF_6)	62.4 mol s^{-1}

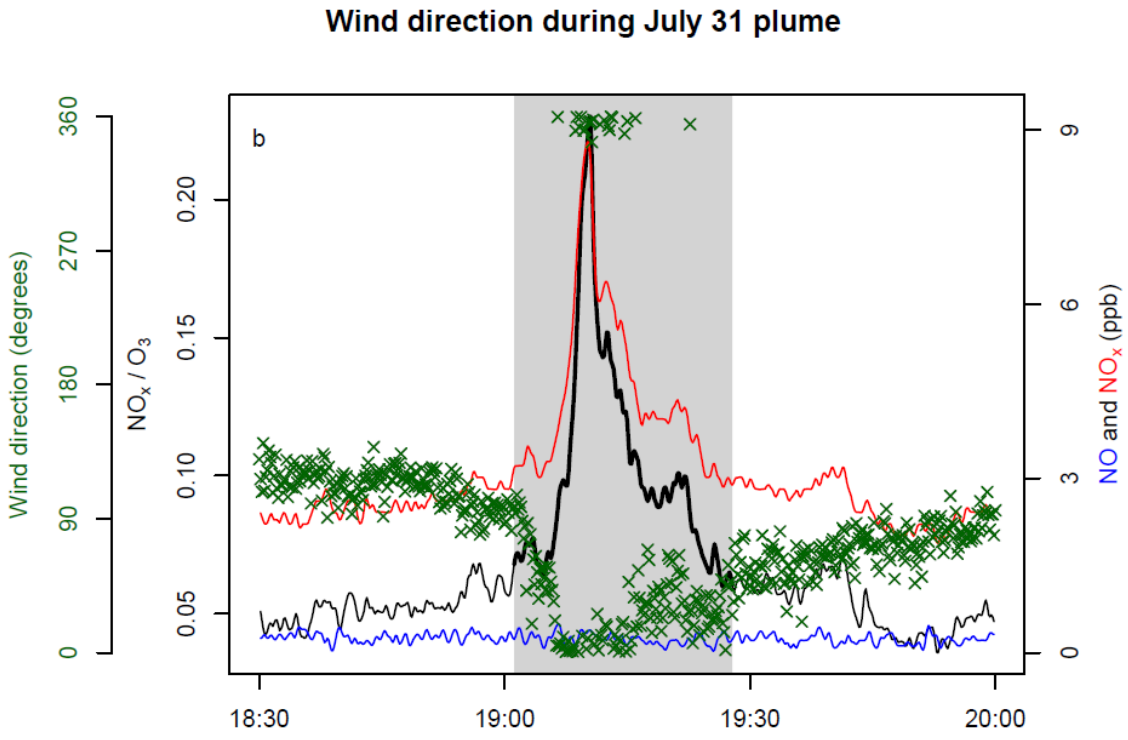

Figure 76: Wind directions during the 31 July plume shifted from SE to N during the plume's passage.

are compared here to our ambient measurements with the assumption that the actual plume did pass over the trailer under NE winds.

Figure 77 shows the enhancement of NO_2 above the background with a transect along the centerline of the plume. For this example, the mean concentration of NO_2 during the final 10 minutes of the model run (19:20 to 19:30 LST) is shown. Peak NO_2 concentrations greater than 10 ppb above background occurred immediately downwind of the plume before the concentration reduced towards the background. Enhancements of NO_2, O_3, CO, and CO_2 along the plume centerline are shown in Fig. 78. Enhancements immediately downwind of the plume reached above 200 ppb for CO, above 40 ppm for CO_2, and O_3 dropped by nearly 15 ppb. The $\Delta NO_x/\Delta CO$ and $\Delta NO_x/\Delta CO_2$ ratios are also shown along the plume centerline. The initial $\Delta NO_x/\Delta CO$ and $\Delta NO_x/\Delta CO_2$ ratios were equal to the ratios associated with the EPA AP-42 emission factors (U.S. Environmental Protection Agency, 2016c) which were used to define the flaring emissions. Both of the ratios decreased as the plume was transported downwind, however only by approximately 10% after more than 10 km of transport. This decrease was attributed to NO_x loss from both chemistry and surface deposition. The relative stability of the emission ratios implies that the ratios of trace gases observed at Shape Ranch are reflective of the emission ratios for nearby sources as they are minimally affected by chemistry and deposition.

While the NARR meteorology did not capture the directional wind shift, Fig. 77 also shows a transect across the plume at a distance of 11.5 km downwind of the source – the same distance between the source and the trailer. The enhancements above

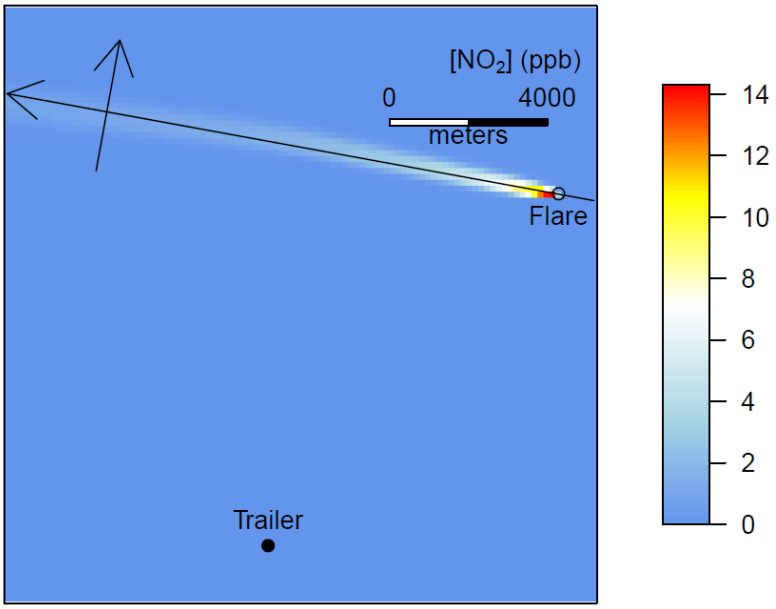

Figure 77: Mean NO_2 enhancements above background during the final 10 min of the model run (19:20 to 19:30 LST), with transects along and across the plume centerline.

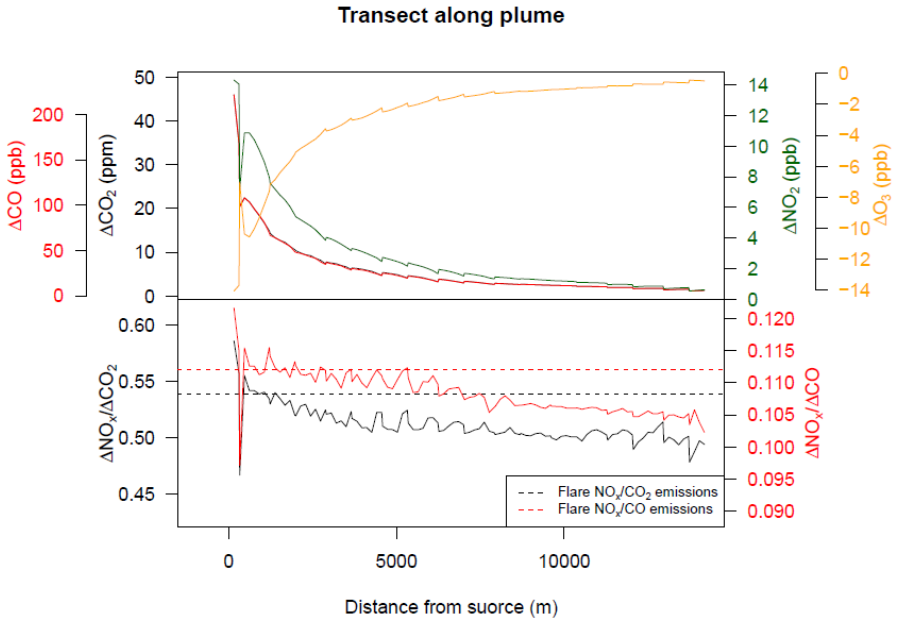

Figure 78: Changes in concentrations along the plume centerline above or below background during the 31 July modeling exercise. The lines for CO and CO_2 are nearly identical. The ratio of the trace gas enhancements are shown for NO_x/CO and NO_x/CO_2, with the emission ratios from the EPA's AP-42 document shown with dashed lines (U.S. Environmental Protection Agency, 2016c).

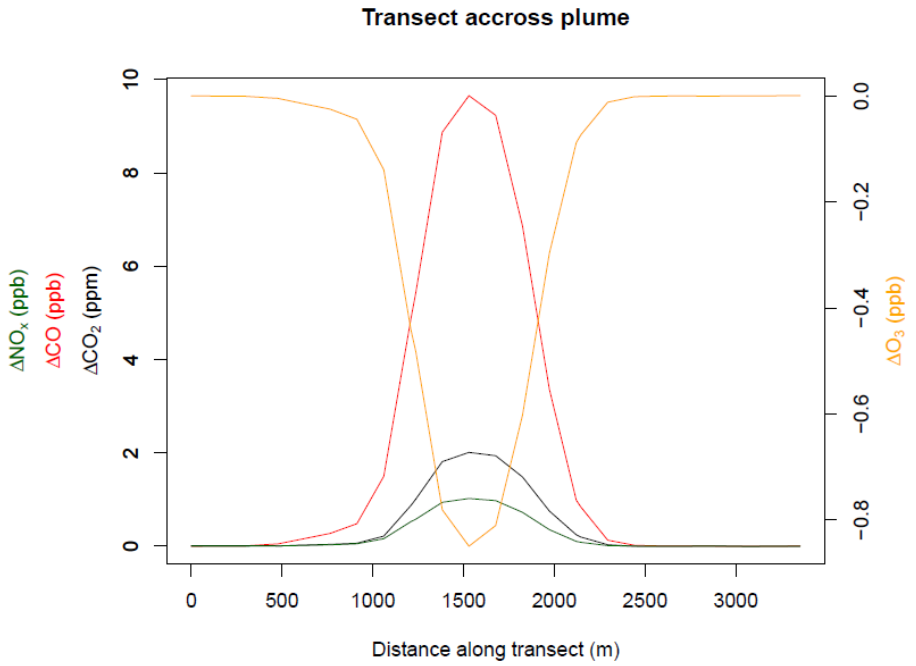

Figure 79: Changes in concentrations across the plume at 11.5 km downwind of the source.

Table 10: Peak enhancements above (or below) background for the observed and modeled plumes on the evening of 31 July 2015.

Species	ΔCO_2 (ppm)	ΔCO (ppb)	ΔNO_x (ppb)	ΔO_3 (ppb)
Obs.	+5.3	< LOD	+6.0	-7.3
Model	+2.0	+9.7	+1.0	-0.85

background along the transect across the plume are shown in Fig. 79 and are presented in Table 10, along with the enhancements within the observed plume at the Shape Ranch trailer.

Emissions of CO_2 are associated with the amount of fuel being burned as even inefficient combustion (i.e. 80%) will have a relatively small change in CO_2 emissions. Thus, the modeled CO_2 enhancement of 2 ppm suggests that either 1) the observed

plume was less diluted than the model plume, and/or 2) the actual emission source was emitting more CO_2 than the modeled flare, and was therefore burning more fuel. Consistent with the latter, the results in Table 10 show that the observed changes were six to ten times higher than the modeled changes for both NO_x and O_3, indicating that the NO_x emissions were higher than what was modeled, and the subsequent O_3 titration resulted in a larger decrease. In addition, the observed $\Delta NO_x/\Delta CO_2$ ratio was higher than the EPA AP-42 emission factors, suggesting that the NO_x emission factor for this source was higher than the EPA's emission factor. However, the influence of the nearby thunderstorm on the transport and dilution of the plume, as well as the potential temporary changes in the background concentrations within the thunderstorm outflow, introduce uncertainties into this analysis.

Another plume on the evening of 12 September 2015 was not influenced by nearby thunderstorms or other meteorological phenomena. The VIIRS Nightfire product detected two flares during the early morning hours of 12 and 13 September 2015, respectively, that were approximately 2.2 km to the southeast of the trailer (Fig. 80). These detections were both matched to a flare in the Elvidge flaring database (Elvidge et al., 2015) located at 28.30952 °N, 100.0505 °W, with an average temperature of 1,860 K and an average natural gas flaring rate of 122,065.2 $ft^3\ hr^{-1}$. It is possible that this flare was burning on the day of 12 September, between these two nighttime detections. The following modeling exercise simulates a plume from this flare from 19:00 to 21:00 LST, assuming a meteorological profile interpolated temporally from the NARR and modeling parameters shown in Table 11. The model grid, shown in Fig. 81, had a horizontal

Table 11: TAMNROM-3D model parameters for 12 September 2015. See Table 7 for the initial and boundary conditions for trace gases.

Parameter	Prescribed condition
Mixing height	500 m
Land use type	Shrub and brush rangeland
Grid cell size	25 m × 25 m
Lower left corner of grid	28.30366 °N, 100.0732 °W
Trailer grid cell	Row 80, column 20
Flare grid cell	Row 26, column 90
Flare NO_x emissions	2.27×10^{-2} mol s^{-1}
Flare CO emissions	0.203 mol s^{-1}
Flare CO_2 emissions (modeled as tracer SF_6)	42.2 mol s^{-1}

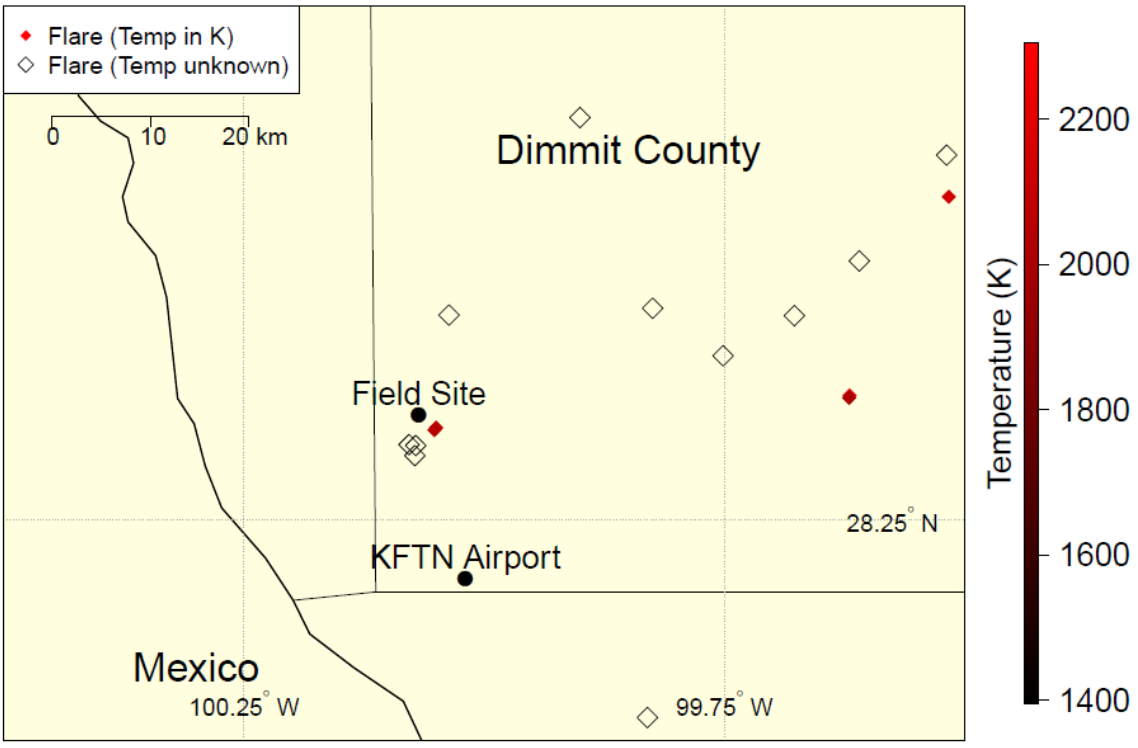

Figure 80: VIIRS Nightfire flaring detections during the early morning hours of 10 through 13 September 2015. Two flares were identified approximately 2.2 km southeast of the field site, with temperatures of 1,843 K on 12 September and 1,807 K on 13 September 2015.

Table 12: Meteorology at the Faith Ranch Airport (KFTN, Fig. 61) from 18:55 to 21:15 LST on 12 September 2015.

Time (LST, HH:MM)	Temperature (° F)	Dew point (° F)	Wind direction (°)	Wind speed (m s^{-1})
18:55	84	63	100 (ESE)	2.6
19:15	84	63	90 (E)	2.6
19:35	82	64	90 (E)	2.1
19:55	82	64	100 (ESE)	2.1
20:15	81	64	100 (ESE)	2.6
20:35	81	66	110 (ESE)	2.1
20:55	81	64	130 (SE)	2.6
21:15	81	66	150 (SE)	2.1

resolution of 25 m × 25 m. Again, there is no independent confirmation that this flare was responsible for the observed plumes on the evening of 12 September 2015, so this modeling exercise should be considered hypothetical. In the absence of non-zero wind observations at the Shape Ranch trailer, data from Faith Ranch Airport (KFTN, Fig. 80) provides insight into surface winds during the passage of the plume (Table 12). With persistent winds from the east to southeast at 2-3 m s^{-1} at 10 m agl, the flare identified in the Elvidge database is located upwind of the Shape Ranch trailer.

Figure 82 shows mean NO_2 enhancements above background during the final 10 min of the model run (20:50 to 21:00 LST) and transects along and across the plume centerline. Note that the plume was transported to the west-northwest, though the winds at Faith Ranch Airport suggest that an actual plume would have traveled to the northwest towards the Shape Ranch trailer (Table 12). The enhancements of NO_x, CO, CO_2, and O_3 above background along the transect are shown in Fig. 83, along with the enhancement ratios of $\Delta NO_x/\Delta CO$ and $\Delta NO_x/\Delta CO_2$. The maximum CO_2 enhancement was nearly 300 ppm above background and CO exceeded 1,440 ppb above background. While NO_2

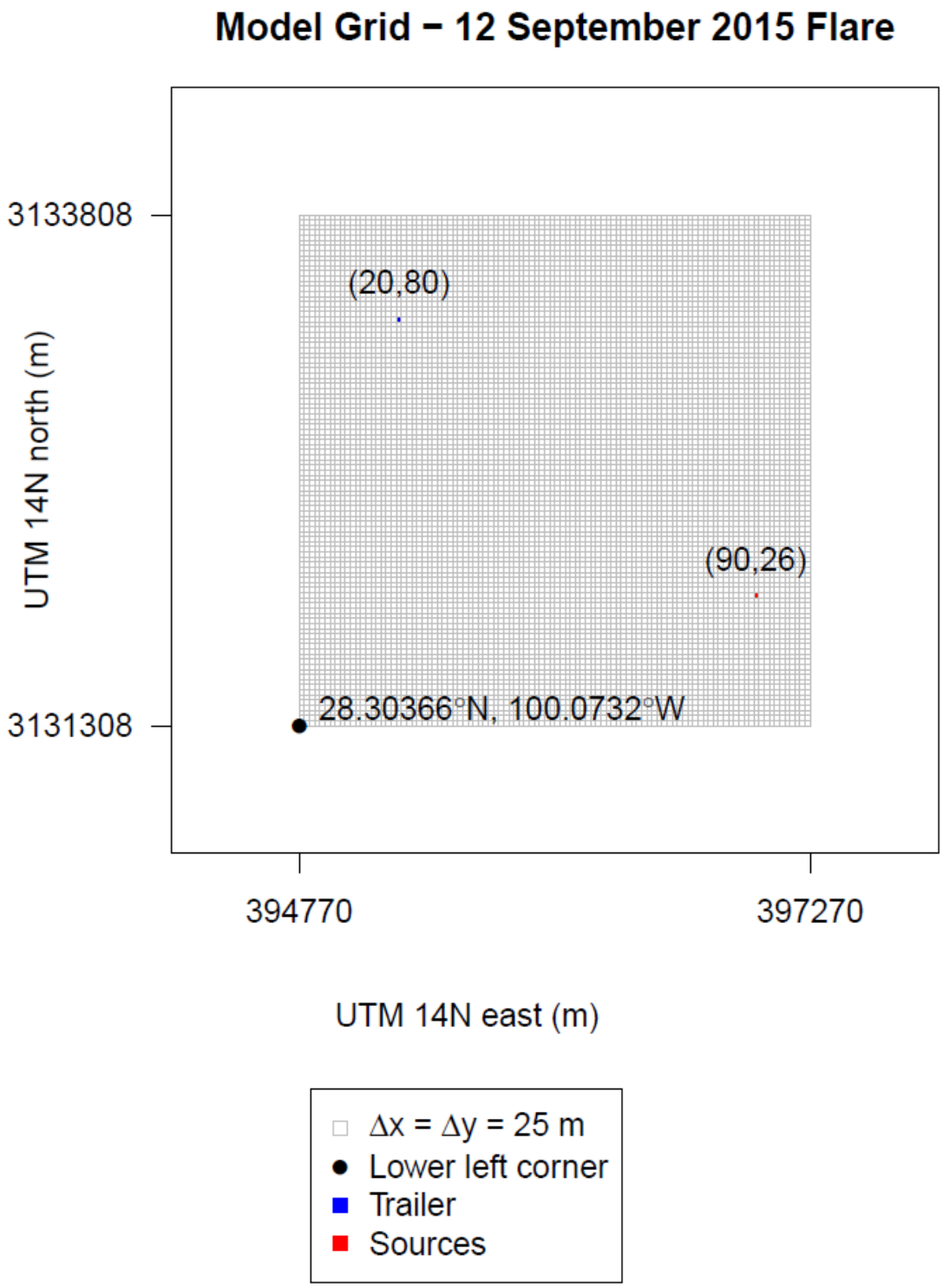

Figure 81: Model grid for the plume on the evening of 12 September 2015.

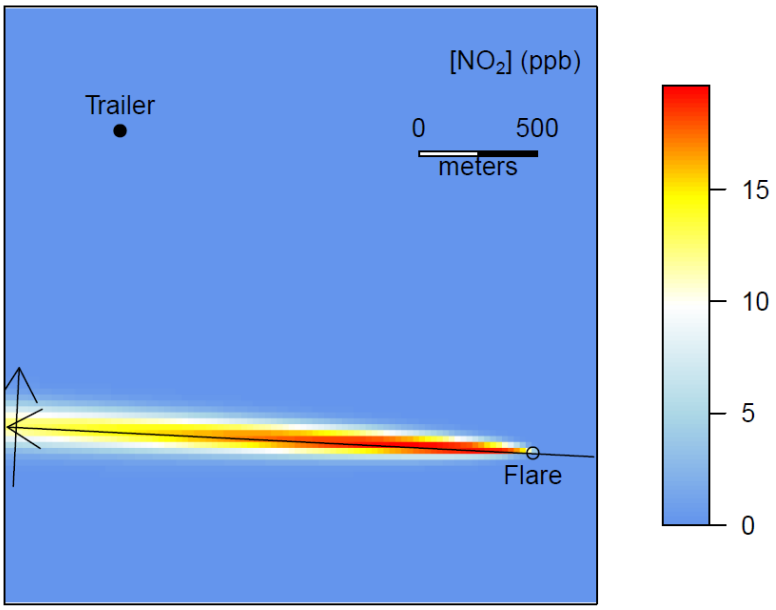

Figure 82: Mean NO_2 enhancements above background during the final 10 min of the model run (20:50 to 21:00 LST), with transects along and across the plume centerline.

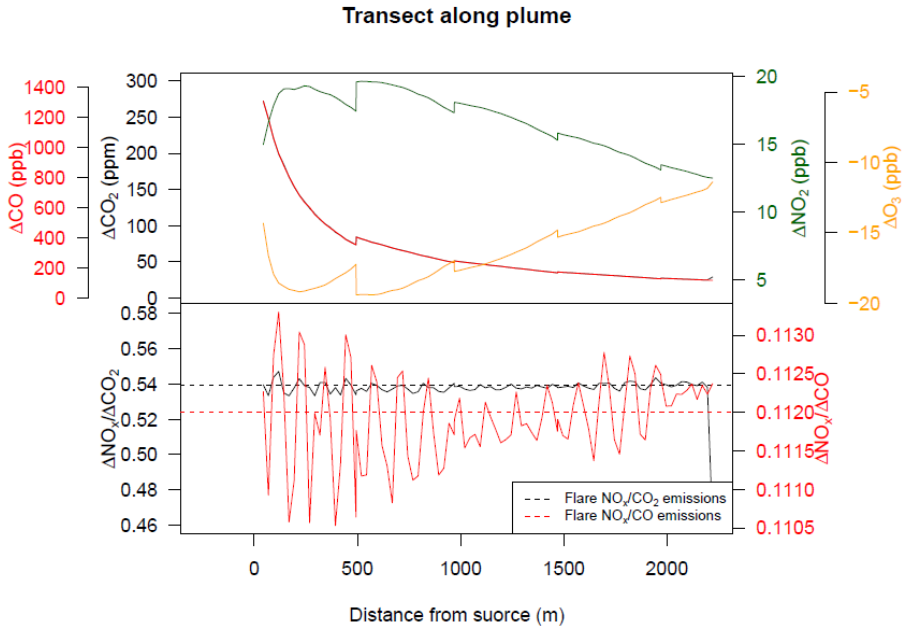

Figure 83: Changes in concentrations along the plume centerline above or below background during the 12 September modeling exercise. The lines for CO and CO_2 are nearly identical. The ratio of the trace gas enhancements are shown for NO_x/CO and NO_x/CO_2, with the ratios from the EPA's AP-42 document shown with dashed lines.

reached nearly 20 ppb above background, total NO_x exceeded 160 ppb immediately downwind of the flare (not shown). The O_3 minimum was more than 19 ppb below background. The $\Delta NO_x/\Delta CO$ and $\Delta NO_x/\Delta CO_2$ ratios exhibited some noise but showed no trend over the roughly 2 km length of the transect, thereby retaining the ratio prescribed in the emissions. The sudden drop in NO_x/CO_2 at the right-hand side of Fig. 84 is a boundary effect.

Figure 82 also shows a transect across the plume at a distance of approximately 2.2 km downwind from the source – the same distance between the source and the Shape Ranch trailer. Maximum mixing ratios above background along the downwind transect were approximately 25 ppm for CO_2, 120 ppb for CO, 13 ppb for NO_x (with less than 1 ppb of NO), while O_3 reached 12 ppb below background (Fig. 84). Table 13 compares

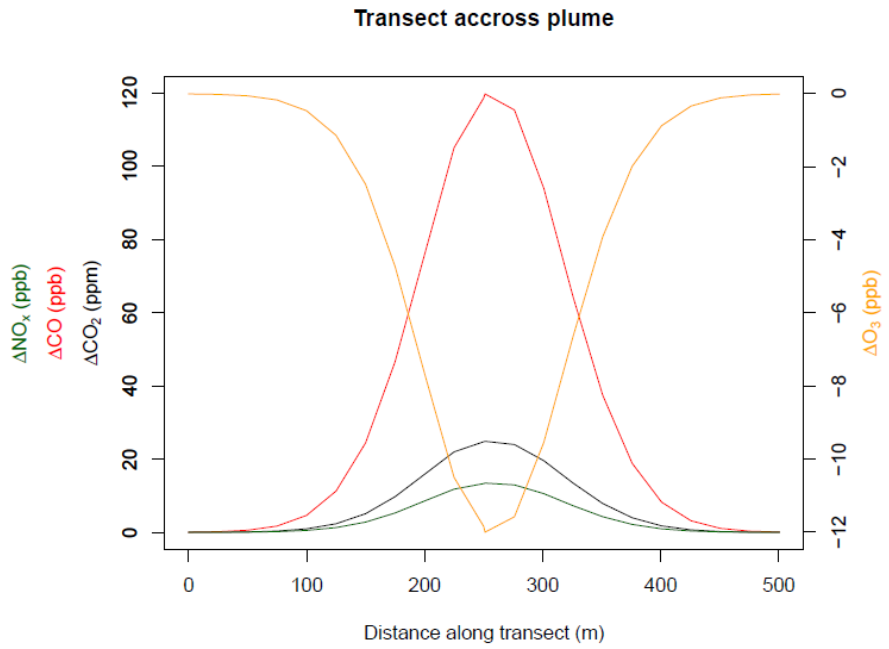

Figure 84: Changes in concentrations across the plume at 2.2 km downwind of the source.

Table 13: Peak enhancements above (or below) background for the observed and modeled plumes on the evening of 12 September 2015.

Species	ΔCO_2 (ppm)	ΔCO (ppb)	ΔNO_x (ppb)	ΔO_3 (ppb)
Obs.	+23.6	+56.3	+8.9	-16.5
Model	+24.9	+119.7	+13.4	-12.0

these values to the peak observed trace gas enhancements at the Shape Ranch trailer between 19:00 to 21:00 LST 12 September 2015. Note that the background levels for CO_2, CO, and NO_x were assumed to be the minimum measured while NO_x/O_3 exceeded 0.35, while background O_3 was assumed to be the maximum observed value during the same time frame. As previously discussed in section 3.3.3.1, it is possible that other sources, including ecosystem respiration, may have caused an increase in CO_2 concentrations during this hour. Other sources may have also impacted CO and NO_x concentrations, and O_3 likely decreased after sunset due to reactions with background NO and NO from other sources. Nonetheless, the CO_2 enhancement above background at Shape Ranch was only 1.3 ppm lower than the peak within the modeled plume, which suggests that the flared natural gas volume used to generate model emissions was accurate. However, observed CO enhancements were less than half of the modeled enhancements, and observed NO_x enhancements were approximately two-thirds as large as the modeled enhancements. However, the measured decrease in O_3 exceeded the modeled decrease, though this may have been caused by decreasing background O_3 over the two-hour measurement period in question. The $\Delta NO_x/\Delta CO_2$ ratio in the observed combustion plume was lower than the modeled plume with emissions based on the EPA

AP-42 factors, suggesting that, given the stability of the CO_2 emission factor, the NO_x emission factor for this source was again lower than the EPA AP-42 NO_x emission factor for flaring.

3.4 CONCLUSIONS

The Shape Ranch dataset provided critical insight into the role of oil and gas activities in local air quality within a rural part of the Eagle Ford Shale. Output from a LS-NMF model suggested that oil and gas operations dominated trace gas variability at the site. High trace gas concentrations appeared episodically during the measurement campaign, leading to skewed distributions of hydrocarbon concentrations. An analysis of trace gas enhancements above background during ozone titration events representing combustion plumes reveals a range of $\Delta NO_x/\Delta CO$ and $\Delta NO_x/\Delta CO_2$ ratios, including high NO_x events and high CO and CO_2 events. The observed spread in these trace gas ratios suggests that there are a number of combustion source types that contribute to the observed enhancements above background, including the occasional high-temperature combustion source (i.e. internal combustion engines) but mostly low-temperature sources, such as flares. An analysis of 10 s data revealed that most of the high NO_x/O_3 events were associated with low-temperature combustion sources, with the median $\Delta NO_x/\Delta CO_2$ ratio close to the expected ratio calculated from EPA and EIA data, though the spread suggests that these events have $\Delta NO_x/\Delta CO_2$ ratios that may vary by more than a factor of 5. Other emissions sources, including ecosystem respiration, probably

contribute small enhancements above background during high NO_x/O_3 events, and it is difficult to remove this influence in an objective analysis.

Several discrete trace gas plumes were observed and attributed to combustion sources using NO_x/O_3 ratios. During a period from 31 July to 1 August 2015, when several plumes were observed leading up to a high-ozone day on 1 August, the general $\Delta NO_x/\Delta CO$ ratios matched the ratio expected for flaring based on AP-42 emission factors. A brief but distinct plume on the evening of 31 July was attributed to a nearby flare based on ratios of 10 s $\Delta NO_x/\Delta CO_2$ observations. However, this plume was associated with a wind shift within thunderstorm outflow, and a different composition of this air mass may add uncertainty to the enhancement of NO_x, CO, and CO_2 within the plume. Another, multi-day event with several distinct plumes occurred from 10 to 13 September 2015. Again, the $\Delta NO_x/\Delta CO$ and $\Delta NO_x/\Delta CO_2$ indicated a low-temperature combustion process as the source for observed trace gas enhancements during episodes of elevated NO_x/O_3 ratios. A detailed examination of plumes on the evening of 12 September 2015 using 10 s data indicated flaring as the probable source, though there exists some uncertainty in the background concentrations during that time period as well.

The 31 July plume and 12 September plume were both modeled using the TAMNROM-3D model. While the employed NARR meteorology failed to capture a wind shift on 31 July associated with a thunderstorm, and a transition from easterly to southeasterly winds on 12 September, in-plume trace gas ratios were compared to the observed plumes at the Shape Ranch site. Location and presence of the flares in both modeling exercises were assumed based on VIIRS Nightfire data, and the flow rate,

heating rate, and emission factors of the flares were prescribed using the Elvidge flaring database (Elvidge et al., 2015) and EPA AP-42 emission factors (U.S. Environmental Protection Agency, 2016c). Thus, the modeling exercises should not be interpreted as a confirmation of the operating parameters of the particular flare. Instead, the modeled flares demonstrate the *potential* impacts that a small flare may have on a local scale in a rural oil and gas field using parameters derived from the best-available input data. Nonetheless, these modeling exercises demonstrated that the assumed emissions produce in-plume trace gas enhancements that are generally within one order of magnitude of observed plume enhancements, with the modeled CO_2 on 12 September agreeing with the observations within 10%. Furthermore, the observed trace gas enhancement ratios within the modeled plumes decreased only by approximately 10% on 31 July, even after more than 10 km of transport, while the ratios remained stable after 2 km transport on 12 September. This suggests that atmospheric chemistry likely has a minimal effect on the ratios of trace gas emissions for nocturnal measurements that are made within 10 km of a plume. The modeling exercise on 12 September 2015 also demonstrated the potential short-term air quality impacts immediately downwind of flares, with NO_x reaching 160 ppb (the EPA regulated pollutant NO_2 reached 20 ppb above background). Many of the local flares are considered *de minimis* sources for permitting purposes, so their activity data and emissions are not quantified on a site-by-site basis. Therefore, the local-to-regional impacts associated with many flares remain uncertain. Scalable photochemical grid models may serve as a valuable tool to address this question.

4. DISCUSSION AND CONCLUSIONS

The Eagle Ford Shale continues to be one of the most prolific oil and gas producing regions in the US, but uncertainties in emission estimates of both VOCs and NO_x prevent an accurate estimate of the regional air quality impacts associated with oil and gas production in the area. A lack of ambient air quality monitoring means that few data exist to assess emissions and the resulting exposure to pollutants of residents and communities within the shale area (*cf.* to Anejionu et al., 2015 for similar aspects in Nigeria as related to flaring).

A mass balance approach was used to estimate emissions of alkanes from a region encompassing the central part of the Eagle Ford Shale using TCEQ monitoring sites in Corpus Christi and Floresville, which are upwind and downwind of the shale, respectively, when winds are from the south to southeast. Using 2013-2014 data, the emissions of ethane, propane, and butanes totaled 200 (IQR of 139 to 341) $\times 10^3$ kg day^{-1} – a factor of two higher than existing estimates for VOC emissions in the central Eagle Ford Shale for 2012. Based on observed alkane enhancement ratios, liquid storage tanks contributed an estimated 17% of methane, 55% of ethane, 82% of propane, 90% of *n*-butane, and 83% of isobutane. Total methane emissions accounted for 1.0% of produced natural gas, with uncertainty bounds of 0.7 to 1.6% overlapping the current EPA estimate for nationwide emissions. Results from the SONGNEX campaign in 2015 (Peischl et al., 2018) suggest that our relative emission rate estimate is biased low, with upwind areas having a smaller methane enhancement across the shale than other portions of the shale, both towards the east and west. Hence, the median estimate of 1.0% is

considered to be conservative, and increased monitoring of both methane and VOCs throughout the region would yield a more thorough understanding of methane and VOC emissions.

Ambient air quality was studied in the sparsely populated western portion of the Eagle Ford Shale, where no state-run air quality monitors exist. Trace gases and meteorology were measured at a trailer on a working bison ranch in southwestern Dimmit County from April to November of 2015. High alkane abundances indicated natural gas production as a dominant emission source, which was confirmed by a nonnegative matrix factorization analysis. Combustion was also identified as a local emission source, though related concentrations of aromatics, alkenes, CO, and NO_x were generally low. Transport of continental air was associated with CO, O_3, isoprene, and short-chain, longer lived alkanes. Daytime boundary layer O_3 production was generally limited by low background NO_x mixing ratios, and a lack of NO_y data prevented an estimate of ozone production efficiency.

Analyzed NO_x/CO_2 ratios during episodes of high NO_x/O_3, dominantly occurring at night and indicative of both discrete combustion plumes and accumulated emissions from combustion sources, suggest that low-temperature combustion is very often responsible for such plumes at Shape Ranch. While flaring is the most likely source for many of these events, the NO_x/CO_2 ratio exhibited variability spanning more than an order of magnitude, suggesting that low-temperature combustion sources have widely varying emission factors and/or other sources of NO_x and CO_2 interfere to introduce larger variability than should be expected in such combustion plumes.

One day during the 2015 filed measurements had a maximum 8-h ozone mixing ratio above the EPA NAAQS of 70 ppb. This day occurred during a multiple-day sequence of apparent combustion emissions leading to high nighttime NO_x and CO_2 at the field site, with O_3 dropping into the single digits in the presence of high NO_x. The ratio of NO_x/CO enhancements was within a factor of two of the expected ratio for flaring emissions. A scalable, photochemical transport model (TAMNROM-3D) was used to model emissions from a flare during the previous evening, and confirmed that even a distant flare (more than 10 km away) can produce a noticeable enhancement of NO_x and CO_2 with a decrease in O_3 in the absence of sunlight, with NO_x/CO and NO_x/CO_2 ratios varying by less than 10% during transport. The flaring emissions were estimated using daily VIIRS Nightfire products cross-referenced with a database of flares produced from an analysis of the same dataset (Elvidge et al., 2015). While a nearby thunderstorm introduced uncertainty into the transport and chemistry of this particular plume, a second multi-day episode with apparent combustion plumes was identified from 10-13 September 2015, during which the excess NO_x/CO indicated low-temperature combustion as an emission source. Another combustion plume on the evening of 12 September was selected for modeling, assuming a detected flare approximately 2 km away was the source. The NO_x/CO and NO_x/CO_2 ratios remained nearly constant during transport, and the modeled CO_2 enhancement 2 km downwind of the source was close to the observed enhancement at the field site. The modeled enhancement ratio of NO_x/CO_2 was within a factor of two of the observations, with the combined results suggesting that this flare was indeed the source of the plume, and that

its emissions reasonably followed published emission factors. The model revealed that close to the flare, NO_x probably exceeded 160 ppb, raising questions about acute air quality impacts associated with high NO_2.

In summary, these results raise a number of questions that challenge current regulations and warrant further study:

1. The VOC emission estimate from Sect. 2 suggests that current emissions inventories underestimate VOC emissions in the Eagle Ford Shale by approximately a factor of two. This finding suggests that previous modeling studies that utilize emissions inventories, such as that of Pacsi et al. (2015), may be underestimating the regional ozone impacts associated with oil and gas activities, especially in light of strongly varying NOx emission from flares found in this study. Giving the ratio of alkanes in the observed enhancements across the shale, emissions from liquid storage tanks and other long-chain alkane emitting sources should be studied in further detail to update the current understanding of VOC emissions within the shale, and identify component- and process-based measures to reduce emissions.
2. Modeled emissions from flares using VIIRS Nightfire detections and the Elvidge et al. (2015) data set demonstrate the potential for significant local air quality impacts from small flares, which are often considered to be *de minimis* emissions sources and are permitted by rule. Even if the existing flaring estimates for the Eagle Ford Shale were improved upon, the emission factors for flares are highly uncertain and probably vary greatly between individual flares. While the

comparison of our dataset and modeling exercises suggests that the ratio of NO_x/CO and NO_x/CO_2 flaring factors are within a factor of two of the expected emission ratios, fence-line measurements of upstream flares in oil and gas fields with high-precision instrumentation would provide a better estimate of the flaring emission factors, especially if the flaring rate and gas composition are known.

3. The Elvidge et al. (2015) database provides a thorough yet uncertain estimate of flaring activity within the Eagle Ford Shale, among other regions with dense flaring activity. This database could be used to parameterize flaring emissions on an oil and gas basin-wide scale, with field measurements, aircraft campaigns, and remote sensing data informing and validating model estimates. Emissions of NO_x may be particularly important for flaring in rural oil and gas basins in which O_3 is often NO_x limited (Parrish et al., 2017).

Further research is needed to develop a more accurate understanding of the climate and air quality impacts associated with oil and gas. However, this work highlights the need for more comprehensive monitoring of air quality and climate pollutants within oil and gas fields – especially regions with activities that are poorly quantified, such as flaring within the Eagle Ford Shale. Existing VOC emissions inventories need to be better validated, especially with respect to emissions factors from liquid storage tanks and other processes that handle liquid hydrocarbons. Emissions from flares can be improved by studying emission factors associated with these relatively small diffusion flares in the field. Closely monitoring and reporting flaring activity data could improve inventories, which in turn would more accurately reflect real-world

flaring in liquids-rich shale plays such as the Eagle Ford Shale, the Permian, and the Bakken shale.

REFERENCES

Abdel-Aal, H. K., Aggour, M., & Fahim, M. A. (2003). *Petroleum and gas field processing*. New York: Marcel Dekker.

Ahmadi, M., & John, K. (2015). Statistical evaluation of the impact of shale gas activities on ozone pollution in North Texas. *Science of The Total Environment*, *536*, 457–467. https://doi.org/10.1016/j.scitotenv.2015.06.114

Ahmadov, R., McKeen, S., Trainer, M., Banta, R., Brewer, A., Brown, S., et al. (2015). Understanding high wintertime ozone pollution events in an oil- and natural gas-producing region of the western US. *Atmospheric Chemistry and Physics*, *15*(1), 411–429. https://doi.org/10.5194/acp-15-411-2015

Alamo Area Council of Governments (AACOG). (2013). *Development of the Extended June 2006 Photochemical Modeling Episode* (Technical Report) (p. 261). San Antonio, Texas. Retrieved from http://www.aacog.com/DocumentCenter/View/19262

Alamo Area Council of Governments (AACOG). (2015). Cities and Counties. Retrieved from http://tx-aacog.civicplus.com/index.aspx?NID=192

Allen, D. T., Torres, V. M., Thomas, J., Sullivan, D. W., Harrison, M., Hendler, A., et al. (2013). Measurements of methane emissions at natural gas production sites in the United States. *Proceedings of the National Academy of Sciences*, *110*(44), 17768–17773. https://doi.org/10.1073/pnas.1304880110

Alvarez, R. A., Pacala, S. W., Winebrake, J. J., Chameides, W. L., & Hamburg, S. P. (2012). Greater focus needed on methane leakage from natural gas infrastructure.

Proceedings of the National Academy of Sciences, *109*(17), 6435–6440. https://doi.org/10.1073/pnas.1202407109

Alvarez, R. A., Zavala-Araiza, D., Lyon, D. R., Allen, D. T., Barkley, Z. R., Brandt, A. R., et al. (2018). Assessment of methane emissions from the U.S. oil and gas supply chain. *Science*. https://doi.org/10.1126/science.aar7204

Anejionu, O. C. D., Whyatt, J. D., Blackburn, G. A., & Price, C. S. (2015). Contributions of gas flaring to a global air pollution hotspot: Spatial and temporal variations, impacts and alleviation. *Atmospheric Environment*, *118*, 184–193. https://doi.org/10.1016/j.atmosenv.2015.08.006

Arguez, A., Durre, I., Applequist, S., Squires, M., Vose, R., Yin, X., & Bilotta, R. (2010). U.S. Climate Normals Product Suite (1981-2010) [Data set]. NOAA National Climatic Data Center. https://doi.org/10.7289/V5PN93JP

Atkinson, R., & Arey, J. (2003). Atmospheric Degradation of Volatile Organic Compounds. *Chemical Reviews*, *103*(12), 4605–4638. https://doi.org/10.1021/cr0206420

Bahadar, H., Mostafalou, S., & Abdollahi, M. (2014). Current understandings and perspectives on non-cancer health effects of benzene: A global concern. *Toxicology and Applied Pharmacology*, *276*(2), 83–94. https://doi.org/10.1016/j.taap.2014.02.012

Baker, A. K., Beyersdorf, A. J., Doezema, L. A., Katzenstein, A., Meinardi, S., Simpson, I. J., et al. (2008). Measurements of nonmethane hydrocarbons in 28 United

States cities. *Atmospheric Environment*, *42*(1), 170–182. https://doi.org/10.1016/j.atmosenv.2007.09.007

Benjamin, M. T., Sudol, M., Bloch, L., & Winer, A. M. (1996). Low-emitting urban forests: A taxonomic methodology for assigning isoprene and monoterpene emission rates. *Atmospheric Environment*, *30*(9), 1437–1452. https://doi.org/10.1016/1352-2310(95)00439-4

Bonney, J. (2014). Port Freeport's Chemical Reaction. *Journal of Commerce (15307557)*, *15*(12), 38.

Brantley, H. L., Thoma, E. D., Squier, W. C., Guven, B. B., & Lyon, D. (2014). Assessment of Methane Emissions from Oil and Gas Production Pads using Mobile Measurements. *Environmental Science & Technology*, *48*(24), 14508–14515. https://doi.org/10.1021/es503070q

Brasseur, G., & Jacob, D. J. (2017). *Modeling of atmospheric chemistry*. Cambridge: Cambridge University Press.

Brunet, J.-P., Tamayo, P., Golub, T. R., & Mesirov, J. P. (2004). Metagenes and molecular pattern discovery using matrix factorization. *Proceedings of the National Academy of Sciences*, *101*(12), 4164–4169. https://doi.org/10.1073/pnas.0308531101

Caulton, D. R., Shepson, P. B., Santoro, R. L., Sparks, J. P., Howarth, R. W., Ingraffea, A. R., et al. (2014). Toward a better understanding and quantification of methane emissions from shale gas development. *Proceedings of the National Academy of Sciences*, *111*(17), 6237–6242. https://doi.org/10.1073/pnas.1316546111

Chauhan, A. J., Krishna, M. T., Frew, A. J., & Holgate, S. T. (1998). Exposure to nitrogen dioxide (NO_2) and respiratory disease risk. *Reviews on Environmental Health*, *13*(1–2), 73–90.

Cheadle, L. C., Oltmans, S. J., Petron, G., Schnell, R. C., Mattson, E. J., Herndon, S. C., et al. (2017). Surface ozone in the Colorado northern Front Range and the influence of oil and gas development during FRAPPE/DISCOVER-AQ in summer 2014. *Elementa: Science of the Anthropocene*, *5*(0), 61. https://doi.org/10.1525/elementa.254

Chin, M., Jacob, D. J., Munger, J. W., Parrish, D. D., & Doddridge, B. G. (1994). Relationship of ozone and carbon monoxide over North America. *Journal of Geophysical Research: Atmospheres*, *99*(D7), 14565–14573. https://doi.org/10.1029/94JD00907

Crutzen, P. J., Lawrence, M. G., & Pöschl, U. (1999). On the background photochemistry of tropospheric ozone. *Tellus B: Chemical and Physical Meteorology*, *51*(1), 123–146. https://doi.org/10.3402/tellusb.v51i1.16264

Duncan, B. N., Lamsal, L. N., Thompson, A. M., Yoshida, Y., Lu, Z., Streets, D. G., et al. (2016). A space-based, high-resolution view of notable changes in urban NO_x pollution around the world (2005–2014). *Journal of Geophysical Research: Atmospheres*, 2015JD024121. https://doi.org/10.1002/2015JD024121

Dunn, O. J. (1964). Multiple Comparisons Using Rank Sums. *Technometrics*, *6*(3), 241–252. https://doi.org/10.1080/00401706.1964.10490181

Elvidge, C., Zhizhin, M., Hsu, F.-C., & Baugh, K. (2013). VIIRS Nightfire: Satellite Pyrometry at Night. *Remote Sensing*, *5*(9), 4423–4449. https://doi.org/10.3390/rs5094423

Elvidge, C., Zhizhin, M., Baugh, K., Hsu, F.-C., & Ghosh, T. (2015). Methods for Global Survey of Natural Gas Flaring from Visible Infrared Imaging Radiometer Suite Data. *Energies*, *9*(1), 14. https://doi.org/10.3390/en9010014

ENVIRON International Corporation. (2010). *Upstream Oil and Gas Tank Emission Measurements: TCEQ Project 2010 - 39* (No. 06-17477X). Novato, CA. Retrieved from https://www.tceq.texas.gov/assets/public/implementation/air/am/contracts/reports/ei/5820784004FY1025-20100830-environ-Oil_Gas_Tank_Emission_Measurements.pdf

Field, R. A., Soltis, J., & Murphy, S. (2014). Air quality concerns of unconventional oil and natural gas production. *Environmental Science: Processes & Impacts*, *16*(5), 954. https://doi.org/10.1039/c4em00081a

Flagan, R. C., & Seinfeld, J. H. (1988). *Fundamentals of air pollution engineering*. Englewood Cliffs, N.J: Prentice Hall.

Franco, B., Mahieu, E., Emmons, L. K., Tzompa-Sosa, Z. A., Fischer, E. V., Sudo, K., et al. (2016). Evaluating ethane and methane emissions associated with the development of oil and natural gas extraction in North America. *Environmental Research Letters*, *11*(4), 044010. https://doi.org/10.1088/1748-9326/11/4/044010

Gaujoux, R., & Seoighe, C. (2010). A flexible R package for nonnegative matrix factorization. *BMC Bioinformatics*, *11*(1), 367. https://doi.org/10.1186/1471-2105-11-367

Gilman, J. B., Lerner, B. M., Kuster, W. C., & de Gouw, J. A. (2013). Source Signature of Volatile Organic Compounds from Oil and Natural Gas Operations in Northeastern Colorado. *Environmental Science & Technology*, *3*(47), 1297–1305. https://doi.org/10.1021/es304119a

Gilman, Jessica B., Kuster, W. C., Goldan, P. D., Herndon, S. C., Zahniser, M. S., Tucker, S. C., et al. (2009). Measurements of volatile organic compounds during the 2006 TexAQS/GoMACCS campaign: Industrial influences, regional characteristics, and diurnal dependencies of the OH reactivity. *Journal of Geophysical Research: Atmospheres*, *114*(D7). https://doi.org/10.1029/2008JD011525

Goldstein, A. H., Fan, S. M., Goulden, M. L., Munger, J. W., & Wofsy, S. C. (1996). Emissions of ethene, propene, and 1-butene by a midlatitude forest. *Journal of Geophysical Research: Atmospheres*, *101*(D4), 9149–9157. https://doi.org/10.1029/96JD00334

Goodman, P. S., Galatioto, F., Thorpe, N., Namdeo, A. K., Davies, R. J., & Bird, R. N. (2016). Investigating the traffic-related environmental impacts of hydraulic-fracturing (fracking) operations. *Environment International*, *89–90*, 248–260. https://doi.org/10.1016/j.envint.2016.02.002

de Gouw, J. A., Parrish, D. D., Frost, G. J., & Trainer, M. (2014). Reduced emissions of CO_2, NO_x, and SO_2 from U.S. power plants owing to switch from coal to natural gas with combined cycle technology. *Earth's Future*, *2*(2), 75–82. https://doi.org/10.1002/2013EF000196

Guenther, A. B., Jiang, X., Heald, C. L., Sakulyanontvittaya, T., Duhl, T., Emmons, L. K., & Wang, X. (2012). The Model of Emissions of Gases and Aerosols from Nature version 2.1 (MEGAN2.1): an extended and updated framework for modeling biogenic emissions. *Geoscientific Model Development*, *5*(6), 1471–1492. https://doi.org/10.5194/gmd-5-1471-2012

Guha, A., Gentner, D. R., Weber, R. J., Provencal, R., & Goldstein, A. H. (2015). Source apportionment of methane and nitrous oxide in California's San Joaquin Valley at CalNex 2010 via positive matrix factorization. *Atmospheric Chemistry and Physics*, *15*(20), 12043–12063. https://doi.org/10.5194/acp-15-12043-2015

Haman, C. L., Lefer, B., & Morris, G. A. (2012). Seasonal Variability in the Diurnal Evolution of the Boundary Layer in a Near-Coastal Urban Environment. *Journal of Atmospheric and Oceanic Technology*, *29*(5), 697–710. https://doi.org/10.1175/JTECH-D-11-00114.1

Hao, Y., Wang, Y., Mei, X., & Cui, X. (2010). The response of ecosystem CO_2 exchange to small precipitation pulses over a temperate steppe. *Plant Ecology*, *209*(2), 335–347. https://doi.org/10.1007/s11258-010-9766-1

Helmig, D., Rossabi, S., Hueber, J., Tans, P., Montzka, S. A., Masarie, K., et al. (2016). Reversal of global atmospheric ethane and propane trends largely due to US oil

and natural gas production. *Nature Geoscience, advance online publication*. https://doi.org/10.1038/ngeo2721

Hendler, A., Nunn, J., Lundeen, J., & McKaskle, R. (2009). *VOC emissions from oil and condensate storage tanks*. The Woodlands, TX: prepared for Texas Environmental Research Consortium. Retrieved from http://files.harc.edu/projects/airquality/projects/H051C/H051Cfinalreport.pdf

Hinwood, A. L., Rodriguez, C., Runnion, T., Farrar, D., Murray, F., Horton, A., et al. (2007). Risk factors for increased BTEX exposure in four Australian cities. *Chemosphere*, *66*(3), 533–541. https://doi.org/10.1016/j.chemosphere.2006.05.040

Ho, K. F., Lee, S. C., Ho, W. K., Blake, D. R., Cheng, Y., Li, Y. S., et al. (2009). Vehicular emission of volatile organic compounds (VOCs) from a tunnel study in Hong Kong. *Atmospheric Chemistry Physics*, *9*(19), 7491–7504. https://doi.org/10.5194/acp-9-7491-2009

Homer, C., Dewitz, J., Yang, L., Jin, S., Danielson, P., Xian, G., et al. (2015). Completion of the 2011 National Land Cover Database for the Conterminous United States - Representing a Decade of Land Cover Change Information. *Photogrammetric Engineering & Remote Sensing*, *81*(5), 345–354. https://doi.org/10.1016/s0099-1112(15)30100-2

Howard, T. (2015). University of Texas study underestimates national methane emissions at natural gas production sites due to instrument sensor failure. *Energy Science & Engineering*, *3*(5), 443–455. https://doi.org/10.1002/ese3.81

Howard, T., Ferrara, T. W., & Townsend-Small, A. (2015). Sensor transition failure in the high flow sampler: Implications for methane emission inventories of natural gas infrastructure. *Journal of the Air & Waste Management Association*, *65*(7), 856–862. https://doi.org/10.1080/10962247.2015.1025925

Howarth, R. W. (2014). A bridge to nowhere: methane emissions and the greenhouse gas footprint of natural gas. *Energy Science & Engineering*, *2*(2), 47–60. https://doi.org/10.1002/ese3.35

Hu, L., Montzka, S. A., Miller, J. B., Andrews, A. E., Lehman, S. J., Miller, B. R., et al. (2015). U.S. emissions of HFC-134a derived for 2008–2012 from an extensive flask-air sampling network. *Journal of Geophysical Research: Atmospheres*, *120*(2), 2014JD022617. https://doi.org/10.1002/2014JD022617

Intergovernmental Panel on Climate Change. (2015). *Climate change 2014: synthesis report*. (R. K. Pachauri & L. Mayer, Eds.). Geneva, Switzerland: Intergovernmental Panel on Climate Change.

Karion, A., Sweeney, C., Pétron, G., Frost, G., Michael Hardesty, R., Kofler, J., et al. (2013). Methane emissions estimate from airborne measurements over a western United States natural gas field. *Geophysical Research Letters*, *40*(16), 4393–4397. https://doi.org/10.1002/grl.50811

Karion, A., Sweeney, C., Kort, E. A., Shepson, P. B., Brewer, A., Cambaliza, M., et al. (2015). Aircraft-Based Estimate of Total Methane Emissions from the Barnett Shale Region. *Environmental Science & Technology*, *49*(13), 8124–8131. https://doi.org/10.1021/acs.est.5b00217

Kort, E. A., Smith, M. L., Murray, L. T., Gvakharia, A., Brandt, A. R., Peischl, J., et al. (2016). Fugitive emissions from the Bakken shale illustrate role of shale production in global ethane shift: Ethane emissions from the Bakken shale. *Geophysical Research Letters*. https://doi.org/10.1002/2016GL068703

Kort, Eric A., Frankenberg, C., Costigan, K. R., Lindenmaier, R., Dubey, M. K., & Wunch, D. (2014). Four corners: The largest US methane anomaly viewed from space. *Geophysical Research Letters*, *41*(19), 2014GL061503. https://doi.org/10.1002/2014GL061503

Koss, A., Yuan, B., Warneke, C., Gilman, J. B., Lerner, B. M., Veres, P. R., et al. (2017). Observations of VOC emissions and photochemical products over US oil- and gas-producing regions using high-resolution H_3O^+ CIMS (PTR-ToF-MS). *Atmospheric Measurement Techniques*, *10*(8), 2941–2968. https://doi.org/10.5194/amt-10-2941-2017

Kota, S. H., Ying, Q., & Zhang, Y. (2010). TAMNROM-3D: Three-Dimensional Eulerian Model to Simulate Air Quality near Highways. *Transportation Research Record: Journal of the Transportation Research Board*, *2158*(1), 61–68. https://doi.org/10.3141/2158-08

Kota, S. H., Park, C., Hale, M. C., Werner, N. D., Schade, G. W., & Ying, Q. (2014). Estimation of VOC emission factors from flux measurements using a receptor model and footprint analysis. *Atmospheric Environment*, *82*, 24–35. https://doi.org/10.1016/j.atmosenv.2013.09.052

Kruskal, W. H., & Wallis, W. A. (1952). Use of Ranks in One-Criterion Variance Analysis. *Journal of the American Statistical Association*, *47*(260), 583–621. https://doi.org/10.1080/01621459.1952.10483441

Lamanna, M. S., & Goldstein, A. H. (1999). In situ measurements of C_2-C_{10} volatile organic compounds above a Sierra Nevada ponderosa pine plantation. *Journal of Geophysical Research: Atmospheres*, *104*(D17), 21247–21262. https://doi.org/10.1029/1999JD900289

Lammel, G., & Cape, J. N. (1996). Nitrous acid and nitrite in the atmosphere. *Chemical Society Reviews*, *25*(5), 361. https://doi.org/10.1039/cs9962500361

Lamsal, L. N., Duncan, B. N., Yoshida, Y., Krotkov, N. A., Pickering, K. E., Streets, D. G., & Lu, Z. (2015). U.S. NO_2 trends (2005–2013): EPA Air Quality System (AQS) data versus improved observations from the Ozone Monitoring Instrument (OMI). *Atmospheric Environment*, *110*, 130–143. https://doi.org/10.1016/j.atmosenv.2015.03.055

Landrigan, P. J., Fuller, R., Acosta, N. J. R., Adeyi, O., Arnold, R., Basu, N. (Nil), et al. (2017). The Lancet Commission on pollution and health. *The Lancet*, *0*(0). https://doi.org/10.1016/S0140-6736(17)32345-0

Lee, D. D., & Seung, H. S. (1999). Learning the parts of objects by non-negative matrix factorization. *Nature*, *401*(6755), 789.

Lee, T. E., Miller, S. D., Turk, F. J., Schueler, C., Julian, R., Deyo, S., et al. (2006). The NPOESS VIIRS Day/Night Visible Sensor. *Bulletin of the American*

Meteorological Society, *87*(2), 191–200. https://doi.org/10.1175/BAMS-87-2-191

Lee, T. R., & De Wekker, S. F. J. (2016). Estimating Daytime Planetary Boundary Layer Heights over a Valley from Rawinsonde Observations at a Nearby Airport: An Application to the Page Valley in Virginia, United States. *Journal of Applied Meteorology and Climatology*, *55*(3), 791–809. https://doi.org/10.1175/JAMC-D-15-0300.1

Liu, S. C., Trainer, M., Fehsenfeld, F. C., Parrish, D. D., Williams, E. J., Fahey, D. W., et al. (1987). Ozone production in the rural troposphere and the implications for regional and global ozone distributions. *Journal of Geophysical Research: Atmospheres*, *92*(D4), 4191–4207. https://doi.org/10.1029/JD092iD04p04191

Lyman, S. N., Mansfield, M. L., Tran, H. N. Q., Evans, J. D., Jones, C., O'Neil, T., et al. (2018). Emissions of organic compounds from produced water ponds I: Characteristics and speciation. *Science of The Total Environment*, *619–620*, 896–905. https://doi.org/10.1016/j.scitotenv.2017.11.161

Lyon, D. R., Zavala-Araiza, D., Alvarez, R. A., Harriss, R., Palacios, V., Lan, X., et al. (2015). Constructing a Spatially Resolved Methane Emission Inventory for the Barnett Shale Region. *Environmental Science & Technology*, *49*(13), 8147–8157. https://doi.org/10.1021/es506359c

Lyon, D. R., Alvarez, R. A., Zavala-Araiza, D., Brandt, A. R., Jackson, R. B., & Hamburg, S. P. (2016). Aerial Surveys of Elevated Hydrocarbon Emissions from

Oil and Gas Production Sites. *Environmental Science & Technology*, *50*(9), 4877–4886. https://doi.org/10.1021/acs.est.6b00705

McKenzie, L. M., Witter, R. Z., Newman, L. S., & Adgate, J. L. (2012). Human health risk assessment of air emissions from development of unconventional natural gas resources. *Science of The Total Environment*, *424*, 79–87. https://doi.org/10.1016/j.scitotenv.2012.02.018

Mesinger, F., DiMego, G., Kalnay, E., Mitchell, K., Shafran, P. C., Ebisuzaki, W., et al. (2006). North American Regional Reanalysis. *Bulletin of the American Meteorological Society*, *87*(3), 343–360. https://doi.org/10.1175/BAMS-87-3-343

Meyers, T. P. (2001). A comparison of summertime water and CO2 fluxes over rangeland for well watered and drought conditions. *Agricultural and Forest Meteorology*, *106*(3), 205–214. https://doi.org/10.1016/S0168-1923(00)00213-6

National Centers for Environmental Prediction (NCEP). (2016). Eta Data Assimilation System (EDAS40). Retrieved from https://www.ready.noaa.gov/edas40.php

Norris, G. A., Vedantham, R., Wade, K., Brown, S., Prouty, J., & Foley, C. (2008). *EPA Positive Matrix Factorization (PMF) 3.0 Fundamentals & User Guide*. Washington, D.C.: Environmental Protection Agency. Retrieved from https://cfpub.epa.gov/si/si_public_record_report.cfm?Lab=NERL&dirEntryId=199368

Olaguer, E. P. (2012). The potential near-source ozone impacts of upstream oil and gas industry emissions. *Journal of the Air & Waste Management Association*, *62*(8), 966–977. https://doi.org/10.1080/10962247.2012.688923

Olsen, S. C., & J. T. Randerson. (2004). Differences between surface and column atmospheric CO_2 and implications for carbon cycle research. *Journal of Geophysical Research*, *109*(D2). https://doi.org/10.1029/2003JD003968

Paatero, P., & Tapper, U. (1994). Positive matrix factorization: A non-negative factor model with optimal utilization of error estimates of data values. *Environmetrics*, *5*(2), 111–126. https://doi.org/10.1002/env.3170050203

Pacsi, A. P., Kimura, Y., McGaughey, G., McDonald-Buller, E. C., & Allen, D. T. (2015). Regional Ozone Impacts of Increased Natural Gas Use in the Texas Power Sector and Development in the Eagle Ford Shale. *Environmental Science & Technology*, *49*(6), 3966–3973. https://doi.org/10.1021/es5055012

Park, C., Schade, G. W., & Boedeker, I. (2010). Flux measurements of volatile organic compounds by the relaxed eddy accumulation method combined with a GC-FID system in urban Houston, Texas. *Atmospheric Environment*, *44*(21), 2605–2614. https://doi.org/10.1016/j.atmosenv.2010.04.016

Parrish, D., Kemball-Cook, S., Grant, J., & Yarwood, G. (2017). *Science Synthesis Report: Atmospheric Impacts of Oil and Gas Development in Texas* (Final Report No. 582-16-63215–16) (p. 178). Austin, Texas: Texas Commission on Environmental Quality. Retrieved from

https://www.tceq.texas.gov/assets/public/implementation/air/am/contracts/reports/oth/582166321516-20170629-environ-oilgas_impact_aq_synthesis.pdf

Peischl, J., Ryerson, T. B., Aikin, K. C., de Gouw, J. A., Gilman, J. B., Holloway, J. S., et al. (2015). Quantifying atmospheric methane emissions from the Haynesville, Fayetteville, and northeastern Marcellus shale gas production regions: CH_4 emissions from shale gas production. *Journal of Geophysical Research: Atmospheres*, *120*(5), 2119–2139. https://doi.org/10.1002/2014JD022697

Peischl, J., Eilerman, S. J., Neuman, J. A., Aikin, K. C., Gouw, J. de, Gilman, J. B., et al. (2018). Quantifying Methane and Ethane Emissions to the Atmosphere From Central and Western U.S. Oil and Natural Gas Production Regions. *Journal of Geophysical Research: Atmospheres*, *123*(14), 7725–7740. https://doi.org/10.1029/2018JD028622

Pétron, G., Frost, G. J., Sweeney, C., Karion, A., Miller, B. R., Montzka, S. A., et al. (2012). Estimation of emissions from oil and natural gas operations in northeastern Colorado. Presented at the 2012 International Emission Inventory Conference, Tampa, Florida. Retrieved from http://www.epa.gov/ttnchie1/conference/ei20/session6/gpetron_pres.pdf

Pétron, G., Karion, A., Sweeney, C., Miller, B. R., Montzka, S. A., Frost, G. J., et al. (2014). A new look at methane and nonmethane hydrocarbon emissions from oil and natural gas operations in the Colorado Denver-Julesburg Basin: Hydrocarbon emissions in oil & gas basin. *Journal of Geophysical Research: Atmospheres*, *119*(11), 6836–6852. https://doi.org/10.1002/2013JD021272

Pikelnaya, O., Flynn, J. H., Tsai, C., & Stutz, J. (2013). Imaging DOAS detection of primary formaldehyde and sulfur dioxide emissions from petrochemical flares. *Journal of Geophysical Research: Atmospheres*, *118*(15), 8716–8728. https://doi.org/10.1002/jgrd.50643

Pouillot, R., & Delignette-Muller, M.-L. (2010). Evaluating variability and uncertainty in microbial quantitative risk assessment using two R packages. *International Journal of Food Microbiology*, *142*(3), 330–40.

Poynter, M. E., Persinger, R. L., Irvin, C. G., Butnor, K. J., van Hirtum, H., Blay, W., et al. (2006). Nitrogen dioxide enhances allergic airway inflammation and hyperresponsiveness in the mouse. *American Journal of Physiology. Lung Cellular and Molecular Physiology*, *290*(1), L144-152. https://doi.org/10.1152/ajplung.00131.2005

Pring, M. (2012). *Condensate Tank Oil and Gas Activities* (Final Report No. ERG. No. 0292.01.011.001). Morrisville, North Carolina: Eastern Research Group, Inc.

R Core Team. (2018). *R: A Language and Environment for Statistical Computing*. Vienna, Austria: R Foundation for Statistical Computing. Retrieved from https://www.R-project.org/

Railroad Commission of Texas. (n.d.). *Oil and Gas Production Data* (Dataset). Austin, Texas. Retrieved from http://webapps.rrc.state.tx.us/PDQ/generalReportAction.do

Randerson, J. T., Van Der Werf, G.R., Giglio, L., Collatz, G.J., & Kasibhatla, P.S. (2015). Global Fire Emissions Database, Version 4, (GFEDv4). https://doi.org/10.3334/ORNLDAAC/1293

Rappenglück, B., Perna, R., Zhong, S., & Morris, G. A. (2008). An analysis of the vertical structure of the atmosphere and the upper-level meteorology and their impact on surface ozone levels in Houston, Texas. *Journal of Geophysical Research: Atmospheres*, *113*(D17). https://doi.org/10.1029/2007JD009745

Reff, A., Eberly, S. I., & Bhave, P. V. (2007). Receptor Modeling of Ambient Particulate Matter Data Using Positive Matrix Factorization: Review of Existing Methods. *Journal of the Air & Waste Management Association*, *57*(2), 146–154. https://doi.org/10.1080/10473289.2007.10465319

Rubin, J. I., Kean, A. J., Harley, R. A., Millet, D. B., & Goldstein, A. H. (2006). Temperature dependence of volatile organic compound evaporative emissions from motor vehicles. *Journal of Geophysical Research: Atmospheres*, *111*(D3). https://doi.org/10.1029/2005JD006458

Ryan, M. (2014, March 21). Boom times on the bay: Dow , other firms fuel development south of Houston. Retrieved July 17, 2015, from http://www.bizjournals.com/houston/print-edition/2014/03/21/boom-times-on-the-bay-dow-other-firms-fuel.html

Sakugawa, H., Kaplan, I. R., Tsai, W., & Cohen, Y. (1990). Atmospheric hydrogen peroxide. *Environmental Science & Technology*, *24*(10), 1452–1462. https://doi.org/10.1021/es00080a002

Schade, G. W., & Roest, G. (2016). Analysis of non-methane hydrocarbon data from a monitoring station affected by oil and gas development in the Eagle Ford shale, Texas. *Elementa: Science of the Anthropocene*, *4*, 000096. https://doi.org/10.12952/journal.elementa.000096

Schade, G. W., & Roest, G. (2018). Source apportionment of non-methane hydrocarbons, NO_x and H_2S data from a central monitoring station in the Eagle Ford shale, Texas. *Elemta: Science of the Anthropocene*, *6*(1). https://doi.org/10.1525/elementa.289

Schade, G. W., & Roest, G. S. (2015). Is the Shale Boom Reversing Progress in Curbing Ozone Pollution? *Eos*, *96*. https://doi.org/10.1029/2015EO028279

Schmid, P., & Niyogi, D. (2012). A Method for Estimating Planetary Boundary Layer Heights and Its Application over the ARM Southern Great Plains Site. *Journal of Atmospheric and Oceanic Technology*, *29*(3), 316–322. https://doi.org/10.1175/JTECH-D-11-00118.1

Schneising, O., Burrows, J. P., Dickerson, R. R., Buchwitz, M., Reuter, M., & Bovensmann, H. (2014). Remote sensing of fugitive methane emissions from oil and gas production in North American tight geologic formations: Remote sensing of fugitive methane emissions from oil and gas production. *Earth's Future*, *2*(10), 548–558. https://doi.org/10.1002/2014EF000265

Schwietzke, S., Griffin, W. M., Matthews, H. S., & Bruhwiler, L. M. P. (2014). Natural Gas Fugitive Emissions Rates Constrained by Global Atmospheric Methane and

Ethane. *Environmental Science & Technology*, *48*(14), 7714–7722. https://doi.org/10.1021/es501204c

Seinfeld, J. H., & Pandis, S. N. (1998). *Atmospheric chemistry and physics: from air pollution to climate change*. New York: Wiley.

Simon, H., Reff, A., Wells, B., Xing, J., & Frank, N. (2015). Ozone Trends Across the United States over a Period of Decreasing NO_x and VOC Emissions. *Environmental Science & Technology*, *49*(1), 186–195. https://doi.org/10.1021/es504514z

Simpson, I. J., Sulbaek Andersen, M. P., Meinardi, S., Bruhwiler, L., Blake, N. J., Helmig, D., et al. (2012). Long-term decline of global atmospheric ethane concentrations and implications for methane. *Nature*, *488*(7412), 490–494. https://doi.org/10.1038/nature11342

Smith, M. L., Kort, E. A., Karion, A., Sweeney, C., Herndon, S. C., & Yacovitch, T. I. (2015). Airborne Ethane Observations in the Barnett Shale: Quantification of Ethane Flux and Attribution of Methane Emissions. *Environmental Science & Technology*, *49*(13), 8158–8166. https://doi.org/10.1021/acs.est.5b00219

SRI Instruments. (n.d.). PeakSimple Chromatography Software (Version Peak388) [Windows 10]. SRI Instruments.

Stein, A. F., Draxler, R. R., Rolph, G. D., Stunder, B. J. B., Cohen, M. D., & Ngan, F. (2015). NOAA's HYSPLIT Atmospheric Transport and Dispersion Modeling System. *Bulletin of the American Meteorological Society*, *96*(12), 2059–2077. https://doi.org/10.1175/BAMS-D-14-00110.1

Strosher, M. T. (2000). Characterization of Emissions from Diffusion Flare Systems. *Journal of the Air & Waste Management Association*, *50*(10), 1723–1733. https://doi.org/10.1080/10473289.2000.10464218

Stull, R. B. (2009). *An introduction to boundary layer meteorology* (1st ed). New York: Springer.

Swarthout, R. F., Russo, R. S., Zhou, Y., Miller, B. M., Mitchell, B., Horsman, E., et al. (2015). Impact of Marcellus Shale Natural Gas Development in Southwest Pennsylvania on Volatile Organic Compound Emissions and Regional Air Quality. *Environmental Science & Technology*, *49*(5), 3175–3184. https://doi.org/10.1021/es504315f

Texas Administrative Code. Permits by rule, 30 TAC Chapter 106 §. Retrieved from https://texreg.sos.state.tx.us/public/readtac$ext.ViewTAC?tac_view=4&ti=30&pt=1&ch=106

Texas Commission on Environmental Quality. (2005). Standard Operating Procedure for the Perkin-Elmer Auto Gas Chromatograph for VOC Ozone Precursors Analysis (FOSTAT-026). Field Operations Division.

Texas Commission on Environmental Quality. (2015). Wind Roses. Retrieved May 27, 2016, from http://www.tceq.state.tx.us/airquality/monops/windroses.html

Texas Department of Transportation. (2018). *AADT and AADT Trucks by Year for 1/1/2008 - 12/31/2017: Criteria: Pt = FM0186-KG* (Transportation Planning and Programming Division's Statewide Traffic Analysis and Reporting System II).

Retrieved from http://txdot.ms2soft.com/tcds/tsearch.asp?loc=Txdot&mod=TCDS

Texas Statutes. Natural Resources Code, Title 3, Subtitle B, Chapter 91, Section 91.052, 91 Title 3: Oil and Gas § 91.052 (1977). Retrieved from http://www.statutes.legis.state.tx.us/Docs/NR/htm/NR.91.htm

Thiem, A., Schlink, U., Pan, X.-C., Hu, M., Peters, A., Wiedensohler, A., et al. (2012). Using non-negative matrix factorization for the identification of daily patterns of particulate air pollution in Beijing during 2004–2008. *Atmospheric Chemistry and Physics Discussions*, *12*(5), 13015–13052. https://doi.org/10.5194/acpd-12-13015-2012

Todd, M. (2011). *Proposed Rulemaking - Oil and Gas Sector Regulations Standards of Performance for New Stationary Sources: Oil and Natural Gas Production and Natural Gas Transmission and Distribution* (Memorandum No. Docket ID No. EPA-HQ-OAR-2010-0505). Washington, DC: American Petroleum Institute. Retrieved from https://www.whitehouse.gov/sites/default/files/omb/assets/oira_2060/2060_03222012-2.pdf

Torres, V. M., Herndon, S., Wood, E., Al-Fadhli, F. M., & Allen, D. T. (2012). Emissions of Nitrogen Oxides from Flares Operating at Low Flow Conditions. *Industrial & Engineering Chemistry Research*, *51*(39), 12600–12605. https://doi.org/10.1021/ie300179x

Tran, H. N. Q., Lyman, S. N., Mansfield, M. L., O'Neil, T., Bowers, R. L., Smith, A. P., & Keslar, C. (2018). Emissions of organic compounds from produced water

ponds II: Evaluation of flux chamber measurements with inverse-modeling techniques. *Journal of the Air & Waste Management Association*, *68*(7), 713–724. https://doi.org/10.1080/10962247.2018.1426654

Tsai, W. Y., Chan, L. Y., Blake, D. R., & Chu, K. W. (2006). Vehicular fuel composition and atmospheric emissions in South China: Hong Kong, Macau, Guangzhou, and Zhuhai. *Atmospheric Chemistry and Physics*, *6*(11), 3281–3288. https://doi.org/10.5194/acp-6-3281-2006

United States Committee on Extension to the Standard Atmosphere. (1976). *U.S. standard atmosphere, 1976*. National Oceanic and Atmospheric Administration : for sale by the Supt. of Docs., U.S. Govt. Print. Off. Retrieved from https://books.google.com/books?id=x488AAAAIAAJ

U.S. Centers for Disease Control. (2014). Benzene - NIOSH Publications and Products. Retrieved May 23, 2016, from http://www.cdc.gov/niosh/idlh/71432.html

U.S. Department of Agriculture. (2014). National Agriculture Imagery Program (NAIP) 2014 1m NC\CIR Orthoimagery. Orthoimagery. Retrieved from https://tnris.org/data-catalog/entry/national-agriculture-imagery-program-naip-2014-1m-nc-cir/

U.S. Energy Information Administration. (2016, February 2). Carbon Dioxide Emissions Coefficients. Retrieved May 23, 2016, from http://www.eia.gov/environment/emissions/co2_vol_mass.cfm

U.S. Energy Information Administration. (2017a). *Tight oil production estimates*. Retrieved from https://www.eia.gov/energyexplained/data/U.S.%20tight%20oil%20production.xlsx

U.S. Energy Information Administration. (2017b). *U.S. Natural Gas Gross Withdrawals from Shale Gas*. Retrieved from https://www.eia.gov/dnav/ng/hist/ngm_epg0_fgs_nus_mmcfa.htm

U.S. Energy Information Administration. (2018a, March 8). How much shale gas is produced in the United States? Retrieved May 16, 2018, from https://www.eia.gov/tools/faqs/faq.php?id=907&t=8

U.S. Energy Information Administration. (2018b, March 8). How much shale (tight) oil is produced in the United States? Retrieved May 16, 2018, from https://www.eia.gov/tools/faqs/faq.php?id=847&t=6

U.S. Energy Information Administration. (2018c, April 30). Crude Oil Production. Retrieved May 14, 2018, from https://www.eia.gov/dnav/pet/pet_crd_crpdn_adc_mbbl_m.htm

U.S. Energy Information Administration. (2018d, May 14). Drilling Productivity Report. Retrieved May 17, 2018, from https://www.eia.gov/petroleum/drilling/faqs.php

U.S. Energy Information Administration. (2018e, May 16). Cushing, OK WTI Spot Price FOB (Dollars per Barrel). Retrieved May 17, 2018, from https://www.eia.gov/dnav/pet/hist/RWTCD.htm

U.S. Environmental Protection Agency. (2009). Provisional Peer-Reviewed Toxicity Values for Complex Mixtures of Aliphatic and Aromatic Hydrocarbons [Reports

& Assessments]. Retrieved October 8, 2018, from https://cfpub.epa.gov/ncea/risk/recordisplay.cfm?deid=339011

U.S. Environmental Protection Agency. (2014, April 9). Criteria Air Pollutants [Policies and Guidance]. Retrieved May 15, 2018, from https://www.epa.gov/criteria-air-pollutants

U.S. Environmental Protection Agency. (2015a). *Inventory of U.S. Greenhouse Gas Emissions and Sinks: 1990-2013* (No. EPA 430-R-15-004). Washington, DC. Retrieved from https://www.epa.gov/ghgemissions/inventory-us-greenhouse-gas-emissions-and-sinks-1990-2013

U.S. Environmental Protection Agency. (2015b, June 5). Health Effects of Ozone Pollution [Overviews and Factsheets]. Retrieved October 27, 2017, from https://www.epa.gov/ozone-pollution/health-effects-ozone-pollution

U.S. Environmental Protection Agency. (2015c, October 20). SPECIATE Version 4.5 through 4.0 [Policies and Guidance]. Retrieved June 8, 2018, from https://www.epa.gov/air-emissions-modeling/speciate-version-45-through-40

U.S. Environmental Protection Agency. (2015d, October 26). National Ambient Air Quality Standards for Ozone; Final Rule. Retrieved from http://www.gpo.gov/fdsys/pkg/FR-2015-10-26/pdf/2015-26594.pdf

U.S. Environmental Protection Agency. (2015e, December 16). Initial List of Hazardous Air Pollutants with Modifications [Reports and Assessments]. Retrieved May 15, 2018, from https://www.epa.gov/haps/initial-list-hazardous-air-pollutants-modifications

U.S. Environmental Protection Agency. (2016a). *Inventory of U.S. Greenhouse Gas Emissions and Sinks: 1990-2014* (No. EPA 430-R-16-002). Washington, DC. Retrieved from https://www.epa.gov/ghgemissions/inventory-us-greenhouse-gas-emissions-and-sinks-1990-2014

U.S. Environmental Protection Agency. (2016b, May 4). Air Quality - National Summary [Data and Tools]. Retrieved October 27, 2017, from https://www.epa.gov/air-trends/air-quality-national-summary

U.S. Environmental Protection Agency. (2016c, September 26). AP-42: Compilation of Air Emissions Factors [Policies and Guidance]. Retrieved May 17, 2018, from https://www.epa.gov/air-emissions-factors-and-quantification/ap-42-compilation-air-emissions-factors

U.S. Geological Survey. (2013). USGS NED 1/3 arc-second 2013. Raster digital data. Retrieved from https://nationalmap.gov/elevation.html

Vigliani, E. C., & Forni, A. (1976). Benzene and leukemia. *Environmental Research*, *11*(1), 122–127. https://doi.org/10.1016/0013-9351(76)90115-8

Vinken, G. C. M., Boersma, K. F., Maasakkers, J. D., Adon, M., & Martin, R. V. (2014). Worldwide biogenic soil NO_x emissions inferred from OMI NO_2 observations. *Atmospheric Chemistry and Physics*, *14*(18), 10363–10381. https://doi.org/10.5194/acp-14-10363-2014

Walters, C. K., Winkler, J. A., Shadbolt, R. P., Ravensway, J. van, & Bierly, G. D. (2008). A Long-Term Climatology of Southerly and Northerly Low-Level Jets

for the Central United States. *Annals of the Association of American Geographers*, *98*(3), 521–552. https://doi.org/10.1080/00045600802046387

Wang, G., Kossenkov, A. V., & Ochs, M. F. (2006). LS-NMF: A modified non-negative matrix factorization algorithm utilizing uncertainty estimates. *BMC Bioinformatics*, *7*, 175. https://doi.org/10.1186/1471-2105-7-175

Watson, J. G., Chow, J. C., & Fujita, E. M. (2001). Review of volatile organic compound source apportionment by chemical mass balance. *Atmospheric Environment*, *35*(9), 1567–1584. https://doi.org/10.1016/S1352-2310(00)00461-1

Wegmann, M., Fehrenbach, A., Heimann, S., Fehrenbach, H., Renz, H., Garn, H., & Herz, U. (2005). NO_2-induced airway inflammation is associated with progressive airflow limitation and development of emphysema-like lesions in C57BL/6 mice. *Experimental and Toxicologic Pathology*, *56*(6), 341–350. https://doi.org/10.1016/j.etp.2004.12.004

Wilbur, S., Williams, M., Williams, R., Scinicariello, F., Klotzbach, J. M., Diamond, G. L., & Citra, M. (2012). *Toxicological Profile for Carbon Monoxide*. Atlanta (GA): Agency for Toxic Substances and Disease Registry (US). Retrieved from http://www.ncbi.nlm.nih.gov/books/NBK153693/

Williams, E. J., Hutchinson, G. L., & Fehsenfeld, F. C. (1992). NOx And N2O Emissions From Soil. *Global Biogeochemical Cycles*, *6*(4), 351–388. https://doi.org/10.1029/92GB02124

Willyard, K. (2017, May 17). The need for better Texas oil and gas industry regulatory data. Retrieved March 13, 2018, from https://www.tribtalk.org/2017/05/17/the-need-for-better-texas-oil-and-gas-industry-regulatory-data/

Worden, H. M., Deeter, M. N., Frankenberg, C., George, M., Nichitiu, F., Worden, J., et al. (2013). Decadal record of satellite carbon monoxide observations. *Atmospheric Chemistry and Physics*, *13*(2), 837–850. https://doi.org/10.5194/acp-13-837-2013

Xiao, Y., Logan, J. A., Jacob, D. J., Hudman, R. C., Yantosca, R., & Blake, D. R. (2008). Global budget of ethane and regional constraints on U.S. sources. *Journal of Geophysical Research*, *113*(D21). https://doi.org/10.1029/2007JD009415

Yew, C. H., & Weng, X. (2015). *Mechanics of hydraulic fracturing* (Second edition). Amsterdam: Elsevier/GPP.

Ying, Q., & Krishnan, A. (2010). Source contributions of volatile organic compounds to ozone formation in southeast Texas. *Journal of Geophysical Research: Atmospheres*, *115*(D17), D17306. https://doi.org/10.1029/2010JD013931

Zeldovich, Y. B. (1992). *Selected Works of Yakov Borisovich Zeldovich* (Vols. 1–2). Princeton, New Jersey: Princeton University Press.

APPENDIX A

DERIVATION OF ALKANE PARTITIONING EQUATION

A puff from two emission sources, source "A" and source "B", are mixed into a volume of air. Assume that there are no other emission sources and no sinks. Both sources emit two compounds, *x* and *y*, with the emission ratios of $\left(\frac{y}{x}\right)_A$ and $\left(\frac{y}{x}\right)_B$. In the absence of source B, the mixing ratios in the volume would result only from source A: $[x]_A$ and $[y]_A$, and their ratio would be equal to the emission ratio:

$$\frac{[y]_A}{[x]_A} = \left(\frac{y}{x}\right)_A \tag{A1}$$

Likewise, considering only the emissions from source B:

$$\frac{[y]_B}{[x]_B} = \left(\frac{y}{x}\right)_B \tag{A2}$$

When the puffs from both sources are mixed into the volume, the total mixing ratios are:

$$[x]_{tot} = [x]_A + [x]_B \tag{A3}$$

$$[y]_{tot} = [y]_A + [y]_B \tag{A4}$$

Thus, the ratio of the total emission ratios is

$$\frac{[y]_{tot}}{[x]_{tot}} \stackrel{\text{def}}{=} \left(\frac{y}{x}\right)_{tot} = \frac{[y]_A+[y]_B}{[x]_A+[x]_B} = \frac{[y]_A+[y]_B}{[x]_{tot}} \tag{A5}$$

From (A1)

$$[y]_A = [x]_A \left(\frac{y}{x}\right)_A \tag{A6}$$

and (A2)

$$[y]_B = [x]_B \left(\frac{y}{x}\right)_B \tag{A7}$$

From (A4),

$$[x]_B = [x]_{tot} - [x]_A \tag{A8}$$

and (A7) becomes

$$[y]_B = ([x]_{tot} - [x]_A)\left(\frac{y}{x}\right)_B \tag{A9}$$

Substituting (A6) and (A9) into (A5):

$$\left(\frac{y}{x}\right)_{tot} = \frac{[x]_A}{[x]_{tot}}\left(\frac{y}{x}\right)_A + \frac{([x]_{tot}-[x]_A)}{[x]_{tot}}\left(\frac{y}{x}\right)_B \tag{A10}$$

$$\left(\frac{y}{x}\right)_{tot} = \frac{[x]_A}{[x]_{tot}}\left\{\left(\frac{y}{x}\right)_A - \left(\frac{y}{x}\right)_B\right\} + \frac{[x]_{tot}}{[x]_{tot}}\left(\frac{y}{x}\right)_B \tag{A11}$$

$$\left(\frac{y}{x}\right)_{tot} - \left(\frac{y}{x}\right)_B = \frac{[x]_A}{[x]_{tot}}\left\{\left(\frac{y}{x}\right)_A - \left(\frac{y}{x}\right)_B\right\} \tag{A12}$$

$$\frac{\left(\frac{y}{x}\right)_{tot}-\left(\frac{y}{x}\right)_B}{\left(\frac{y}{x}\right)_A-\left(\frac{y}{x}\right)_B} = \frac{[x]_A}{[x]_{tot}} \stackrel{\text{def}}{=} f_{x,A} \tag{A13}$$

$f_{x,A} = \frac{[x]_A}{[x]_{tot}}$ is the fraction of the observed mixing ratio of *x* that came from source A. (A13) shows that it can be derived only from the ratio of the observed *x* and *y* mixing ratios and knowledge of the emissions factors for the two sources. The fraction of *y* from source A:

$$f_{y,A} = \frac{[y]_A}{[y]_{tot}} \tag{A14}$$

can be derived from (A5)

$$[y]_{tot} = [x]_{tot}\left(\frac{y}{x}\right)_{tot} \tag{A15}$$

and (A6) to yield:

$$f_{y,A} = \frac{[y]_A}{[y]_{tot}} = \frac{[x]_A\left(\frac{y}{x}\right)_A}{[x]_{tot}\left(\frac{y}{x}\right)_{tot}} \tag{A16}$$

From (A13), (A16) can be expressed as

$$f_{y,A} = f_{x,A} \frac{\left(\frac{y}{x}\right)_A}{\left(\frac{y}{x}\right)_{tot}} \tag{A17}$$

This demonstrates that once one species is partitioned between the sources, the other species can be partitioned as well.